Melt Processing of Metastable Acrylic Copolymer Carbon Precursors

By

Michael J. Bortner

Dissertation submitted to the Faculty of
Virginia Polytechnic Institute and State University
in partial fulfillment of the requirements for the degree of

DOCTOR OF PHILOSOPHY

in

Chemical Engineering

Dr. Donald G. Baird, Chairman
Dr. James E. McGrath
Dr. Richey M. Davis
Dr. Thomas C. Ward
Dr. Garth L. Wilkes
Dr. Ravi Saraf

November 14, 2003

Blacksburg, VA

Keywords: Carbon fiber, melt processing, carbon dioxide, plasticizer, acrylonitrile, rheology

Melt Processing of Metastable Acrylic Copolymer Carbon Precursors

Michael J. Bortner

(ABSTRACT)

This thesis is concerned with the development of engineering technologies that facilitate melt spinning of carbon fiber precursors in both an environmentally sound and cost effective manner. More specifically, methods were developed to avoid a degradative process in acrylonitrile copolymers (typically used in textiles and as carbon fiber precursors) that occurs as melt spinning temperatures are approached. The following set of analyses was developed to define the rheological properties required for a melt processable acrylic copolymer suitable for use as a carbon fiber precursor, and accordingly facilitated development of a processing window: measurement of steady shear viscosity as a function of both temperature and time, measurement of the magnitude of the complex viscosity ($|\eta^*|$) as a function of temperature using a temperature sweep, and measurement of the angular frequency dependence of $|\eta^*|$. Through a systematic screening process, the following properties were identified to afford melt spinnable acrylic precursors suitable for conversion to carbon fibers: emulsion polymerization, 85-88 mole % acrylonitrile, 11-14 mole % methyl acrylate, 1 mole % acryloyl benzophenone, intrinsic viscosity < 0.6 dL/g, steady shear viscosity $\leq$ 1000-2000 Pa*s at a shear rate ($\dot{\gamma}$) of 0.1 s^{-1}, viscosity increases $\leq 45\%$ over a period of 1800 seconds at 200-220^{o}C and $\dot{\gamma}$=0.1 s^{-1}. Use of the rheological analyses assisted in development of a melt spinnable carbon fiber precursor, which resulted in carbon fibers possessing a tensile strength and modulus of approximately 1.0 and 120 GPa, respectively.

A second approach was evaluated using carbon dioxide (CO_2) to plasticize AN copolymers to an extent that facilitates processing at reduced temperatures, below where thermal degradation is significant. A batch saturation method to absorb CO_2 in AN copolymers was developed. Differential scanning calorimetry and thermogravimetric analyses were used to measure the glass transition temperature (T_g) reduction and amount of absorbed CO_2 (respectively). A pressurized rheometer and measurement procedure was designed to obtain viscosity measurements of saturated AN copolymers. Up to 6.7 wt. % CO_2 was found to absorb into a 65 mole % AN copolymer with the saturation method used, resulting in a 31^{o}C glass transition temperature (T_g) reduction, 60% viscosity reduction, and 30^{o}C potential processing temperature reduction. It was found that CO_2 can absorb into copolymers containing up to 90 mole % AN (with the absorption methods used) with the following results (for a 90/10 mole % AN/MA copolymer): 3.0 wt. % uptake, 27^{o}C T_g reduction, 56% viscosity reduction, and potential processing temperature reduction of 9^{o}C. Via estimates of the required pressure, sealing fluid flow rate, and length of a pressure chamber to prevent foaming of the saturated polymer melt during extrusion, melt spinning of saturated AN copolymers appears feasible.

Acknowledgments

The author would like to express his appreciation to Professor Donald G. Baird for guidance and support throughout the completion of this work. In addition, the author wishes to extend special thanks to Prof. James E. McGrath, who also provided a great deal of guidance during this work. The author would also like to thank Prof. Garth Wilkes, Prof. Tom Ward, Prof. Richey Davis, and Prof. Ravi Saraf for serving on his research committee.

The author would also like to give special recognition to the following groups and individuals:

- His wife, Lori, for providing immeasurable support and peace of mind.
- His parents and sister for helping him to become the person he is today.
- Lynn and Fred, Jimbo, and the Selembos for their encouragement and wisdom.
- All of the graduate students and post-docs he has had the pleasure to know and work alongside at Virginia Tech. Special gratitude is extended to the following individuals for providing assistance on numerous occations: Dr. Phillip Doerpinghaus, Dr. Ashish Aneja, Dr. Emmett O'Brien, Eric Scribben, Matt Wilding, and Quang Nguyen.
- Prof. Dan Edie for providing a wealth of information, and for use of his laser micrometer
- Members of the departmental staff who have helped make this work easier over the years: Chris, Diane, Riley, and Wendell.

Original Contributions

The following are considered to be significant original contributions of this research:

1) Identification of a set of rheological measurements that can be used to evaluate the ability to melt process AN copolymers, which could also be applied to other thermally unstable/metastable systems to develop a processing window. Incorporation of a chemorheological model to quantify the melt stability.

2) Development of a batch saturation procedure that facilitates absorption of CO_2 into metastable AN copolymers with minimal degradation. Establishment of the conditions necessary for batch absorption, including the temperature, pressure, and time dependence.

3) Development of a pressurized capillary rheometer and measurement procedure to obtain the viscosity of AN copolymer systems that contain absorbed CO_2. In particular, conditions were identified to minimize degradation, hinder bubble nucleation, prevent foaming, and maintain a single phase melt during the measurements.

4) Estimation of the feasibility of a step down pressure chamber that will facilitate melt processing of AN copolymers containing absorbed CO_2 without foaming.

Table of Contents

List of Figures

Chapter 3.0

Chapter 4.0

Chapter 5.0

Chapter 6.0

LIST OF TABLES

1.0 Introduction

1.0 Introduction

Carbon fibers may be one of the most successful newly commercialized carbon products in the past 35 years[1]. Carbon fibers have a wide range of desirable properties, including light weight and high strength. Such properties make carbon fibers attractive for a multitude of applications, including automotive, sporting goods, and aircraft structures. A great deal of research and progress has refined carbon fibers and their production into the materials that we use today.

The notion of cellulose based carbon fibers was first studied as long ago as 1880 with the patent of an incandescent lamp by Thomas Edison[2]. The filaments were made of carbon and produced by pyrolyzing cellulose fibers. Much work was performed in the following 30 years to coat the filaments and improve their durability. With the introduction of flexible tungsten filaments, interest in carbon fibers dropped significantly thereafter[3].

When the aerospace industry requirement for lightweight materials became urgent in the 1950s and 60s, carbon fibers as we know them today evolved[4]. The excellent properties of carbon fibers, including low density, high stiffness and strength, good resistance to chemical and environmental effects, low thermal expansion, good fatigue resistance and vibration damping, and ability to withstand high temperatures, have earned carbon fibers an important place in today's high-tech areas[1;5;6]. Carbon fibers are found in a multitude of applications, ranging from sporting goods to aircraft structures[1].

There are three major methods of commercial carbon fiber production that result in fibers with significantly different properties. Rayon based carbon fibers, first commercially produced by Union Carbide in the early 1960s (Thornel), have been losing importance because of poor carbon yield[7]. These fibers had a tensile modulus of 520 GPa and a tensile strength of 2.65 GPa.

During the same time frame, pitch based carbon fibers were being produced from a low-cost, isotropic pitch (byproduct of petroleum refinement) that resulted in poor mechanical properties. In 1973, a process was patented to transfer the pitch into an anisotropic liquid crystalline (mesophase) state prior to filament spinning, resulting in carbon fibers with improved mechanical properties, including a tensile modulus as high as 690 GPa.

The advent of a polyacrylonitrile, or PAN, precursor by Tsunoda in 1960 brought about the most widely accepted method of carbon fiber production today[6]. PAN based fibers generally have a lower volume fraction of voids and higher strength than the pitch based fibers, as well as flexibility for tailoring a final product. Fibers with a tensile modulus of 210-800 GPa and tensile strengths of 1.62-3.28 GPa can be commercially produced. The isotropic pitch process is lower cost but does not provide the superior mechanical properties observed in PAN based carbon fibers[5]. Carbon fibers produced from the mesophase pitch process do possess higher moduli, but inferior properties otherwise. In addition, the extra step required to transfer the pitch into mesophase form results in a higher cost of production than with PAN. Figure 1.1 compares the mechanical properties of PAN and pitch based carbon fibers. Note the superior tensile strength of the acrylic based fibers, in some instances with a three-fold increase in tensile strength.

Successful production of an acrylic based carbon fiber requires the formation of a precursor fiber that possesses specific traits, including a small diameter, specific chemical composition, and certain thermal characteristics, that allow it to be thermally oxidized (cyclized) into the form of a ladder polymer[4]. The ladder form is then carbonized or graphitized into either a carbon or graphite fiber, respectively. Thermal oxidation, as the name itself implies, is a process that requires an elevated temperature in an oxygen-enriched atmosphere. Cyclization of a stretched precursor fiber takes place during this step as a result of thermal instability between the

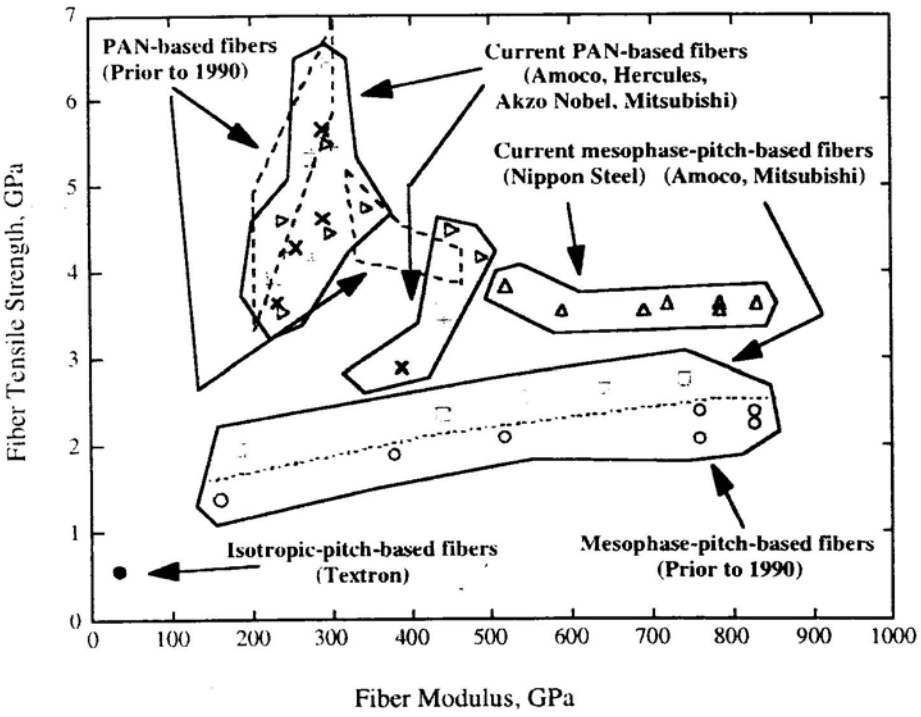

Figure 1.1: Mechanical property comparison of pitch and acrylic based carbon fibers[1].

acrylonitrile groups.

In order to avoid cyclization and decomposition of the precursor polymer prior to fiber formation, commercial acrylic based carbon fiber precursors are generally formed via a solution spinning fiber production process. Solution spinning involves the extrusion of a concentrated solution of up to thirty weight percent precursor polymer through a spinneret and into a coagulation bath. The polarity of the PAN homopolymer requires the use of highly polar organic solvents, which are generally considered environmentally unfriendly and must be recovered in the process.

Currently, the market for carbon fibers is over saturated[8]. Annual global demand for PAN based carbon fibers is approximately 31 million pounds, with the global production capacity at 51 million pounds. The result is the plummet of carbon fiber prices from as high as $16/lb a few years ago to as low as $6.50/lb, depending on the grade of fiber[8]. For most industries, such as in the automotive sector, $6.50/lb is still too high for large-scale incorporation of carbon fibers. In such a competitive market, the need arises for a lower cost carbon fiber production process. A melt spinning process then becomes attractive to negate the extra costs incurred with solvent use and recovery and increase the solid throughput on a per pound basis.

A melt spinning fiber production process requires the extrusion of only the pure polymer precursor directly into fiber form, eliminating the extra expense of solvent recovery and providing a more environmentally sound solution[1]. However, melt spinning of traditional acrylic precursors requires elevated temperatures (~220^{o}C) at which the PAN would cyclize and decompose in the extrusion process, rendering the material intractable prior to fiber spinning. In order to successfully melt spin an acrylic carbon fiber precursor, a processable material must be selected. A copolymer precursor of acrylonitrile and a suitable comonomer is the widely

accepted material for wet spun precursor fiber production[3]. The comonomer was originally used to assist in dye uptake (for textiles) and to lower the glass transition temperature of the pure homopolymer, facilitating stretching of the precursor fiber prior to thermal treatment[7]. Previous reports have indicated the importance of comonomer use, chemistry, and content in an acrylic precursor polymer during the extrusion process, as well as the impact of the comonomer during the thermal oxidative stabilization step[5;7;9;10]. To obtain a melt spinnable material, a careful selection of the copolymer ratio and the copolymer itself must be made, especially to avoid material cyclization and degradation. The comonomer also needs to effectively lower the viscosity of the copolymer so it can be extruded and processed.

Melt extrusion of carbon fiber precursors has been attempted using acrylic based resins, but the methods still require high plasticizer contents and/or solvents. Daumit *et al.*[11;12] have reported the use of a monohydroxy alkanol, water, and either acetonitrile or nitroalkane to reduce the processing temperature of PAN sufficiently to be melt extruded (without material degradation) into precursor fibers suitable for conversion to carbon fibers. However, these solvents still needed to be recovered and comprised approximately 35-40 weight percent of the extruded material. Atureliya and Bashir[13] have also reported the use of a crystallization solvent, which is a solvent from which the polymer crystallizes at a given temperature (propylene carbonate in this case crystallized PAN at ambient conditions), to melt extrude PAN homopolymer without the need for a coagulation bath. The solvent plasticized PAN at elevated temperatures and solidified the fibers online. However, the plasticizing solvent was still environmentally unfriendly and required recovery.

Supercritical fluids have been a recent focal point in a multitude of processing scenarios, most notably for extraction and plasticization[14]. In particular, supercritical carbon dioxide has

been found to adsorb into and plasticize polystyrene (PS), poly (dimethyl siloxane) (PDMS), polyethylene (PE), poly(methyl methacrylate) (PMMA), poly(vinylidene fluoride) (PVDF), poly(ethylene terephthalate) (PET), and nylon 6,6[15-20]. The result is a lowered melt viscosity upon CO_2 adsorption, facilitating the ability to process a given material at a lower temperature. However, the current applications do not control the release of CO_2 following extrusion, resulting in rapid diffusion (flashing) of the gas, bubble nucleation, and the consequential formation of voids and/or microcellular foams (foaming).

Melt spinning of acrylic based precursors still has a great deal of unanswered questions that need to be addressed. For a true melt spinning process, the use of solvents needs to be eliminated. The material needs to be carefully selected and tailored so the desired extrusion properties, namely resistance to degradation and suitable viscosity, are obtained. Consequently, the extruded material also needs to have properties sufficient for conversion to carbon fibers.

This study will attempt to determine the feasibility of melt spinning acrylic based carbon fiber precursors via two main approaches that encompass three main objectives. The first approach is to establish if variations in the chemical structure and composition of a PAN copolymer will facilitate a melt processable material. The second approach is to establish the effect of CO_2 on the viscosity reduction of PAN copolymers. The final aspect is to determine the feasibility of a process to prevent foaming and control bubble growth during the melt spinning of CO2 plasticized PAN copolymer fibers suitable for textiles and carbon fiber precursors.

1.1 References

(1.) Edie, D. D. *Carbon* **1998**, *36*, 345-362.

(2.) Edison, T. A. Patent US 223,898, **1880**.

(3.) Riggs, D. M.; Shuford, R. J.; Lewis, R. W. *Handbook of composites*; Van Nostrand Reinhold: New York, **1982**; Chapter 11, pp 196-271.

(4.) Johnson, D. J. *Carbon Fibers, Filaments, and Composites*; Kluwer Academic Publishers: Dordrecht, **1990**, pp 119-146.

(5.) Gupta, A. K.; Paliwal, D. K.; Bajaj, P. *Journal of Macromolecular Science-Reviews in Macromolecular Chemistry and Physics* **1991**, *C31*, 1-89.

(6.) Riggs, J. P. *Encyclopedia of polymer science and engineering*; Wiley: New York, **1989**.

(7.) Bajaj, P.; Roopanwal, A. K. *Journal of Macromolecular Science-Reviews in Macromolecular Chemistry and Physics* **1997**, *C37*, 97-147.

(8.) Tullo, A. H. *Chemical and Engineering News* **2000**, *78*, 11-12.

(9.) Jain, M. K.; Balasubramanian, M.; Desai, P.; Abhiraman, A. S. *Journal of Materials Science* **1987**, *22*, 301-312.

(10.) Tsai, J. S.; Lin, C. H. *Journal of Applied Polymer Science* **1991**, *42*, 3039-3044.

(11.) Daumit, G. P., Ko, Y. S., Slater, C. R., Venner, J. G., and Young, C. C. Charlotte, NC Patent 4,921,656 **1990**.

(12.) Daumit, G. P., Ko, Y. S., Slater, C. R., Venner, J. G., Young, C. C., and Zwick, M. M. Charlotte, NC Patent 4,981,752 **1991**.

(13.) Atureliya, S. K.; Bashir, Z. *Polymer* **1993**, *34*, 5116-5122.

(14.) Moore, S.; Samdani, S.; Ondrey, G.; Parkinson, G. *Chemical Engineering* **1994**, *101*, 32.

(15.) Bae, Y. C.; Gulari, E. *Journal of Applied Polymer Science* **1997**, *63*, 459-466.

(16.) Gerhardt, L. J.; Manke, C. W.; Gulari, E. *Journal of Polymer Science Part B-Polymer Physics* **1997**, *35*, 523-534.

(17.) Royer, J. R.; Gay, Y. J.; DeSimone, J. M.; Khan, S. A. *Journal of Polymer Science Part B-Polymer Physics* **2000**, *38*, 3168-3180.

(18.) Royer, J. R.; DeSimone, J. M.; Khan, S. A. *Journal of Polymer Science Part B-Polymer Physics* **2001**, *39*, 3055-3066.

(19.) Lee, M. H.; Tzoganakis, C.; Park, C. B. *Polymer Engineering and Science* **1998**, *38*, 1112-1120.

(20.) Kwag, C.; Manke, C. W.; Gulari, E. *Industrial & Engineering Chemistry Research* **2001**, *40*, 3048-3052.

2.0 Literature Review

2.0 Literature Review

In this chapter, previous studies that are pertinent to accomplishing the research objectives are discussed. Sections 2.1 and 2.2 discuss the use of rayon and pitch based precursors for the production of acrylic fibers. Both sections include the advantages and disadvantages of each system. Section 2.3 discusses the processing of acrylic (PAN) based fibers in detail. Particular attention is given in regards to the thermal instability of the precursor and research that has been conducted on plasticization techniques for the melt spinning of these precursors. Section 2.4 details the use of carbon dioxide for melt processing, focusing on the characterization and rheology of polymer/CO_2 systems. The research objectives of this study conclude the chapter.

2.1 Rayon Based Fibers

Rayon is a cellulose-based material produced by wet spinning a product extracted from wood pulp. Traditionally, rayon has been used for textile production, commonly found in clothing and tire cord. However, rayon based carbon fibers gained commercial significance in the late 1950s and became dominant during the 1960s and early 1970s[1].

A variety of rayon-fiber types are manufactured, including viscose, cuprammonium, and saponified acetate types. Cuprammonium and saponified acetate fiber types have been investigated for carbon fiber precursor use, but these materials produce weak carbon fibers because of their high internal void content[2]. Viscose rayon generally has the fewest defects and therefore is normally used for the carbon fiber production process. A special grade that possesses a high degree of polymerization must be manufactured for successful carbon fiber production. The molecular structure of rayon is depicted in Figure 2.1.

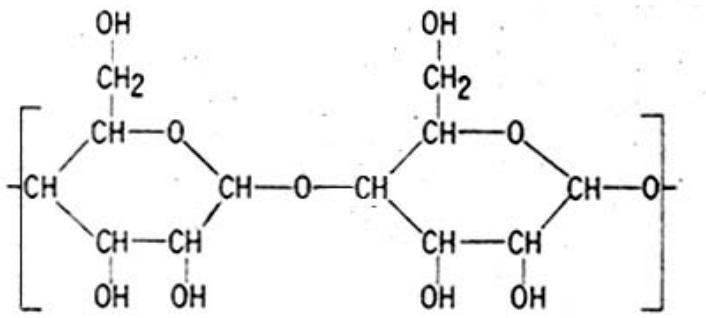

Figure 2.1: Molecular structure of rayon (cellulose)[2].

A large portion of the cellulosic structure is hydrogen and oxygen, which results in a low theoretical char yield of only about 55%[3]. In practice, a range between 10 and 30% carbon yield actually exists following conversion of the precursor[4]. In addition to the low carbon yield, a standard thermal stabilization and carbonization of the rayon precursor fibers results in a material with relatively low mechanical properties when compared to the pitch and acrylic based carbon fibers. A process called stretch graphitization is used to produce high strength, high modulus carbon fibers from rayon based precursors. However, the process is technically difficult and incurs high manufacturing costs[5].

Considering the oversaturation of the carbon fiber market that has resulted in the plummeting of carbon fiber prices[6], rayon fibers cannot withstand such a competitive market and are hence being phased out[7]. High strength rayon based carbon fibers require a costly stretch graphitization process. Combined with a low carbon yield, rayon fibers are losing importance in the carbon fiber market[8]. However, rayon fibers still play an important role in the textile industry and could possibly benefit from a processing aid to reduce solvent usage.

2.2 Pitch Based Fibers

Pitch based carbon fibers are well known for their use as composite reinforcements and heat resistant end uses[9]. These materials are often considered engineering materials and rarely used for textile products. Pitch based carbon fiber precursors are manufactured utilizing a melt spinning process. The precursor materials are derived from a complex mixture of organic compounds that are based on the by-products of the destructive distillation of coal, crude oils, and other petroleum refining processes, most often in the form of coal tar and petroleum asphaltenes. Representative molecular structures appear in Figure 2.2. Two forms of the precursor material, isotropic pitch and mesophase pitch, exist and play an important role in the method of carbon fiber production. Each precursor produces fibers with very different properties and result in varying process economics.

2.2.1 Isotropic Pitch

Isotropic pitch is an inexpensive, readily available source of carbon for use as a carbon fiber precursor[2]. Figure 2.3 illustrates the generic process used to manufacture isotropic pitch fibers. Isotropic pitch has a low softening point and is easily melt spun into a fiber precursor form. Raw coal tar and asphaltene pitches, i.e. with no chemical or mechanical treatments, are isotropic in nature and were used to produce early pitch based carbon fibers. The lack of orientation of the precursor material resulted in carbon fibers with poor mechanical properties[5]. The oxidation process for these fibers is also quite lengthy and proved to be industrially unattractive. Such low-quality fibers have found uses as fillers with various plastics and as thermal insulation materials.

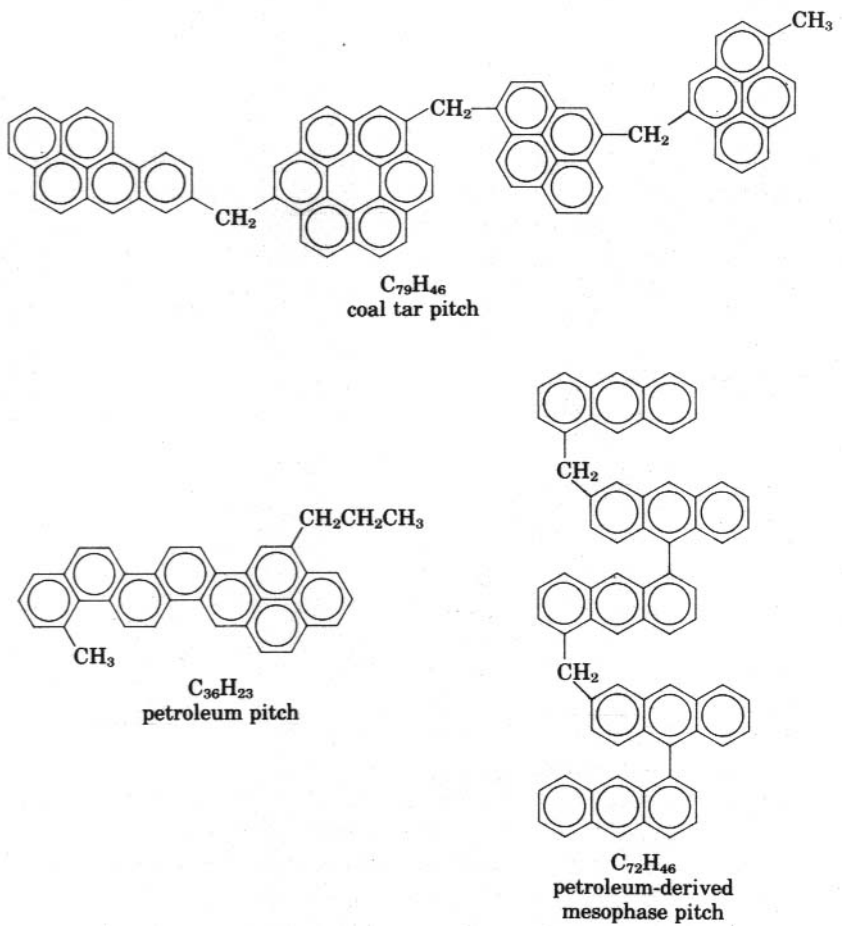

Figure 2.2: Representative molecular structures of various pitches[1].

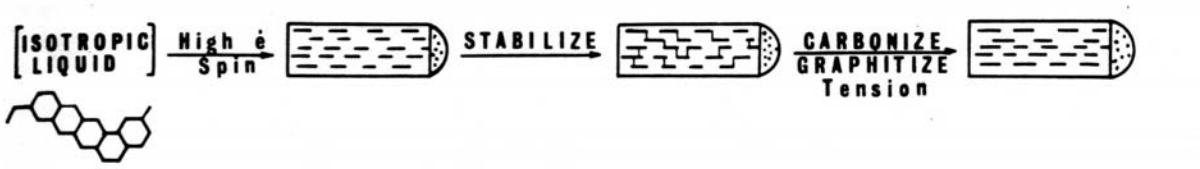

Figure 2.3: Schematic of isotropic pitch processing steps[10].

A heat stretching process can produce high orientation and modulus in isotropic pitch based fibers. However, the process is difficult and costly, eliminating the price advantage of using an isotropic pitch precursor material[11]. Isotropic pitch processes have hence become commercially insignificant, with the focus emphasized on anisotropic, mesophase pitch processes[2].

2.2.2 Anisotropic Mesophase Pitch

The primary difference between mesophase and isotropic pitches is a process to transform the isotropic pitch into a liquid crystalline state (mesophase) prior to melt spinning. The pitch conversion process into mesophase form most often involves the use of either a thermal polymerization or a solvent extraction technique to form an anisotropic (mesophase) precursor. The thermal polymerization technique is environmentally attractive, but results in a broad molecular weight distribution and often an inhomogeneous precursor that renders melt spinning difficult[12]. The solvent extraction technique produces a homogeneous starting material with a narrow molecular weight distribution, but requires large amounts of solvents (requiring extensive solvent recovery). The extra cost for solvent recovery and toxic nature of the solvents are important factors for industrial consideration when choosing a pitch treatment method[12]. Regardless of the technique used to transform the pitch into a mesophase structure, the need for applied tension in the carbonization step, as illustrated in the process overview depicted in Figure 2.4, is eliminated.

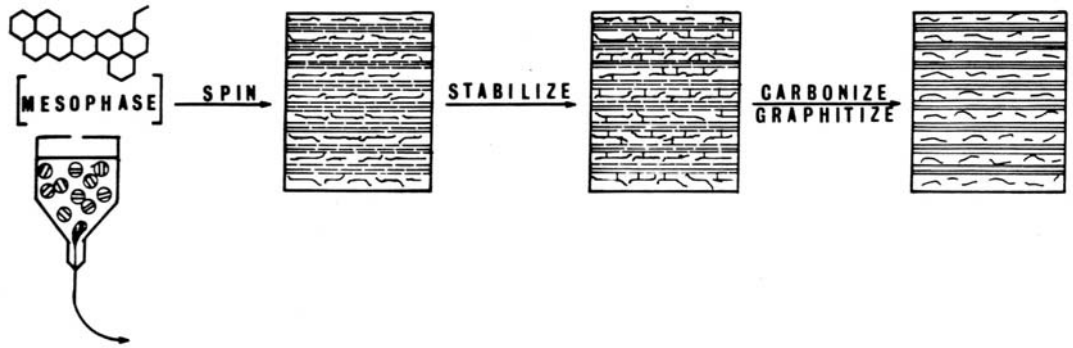

Figure 2.4: Schematic of mesophase pitch processing steps[10].

The production process for mesophase pitch based fibers is extremely sensitive to process parameters, especially in the heat treatment processes, and needs to be perfectly controlled to obtain high performance carbon fibers[13]. In particular, the tensile stress applied to the fibers during the stretching process is approximately 20% of that required to break the fibers, as opposed to the low applied tension in a typical PAN process (<1% of filament breaking strength)[12]. The fibers are well below their glass transition temperature (T_g) almost immediately following the die exit, and as a result are difficult to handle prior to carbonization[12]. In addition, the liquid crystalline nature of the mesophase pitch has a complex rheology that makes melt spinning more difficult than traditional PAN based polymeric precursors[12].

Mesophase pitch carbon fibers generally have a higher modulus but lower tensile strength and strain to failure than PAN based fibers. Mechanical properties of some commercially produced mesophase pitch fibers are illustrated in Table 2.1. Their range of application has been limited due to the brittle nature and handling difficulty of the as spun materials[1]. The thermal stability of the pitch precursors and ability to avoid toxic solvents is attractive, but the economics are not as favored when compared to PAN based fibers.

	Density ($g\ cm^3$)	Average tensile strength (GPa)	Average tensile modulus (GPa)	Average electrical resistivity ($\mu\Omega\ m^{-1}$)
Amoco				
P-25	1.90	1.38	159	13.0
P-55S	2.00	1.90	379	8.5
P-75S	2.00	2.10	517	7.0
P-100S	2.16	2.41	758	2.5
P-100S	2.16	2.07	758	2.5
P-120	2.17	2.41	827	2.2
P-120S	2.18	2.41	827	2.0
K-800x	2.18	2.93	931	1.6
K-1100	2.20	3.10	931	1.2
Nippon				
XN-50A	2.14	3.83	520	7.0
XN-70A	2.16	3.63	720	4.0
XN-8-A	2.17	3.63	785	3.0
XN-85-A	2.17	3.63	830	3.0
YS-50A*	2.09	3.83	520	7.0
YS-70A*	2.14	3.63	720	6.0
YS-50*	2.09	3.73	490	7.0
YS-60*	2.12	3.53	590	7.0
YS-70*	2.14	3.53	690	6.0
YS-80*	2.15	3.53	785	5.0
Mitsubishi Kasei Co.				
K133	2.08	2.35	440	--
K135	2.10	2.55	540	-
K137	2.11	2.65	640	-
K139	2.12	2.75	740	--
K321	1.90	1.96	180	--
Textron				
Carboflex†	1.57	0.55	35	60.0

*Coal tar mesophase pitch precursor.
†Isotropic pitch precursor.

Table 2.1: Mechanical properties of selected commercially produced pitch based carbon fibers[12].

2.3 Acrylic (PAN) Based Fibers

PAN (or acrylic) based fibers are currently used for several applications, most notably for the mass production of textile fibers and both low and high strength carbon fibers. The versatility of acrylic based carbon fibers and textile fibers leads to a wide range of mechanical properties in many various applications. Acrylic textile fibers are highly desirable in the textile industry, with soft, supple properties that make them desirable in both apparel and certain industrial applications[9]. Acrylic fibers have in fact replaced wool in many applications, particularly in knitting yarns, hosiery garments, blankets, and carpets, due to its high elasticity, good light and colorfastness, resistance to piling, and other desirable mechanical properties[8]. Acrylic based carbon fibers represent the most important carbon fibers used today, offering a wide range of structural properties, compatibility in matrix systems, and positions in expanding manufacturing applications[1].

2.3.1 Acrylic Fiber Process Overview

The typical chemical transformation of PAN in the process for production of acrylic based carbon fibers is illustrated in Figure 2.5. Precursor fibers are typically formed via a solution based extrusion and drawing process in which the fibers are drawn at draw ratios typically between 1.5-5 to approximately 10-12 μm in diameter[7]. The fibers are then subjected to a thermo-oxidative stabilization process in which a thermally stable ladder polymer is formed. The ladder polymer is then carbonized (or graphitized, depending on the application) into the final carbon fiber form, resulting in a fiber of usually 6-10 μm in diameter[1].

Successful production of acrylic fibers requires starting materials with appropriate properties. In general, solution spun carbon fiber precursor copolymers should have a high

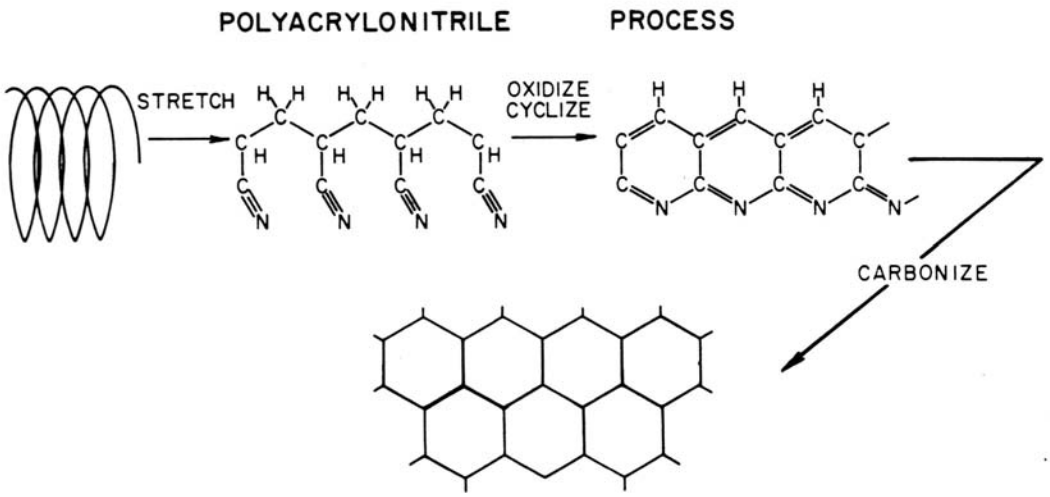

Figure 2.5: Typical process for manufacturing PAN based carbon fibers[10].

molecular weight (approximately 10^5 g/mol), a correspondingly appropriate intrinsic viscosity (between 1.25 and 2.36 dL/g), an appropriate molecular weight distribution (polydispersity ~ 2-3), and minimal molecular defects. Such traits are necessary for successful high temperature conversion into carbon fibers with high strength, minimal defects, and desired mechanical properties[7].

The processing of textile grade materials requires similar material properties to that of carbon fiber precursors. However, the ultimate mechanical properties of acrylic textile fibers are lower, allowing more flexibility in precursor properties and processing conditions. Acrylic textile fiber production is also much simpler, not requiring heat treatment following the initial fiber spinning and stretching[9].

Typically, PAN based fibers are formed via a solution spinning process. A dope of organic solvent and polymer precursor is prepared for the process. Various organic solvents are used, including N,N-dimethylformamide (DMF) and N-N dimethyl acetamide (DMAC), as well as aqueous inorganic solvents, including sodium thiocyanate[14]. The solvent is generally environmentally unfriendly and requires recovery and recycling. In addition, the prepared dope contains very low solids content, between 7-30% solids depending on whether the materials are dry-jet or wet spun[7]. A schematic of the industrial wet spinning process to produce the PAN precursor fibers (that undergo the chemical transformation in Figure 2.5) is illustrated in Figure 2.6. The dry spinning process is very similar, except the dry spun fibers solidify via solvent evaporation instead of washing, so the coagulation bath is replaced with a heated gas chamber[15]. The same solvents are used for both the wet- and dry-spinning processes.

The need for solution spinning of PAN based fibers arises from the thermal instability of the starting copolymer materials. The melt viscosity for the majority of the starting materials

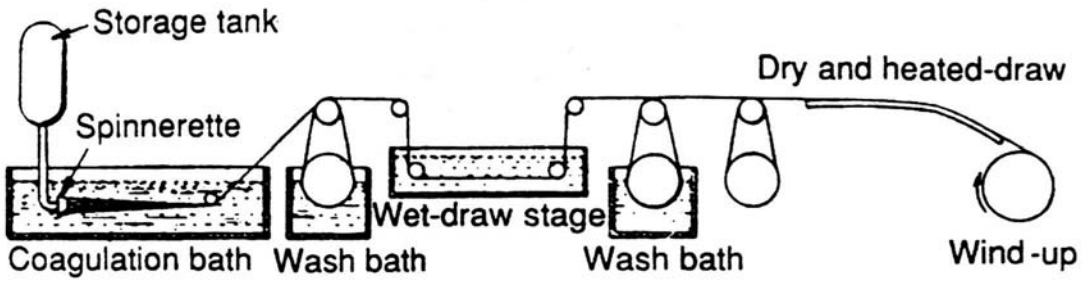

Figure 2.6: Typical industrial wet spinning process to produce PAN precursor fibers[12].

becomes suitable for melt extrusion at around 220°C. However, temperatures in this range are also typically utilized for the thermal stabilization of the precursor fibers, in which crosslinking of the copolymer starting material for both acrylic and carbon fibers begins at temperatures between 220-250°C[8]. The implication is that crosslinking prior to fiber formation renders the material intractable. As a result, melt extrusion is not feasible for traditional starting copolymers and solvents are utilized to permit processing at temperatures well below the crosslinking temperatures for these materials.

Following spinning of fine denier fibers of diameter 10-12 μm, stretching of the fibers is performed. The stretching process is usually performed either through an oven or over a hot godet to impart a high degree of orientation[16]. Typical textile fibers would then undergo a surface treatment corresponding to their ultimate use, bypassing any further heat treatment. If the fiber is to be converted to a carbon fiber, it undergoes a series of heat treatments to obtain its final form.

The first heat treatment of carbon fiber precursors is known as thermal oxidative (or thermooxidative) stabilization. Thermal stabilization is the rate-controlling step in carbon fiber manufacture, in practice taking several hours to achieve complete stabilization[17]. Therefore, the stabilization process imparts a large portion of the cost to produce carbon fibers, in addition to requiring solvent-based extrusion to avoid cyclization during fiber formation.

2.3.2 Chemistry of Thermal Stabilization

The primary function of the thermal stabilization step is to stabilize the carbon fiber precursor so it is thermally stable during further heat treatment steps. The as spun precursor fiber structure is crosslinked so that orientation will not be lost and extensive chain relaxation and chain scission will not occur during carbonization[12]. The stabilization reaction is the rate

limiting step of the PAN based carbon fiber production process, and a great deal of effort has been put forth to accelerate the process[14].

Following the prestretching process, carbon fiber precursors are heated to suitable temperatures (220-280^{o}C) for stabilization. During this process, an exothermic cyclization reaction leads to the formation of a ladder polymer, as pictured in Figure 2.7. As depicted in the schematic of a commercial PAN stabilization oven in Figure 2.8, the precursor fibers are kept under tension during the stabilization process to maintain alignment of the PAN polymer. Otherwise, relaxation occurs and the resulting ladder polymer loses orientation with respect to the fiber axis. Formation of the ladder polymer results in significantly enhanced thermal stability, easily facilitating heating to higher temperatures for carbonization[2].

Cyclization that occurs in the thermal stabilization reaction could be quite undesirable if attempting to melt spin such precursor materials at elevated temperatures. It is important to understand the role of the factors that strongly influence the crosslinking/stabilization reaction when assessing the feasibility of melt extrusion of acrylic copolymers. Understanding the influence of the nature of the comonomer incorporated into the precursor, the molecular weight of the precursor itself, the AN content of the precursor copolymer, and the atmosphere in which the stabilization reaction takes place will facilitate the tailoring of a suitable precursor material for melt extrusion into carbon fiber precursors.

2.3.2.1 Influence of atmosphere

Thermal stabilization of PAN precursor fibers consists of two primary reactions, a cyclizing and dehydrogenation of the precursor fiber. The cyclizing reaction is a condensing of the nitrile groups to form a ladder polymer, and the dehydrogenation is a chain scission reaction that gives rise to volatile products, such as HCN and NH_3, and also results in chain

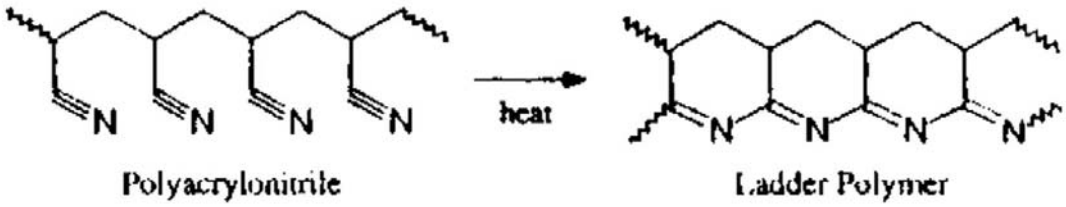

Figure 2.7: Ideal stabilization of acrylic precursor into a ladder polymer[13].

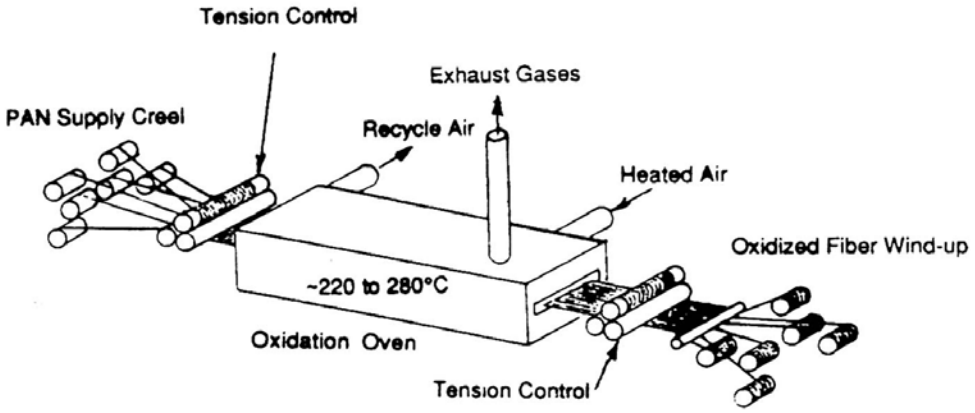

Figure 2.8: Schematic of a typical thermo-oxidative stabilization oven[12].

shrinkage[11;14]. The two reactions are depicted in Figure 2.9. At approximately 270°C in a dynamic heating of the precursor fiber, the cyclization reaction takes place very quickly (if the fiber had not previously begun to cyclize), resulting in a large exotherm that further induces chain scission and worsens the resulting carbon fiber mechanical properties[2]. If the fiber is stabilized isothermally, less scission occurs and the cyclization sequences are longer, maintaining the orientation of the fiber. However, the ladder backbone remains saturated and is prone to scission during carbonization[18].

Treating the precursor fiber with air fixes oxygen onto the PAN ladder structure. Numerous studies have shown that better mechanical properties are obtained when stabilization is performed in an oxidizing medium (including air) as opposed to an inert atmosphere, which is the common practice of carbon fiber manufacturers[7]. The presence of oxygen has a significant role in the kinetics and thermodynamics of the cyclization reaction[5]. Studies have demonstrated that oxygen acts in two opposing manners during stabilization: it initiates the formation of activated centers for cyclization and in contrast increases the activation energy (which retards the reactions)[7]. Despite the conflicting mechanisms, stabilization in an oxidizing medium is preferred because of the resulting formation of oxygen containing groups in the ladder backbone[7]. These groups assist in the fusion of the polymer backbone during carbonization and help to eliminate water during aromatization, essential for basal plane formation on the resulting carbon fiber[14].

2.3.2.2 Influence of Temperature

The stabilization process is greatly influenced by the heat treatment temperatures employed on the fibers[8]. Excessive heating burns out the fiber, and insufficient heating results in an improperly stabilized fiber that cannot withstand the carbonization process. Depending on the

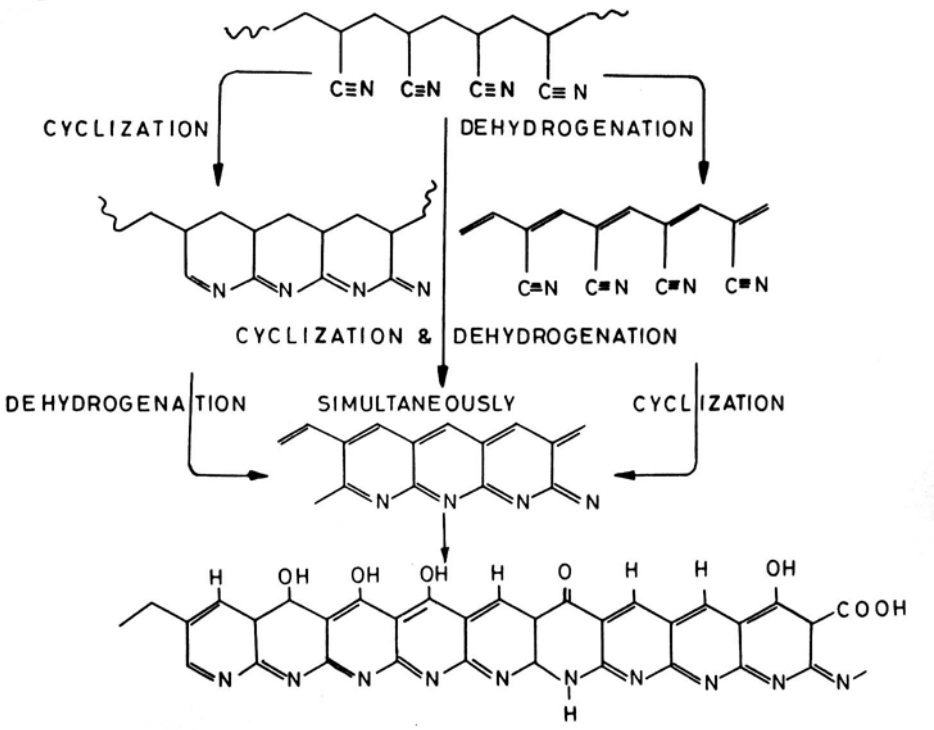

Figure 2.9: Sequence of reactions in thermooxidative stabilization of PAN precursors[7].

comonomer used for an acrylic precursor material, cyclization generally begins to occur around 180°C, but is typically carried out between 200-300°C to accelerate the reaction[7]. Above 220°C, cyclization becomes spontaneous and has the potential to rapidly and uncontrollably release heat. Therefore, it is usually performed in a manner to slowly release heat in a controlled manner, optimizing final properties by preventing excessive fragmentation[11]. Above 300°C, violent exothermic reactions often take place resulting in the formation of "tarry" substances with significant weight loss[14].

2.3.2.3 Influence of comonomer content and structure

Typical PAN based carbon fiber precursors are copolymers of acrylonitrile and a suitable comonomer. Table 2.2 shows the name and chemical structure of some of the more common comonomers used for acrylic precursor copolymers. The comonomer has a great impact on the rate of the reaction[12]. Comonomers typically enhance segmental mobility of the polymer chains as well as reduce the initiation temperature of cyclization. The proportion of the comonomer is also important; higher comonomer contents increase the time required for thermal oxidation[8], which is especially important for the design of a melt spinnable PAN based material.

During the propagation step of the cyclization reaction in PAN homopolymer, excessive heat is built up which results in chain scission and fusion of the precursor fibers. A properly chosen comonomer, such as the typical acidic comonomer incorporated into PAN copolymer precursors, will slow down the cyclization propagation step and allow better heat dissipation[7]. This is accomplished by effectively lowering the initiation temperature and peak exotherm temperature of the cyclization reaction[8].

Amide and ester comonomers have also been used as comonomers. Amide comonomers, such as acrylamide, have similar but less pronounced effects as the acid comonomers[7]. The ester

Various Comonomers for Acrylic Precursors

No.	Comonomer	Chemical structures
1	Acrylic acid (AA)	CH_2=CHCOOH
2	Methacrylic acid (MAA)	CH_2=C(CH_3)COOH
3	Itaconic acid (IA)	CH_2=C(COOH)CH_2COOH
4	Methacrylate (MA)	CH_2=CHCOOHCH_3
5	Acrylamide (AM)	CH_2=CHCONH_2
6	Aminoethyl-2-methyl propenoate (quaternary ammonia salt)	CH_2=CH(CH_3)COO$C_2H_4NH_2$

Table 2.2: Table of comonomers commonly incorporated into acrylic precursors[7].

comonomers, such as methyl acrylate and methyl methacrylate, have been shown to have no initiating effect on the cyclization reaction, but do seem to have an advantageous role in the precursor structure and resulting carbon fibers[8]. Ester comonomers with bulky side groups enhance segmental mobility, resulting in higher orientation and translating into improved mechanical properties of both the precursor and resulting carbon fiber. If the ester content is too high (over approximately 1.5 mole percent), the resulting carbon fibers have a lower orientation and reduced mechanical properties due to lower degrees of cyclization[19]. Also, as the size of the side group of the ester comonomer is increased, an increase in weight loss is observed in the carbon fiber due to extra chain scission[20]. A large side chain comonomer will increase the orientation of the precursor, but the orientation of the resulting carbon fiber decreases. The use of a small side chain ester comonomer (such as methyl acrylate) could be advantageous in melt spinning: the initiation temperature is not lowered, so cyclization occurs at higher temperatures; the glass transition temperature is lowered (as a result of increased chain mobility), resulting in a lower melt viscosity of the precursor; and a carbon fiber with reasonable mechanical properties can be produced if the precursor contains a suitable ester comonomer content. Recent studies have shown that 10 to 15 mole percent methyl acrylate can produce a copolymer that has suitable viscosity and sufficient thermal stability (at processing temperatures of 220^{o}C) for melt extrusion[21].

2.3.3 Current Plasticization Techniques for Melt Spinning Acrylic Fibers

A need for a less expensive and nonpolluting fiber production process (compared to solution spinning) exists, evidenced by the efforts to melt spin acrylic precursor fibers for both textiles and carbon fibers[22]. Numerous patents and journal articles have been published regarding the melt spinning of plasticized polyacrylonitrile copolymers. The majority of studies

focus on the use of water (often in conjunction with other plasticizers) to plasticize a PAN homopolymer or copolymer for melt extrusion.

In general, studies on water plasticized PAN focused on melt extrusion for textile use. However, none of the systems were commercially incorporated for acrylic textile fiber production. More recent studies from Daumit, et al, have looked at the use of mixtures of water, acetonitrile, a C_1 to C_4 monohydroxy alkanol, and/or a C_1 or C_2 nitroalkane to plasticize PAN for melt spinning of particularly high strength carbon fiber precursors[23;24]. Even more recent studies have looked at propylene carbonate, termed a "crystallization solvent", to produce melt extruded PAN fibers[25]. None of these studies have been practiced commercially, but provide a great deal of insight into the problems associated with melt extrusion and must be investigated.

C. D. Coxe [26] first discovered in 1952 that water hydrated the pendant nitrile groups of PAN, decoupling the nitrile-nitrile associations that cause cyclizing and thermal degradation well below the melting temperature of pure PAN (320^{o}C). The melting point is significantly lowered, and hydrated PAN can be melt extruded without significant degradation. Studies confirmed that the melting temperature of pure PAN could be reduced to 200^{o}C with only 0.2 weight percent water[27]. Despite the effectiveness of water on PAN, Coxe was not able to control the release of steam upon leaving the spinneret and consequently failed to develop a melt spinning process from the resulting foaming problems[22]. Coxe's process was suitable for making fibrillar materials for paper or strands for fused, sintered, or foamed particles, but could not be used to form a homogeneous fiber suitable for textiles[15]. Further studies were conducted to attempt to melt spin reasonable fibers from a 'fusion melt' of PAN and water for the textile industry, but the rate of water evaporation was not controlled properly and sheath-core filaments were produced[28].

In 1979, Porosoff solved the foaming problem by extruding a single phase fusion melt of water and PAN into a steam pressurized solidification zone that prevents rapid water evaporation (which previously led to foaming of the fibers)[15]. A schematic of the Porosoff process is shown in Figure 2.10. The invention of Porosoff completely eliminated the need for an environmentally unfriendly solvent, consequently eliminating its recovery and the associated pollution. Effectively stretching the fiber in conjunction with the extrusion step also lowers energy requirements by eliminating the need for a separate stretching step. The controlled diffusion of water helps prevent the formation of sheath-core development (seen in previous PAN melt extrusion studies) as well as maintains a stretchable state following fiber solidification. DeMaria *et al*.[29] found that wetting the fiber with hot liquid water in the steam pressurized solidification zone improved orientation and more easily facilitated stretching of the fibers. Initial problems with filaments sticking together were resolved in 1982 via a modified spinneret plate for extruding the fusion melt of PAN and water[30].

To determine the feasibility for implementation of the Porosoff process for carbon fiber production, various studies were performed to determine the structure and mechanical properties of such melt spun PAN fibers. Grove *et al.* [28] reported that carbon fibers with reasonable strength and modulus could be produced via a process similar to that of Porosoff. However, the resultant fibers had numerous surface and internal flaws. Microholes and broken filaments were observed, and the authors felt that this would prevent the implementation of such a process in place of wet or dry spinning. Figure 2.11 illustrates the SEM photograph of a carbonized melt spun PAN fiber. Voids are observed in the fiber, especially near the core. The size of the voids was not reported, but appears to be on the order of between less than 1 μm up to 3 or 4 μm.

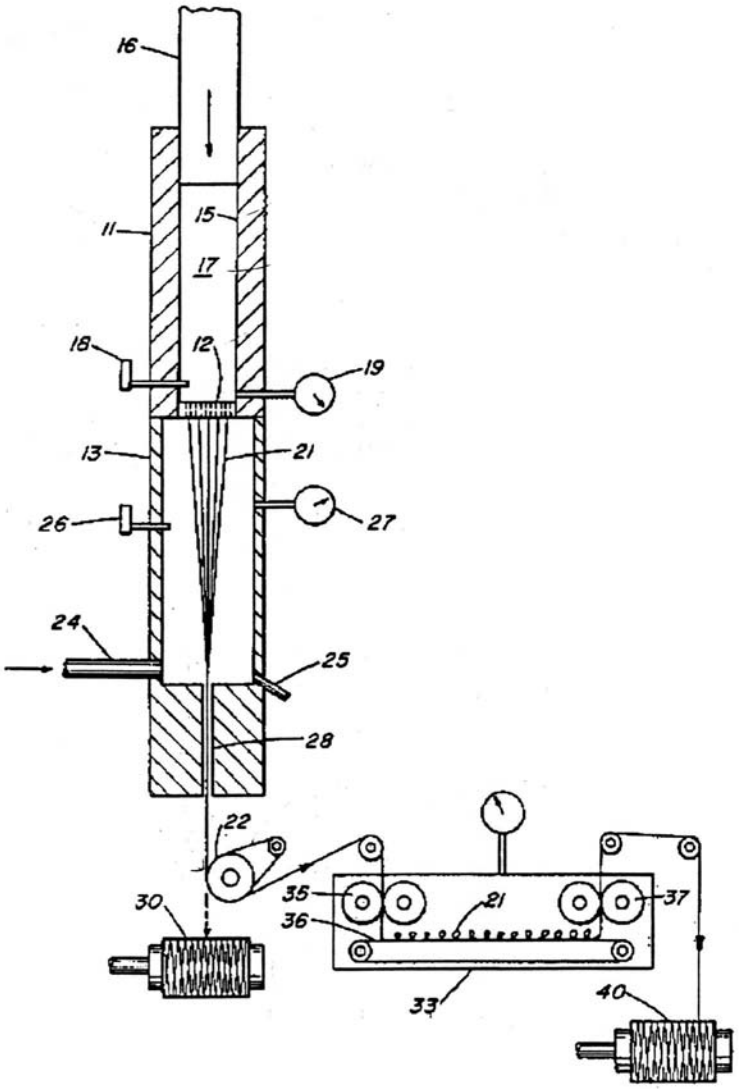

Figure 2.10: Process developed by Porosoff for melt extrusion of PAN[15].

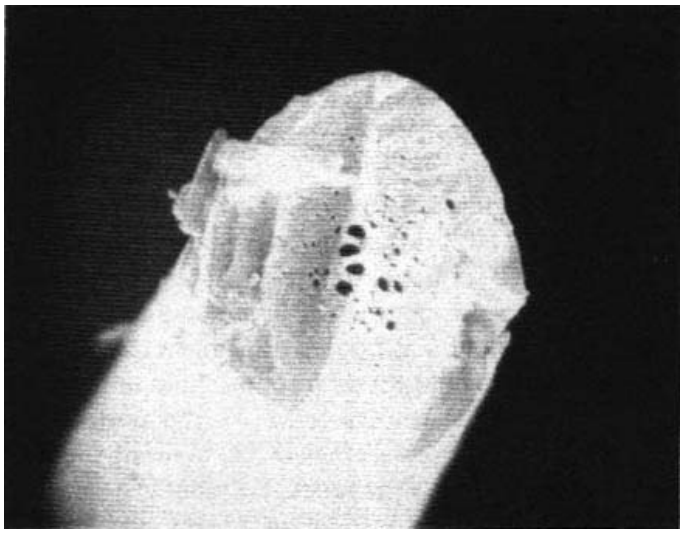

Figure 2.11: SEM photograph of carbonized, melt spun PAN fiber[28].

Min *et al.*[22] published similar results, except for as-spun fibers prior to stabilization or carbonization. SEM photographs indicated that a microporous structure at the fiber core was obtained in the as spun fibers, as depicted in Figure 2.12. Here the fiber was stretched from a supercooled melt at 150°C, at which the viscosity of the melt was increased (suppressing steam emission) and the steam pressure was lowered (reduced steam pressure). The combined effects seemed to suppress foaming, but the core still exhibited microholes similar to those reported by Grove *et al*[28].

Daumit and coworkers[23] at BASF patented a method for producing melt spun acrylic fibers with an internal structure suitable for conversion into carbon fibers. The process is depicted in Figure 2.13. A mixture of water, acetonitrile, and a C_1 to C_4 monohydroxy alkanol (preferably methanol) are used in the amount of 23 to 48 weight percent to plasticize an acrylic copolymer melt (of at least 85% acrylonitrile). The homogeneous melt is then extruded at a temperature between 160 and 185°C into a pressure chamber, illustrated by #8 and 10 in Figure 2.13, which is pressurized by steam preferably between 10 and 50 psig above atmospheric pressure and at a temperature between 90 and 200°C. The pressure chamber is used to control the release of the plasticizer and minimize void formation during initial drawing of the fibers. Upon leaving the pressure chamber and entering an oven (depicted by #38 in Figure 2.13), most of the remaining plasticizer is removed (less than 1 weight percent was observed). The majority of voids resulting from plasticizer removal are then collapsed during post spin drawing (at a draw ratio of 8.4:1) in a steam atmosphere at 18 psig (#46 in Figure 2.13).

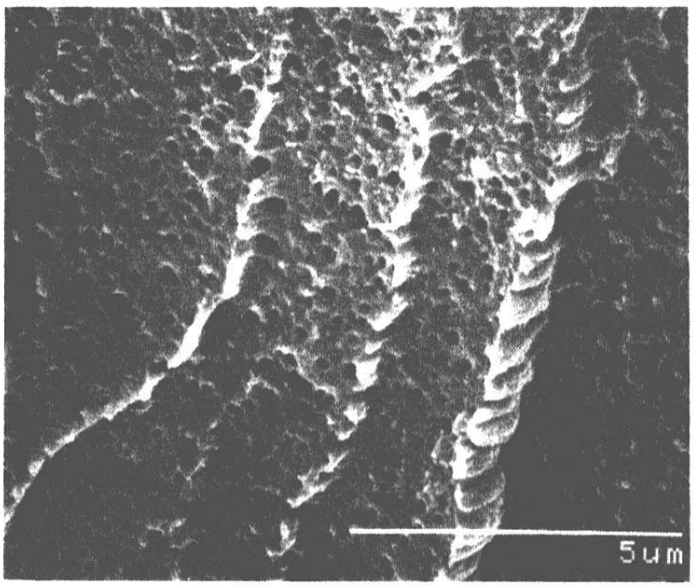

Figure 2.12: SEM of magnified core cross-section of melt extruded PAN[22].

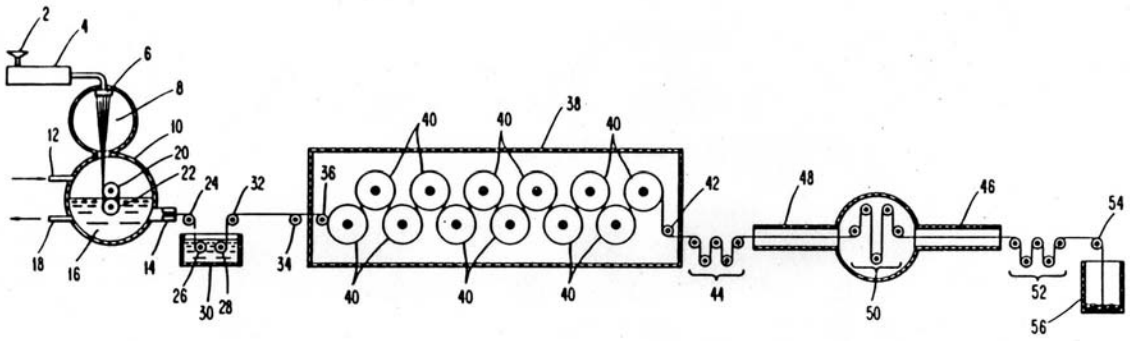

Figure 2.13: Process for melt extruded PAN precursor fibers (for carbon fibers)[23].

The BASF process proved that carbon fibers could be obtained via a pseudo-melt spinning process. It also demonstrated the ability to form various cross-sectional configurations (i.e. trilobal configuration) and still process a suitable fiber for carbonization[23]. The versatility of the process was expanded in 1991, when Daumit and coworkers[24] patented the use of nitromethane and nitroethane in place of acetonitrile for melt plasticization of acrylic copolymers. However, plasticization still required at least 25% (and up to 47%) plasticizers to facilitate melt spinning of a PAN copolymer containing approximately 85-90% acrylonitrile.

The BASF process was never commercialized. A high plasticizer content was still required, which implied that recovery must still be implemented. The solvents themselves were extremely toxic and required very careful use, especially at elevated temperatures near the boiling point of the solvents (in particular, the acetonitrile solvent can degrade into cyanide). The use of a high amount of plasticizer also produces minimal environmental benefits, and the recovery requirements produce little financial gain over solution spinning processes. In fact, the process provided no economic benefit over solution spinning once commercial production levels were reached (~$2x10^6$ lb/year). It is important to note that the amount of solvent required for wet (80%) or dry (70%) solution spinning is considerably higher than the amount of plasticizer required for the BASF melt extrusion process.

Various processes, other than water based, have been investigated for the melt processing of acrylic polymers. Atureliya and Bashir[25] looked at the use of propylene carbonate to plasticize PAN homopolymer. Propylene carbonate, with a boiling point of 240^{o}C, is a non-toxic solvent that only needs heated to 130-150^{o}C to solubilize PAN. Following extrusion of the plasticized melt, a pressure chamber is not required because the plasticizer is well below its boiling point and does not foam in the fiber.

There are many drawbacks to the use of a propylene carbonate plasticization technique. High degrees of orientation were not obtained (in fact, no chain axis order was observed), which is necessary to obtain the desired mechanical properties in both textile and carbon fibers. Fifty weight percent of plasticizer is required, even higher than that reported for the water-hydrated systems. The extrusion process is simpler than the water hydrated systems (not requiring a pressure chamber), but still requires heating and drawing steps to remove the plasticizer from the fiber.

2.4 Melt processing with CO_2

A number of commercial polymers, including acrylic (PAN) fibers and Lycra, are currently produced using solution-based processes. Solution produced polymers usually require the use of toxic, organic solvents, commonly including dimethlyl formamide (DMF) and dimethylacetamide (DMAC), to process the materials into their desired final form. Solvents are typically used to make a material processable at a lower temperature to prevent degradation or to produce materials difficult to obtain via conventional processing techniques. In the case of PAN systems, solvents are required to prevent material degradation prior to fiber formation.

Concern over volatile organic solvent emissions has initiated searches to find cleaner solvents for both polymer synthesis and polymer processing[31]. Use of a supercritical gas, in particular supercritical carbon dioxide (Sc-CO_2), is known to effectively act as a plasticizer for many polymer systems, including polystyrene and PMMA[32]. The result is a reduction in the glass transition temperature, leading to a melt viscosity reduction and enabling processing at lower temperatures.

The benefits of carbon dioxide use over typical organic solvents are numerous. Carbon dioxide is non-toxic, non-flammable, environmentally friendly, completely recoverable, and easy to get supercritical (T_c=31.1^{o}C, P_c=1073 psi). In the supercritical state, CO_2 is known to have similar solubilization characteristics to organic solvents (such as hexane) and CFC's and is well documented to plasticize a number of amorphous polymers[32;33]. Sc-CO_2 also possesses a diffusivity similar to that of a gas, but a density like that of a liquid, which promotes rapid plasticization in amorphous materials[34]. For these and many more reasons, Sc-CO_2 has proven to be a very versatile alternative to many solvent based applications and consequently has been the focus for a surge of interest in many commercial applications[31].

2.4.1 Current Uses and Applications of CO_2 in Processing

Replacing environmentally toxic solvents with benign fluids is a major motivation in today's industry and ranges over a wide variety of applications including ceramics processing, paper deacidification, metal cleaning, and plastics and textiles processing[35]. Supercritical carbon dioxide is one such benign fluid that is commonly used in a wide variety of applications and has been a focal point for numerous innovative studies. Sc-CO_2 use has been studied in novel polymerization techniques, microcellular foaming processes, morphology control, extraction of impurities, and even impregnation of polymers with various materials. Some of the various commercial applications for Sc-CO_2, and the stage of development, are illustrated in Table 2.3.

Polymerization in CO_2 has proven useful for materials that are difficult to synthesize with traditional methods. Energetic polymers and pyrotechnics are typically processed with volatile organic compounds and ozone depleting substances. High pressure liquid carbon dioxide has been shown to not only eliminate the need for these solvents, but in fact acts as a precipitator for such materials as poly-3-nitratomethyl-3-methyl oxetane and magnesium, Teflon and Viton pyrotechnic material[36]. The result is a minimization (and almost complete elimination) of hazardous waste generation. In addition, the CO_2 was easy to remove following polymerization, eliminating yet another step in the processing of such materials.

Sc-CO_2 has also proven effective in the polymerization of polyacrylonitrile (PAN), which traditionally requires the use of aqueous and/or organic solvents. Most industrially important hydrocarbon based polymeric materials are insoluble in CO_2, but a heterogeneous polymerization in Sc-CO_2 proved successful for PAN when stabilized with PS and poly(1,1-dihydroperfluorooctyl acrylate)[37]. The molecular weight of the resulting acrylic polymer (or the

STATUS	APPLICATION	COMPANIES
Commercial	Spray Painting without VOCs	Union Carbide Corp. (Danbury, CN)
Commercial	Deasphalting	Kerr-McGee Corp (Oklahoma City, OK)
Developmental	Ceramics Processing	Fairey Industrial Ceramics Ltd. (Filleybrooks, U.K.)
Developmental	Paper Deacidification and Preservation	France's Energy Commission (Pierrelattie) & Separex S.A. (Champigneulles)
Developmental	Metal Parts Cleaning	Joint Assn. for Advancement of SCFs
Commercial	Metal Parts Cleaning	CF Technologies (Hyde Park, MA)
Pilot	Thermoplastics Processing	Axiomatics Corp. (Woburn, MA)
Advanced Pilot	Textile Dyeing	Joseph Jasper GmbH (Velen, Germany)
Developmental	Textile Dyeing	Batelle Pacific Laboratories (Richland, WA)
Developmental	Materials Deposition	Phasex Corp. (Lawrence, MA)
Developmental	Fine Particle	Phasex, Battelle & Upjohn Co. (Kalamazoo, MI)
Developmental	Separation	Tohoku Univ. & Idemitsu Corp. (Tokyo) & Phasex
Developmental	Plastics Recycling	Tohoku Univ.

Table 2.3: Commercial applications of $ScCO_2$ with corresponding stages of development[35].

particle size at which precipitation occurred) could be controlled by simply varying the pressure (or temperature in a closed system) of the Sc-CO_2.

In similar studies, Sc-CO_2 has been found useful for controlling the miscibility conditions that regulate the molecular weight, molecular weight distributions, and morphology during polymerization. For instance, Sc-CO_2 was used as an antisolvent during the production of epoxy resins[38]. The antisolvent precipitates polymer molecules once they have obtained a desired size. Control of particle size, and ultimately morphology, is obtained by utilizing Sc-CO_2 (at pressures of 1400 psi) to control the rates of particle nucleation and growth. It is reported that the density of Sc-CO_2, which is similar to that of a liquid and easily adjustable via pressure, allows such exacting control of the resultant particle size and morphology[38]. Morphologies ranging from spherical to rod-like structures were obtained by simply varying the pressure (density) of the Sc-CO_2.

Probably the most exploited use of Sc-CO_2, and other supercritical fluids in general, is for extraction purposes in almost any industrial processing or waste cleanup situation[35]. Controlling the solubility to bring about selective extractions, fractionation or separations-unit operations is very common, for instance in the extraction of oilseed[39] or the extraction of cocoa butter from cocoa beans[40]. Fat extraction for low-fat foods can also easily be accomplished with Sc-CO_2, as studies have shown in the refinement of palm oil[41]. Many food processing and pharmaceutical processes are using Sc-CO_2 to replace organic and aqueous solvents for extraction of unwanted by-products from the desired product[35].

In many processing situations, it is desired to introduce additives to a product. This becomes especially difficult with glassy polymers, as the diffusion into these materials is very slow. When exposed to Sc-CO_2, and even high pressure CO_2 gas, a number of glassy polymeric

materials are plasticized into the rubbery state, dramatically accelerating the impregnation of additives[42]. The CO_2 effectively swells the glassy polymeric materials, which allows controlled diffusivity and phase separation conditions to regulate impregnations. Poly (vinyl chloride), polycarbonate, poly (methyl methacrylate), and poly (vinyl acetate) have all been observed to plasticize and facilitate rapid impregnation in the presence of CO_2[42].

The plasticizing behavior of Sc-CO_2 can also be very useful for the reduction of melt viscosity in amorphous polymer melts. Controlling viscosity to regulate the rheological properties of polymer melts or solutions at the final processing stage, such as extrusion of corn starch using CO_2 as a blowing agent, has been investigated[43]. Sc-CO_2 has also been found to plasticize, swell, and reduce the melt viscosities of polydimethylsiloxane[44;45], polystyrene[46;47], polyethylene/polystyrene blends[48], polypropylene, low-density polyethylene, poly(methyl methacrylate), and poly(vinylidene fluoride)[49]. Reduction of melt viscosities permits processing at lower temperatures, which can be of great importance when working with thermally unstable materials such as PAN.

When processing with CO_2, the polymer material will usually foam and in many cases the material is intentionally foamed. Park *et al*.[50] used a continuous extrusion process for the manufacture of low-density microcellularly foamed high impact polystyrene (HIPS). A metered amount of gas was delivered to the polymer melt in the extrusion barrel. The injected gas diffused into the polymer matrix at a much higher rate than batch processing because of the convective diffusion induced in the extrusion barrel at an elevated temperature. Microcell nucleation was successfully promoted using a nucleation nozzle where thermodynamic instability was induced by a rapid pressure drop in the flowing polymer/gas solution. This caused a rapid drop in the solubility of gas in the polymer that promoted nucleation of billions of

bubbles. The rate of nucleation was found to be a function of the pressure drop, the pressure drop rate and the amount of gas dissolved in the polymer. The basic approach for promotion of a large volume expansion ratio and a high cell-population density was to prevent gas loss during expansion by freezing the extrudate surface while suppressing cell coalescence via a decrease in melt temperature.

Although limited studies have been done in continuous high-pressure extrusion to study microcellular foams and polymer blending using CO_2, the improvement in processability of polymer systems due to suppressed melt viscosities has not been fully explored. In order to successfully incorporate Sc-CO_2 into a process, it is important to understand the characterization of plasticized systems, in both a thermodynamic and chemical sense, which facilitates an understanding of the rheological effects of plasticization.

2.4.2 Characterization of CO_2 Plasticized Systems

Both qualitative and quantitative approaches have been taken in different studies to successfully describe the plasticizing behavior of CO_2 on polymeric systems. Various equations of state to describe the polymer solution density, such as the Sanchez-Lacombe[51] equation, have been studied to describe the thermodynamics of a CO_2 plasticized polymer system. The influence of thermodynamic variables, including pressure, temperature, fluid type, and density, have been studied to quantitatively describe the miscibility of polymers with high-pressure and supercritical CO_2. From a much different approach, studies have also focused on the roles of morphology, polarity, and chemical interactions to provide a more qualitative interpretation of CO_2 plasticization. Both methodologies deserve further investigation to ascertain a better understanding of the physical phenomenon of CO_2 plasticization.

2.4.2.1 Thermodynamic interpretations of CO_2 plasticization

The solubility of polymers in supercritical fluids has been successfully correlated by two lattice-theory based equations of state (EOS): the Sanchez-Lacombe EOS

$$\frac{P}{T} = -\ln(1-\rho) - \left(1 - \frac{1}{r}\right)\rho - \frac{\rho^2}{T} \tag{2.1}$$

where P, T, and ρ are reduced pressure, temperature, and density, respectively, with respect to characteristic parameters (optimized for each polymer based on solubility data, see equations 3.2-4), and r is the number of lattice sites occupied by a molecule of molecular weight M[51], and the Panayiotou-Vera EOS

$$\frac{P}{T} = \ln\left(\frac{\upsilon}{1-\upsilon}\right) + \frac{Z}{2}\ln\left(\frac{\upsilon + \frac{q}{r} - 1}{\upsilon}\right) - \frac{\theta^2}{T} \tag{2.2}$$

where P, T, and υ are reduced pressure, temperature, and volume (respectively) with respect to characteristic parameters, Z is the finite coordination number, q is the effective chain length, r is the number of lattice sites, and θ is the fraction of total external contacts in the system that are mer-mer contacts in a random array of molecules and holes[52]. Both equations of state treat a plasticized polymer as an essentially solid-like structure. The S-L EOS is modeled after the Flory-Huggins theory with both occupied and unoccupied sites, component dependent site volumes, and an approximation of infinite coordination number[51]. The P-V EOS has a finite coordination number, with constant site volumes and a nonrandom distribution of unoccupied sites[52]. The implication is the requirement of different mixing rules to calculate mixture properties for each EOS[34].

Both equations of state are known to accurately predict PVT behavior in pure polymer melts which are generally incompressible. Detailed studies on PDMS/Sc-CO_2 systems have

been concerned with the validity and discrepancies reported with using the Sanchez-Lacombe equation of state, but in fact have determined the EOS is quite good at modeling equilibrium solubility and mixture properties of PDMS in supercritical CO_2[53]. However, the highly compressible nature of supercritical CO_2 must be accounted for by a temperature dependent binary interaction parameter to accurately predict mixture properties[34]. When the interaction parameter is optimized for a given temperature or pressure regime, equilibrium solubility data and mixture properties can be accurately described well into the supercritical regime for polymer-diluent systems[34;53]. The result is the ability to determine solubility, swollen volume, isothermal compressibility, and thermal expansion coefficients in a highly non-ideal mixing situation (high pressure or supercritical mixture of gas and polymer). By using the adjustable, optimized interaction parameter, successful calculations of density variations for polymer/CO_2 rheological measurements have been carried out[48].

A more traditional approach to the modeling of PVT behavior of CO_2/polymer systems used a dual mode Henry's law model to describe the sorption of CO_2 in PPS[54]. The two modes corresponded to Henry's law behavior and Flory-Huggins behavior. While the model accurately described the author's experimental data, it is important to note that a narrow temperature range (25-85^oC) and a low-pressure range (up to 50 atm) were fitted. In particular, the pressure range is well below the supercritical pressure of CO_2 (and most other fluids for that matter) and would be unsuitable for describing supercritical fluid/polymer phase behavior.

2.4.2.2 Role of chemistry and morphology on CO_2 plasticization

Carbon dioxide under high pressure has an unusual combination of effects in its interactions with polymers. At temperatures and pressures approaching its critical conditions (T_c=31^oC and P_c=1073 psi) the solubility of CO_2 in many polymers is quite high and ranges from

about 10-30% by weight[32]. In addition, CO_2 also has a high plasticizing effect, causing up to a 45°C reduction in the glass transition temperature (T_g) for a number common amorphous polymers, including PMMA, HIPS, and ABS[32]. Furthermore, CO_2 can also act both as a pressure-transmitting medium and as a diluent, whose interaction with materials varies significantly depending on the treatment and decompression pressures and temperatures.

The morphology of the polymer has a high impact on its ability to absorb CO_2. In semi-crystalline polymers, diffusion, absorption, and plasticization effects are less pronounced than amorphous polymers[32]. Semi-crystalline polymers can still benefit from the extraction and cleaning abilities of Sc-CO_2. The crystallinity has also been observed to increase during the outgas process for PET and other structurally regular polymers, leading to an increase in tensile strength and decrease in ultimate elongation[33].

Highly amorphous polymers tend to absorb much more CO_2 and plasticize to a much greater extent than crystalline polymers[32]. The solubility of the CO_2 ("tuned" by the pressure of saturation) plays an important role in the plasticization behavior. Shieh *et al.*[32] noticed that sub-critical saturations produced only surface effects on amorphous polymers (for the given saturation times), while supercritical plasticization foamed and/or distorted the polymers upon decompression, indicating a more complete saturation. In all the amorphous polymers tested, a higher uptake of CO_2 resulted in a greater lowering of the glass transition temperature (T_g), implying a higher degree of plasticization.

In addition to morphological effects, Shieh *et al.*[32] found that the polarity of the polymer constituents plays a key role in the amount of CO_2 adsorption observed, especially following decompression of the sample. The general trends suggest that the more polar a polymer, the more soluble the carbon dioxide will be and the extent of saturation will also increase. The

results suggest that PAN copolymers, which are both highly amorphous and polar, should be ideal candidates for CO_2 plasticization. Crank and Park[55] published encouraging results that examined the solubility of various gases in butadiene-acrylonitrile copolymers. As shown in Figure 2.14, an increase in the acrylonitrile content generated an increase in the solubility of CO_2 into the copolymer, at least over the range reported in Figure 2.14.

2.4.3 Rheology of CO_2 Plasticized Systems

A limited number of studies have focused on the use of CO_2 to change the melt rheology of various polymer systems. However, information on the rheology of polymer-solvent systems at high fluid pressure and its influence on the processability is rather limited. Hence, it is necessary to understand the rheology of the high-pressure system to determine how the melt processability of the polymer system can be improved by its plasticization with CO_2. In particular, it is important to understand the rheological impact of approximately 1-20 weight percent CO_2 adsorption on the flow behavior of a polymeric precursor material, instead of the effects of CO_2 on low viscosity (low molecular weight <1000 g/mol) polymeric liquids, which is a focus of many studies.

2.4.3.1 Experimental measurement techniques

Gerhardt *et al.*[45] studied the rheology of high molecular weight (M_w=3.8E+5 g/mol) poly(dimethyl siloxane) (PDMS) swollen with supercritical carbon dioxide. A capillary rheometer modified with a pressurized extrudate chamber was used to measure viscosity versus shear rate for mixtures of PDMS containing dissolved carbon dioxide. Two major changes were made to the capillary rheometer assembly: a sealed loading apparatus at the top of the rheometer was used for transferring an equilibrated sample to the rheometer and a back pressure assembly at the outflow of the capillary was used to hold the extruded solution above its foaming (bubble

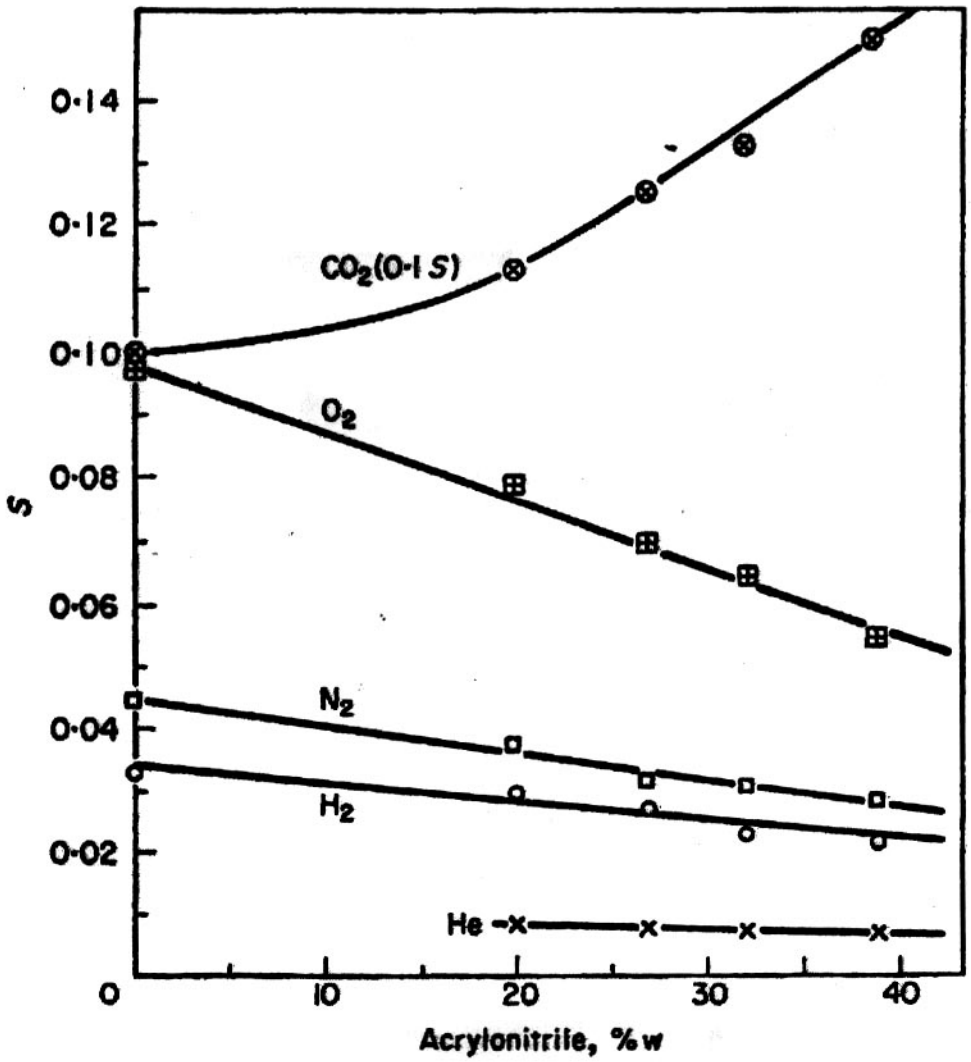

Figure 2.14: Solubility of CO_2 with increasing AN content in butadiene-acrylonitrile copolymers[55].

nucleation) pressure during viscosity measurements. A constant back (static) pressure, approximately 4 MPa greater than the sample equilibration, was applied during the loading and testing phases of the experiment. The excess pressure prevented the degassing of the sample during loading and viscosity measurements. The associated pressure differential across the capillary was determined by subtracting the static pressure from the total upstream pressure. The pressurized rheometer was capable of measuring data with pressures in excess of 25 bars at elevated temperatures (80^{o}C).

Kwag *et al*.[56] studied the rheology of molten polystyrene (PS) and dissolved supercritical and near critical gases including CO_2. The measurements were also performed in a sealed high-pressure capillary rheometer at 150-175^{o}C. Large reductions in melt viscosity were observed at gas loading of 10% and above, up to three orders of magnitude reduction relative to pure polystyrene. Kwag and co-workers[56] successfully demonstrated the ability to use a high pressure sealed capillary rheometer to measure the melt viscosity of viscoelastic materials saturated with CO_2 at supercritical conditions.

Bae and Gulari[44] performed a study on PDMS in which a falling ball viscometer was instead employed for the viscosity measurements. A magnetized metal rod was used to accurately control the shear rate (especially lower rates) at elevated testing pressures. Only sub critical CO_2 measurements were obtained, with pressures not exceeding 30 bars. In addition, only ambient temperatures were studied, a possible indication of other limitations for Sc-CO_2 measurements with this technique. It is important to note that despite the low temperatures and pressures, the authors observed viscosity reductions of up to 30%. The modified falling ball viscometer used for this study, similar to traditional falling body designs, are not suitable for more viscous polymer melt measurements because of the proportional response of the equipment

relative to the experimental time[57], and it is important to note that the measurements in this study were limited to low viscosity, low molecular weight materials.

Royer *et al*.[57] also used a similar method to measure the viscosity of PDMS with a magnetically levitated sphere, with which the difference in magnetic force required to hold the sphere in a fixed place was directly correlated to viscosity. Pressures up to 207 bars (well above the critical pressure of CO_2), with CO_2 concentrations up to 30 weight percent, were measured with this technique. In addition, the rheometer allows the direct decoupling of the effects of CO_2 concentration and pressure[57]. Despite the benefits that can be reaped from this rheometer, the authors required the sample to equilibrate in the rheometer with the CO_2 for 48 hours to obtain complete equilibration (no CO_2 bubbles), which is the only way that the pressure and concentration effects could accurately be separated with this technique[57]. For a thermally unstable material, such as a PAN copolymer, degradation will occur well before an equilibrium is established between the polymer and CO_2 for this particular measurement. In addition, the authors make no mention of high temperature testing (above 80^{o}C), which may not be possible with the rheometer design. In general, both the falling ball and magnetically levitated sphere rheometers were used for low viscosity measurements of low molecular weight polymeric liquids and would not be suitable for measuring viscous, high molecular weight polymeric systems.

Online viscosity measurements during an extrusion process have proven to be very effective and informative for measuring the rheology of CO_2 saturated systems[48]. Single screw extruders have easily facilitated injection of high pressure and Sc-CO_2 directly into polymer melts, with which immediate mixing and diffusion occurred. Lee *et al*.[48] used a wedge die with three pressure transducers to measure viscosities of PE/PS blends at various shear rates, controlled by the resistance of a second downstream die. Traditional slit dies and capillaries can

also be utilized on an extruder by simply varying the flow rate of the polymer melt to obtain viscosities at various shear rates[49]. Such online measurements are beneficial for establishing feasibility of a method in a true processing situation. However, extrusion measurements require large amounts of material that are typically not available on a laboratory scale. In addition, thermally unstable materials, such as PAN, could create problems in the extruder if degradation (crosslinking) occurs prior to sample extrusion. Therefore, pressurized capillary rheometry presents itself as an ideal candidate to study the effects of Sc-CO_2 on thermally unstable polymeric systems.

2.4.3.2 Viscosity modeling of polymer/CO_2 systems

Viscosity modeling of any polymeric material has proven to be a challenging task. When one creates a multicomponent system, the modeling becomes even more difficult, especially if trying to model the entire flow curve for a material. For this reason, few studies have focused on the actual viscosity modeling of a CO_2 saturated polymer, instead concentrating on the viscoelastic scaling and ability to generate master viscosity curves. Viscosity modeling of polymer/CO_2 (plasticized) systems has focused on modeling the shear thinning behavior, and in particular at sub-critical pressures. The shear-thinning regime of the flow curve is most frequently measured via the common experimental techniques, such as pressurized capillary rheometry, because it is difficult to obtain accurate force or pressure drop measurements for low shear rate viscosity data at such elevated pressures.

The limited studies for viscosity modeling of polymer/CO_2 systems incorporate free volume models to account for the effects of the plasticizing CO_2. Bae and Gulari[44] modified the Kelley-Bueche theory, which is typically used to calculate viscosities of concentrated polymer solutions based on the total available free volume in solution. The modification, which accounts

for compressibility effects, uses the WLF equation[58] to account for temperature dependence on fractional free volume and arrive at the following relationship for a polymer/CO_2 system:

$$\eta = \eta_P \phi_P^4 \exp\left[\frac{1}{B_P \phi_P f_P + A_S(1-\phi_P) f_S} - \frac{1}{f_P}\right] \tag{2.3}$$

where η_p is the viscosity of the pure polymer, ϕ_p is the volume fraction of polymer, f_p and f_s are the fractional free volume of polymer and CO_2, respectively, and A_s and B_p are model parameters that can be calculated by fitting the pure material viscosity data. The viscosity model accurately predicted viscosity data for PDMS/CO_2 systems (with various molecular weight grades of PDMS). However, pressures were only measured up to 30 bars, well below the critical pressures for CO_2.

Lee *et al*.[59] also incorporated a free volume model into a well-known viscosity model (Carreau-Yasuda) used for shear thinning. The authors used a WLF temperature dependence on fractional free volume to arrive at an expression for the approximation of zero shear viscosity η_o:

$$\eta_o \approx A \exp\left[\begin{array}{l}\dfrac{\alpha}{(T-T_r)} + \beta P + \psi C + \dfrac{\kappa P}{(T-T_r)} + \delta P C + \dfrac{\varepsilon C}{(T-T_r)} \\ + \dfrac{\xi}{(T-T_r)^2} + \zeta(P-P_r)^2 + \omega(C-C_r)^2\end{array}\right] \tag{2.4}$$

where T_r, P_r, and C_r are reference temperature, pressure, and CO_2 concentration respectively; T, P, and C are temperature, pressure, and concentration; and the constants can be estimated via nonlinear regression. This allows easy substitution into the generalized Carreau-Yasuda model:

$$\eta = \frac{\eta_o}{\left[1 + \left(\dfrac{\eta_o \dot{\gamma}}{\tau}\right)^a\right]^{\frac{1-\eta}{a}}} \tag{2.5}$$

where $\dot{\gamma}$ is the shear rate and τ, n, and a are unique characteristics of the polymeric material that determine the shape of the master curve. The authors found that the viscosity of PS could be accurately modeled with the incorporation of the second order concentration terms in equation 4, resulting in a nonlinear viscosity dependence on concentration. The first order interaction and pressure terms were also found to have a significant effect on the viscosity.

The modeling attempts of Bae and Gulari[44] and Lee *et al*.[59] were limited in their ability to model polymer/CO_2 systems, making no account for the behavior of CO_2 under supercritical conditions. In addition, the goal of the viscosity modeling was geared towards accurately scaling the data into a master curve. As observed in much of the literature, a focus on the ability to shift data for both pure and CO_2 adsorbed systems into a single master plot is observed, and consequently the viscoelastic scaling of such systems will be addressed.

2.4.3.3 Viscoelastic scaling of rheological data

Numerous attempts have been made to correlate the rheology of polymer/CO_2 systems. The general approach is to utilize a free volume theory to quantitatively predict rheological behavior and, more importantly, determine the nature of viscoelastic scaling in such systems. Both Arrhenius and WLF analyses have been incorporated to scale the data. Various results on the methods of scaling have been reported and will be discussed in further detail.

Gerhardt *et al*.[45] initially reported the ability to shift data for PDMS/CO_2 systems with various amounts of dissolved CO_2 in the polymer. Up to 21 weight percent CO_2 was adsorbed into the PDMS samples (pressures up to 120 bar), which corresponded to approximately one order of magnitude reduction in viscosity relative to pure PDMS at 50^oC[45]. Similar to the temperature dependent shift factor, a_T, traditionally employed in time-temperature superposition[55], the authors developed a concentration dependent shift factor, a_C. As illustrated

by the master curve in Figure 2.15, a concentration dependent shift factor adequately scales the data for the PDMS systems with varying CO_2 concentration (data at 50°C). The shift factor a_C represents the reduction of viscosity as compared to the pure polymer melt, where the viscosity reduction mechanism entails both the dilution of the concentration of entangled polymer chains and the increase of chain mobility resulting from the addition of dissolved gas[45]. The viscosity reduction of entangled polymers in solvents and plasticizers is usually mostly attributed to dilution of the entangled polymer chains, with little effect of increased free volume. To emphasize the importance of free volume, Gerhardt and co-workers[45] made a series of nearly constant density solutions using a high molecular weight PDMS polymer dissolved in a low molecular weight PDMS liquid (both of very similar density at ambient conditions). The result was a series of solutions that had nearly constant free volume (iso-free volume) as composition was changed, allowing the authors to isolate the concentration (free volume) effects of CO_2. As illustrated in Figure 2.16, the difference between the iso-free volume curve and the PDMS-Carbon Dioxide curve is solely associated to free volume increase, indicating the high magnitude of free volume effect upon increased dissolution of CO_2.

Gerhardt *et al*.[60] did further work on the PDMS/CO_2 systems by utilizing the Sanchez-Lacombe EOS to calculate the specific volume for the dilution and free volume terms needed for the Kelley-Bueche free volume treatment for viscosity. The viscosity data for PDMS swollen with various amounts of CO_2 was effectively reduced to a master curve identical to the viscosity curve for the pure PDMS melt[60]. Using thermodynamic variables, the authors were able to predict the concentration dependent shift factor a_C, which compared well with the experimentally determined values. The significance is the ability to determine the rheological data for a gas-swollen melt by only having the viscosity curve for a pure polymer melt.

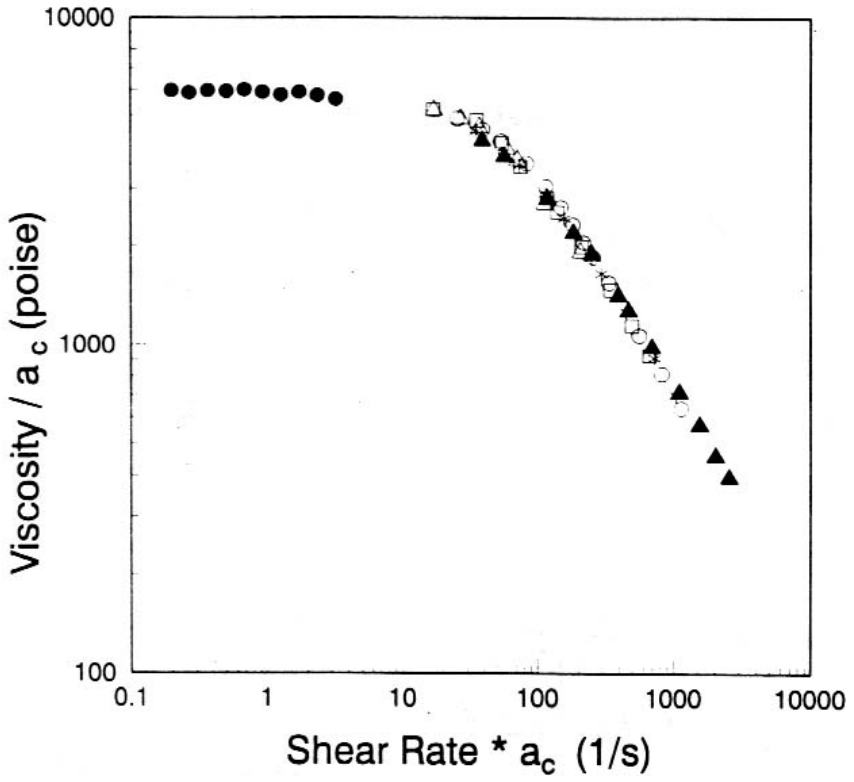

Figure 2.15: Master curve for PDMS swollen with various amounts of CO_2 at 50°C[45].

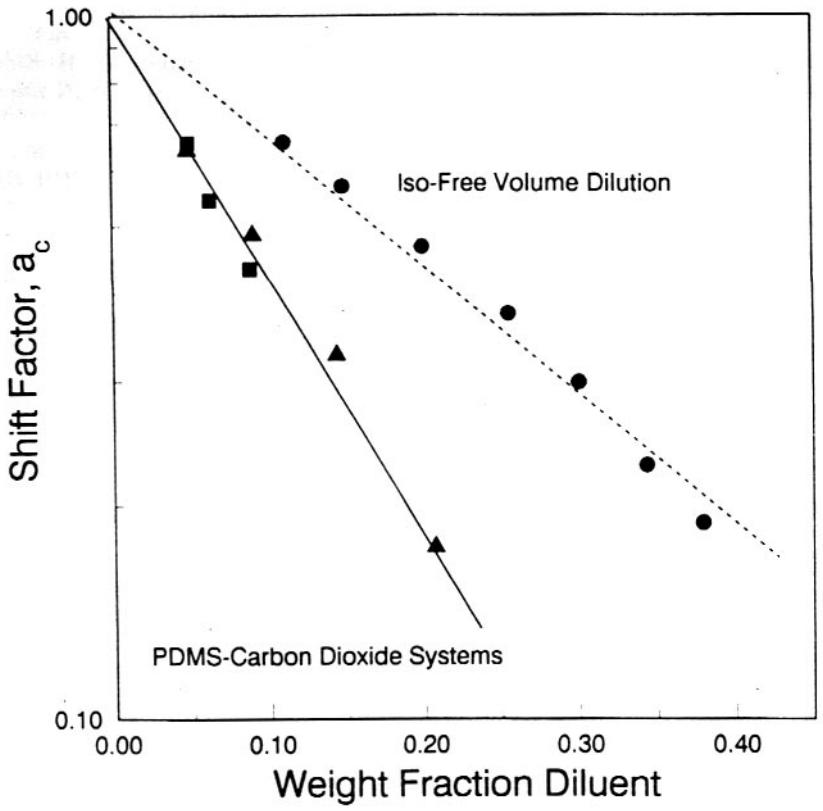

Figure 2.16: Demonstration of free volume effects resulting from CO_2 adsorption[45].

However, some thermodynamic information is required for the mixed gas-polymer system, but can be predicted with some accuracy using pure component properties[60].

Kwag *et al*.[56] reported on the viscosity reduction of polystyrene (PS) using high pressure and supercritical CO_2, reporting up to 10 weight percent uptake with up to three orders of magnitude viscosity reduction. This reduction in viscosity is two orders of magnitude greater at similar gas compositions as compared to that obtained for PDMS-CO_2 systems studied by Gerhardt[45], which were at temperatures 180-200^oC above the T_g of PDMS. At the test conditions, the pressure effects on the PDMS-CO_2 system were not important[56]. The PS-CO_2 systems studied by Kwag *et al*.[56] were tested at temperatures only 50-75^oC above the T_g of pure PS, where the effect of pressure on viscosity became important. Thus, scaling factors that incorporate effects of both gas composition and pressure were introduced for the PS-CO_2 systems, one for pressure and one for gas composition. The master curve, which could be constructed for PS swollen with three different gases at high pressure, is illustrated in Figure 2.17. A temperature scaling factor was needed for pure polystyrene, in conjunction with a_C and a_P for the concentration and pressure effects of dissolved gas. The gas composition shift factor a_C was found to be highly dependent on temperature as the operation temperature approached the glass transition temperature[56]. The pressure dependence on scaling is quantitatively represented via the methods of Penwell *et al*.[61], which correlates localized pressure gradients to overall pressure gradients for polystyrene.

Royer *et al*.[47] also utilized a free volume treatment to collapse data for PS swollen with CO_2 onto a single master curve. A slightly different approach was taken to measure the viscosity: the measurements were taken via an extrusion slit die as opposed to a capillary

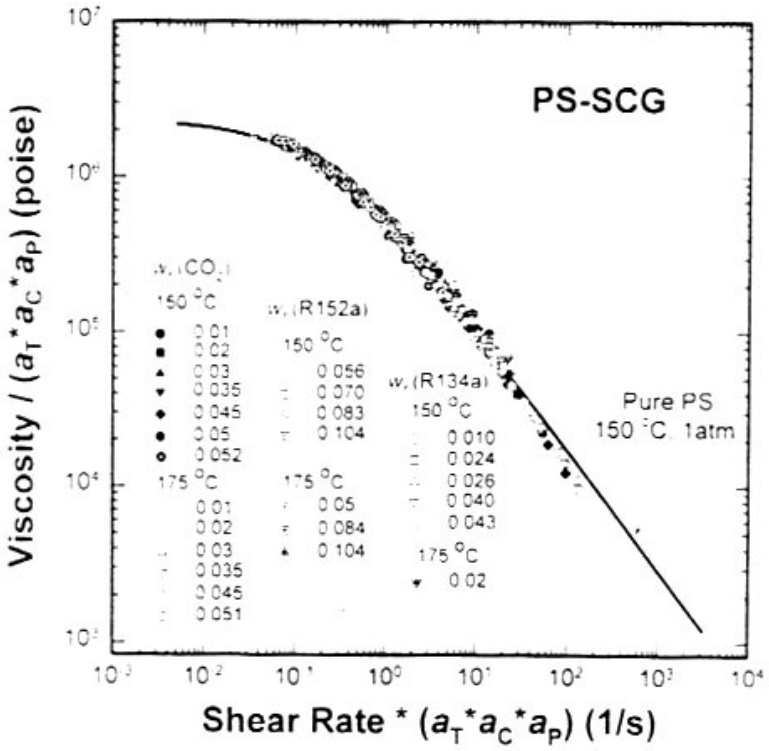

Figure 2.17: Incorporation of pressure dependent shift factor to generate a master curve for PS[56].

rheometer as used by Kwag *et al*.[56] and Gerhardt[45;60]. The Sanchez-Lacombe EOS was again used for density determination. To accurately determine the effects of CO_2 concentration on viscosity, the authors combined the traditional WLF model with the proposed method of Chow (1980) to predict the T_g of the PS-CO_2 system:

$$\log(a_P) = \frac{c_1\left(T - T_{g,mix,P_o}\right)}{c_2 + T - T_{g,mix,P_o}} - \frac{c_1\left(T - T_{g,mix,P}\right)}{c_2 + T - T_{g,mix,P}} \tag{2.6}$$

$$\log(a_C) = \frac{c_1\left(T - T_{g,P_o}\right)}{c_2 + T - T_{g,P_o}} - \frac{c_1\left(T - T_{g,mix,P_o}\right)}{c_2 + T - T_{g,mix,P_o}} \tag{2.7}$$

The model accounts for both the T_g reduction upon CO_2 adsorption and the T_g increase resulting from hydrostatic pressure in the extruder. In addition, the Chow-WLF treatment only depends on directly measurable material parameters (except for the WLF constants c_1 and c_2, which can be determined by measuring the viscosity of the polymer without CO_2 at various temperatures)[47]. Despite the ease of the analysis, it is apparent in Figure 2.18 that the data does not collapse into a master curve as well as the method of Kwag *et al*.[56] and Gerhardt[45;60]. In addition, the data for Royer is more ideal than that taken by the other authors: Royer's data only extends to a maximum CO_2 concentration of 4 percent. Royer *et al*.[49] extended the Chow-WLF analysis for poly(methyl methacrylate) (PMMA). As seen in Figure 2.19, the data for PMMA swollen with CO_2 collapse very well into a master curve. Royer *et al*. (2001) also developed an Arrhenius model for viscoelastic scaling of polymer/Sc-CO_2 systems. The Chow method for predicting T_g's of polymer-diluent systems was combined with the Arrhenius analysis to obtain the following relationships:

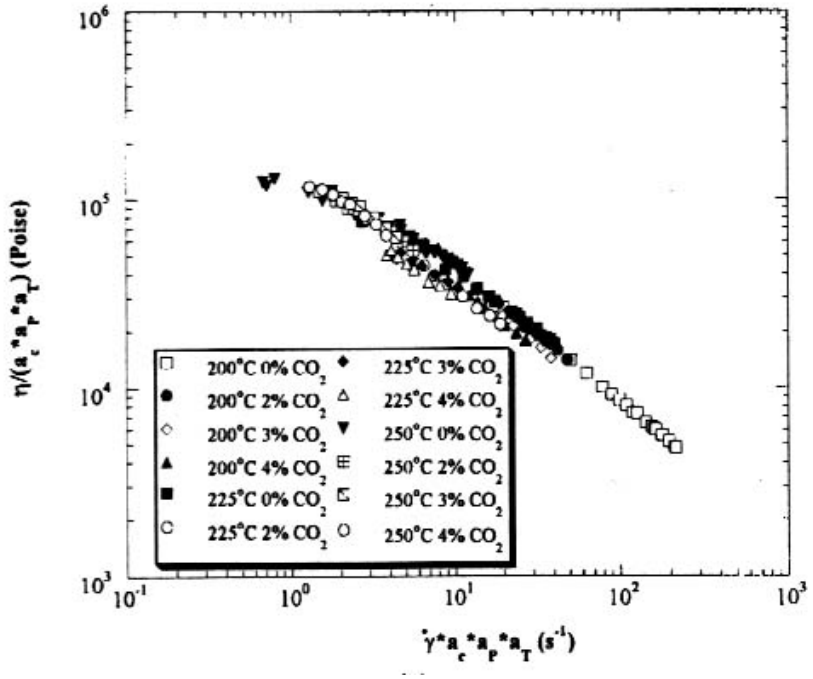

Figure 2.18: Master curve for PS using the Chow-WLF model[47].

$$\ln(a_P) = \left[\frac{E_a}{R} \left(\frac{1}{T_{g,P_o,mix}} - \frac{1}{T_{g,P,mix}} \right) \right] \tag{2.8}$$

$$\ln(a_C) = \left[\frac{E_a}{R} \left(\frac{1}{T_{g,P_o}} - \frac{1}{T_{g,P_o,mix}} \right) \right] \tag{2.9}$$

where E_a is the activation energy for viscous flow and R is the ideal gas constant. Data for polypropylene (PP), low density polyethylene (LDPE), and poly(vinylidene fluoride) (PVDF) swollen with CO_2 at various concentrations (up to 6 weight percent) were collapsed onto a master curve. In all cases, significant discrepancies were observed when the data was shifted, similar to the discrepancies observed in Figure 2.18 for PS. The implication is that neither analysis, the Chow-WLF nor the Chow-Arrhenius models, proposed by Royer *et al*.[49] is universal. However, the data does seem to collapse well enough to validate the Chow model for predicting the T_g of polymer-diluent systems[49].

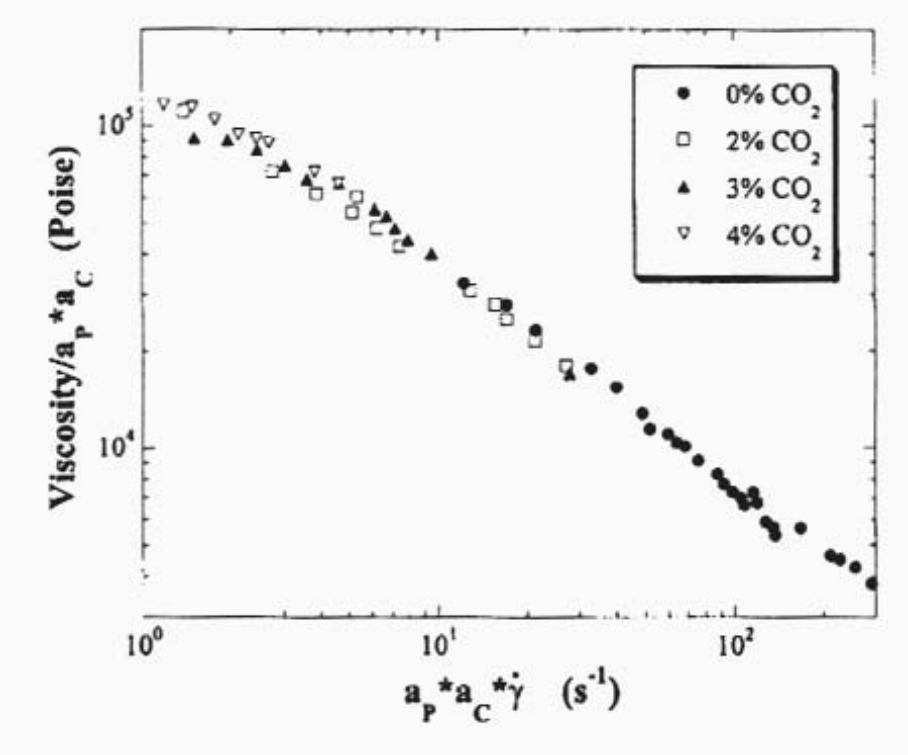

Figure 2.19: Master curve for PMMA using the Chow-WLF model[49].

2.5 Research Objectives

Carbon fiber precursors and acrylic based textile fibers are currently produced using either a wet or wet/dry fiber spinning process. Environmentally unfriendly solvents must be utilized in the solution spinning processes, contributing to the high cost of producing carbon fibers. In addition, solution spinning processes require the removal of solvent from the precursor itself, resulting in a net weight loss of up to 80% and ultimately low carbon yield. A competing cyclization reaction that degrades the resin at melt processing temperatures also creates a problem and limits the processing window for creating precursors. The goal of this research is to develop and establish the processing window for an acrylonitrile based resin that can be melt spun into fiber form, eliminating the need for solvent recovery and resulting in a higher carbon content and ultimately lower cost per pound of carbon or textile fiber.

Traditionally, PAN copolymers are solution spun into textile fibers and carbon fiber precursors. The copolymer used with the acrylonitrile, usually methyl acrylate (MA), lowers the viscosity of the resin and hinders the degradation that occurs at processing temperatures. The solution spun copolymer typically has a melt viscosity much too high for a melt spinning process, which when combined with the thermal degradation necessitates a solution spinning process. For a melt spinning process, the melt viscosity of the starting resin would have to be much lower than that used in current commercial processes, requiring a higher copolymer content. This leads to the first research objective:

Establish if variations in the chemical structure and composition of a PAN copolymer will facilitate a melt processable material.

If the glass transition temperature (T_g) of the starting material could be lowered without altering the copolymer ratio, the viscosity would also be lowered and the material could be processed at a

lower temperature. At the lower processing temperature, the kinetics of the cyclization reaction would be significantly reduced, potentially facilitating melt processing of the precursor with minimal degradation. Carbon dioxide is an inert, environmentally friendly gas that is known to plasticize a number of polymers, reducing the T_g and lowering melt viscosity. This leads to research objective 2:

Establish the effect of varying levels of CO_2 on the viscosity reduction of melt processable PAN copolymers.

The feasibility of melt spinning carbon fiber precursors using absorbed CO_2 can be initially evaluated by establishing the design equations for spinning of the precursor melt containing absorbed CO2. The design equations will be used to estimate the feasibility of developing a pressurized step-down chamber that prevents bubble nucleation and foaming of the precursor fiber melt at the capillary exit of the extruder. The design equations involve coupled partial differential equations describing the momentum, heat, and mass transfer of the spinning and drawing of the fiber, as well as the necessary constitutive equations. Research objective 3 addresses this issue:

Determine the feasibility of a process to prevent foaming and control bubble growth during the melt spinning of CO_2 plasticized PAN copolymer fibers suitable for textiles and carbon fiber precursors.

2.6 References

(1.) Riggs, J. P. *Encyclopedia of polymer science and engineering*; Wiley: New York, **1989**.

(2.) Riggs, D. M.; Shuford, R. J.; Lewis, R. W. *Handbook of composites*; Van Nostrand Reinhold: New York, **1982**; Chapter 11, pp 196-271.

(3.) Goodhew, P. J.; Clarke, A. J.; Bailey, J. E. *Materials Science and Engineering* **1955**, *17*, 3.

(4.) Goodhew, P. J.; Clarke, A. J.; Bailey, J. E. *Materials Science and Engineering* **1955**, *17*, 3.

(5.) Ehrburger, P.; Donnet, J. B. *Handbook of fiber science and technology: Volume III, high technology fibers*; M. Dekker: New York, **1983**; Chapter 5, pp 169-220.

(6.) Tullo, A. H. *Chemical and Engineering News* **2000**, *78*, 11-12.

(7.) Gupta, A. K.; Paliwal, D. K.; Bajaj, P. *Journal of Macromolecular Science-Reviews in Macromolecular Chemistry and Physics* **1991**, *C31*, 1-89.

(8.) Bajaj, P.; Roopanwal, A. K. *Journal of Macromolecular Science-Reviews in Macromolecular Chemistry and Physics* **1997**, *C37*, 97-147.

(9.) Smith, W. C. *Textile World* **1998**, *148*, 53-63.

(10.) Diefendorf, R. J.; Tokarsky, E. *Polymer Engineering and Science* **1975**, *15*, 150-159.

(11.) Johnson, D. J. *Carbon Fibers, Filaments, and Composites*; Kluwer Academic Publishers: Dordrecht, **1990**, pp 119-146.

(12.) Edie, D. D. *Carbon* **1998**, *36*, 345-362.

(13.) Dunham, M. G.; Edie, D. D. *Carbon* **1992**, *30*, 435-450.

(14.) Jain, M. K.; Abhiraman, A. S. *Journal of Materials Science* **1987**, *22*, 278-300.

(15.) Porosoff, H. Stamford, CT, U.S. Patent 4,163,770 **1979**.

(16.) Jain, M. K.; Balasubramanian, M.; Desai, P.; Abhiraman, A. S. *Journal of Materials Science* **1987**, *22*, 301-312.

(17.) Bhat, G. S.; Abhiraman, A. S.; Cook, F. L. *Processing and Fabrication of Advanced Materials for High Temperature Applications II proceedings of a Symposium sponsored by the Struuctural Materials Division (SMD), held at Materials Week '92 in Chicago, Illinois, November 1-5, 1992*; The Minerals, Metals & Materials Soc: Warrendale, PA, **1993**, pp 449-463.

(18.) Grassie, N.; McGuchan, R. Pyrolysis of Polyacrylonitrile and Related Polymers-IV. European Polymer Journal 7, 1503-1514. **1971**. England, Pergamon Press.

(19.) Tsai, J. S.; Lin, C. H. *Journal of Applied Polymer Science* **1991**, *43*, 679-685.

(20.) Tsai, J. S.; Lin, C. H. *Journal of Applied Polymer Science* **1991**, *42*, 3039-3044.

(21.) Rangarajan, P.; Yang, J.; Bhanu, V.; Godshall, D.; McGrath, J.; Wilkes, G.; Baird, D. *Journal of Applied Polymer Science* **2002**, *85*, 69-83.

(22.) Min, B. G.; Son, T. W.; Kim, B. C.; Jo, W. H. *Polymer Journal* **1992**, *24*, 841-848.

(23.) Daumit, G. P., Ko, Y. S., Slater, C. R., Venner, J. G., and Young, C. C. Charlotte, NC, U.S. Patent 4,921,656 **1990**.

(24.) Daumit, G. P., Ko, Y. S., Slater, C. R., Venner, J. G., Young, C. C., and Zwick, M. M. Charlotte, NC, U.S. Patent 4,981,752 **1991**.

(25.) Atureliya, S. K.; Bashir, Z. *Polymer* **1993**, *34*, 5116-5122.

(26.) Coxe, C. D. Wilmington, DE, U.S. Patent 2,585,444 **1952**.

(27.) Frushour, B. G. *Polymer Bulletin* **1982**, *7*, 1-8.

(28.) Grove, D.; Desai, P.; Abhiraman, A. S. *Carbon* **1988**, *26*, 403-411.

(29.) DeMaria, F and Young, C. C. Stamford, CT, U.S. Patent 4,303,607 **981**.

(30.) Pfeiffer, R. E. and Peacher, S. E. Stamford, CT, U.S. Patent 4,318,680 **1982**.

(31.) Cooper, A.; Howdle, S. *Materials World* **2000**, *8*, 10-12.

(32.) Shieh, Y. T.; Su, J. H.; Manivannan, G.; Lee, P. H. C.; Sawan, S. P.; Spall, W. D. *Journal of Applied Polymer Science* **1996**, *59*, 707-717.

(33.) Shieh, Y. T.; Su, J. H.; Manivannan, G.; Lee, P. H. C.; Sawan, S. P.; Spall, W. D. *Journal of Applied Polymer Science* **1996**, *59*, 695-705.

(34.) Garg, A.; Gulari, E.; Manke, C. W. *Macromolecules* **1994**, *27*, 5643-5653.

(35.) Moore, S.; Samdani, S.; Ondrey, G.; Parkinson, G. *Chemical Engineering* **1994**, *101*, 32.

(36.) Farncomb, R. E.; Nauflett, G. W. *Waste Management* **1997**, *17*, 123-127.

(37.) Shiho, H.; DeSimone, J. M. *Macromolecules* **2000**, *33*, 1565-1569.

(38.) Heater, K. J.; Tomasko, D. L. *Journal of Supercritical Fluids* **1998**, *14*, 55-65.

(39.) Eggers, R.; Sievers, U. *Journal of Chemical Engineering in Japan* **1989**, *22*, 641.

(40.) Li, S. F.; Hartland, S. *Journal of the American Oil Chemists Society* **1996**, *73*, 423-429.

(41.) Ooi, C. K.; Bhaskar, A.; Yener, M. S.; Tuan, D. Q.; Hsu, J.; Rizvi, S. S. H. *Journal of the American Oil Chemists Society* **1996**, *73*, 233-237.

(42.) Berens, A. R.; Huvard, G. S.; Korsmeyer, R. W.; Kunig, F. W. *Journal of Applied Polymer Science* **1992**, *46*, 231-242.

(43.) Lee, F. Y.; Ryu, G. H.; Lim, S. T. *Cereal Chemistry* **1999**, *76*, 63-69.

(44.) Bae, Y. C.; Gulari, E. *Journal of Applied Polymer Science* **1997**, *63*, 459-466.

(45.) Gerhardt, L. J.; Manke, C. W.; Gulari, E. *Journal of Polymer Science Part B-Polymer Physics* **1997**, *35*, 523-534.

(46.) Kwag, C.; Manke, C. W.; Gulari, E. *Industrial & Engineering Chemistry Research* **2001**, *40*, 3048-3052.

(47.) Royer, J. R.; Gay, Y. J.; DeSimone, J. M.; Khan, S. A. *Journal of Polymer Science Part B-Polymer Physics* **2000**, *38*, 3168-3180.

(48.) Lee, M. H.; Tzoganakis, C.; Park, C. B. *Polymer Engineering and Science* **1998**, *38*, 1112-1120.

(49.) Royer, J. R.; DeSimone, J. M.; Khan, S. A. *Journal of Polymer Science Part B-Polymer Physics* **2001**, *39*, 3055-3066.

(50.) Park, C. B.; Behravesh, A. H.; Venter, R. D. *Polymer Engineering and Science* **1998**, *38*, 1812-1823.

(51.) Sanchez, I. C.; Lacombe, R. H. *Macromolecules* **1978**, *11*, 1145-1156.

(52.) Panayiotou, C.; Vera, J. H. *Polymer Journal* **1982**, *14*, 681-694.

(53.) Xiong, Y.; Kiran, E. *Polymer* **1995**, *36*, 4817-4826.

(54.) Bourbon, D.; Kamiya, Y.; Mizoguchi, K. *Journal of Polymer Science Part B-Polymer Physics* **1990**, *28*, 2057-2069.

(55.) Crank, J.; Park, G. S. *Diffusion in Polymers*; Academic Press: London, **1968**.

(56.) Kwag, C.; Manke, C. W.; Gulari, E. *Journal of Polymer Science Part B-Polymer Physics* **1999**, *37*, 2771-2781.

(57.) Royer, J. R.; Gay, Y. J.; Adam, M.; DeSimone, J. M.; Khan, S. A. *Polymer* **2002**, *43*, 2375-2383.

(58.) Ferry, J. D. *Viscoelastic properties of polymers*; Wiley: New York, **1980**.

(59.) Lee, M. H.; Park, C. B.; Tzoganakis, C.; Naguib, H. E. Comparison of Various Viscosity Models for PS/CO2 Solutions. **2002**.

(60.) Gerhardt, L. J.; Garg, A.; Manke, C. W.; Gulari, E. *Journal of Polymer Science Part B-Polymer Physics* **1998**, *36*, 1911-1918.

(61.) Penwell, R. C.; Porter, R. S.; Middleman, S. J. *Journal of Polymer Science Part A: Polymer Physics* **1971**, *9*, 731.

3.0 Materials and Experimental Methods

Preface

This chapter provides additional information regarding the materials and experimental procedures used for this research. This information is included to supplement the descriptions in the later chapters (manuscripts). Also, this provides a guide for future personnel in the Polymer Processing Laboratory.

3.0 Materials and Experimental Methods

This chapter presents relevant details regarding the materials studied and the experimental apparatus and procedures followed. Section 3.1 identifies the materials used, and discusses the evolution of the materials throughout the course of the project. Section 3.2 presents the preparation techniques used for measurements in the torsional rheometer, and discusses rheological screening of the materials in Section 3.1. Lastly, Section 3.3 discusses the methods and procedures used to characterize resins containing absorbed CO_2.

3.1 Materials

This work generally utilized two classes of AN polymers, one series of tailored, melt processable AN copolymers designed by Prof. McGrath in Chemistry at VA Tech, and another set of commercially produced, melt processable AN copolymers. Both sets of resins were incorporated into the rheological studies of this work. The resins used in each specific study are specifically discussed in their respective chapters. However, the rationale for using each set of copolymers is investigated in the following sections.

3.1.1 Virginia Tech Co- and Terpolymers

The first series of tailored materials was polymerized by Drs.V.A. Bhanu and T. Mukundan, under the direction of Prof. McGrath, in an effort to produce low cost, melt processable carbon fiber precursors for use in lightweight automotive composites[1]. Approximately 400 copolymers were created over the course of the project in approximately 5-10 gram quantities, in which a suitable polymerization technique, comonomer, copolymer, molar composition, and molecular weight were identified. The recipe was provided to Monomer Polymer Inc. of Feastersville, PA to scale-up the laboratory polymerizations, and four-one kg

batches were produced. One batch was an 85/15 mole % acrylonitrile/methyl acrylate (AN/MA) copolymer, and the other three batches were 85/14/1 mole % acrylonitrile/methyl acrylate/acryloyl benzophenone (AN/MA/ABP) terpolymers.

The weight and number average molecular weights (M_n and M_w), intrinsic viscosities (IV), and polydispersity (PDI) for these four scaled up batches are listed in Table 3.1. Figure 3.1 shows the molecular weight distribution (MWD) data for each of these resins. Intrinsic viscosities were measured using a Cannon Ubbelhode viscometer at 25^{o}C. Absolute molecular weight measurements from gel permeation chromatography (GPC) were obtained at 60^{o}C with a Waters 2690 Separation Module equipped with a differential refractometer detector and an on-line differential viscometric detector (Viscotek T60A) coupled in parallel. NMP containing 0.2 M P_2O_5 was used as a solvent. A typical Gaussian MWD was observed for the 85/15 AN/MA copolymer and the 85/14/1 AN/MA/ABP resin 2 and resin 3 terpolymers. However, the resin 1 terpolymer has a high MW tail in the MWD, and also had a significantly higher M_w and M_n than the other three scaled up resins. This particular resin degraded before flowing when attempting to measure the rheological properties, and as a result was not used to any significant degree in this work. The other three resins have a similar narrow MWD (1.7-2.5), but varying molecular weights (M_w from 27,300-65,900 g/mol) and IV (0.36-0.52).

These three resins were a culmination of experimental screenings throughout the course of the project, and provided a framework for a great deal of the research in this work. Three other AN/MA copolymers, containing 93, 95, and 98 mole % AN, were used for identification of the effects of AN on the ability to absorb CO_2. These resins were polymerized by Dr. Bhanu[1] in 10 gram quantities.

AN/MA molar ratio	Intrinsic Viscosity (NMP/25°C)	M_n (GPC, g/mol)	M_w (GPC, g/mol)	PDI
85/15	0.50	26,500	65,900	2.5
85/14/1 batch 1	1.20	47,800	205,900	4.3
85/14/1 batch 2	0.36	16,300	27,300	1.7
85/14/1 batch 3	0.52	22,000	41,700	1.9

Table 3.1: Molecular weight information for the AN/MA copolymer and AN/MA/ABP terpolymers.

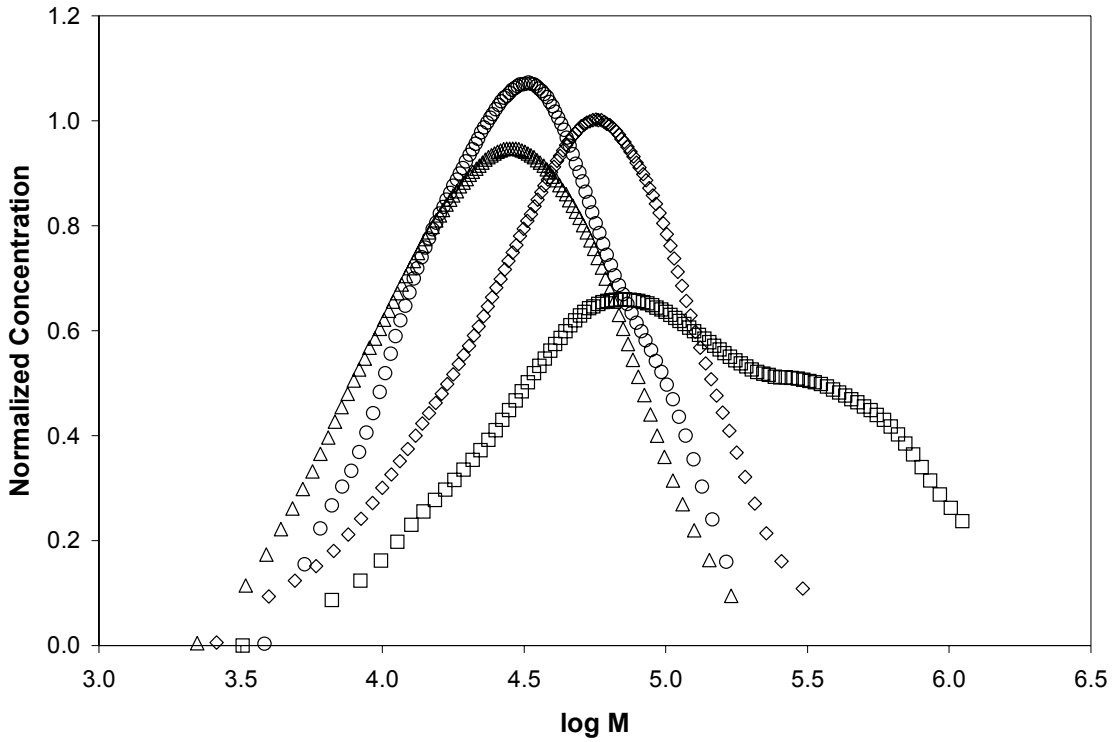

Figure 3.1: Molecular weight distribution for the AN/MA copolymer and AN/MA/ABP terpolymers. (◊) AN/MA copolymer; (□) batch 1 terpolymer; (Δ) batch 2 terpolymer; (o) batch 3 terpolymer.

3.1.2 Commercially Produced Resins

Two commercially produced resins were utilized in this work. The first resin is Barex, an extrudable grade AN/MA copolymer made by BP/Amoco, containing 65 mole percent acrylonitrile (AN), 25 mole percent methyl acrylate (MA) and 10 mole percent elastomer. Barex is currently produced for production of barrier films, and was available in 50 kg quantities. The second resin is an extrudable grade 90/10 mole percent AN/MA copolymer named Amlon, also produced by BP/Amoco. Amlon was developed as a melt processable AN precursor containing less than one mole percent of a stabilizer, but is no longer produced, and as a result only a small quantity (roughly 100 grams) of the copolymer was obtained for our measurements.

Because of its extreme melt stability, especially compared to higher AN content copolymers, Barex was an ideal resin to establish a framework for the ability of CO_2 to absorb in and plasticize AN copolymers. This resin facilitated experimental analyses at elevated temperatures (above the Tg of the copolymer) for significant lengths of time with minimal degradation. The Amlon resin provided a relatively high AN content copolymer that is melt stable, again suitable for time consuming, high temperature experimental measurements.

3.2 Torsional Rheometry of AN Copolymers

Shear rheological measurements were used to identify the small amplitudes dynamic oscillatory rheological properties, as well as the steady shear flow properties at low shear rates ($\dot{\gamma} < 10\ s^{-1}$), of the AN containing resins. A Rheometrics RMS800 with 25.0 mm parallel plate fixtures was used to obtain the data. The operating procedures used to obtain the shear rheological data, and to minimize degradation prior to data acquisition, are discussed in this section.

3.2.1 Sample Preparation

Samples in powder form were compression molded into circular disks of 25.0 mm diameter and 1.0 mm thickness using a press at room temperature. The Amlon copolymer was compression molded into circular disks of the same dimensions at 210°C. Barex was compression molded into disks at 180°C.

3.2.2 Sample Loading and Equilibration

During loading, heating, and equilibration of the samples in the rheometer, an inert nitrogen atmosphere was used in the rheometer oven. The presence of oxygen has been shown to accelerate the crosslinking reaction, and use of an inert atmosphere helped to prevent significant degradation prior to rheological measurements[2]. The samples were loaded into the hot rheometer and allowed to equilibrate for five minutes prior to data acquisition. Five minutes was found to be the minimal time for (relative) temperature equilibration in the rheometer oven.

3.2.3 Screening of Tailored AN Copolymers

During the course of the project, torsional rheometry was used to screen the polymers polymerized by VT Chemistry. In particular the steady shear viscosity (η) increase was monitored as a function of time. Feedback was provided to Chemistry at VT regarding η levels and their magnitude of increase as a function of time. This feedback screening process narrowed down the experimental polymerization variables to produce the previously mentioned scaled-up copolymers.

3.3 Characterization of AN Copolymers Containing Absorbed CO_2

The method used to absorb CO_2 into the AN copolymers is detailed in this section. The apparatus and measurement procedures used to measure the amount of absorbed CO_2, reduction in glass transition temperature (T_g), and viscosity reduction in the AN copolymers containing absorbed CO_2 are discussed.

3.3.1 Sample Preparation

The samples produced via the VT recipe were available in powder form, and were compression molded into pellets of similar size to the Barex and Amlon copolymers to ensure that the CO_2 absorption experiments would be performed on samples of equal dimension. The AN samples in powder form could be molded into pellets at temperatures between 180-200^oC in 5 minutes or less, which we believe prevented significant crosslinking (thermal degradation). Approximately 1-2 grams of polymer powder were compression molded into pellets for each set of thermal analyses.

For the viscosity measurements of the 85/15 AN/MA copolymer containing absorbed CO_2, larger quantities of pellets (15-20 grams) were prepared by extrusion into fiber form using a capillary rheometer at 200^oC (residence time no greater than 15 minutes). The fibers were then chopped into pellets of similar size to the Amlon and Barex with a pelletizer.

3.3.2 Saturation of Samples with CO_2

The copolymer pellets were saturated with CO_2 in a sealed, constant volume, pressurized bomb for various amounts of time. A Parr Instruments model 4760 pressure vessel was used to saturate the samples. For the thermal analyses, approximately one gram of polymer was saturated for each test. For the viscosity measurements, approximately 20 grams of polymer were saturated. The procedure to saturate the copolymers is as follows:

1. Load sample in pressure vessel.
2. Charge pressure vessel with CO_2 at room temperature in the form of a high pressure gas at 850 psi.

3. Heat to a specific saturation temperature above the T_g of the copolymers (generally ranging from 84-100^oC) .. this increases free volume and ensures dispersion of the CO_2 into the polymer.
4. Soak samples at 120^oC (which was commonly used as the soak temperature because it is above the T_g of the majority of the copolymers but below the temperature at which significant crosslinking began to occur).
5. Hold sample at 120^oC for specified "soak time" for the CO_2 absorption.
6. Cool to room temperature via forced convection.
7. Decompress over the course of 12 minutes.

High pressure saturations were performed using a Trexel TR-1-5000L high pressure CO_2 pump. Following the batch pressurization and heating to 120^oC (corresponding to 1500 psi), the high pressure pump was used to directly inject liquid CO_2 into the heated pressure vessel and raise the pressure to 2500 psi.

3.3.3 Differential Scanning Calorimetry

A Seiko model 220 differential scanning calorimeter (DSC) and a TA Instruments model 2920 modulated DSC were used to make the DSC measurements. Heating and cooling rates of 10^oC/min were used. A nitrogen purge was used during measurements in both DSC units. Pierced lids were used with the aluminum sample pans, which allowed the escape of the absorbed CO_2. Two heats were performed on each sample: the first heat allowed direct visualization of the T_g reduction resulting from absorbed CO_2, and the second heat verified that no residual CO_2 was present, which was confirmed if the T_g of the pure material was obtained. Samples containing absorbed CO_2 were cooled to -20^oC to further prevent any degassing prior to running the thermal scan, as well as to establish a baseline. The test comprised heating from -

20°C to 180°C to ensure that all CO_2 had flashed out of the system, cooling back to -20°C, and then performing the second heat.

3.3.4 Thermogravimetric Analysis

A TA Instruments Hi Res TGA 2950 thermogravimetric analyzer (TGA) was used to measure the weight percent of CO_2 that was absorbed into the AN copolymer. A nitrogen purge of 24 ml/min and platinum pans were used. Measurements were started at room temperature (25°C) and ramped to 250°C at a heating rate of 10°C/min. The weight fraction was monitored to determine the amount of CO_2 lost following heating through the T_g of the copolymer.

3.3.5 Pressurized Capillary Rheometry

An Instron model 3211 capillary rheometer was modified to measure the viscosity of the AN copolymers containing absorbed CO_2. The rheometer was modified with the addition of a sealed chamber at the capillary exit for the purpose of creating a static pressure to prevent flashing off of the CO_2 from the copolymer, maintaining a single phase melt. A schematic of the experimental apparatus is shown in Figure 3.2. A specially constructed pressure assembly was used to apply a constant static pressure to the capillary exit and collect the extrudate during the viscosity measurements. The use of an adjustable pressure relief valve ensured that the applied static pressure remained constant. The rheometer piston was sealed using Teflon O-rings, and the pressure chamber assembly was sealed to the capillary using Teflon spacers. An Omega CN9000 temperature controller was used to control the temperature of the pressurized chamber. Two 150-Watt Fire Rod cartridge heaters were used to heat and maintain the chamber temperature.

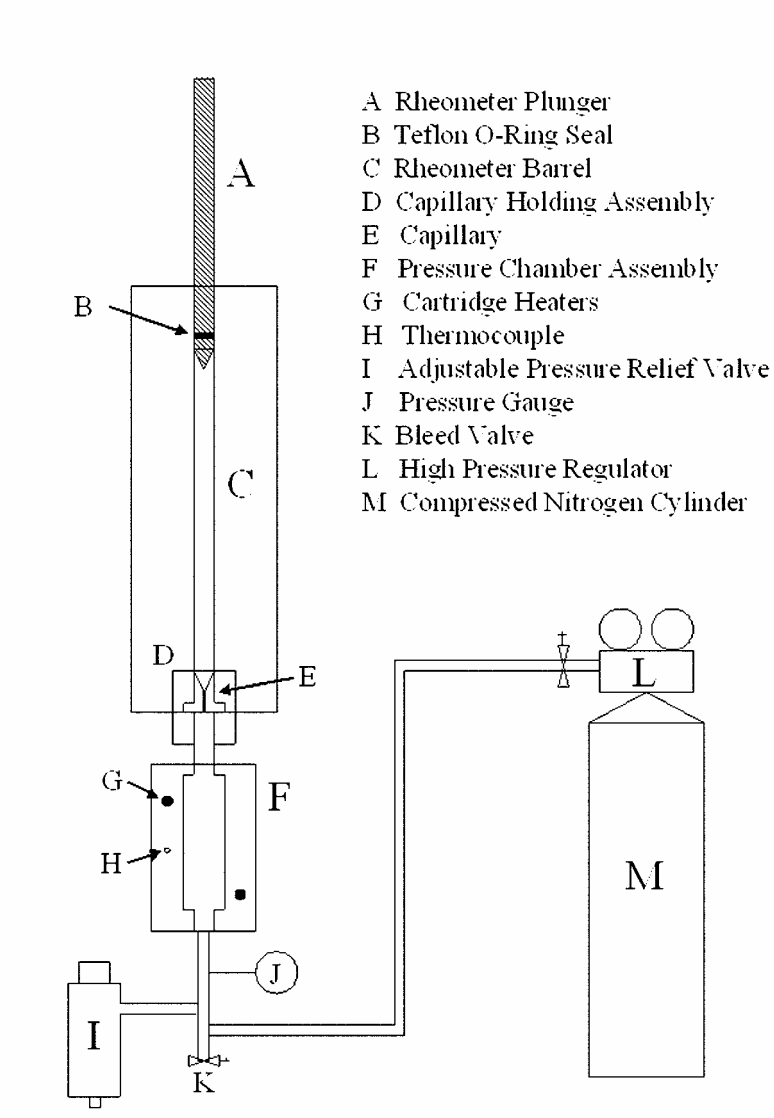

Figure 3.2: Schematic of the pressurized capillary rheometer used to obtain the viscosity of AN melts plasticized with CO_2.

In order to minimize the loss of CO_2 on loading the barrel of the capillary rheometer with samples containing absorbed CO_2, the following procedure was utilized:

1. Insert capillary and attach pressure chamber to rheometer, apply power to rheometer and allow to equilibrate for at least 15 minutes.
2. Zero the load cell as described in the rheometer manual.
3. Load the polymer sample containing absorbed CO_2 into the rheometer barrel, being sure to fill the rheometer to within approximately 3 cm of the top of the barrel.
4. Lower the plunger into the rheometer barrel until the Teflon O-rings provide a tight seal.
5. Apply static pressure to the pressure chamber.
6. Begin to heat the rheometer barrel. Set the pressure chamber temperature with the Omega temperature controller.
7. Once both the pressure chamber and rheometer barrel are heated to measurement temperature, lower the plunger at a rate of 2.0 cm/min until a significant and relatively steady force are obtained (this forces polymer melt into capillary and reduced possibility for incorrect force measurement, especially at low rates).
8. Begin the measurements, working from lowest to highest plunger speed (shear rate).
9. When measurements are completed, turn off static pressure feed line and release pressure. Remove pressure chamber and immediately remove extrudate.

With the system pressurized, the polymer could be heated to test temperatures without losing the absorbed CO_2 to the atmosphere, and the effects of plasticization on viscosity could be measured.

3.4 References

(1.) Bhanu, V. A.; Wiles, K. B.; Rangarajan, P.; Glass, T. E.; Godshall, D.; Sankarpandian, M.; Baird, D. G.; Wilkes, G. L.; Banthia, A. K.; McGrath, J. E. *Abstracts of Papers of the American Chemical Society* **2001**, *222*, U332.

(2.) Ehrburger, P.; Donnet, J. B. *Handbook of fiber science and technology: Volume III, high technology fibers*; M. Dekker: New York, **1983**; Chapter 5, pp 169-220.

4.0 Shear Rheology of Melt Processable Carbon Fiber Precursors

Preface

This chapter addresses research objective 1, and is organized as a manuscript for publication. In particular, this chapter examines the shear rheological properties of three melt processable carbon fiber precursors. The rheological properties include the steady shear viscosity, measured as a function of temperature and time, and the magnitude of the complex viscosity, measured as a function of temperature and frequency. The effects of copolymerization of a UV sensitive termonomer, acryloyl benzophenone, and of molecular weight on the rheology are analyzed. The rheological techniques established in this chapter were used to develop a processing window for AN copolymers, which is presented in further detail by the rheological data in Appendix D.

Shear Rheological Properties of Acrylic Copolymers and Terpolymers Suitable for Potentially Melt Processable Carbon Fiber Precursors

Michael J. Bortner[1], Priya Rangarajan[1], Vinayak Bhanu[2], James E. McGrath[2], and Donald G. Baird[1]

[1]Department of Chemical Engineering
[2]Materials Research Institute and Department of Chemistry
Virginia Polytechnic Institute and State University
Blacksburg, VA 24061-0211

Abstract

In an effort to generate melt processable polyacrylonitrile (PAN) precursor fibers suitable for conversion to carbon fibers, an acrylonitrile/methyl acrylate (AN/MA) copolymer and two acrylonitrile/methyl acrylate/acryloyl benzophenone (AN/MA/ABP) terpolymers were synthesized at molar ratios of 85/15 and 85/14/1, respectively. The termonomer (ABP) was incorporated to accelerate crosslinking via UV irradiation, which serves to prevent relaxation of orientation and flow as the temperature of the fiber is raised during thermo-oxidative stabilization. Two molecular weights of the terpolymer and one molecular weight of the copolymer were studied to determine the effect of the termonomer, and the effect of molecular weight (MW), on the steady shear viscosity (η) and magnitude of the complex viscosity ($|\eta^*|$). A higher rate of increase of η as a function of time was observed for the high MW terpolymer relative to that of the copolymer over the temperature range used. Using a temperature sweep and monitoring levels of $|\eta^*|$, a minimum was observed at lower temperatures for both terpolymers. These results suggest that copolymerization with ABP significantly increased the thermally induced kinetics of crosslinking. Comparison of the η and $|\eta^*|$ data for the low and high MW terpolymers suggested that molecular weight also significantly reduced the melt stability (increased the kinetics of crosslinking). A chemorhelogical correlation was then used to

quantify the effects of the termonomer and of molecular weight on the kinetics of crosslinking of the AN terpolymers.

4.1 Introduction

Currently, carbon fiber precursors are industrially produced via two main techniques: melt spinning of mesophase pitch and those produced from PAN precursors (usually a copolymer of acrylonitrile and a suitable comonomer) lead to carbon fibers with a high tensile strength and a high elongation to break (>1%). Edie[1] reported that PAN based carbon fibers have approximately three times the value of tensile strength over pitch based solution spinning of high (~97 mole %) polyacrylonitrile (PAN) containing copolymers. Carbon fiber precursors produced from mesophase pitch usually lead to high modulus fibers, whereas fibers, but the value of the modulus is generally 50 percent of the pitch fibers. Because carbon fibers generated from mesophase pitch are more expensive, low cost production may be more easily attainable using PAN based systems.

Production of PAN based carbon fibers involves three major steps: precursor fiber formation, thermo-oxidative stabilization, and carbonization. PAN acrylic textile fibers that serve as carbon fiber precursors are usually generated by wet-spinning[2]. The precursor fibers are then subjected to a thermo-oxidative "stabilization" procedure at 220-300^{o}C, during which a crosslinking and cyclization reaction takes place to form a "ladder" structure that can withstand higher temperature heat treatments[2]. The "stabilized" fibers are then subjected to a high temperature (400-1200^{o}C) carbonization step in an inert atmosphere for conversion into carbon fibers[2].

The precursor for PAN based carbon fibers is generally copolymerized with a low percentage (2-7 mole %) of a suitable comonomer, such as methyl acrylate (MA), itaconic acid,

or methacrylic acid[3]. The comonomers enhance solubility and decrease the kinetics of crosslinking during the exothermic stabilization procedure, and subsequently reduce heat buildup and thermally induced chain scission reactions[2]. As a result, improved mechanical properties of the carbon fibers are obtained by minimizing the chain scission reactions during the stabilization step[2].

PAN based carbon fibers have found numerous applications in engineering and structural polymer composites for aerospace and defense applications, as well as in sporting goods and automotive applications, because of their high specific strength and modulus and low coefficient of thermal expansion[4]. However, the prohibitive cost of carbon fiber production has limited their usage[5]. The rapid crosslinking reaction that can occur concurrently with the stabilization step requires that acrylonitrile (AN) copolymer precursor fibers be solution processed in the presence of toxic, environmentally unfriendly organic solvents, commonly including dimethyl formamide (DMF) and dimethylacetamide (DMAC)[3]. These polar organic solvents are usually used in the range of 70-93 weight percent solvent (7-30 wt % solids) to permit processing at temperatures well below the onset of the crosslinking reaction[2]. As a result, high production costs are incurred during carbon fiber production from both solvent use and recovery in the precursor generation step. The thermo-oxidative procedure requires a significantly longer amount of time than the precursor fiber generation step and prevents continuous carbon fiber generation directly from solution spinning of the precursor. As a result, the stabilization step also significantly contributes to the high production costs associated with PAN based carbon fibers. For these reasons, there is interest in developing alternative methods to produce PAN based carbon fibers, in particular suitable for use as reinforcements in automotive structural applications, in a more economical and environmentally friendly manner.

Melt processing of AN copolymers could potentially provide a less expensive and environmentally benign method of carbon fiber production by eliminating the need for solvent use and recovery in the precursor generation step, resulting in reduced capital and operating costs[5]. Melt spinning would also reduce costs by providing 100% solids throughput on a per pound basis, compared to the 7-30 wt. % obtained from solution processing. In order to melt spin AN precursor fibers, the kinetics of crosslinking described above must be kept to a level that facilitates a relatively stable steady shear viscosity (η) as a function of time. In particular, an arbitrarily selected increase of approximately 10-20% in the levels of η was found to be acceptable over a period of 1800 s, which was believed to be sufficient to extrude approximately 99% of the material[6]. However, the precursor fibers must subsequently have the ability to be crosslinked and converted into carbon fiber form following melt spinning.

Extensive efforts have been documented by Bhanu et al.[7;8], Rangarajan et al.[5;9], Wiles[10] and Godshall et al.[11], which had the goal of establishing a suitable polymerization technique, copolymer composition, comonomer types, and molecular weight to produce melt spinnable acrylic precursors that can be processed in the range of 200-220^{o}C. These studies focused largely on the use of suitable comonomers (primarily MA) in the range of 10 to 15 mole percent to disrupt the long range order and modestly reduce the T_g of AN copolymers, affording melt stability. AN/MA copolymers were preferably generated via a heterogeneous free radical (emulsion) polymerization, and a molar ratio of about 85/15 mole % AN/MA was identified as melt processable. The kinetics of crosslinking was found to be relatively slow, with increases in the levels of η of approximately 3 and 7% over a period of 1800 s and shear rate ($\dot{\gamma}$) of 0.1 s^{-1} at 200 and 210^{o}C, respectively. The copolymer precursor could be melt spun, but it was noted that an extremely long thermo-oxidative stabilization procedure was required to prevent the fibers

from flowing and losing orientation. As a result, a thermally stable but photochemically active termonomer (acryloyl benzophenone) was identified that could be terpolymerized to accelerate crosslinking in the drawn precursor fibers via UV irradiation[7]. However, the effects of addition of the termonomer on the melt stability and rheology of the precursor copolymer were unknown.

Although the overall goal of this study was geared towards production of low cost carbon fibers (<$5/lb.) with high mechanical properties (e.g. tensile modulus = 170 GPa, tensile strength = 2.7 GPa), the goal of this paper is to determine whether the viscosity levels and melt stability of the AN/MA/ABP terpolymers are suitable for melt spinning. Changes in the steady shear viscosity (η) versus time are measured to quantify the melt stability of the co- and terpolymers in the temperature range 200-260^{o}C. Dynamic oscillatory frequency sweeps, used over the temperature range of 200-220^{o}C, provide information about the frequency dependence of the magnitude of the complex viscosity ($|\eta^*|$). A temperature sweep is also used over the range of 180-280^{o}C, in which the levels of $|\eta^*|$ are monitored to determine the temperature dependence of the magnitude of the complex viscosity.

4.2 Experimental

4.2.1 Materials

The base copolymer for this study is an 85/15 mole % AN/MA copolymer. The AN/MA/ABP terpolymers are both 85/14/1 mole % copolymers, differentiated as batch 1 and batch 2. The AN/MA and AN/MA/ABP copolymers were produced via a heterogeneous free radical (emulsion) polymerization by Monomer Polymer, Inc. of Feastersville, PA. The emulsion polymerization recipe provided by Bhanu and coworkers[8] is different than for solution and suspension polymerizations. One kg quantities of each co- and terpolymer were scaled up, and the co- and terpolymers were available in powder form for rheological measurements.

AN/MA molar ratio	Intrinsic Viscosity *(NMP/25° C)*	M_n *(GPC, g/mol)*	M_w *(GPC, g/mol)*	PDI
85/15	0.50	26,500	65,900	2.5
85/14/1 batch 1	0.36	16,300	27,300	1.7
85/14/1 batch 2	0.52	22,000	41,700	1.9

Table 4.1: Intrinsic viscosity and molecular weight data for the 85/15 AN/MA and 85/14/1 AN/MA/ABP polymers.

4.2.2 Molecular Weight Analyses

Intrinsic viscosities (IV) and number and weight average molecular weights, M_n and M_w, respectively, for each sample are indicated in Table 4.1. Intrinsic viscosities were measured using a Cannon Ubbelhode viscometer. Absolute molecular weight measurements from gel permeation chromatography (GPC) were obtained at 60°C with a Waters 2690 (Waters Associates, Milford, MA) Separation Module equipped with a differential refractometer detector and an on-line differential viscometric detector (Viscotek T60A) coupled in parallel. NMP containing 0.2 M P_2O_5 was used as a solvent. As indicated in Table 4.1, the IV of the 85/15 copolymer and batch 2 are comparable, but batch 1 has a significantly lower IV. The molecular weights of the polymers are decreasing in the order AN/MA copolymer>batch2>batch1. The polydispersity is similar for all three materials, in the range of 1.7-2.5.

4.2.3 Dynamic Oscillatory Rheology

Dynamic oscillatory rheological measurements were performed using a Rheometrics RMS 800 Mechanical Spectrometer. Frequency sweeps were made over the range of 0.1-100 rad/s using 25.0 mm parallel plates and 1-5% strain. Temperatures in the range of 200-220°C were used. In order to minimize degradation during measurements of the magnitude of the complex viscosity, $|\eta^*|$, angular frequencies (ω) below 0.1 rad/s were not used because of the length of time required to obtain data. Strain sweeps were performed at 220°C and an angular frequency of 10 rad/s over the range of strain of 0.6 – 100%. The temperature sweep was performed at a rate of 0.033 °C/s over the range of 180-280°C, using an angular frequency of 10 rad/s.

4.2.4 Rheological Measurement Procedure

Specific steps were taken to minimize any significant crosslinking in the copolymers prior to the dynamic oscillatory rheological measurements. Samples were compression molded into circular samples of 25.0 mm diameter and 1.0 mm thickness using a press at room temperature, which compacted the powder samples using high pressures (~60 MPa). As a result, the compacted powder samples had no thermal history prior to loading into the rheometer. During loading, heating, and equilibration of the samples in the rheometer, an inert nitrogen atmosphere was used in the rheometer oven. The presence of oxygen has been shown to accelerate the crosslinking reaction, and use of an inert atmosphere helped to prevent significant degradation prior to rheological measurements[12].

4.2.5 Steady Shear Viscosity

Steady shear viscosity (η) measurements were carried out using a RMS 800 Mechanical Spectrometer. Measurements were taken using 25.0 mm parallel plates and a sample thickness of 1.0 mm over the temperature range 200-260^{o}C. A shear rate, $\dot{\gamma}$, of 0.1 s^{-1} was used for the measurements at each temperature. Measurements were conducted for 1800 s, which was estimated to be significantly longer than the residence time in an extruder[13].

4.3 Results and Discussion

In the following sections, the time dependent steady shear viscosity (η) behavior and both the time and frequency dependence of the magnitude of the complex viscosity, $|\eta^*|$, of a potentially melt processable AN/MA copolymer suitable for use as a carbon fiber precursor are evaluated. The effects of copolymerization of a UV sensitive terpolymer (ABP) on the viscosity and melt stability are then determined.

4.3.1 Strain sweeps

In order to ensure that dynamic oscillatory measurements were made in the linear viscoelastic region for the polymers in this study, strain sweeps were performed at 200°C. 200°C was chosen because the kinetics of the crosslinking reaction was slow at this temperature, and accordingly significant thermal degradation did not occur during the measurements. The data in Fig. 4.1 indicate that the storage modulus, G', is constant up to a strain of 10% for the AN/MA copolymer and the batch 2 terpolymer, and constant up to approximately 5% strain for the batch 1 terpolymer. As a result, strains above 5% were not used for any of the dynamic oscillatory measurements to ensure that the measurements were made in the linear viscoelastic regime.

4.3.2 Melt viscosity of AN/MA copolymer

4.3.2.1 Dynamic oscillatory measurements

The dependence of the magnitude of the complex viscosity, $|\eta^*|$, as a function of angular frequency, ω, was evaluated for a melt processable 85/15 AN/MA copolymer suitable for use in the manufacture of carbon fibers. Values of $|\eta^*|$ obtained over the temperature range of 200-220°C are shown in Fig. 4.2. The low frequency (0.1 rad/s) values of $|\eta^*|$ decrease by a factor of 2 between 200 and 220°C. A similar decrease in $|\eta^*|$ is observed over the range of frequencies used, 0.1-100 rad/s. At each temperature, the general shape of the curves is the same, but the copolymer does not reach a zero shear viscosity, η_o, at the lowest measured frequency of 0.1 rad/s at any of the temperatures used. Above an angular frequency of approximately 10 rad/s, $|\eta^*|$ appears to decrease at a higher rate (as a function of ω) than at the lower frequencies.

We assumed that the levels of $|\eta^*|$ are representative of the steady shear viscosity (η) levels. This assumption is confirmed by the steady shear data in Fig. 4.2, obtained for shear rates ($\dot{\gamma}$) from 0.1-2.51 s^{-1} at 200°C. The levels of η approach those of $|\eta^*|$ at the lowest measured

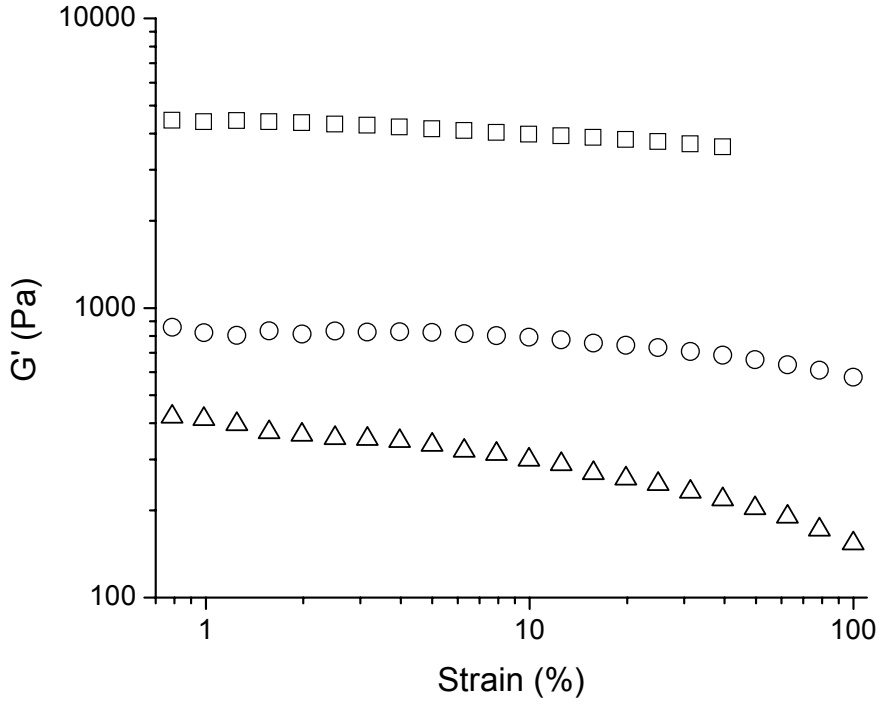

Fig. 4.1: Strain sweeps at ω = 10 rad/s and 200°C for (□) AN/MA copolymer; (o) batch 2 terpolymer; (Δ) batch 1 terpolymer.

rate and frequency of $\dot{\gamma} = 0.1\ s^{-1}$ and $\omega = 0.1$ rad/s, respectively, and deviate by less than 15% at the highest measured rate of $2.51\ s^{-1}$. Values of η for rates above $2.51\ s^{-1}$ could not be measured because edge fracture occurred. These results suggest that the Cox-Merz rule [14] holds reasonably well for this material, and that the dynamic oscillatory (complex viscosity) measurements are representative of the steady shear measurements.

The data in Fig. 4.3 evaluate the temperature dependence of $|\eta^*|$. Levels of $|\eta^*|$ for the AN/MA copolymer continue to decrease up to a temperature of approximately 268°C, at which $|\eta^*|$ begins to increase. These results suggest that 268°C is the maximum temperature at which melt processing should be performed, above which the kinetics of crosslinking becomes too rapid. The temperature sweep used to obtain the data in Fig. 4.3 is a relative comparison that is rate dependent, i.e. for a slower heating rate, it is possible that a minimum in $|\eta^*|$ would be observed at a lower temperature. To address this issue, the changes in viscosity as a function of time (melt stability) are determined, which are of particular interest at temperatures below 268°C where the kinetics of crosslinking may be slow enough to facilitate melt processing.

4.3.2.2 Steady shear viscosity

In order to quantify the melt stability of the AN/MA copolymer system, changes in the steady shear viscosity, η, were measured as a function of time. If levels of η increased with increasing time, then it was implied that crosslinking was occurring. Previously, the time dependence of $|\eta^*|$ was used to quantify the melt stability of the material [5]. However, copolymers for which minimal increases in $|\eta^*|$ were observed (over the measurement time) became intractable during monofilament extrusion through a capillary rheometer[15]. It was believed that measuring η as a function of time would more closely mimic melt extrusion, in

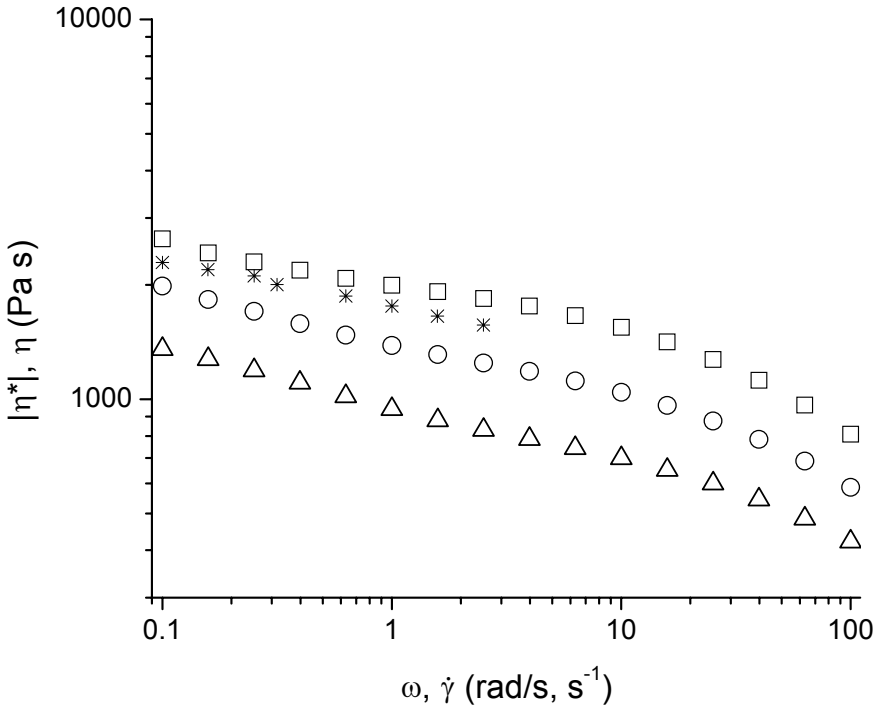

Fig. 4.2: Magnitude of the complex viscosity of AN/MA copolymer at (□) 200°C; (o) 210°C; (Δ) 220°C. (✳) steady shear viscosity at 200°C.

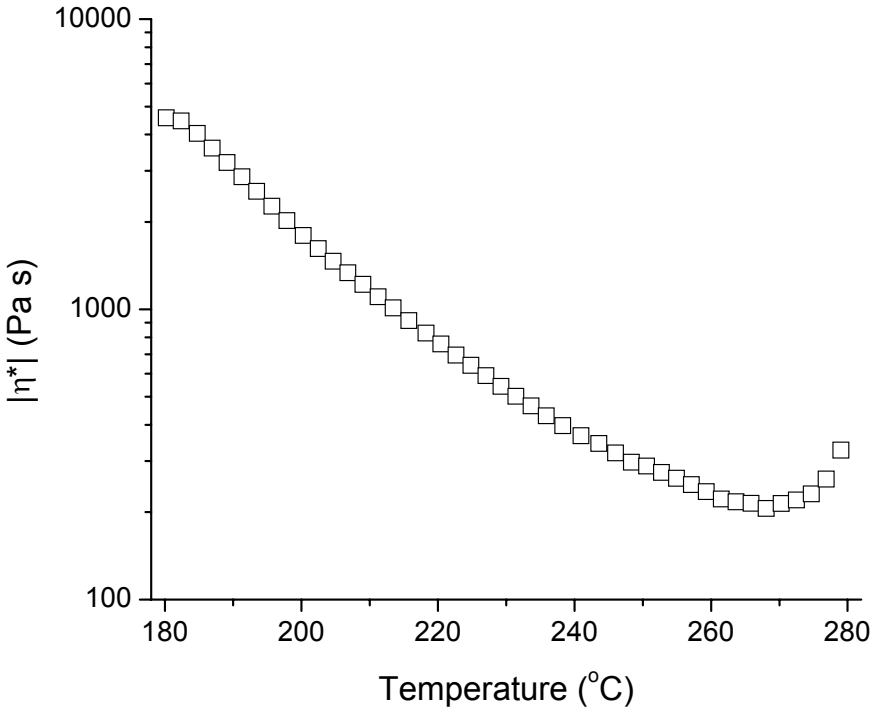

Fig. 4.3: Temperature dependence of the complex viscosity (magnitude) of the AN/MA copolymer. Heating rate 0.033°C/s, ω = 10 rad/s, strain = 2%.

which a high degree of mixing introduces the reactive nitrile groups of the polymer chains to each other[15]. During the small strain dynamic oscillatory measurements, the polymer oscillates back and forth over a small value of strain, and as a result the polymer chains did not mix to the same extent.

Values of η for the AN/MA copolymer in Fig. 4.4, which were obtained at a shear rate, $\dot{\gamma}$, of 0.1 s^{-1}, provide an indication of the melt stability of the AN/MA copolymer over the temperature range of 200-220^{o}C. At 200 and 210^{o}C, the kinetics of the crosslinking reaction is slow, and as a result the level of η only increases by 3 and 7%, respectively, over a 30 minute measurement. At 220^{o}C, a 31% increase in the level of η is observed. These results suggest that the kinetics of the crosslinking reaction increases significantly between 210 and 220^{o}C. At 200 and 210^{o}C, the levels of η are suitable for extrusion, and the kinetics of crosslinking appears slow enough to produce carbon fiber precursors with minimal degradation. These results have been confirmed experimentally[13].

In general, increasing the temperature above 220^{o}C has been shown to significantly increase the kinetics of crosslinking[2]. The data in Fig. 4.5 illustrate the time dependence of η over the temperature range of 220-260^{o}C and $\dot{\gamma}$=0.1 s^{-1}. The level of η increases by a factor of 6 over a period of 1800 s at 240^{o}C, and by a factor of 126 over a period of 735 s at 260^{o}C. These results indicate that the kinetics of crosslinking significantly increases between 220 and 240^{o}C, and to a greater extent between 240 and 260^{o}C. In fact, significant degradation had occurred during sample loading and temperature equilibration prior to the η measurements (which took approximately 360 s) at 260^{o}C. This is somewhat apparent in the results in Fig. 4.5, in which an increase is observed in the levels of η from 240^{o}C to 260^{o}C

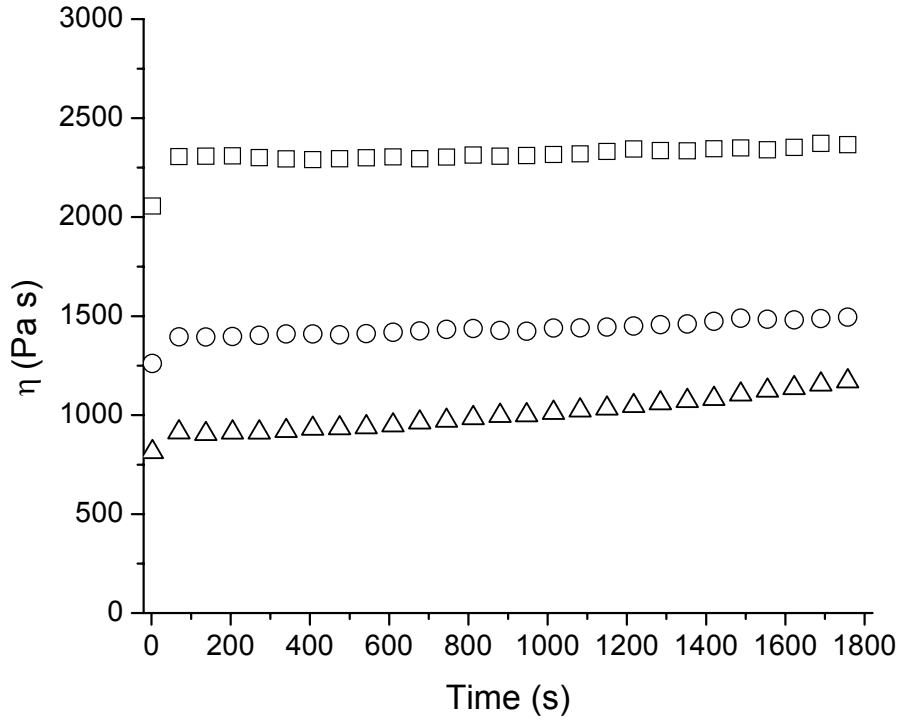

Fig. 4.4: Time dependence of the steady shear viscosity for the AN/MA copolymer at $\dot{\gamma}$ = 0.1 s^{-1} and (□) 200°C; (o) 210°C; (Δ) 220°C.

at time t = 0, contrary to the expected decrease of levels of η with increasing temperature. Studies have shown that the kinetics of crosslinking for this AN/MA copolymer becomes sufficiently rapid at 260°C for thermo-oxidative stabilization of the precursor fibers[15]. However, relaxation of the fibers during the stabilization step resulted in loss of orientation and carbon fibers with poor mechanical properties[15].

4.3.3 Characterization of AN/MA/ ABP Terpolymer

To prevent flow and loss of orientation of the precursor fibers during thermo-oxidative stabilization, a UV sensitive monomer, acryloyl benzophenone (ABP), was terpolymerized with AN and MA to accelerate the kinetics of the crosslinking reaction via UV irradiation. In the following sections, the effects of ABP on the melt stability and levels of η and |η*| are evaluated.

4.3.3.1 Molecular Weight

The polymerization method was almost identical for synthesizing both the AN/MA copolymer and AN/MA/ABP terpolymer, and similar molar compositions of AN (85 mole %) were used. Therefore, it was expected that the molecular weight and intrinsic viscosities of the polymers would follow similar trends, i.e. for an increase in molecular weight, the intrinsic viscosity would correspondingly increase. The GPC data in Table 4.1 indicate that the molecular weights and molecular weight distributions follow the trend AN/MA>batch2>batch1. However, the intrinsic viscosities (IV) follow the trend batch2>AN/MA>batch1, which is interesting considering that IV is expected to scale directly with weight average molecular weight (M_w). The data suggest that copolymerization of only 1 mole % of the ABP termonomer causes the IV to scale to a different power of molecular weight (corresponding to a significantly different value of "a" in the Mark-Houwink equation[16]) than with the AN/MA copolymer.

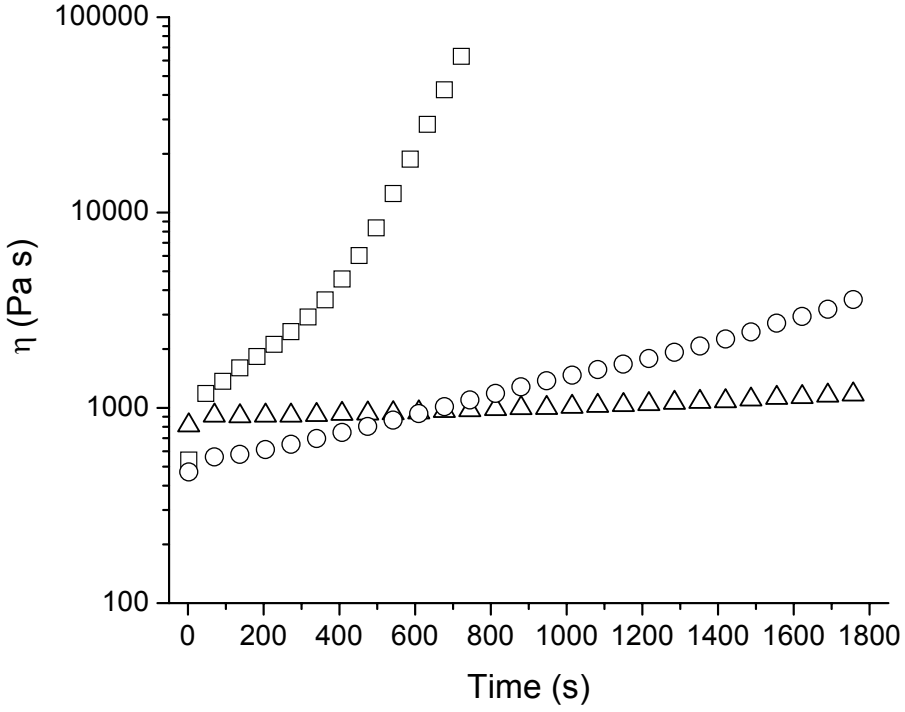

Fig. 4.5: Time dependence of the steady shear viscosity of the AN/MA copolymer at $\dot{\gamma} = 0.1\ s^{-1}$ and (□) 260°C; (o) 240°C; (Δ) 220°C.

4.3.3.2 Complex viscosity measurements

Dynamic frequency sweeps and a temperature sweep were used to determine the effect of copolymerization of the ABP termonomer on the levels of $|\eta^*|$. The same temperature ranges were used as for the AN/MA copolymer for direct comparison of the dependence of $|\eta^*|$ on angular frequency and temperature. Levels of $|\eta^*|$ for the AN/MA/ABP terpolymers and the AN/MA copolymer are shown in Figs. 4.6 and 4.7 at 200 and 220^{o}C, respectively. As expected, levels of $|\eta^*|$ decrease with molecular weight over the range of frequencies used at both temperatures, with the highest levels obtained for the AN/MA copolymer and the lowest levels for the batch1 terpolymer. However, the shape of the curves is slightly different upon copolymerization with ABP. The data at 200^{o}C suggest that above $\omega = 10$ rad/s, levels of $|\eta^*|$ for the AN/MA copolymer decrease with increasing ω at a higher rate than both of the terpolymers. At 220^{o}C, it appears that a plateau in $|\eta^*|$ at the low frequency range ($\omega < 0.3$ rad/s) is observed for both of the ABP terpolymers, which is not observed at either temperature for the AN/MA copolymer.

A temperature sweep was used over the temperature range 180-280^{o}C to determine the effect of ABP on the temperature dependence of the levels of $|\eta^*|$. As seen from the data in Fig. 4.8, a minimum in $|\eta^*|$ for the lower molecular weight (batch 1) AN/MA/ABP terpolymer is observed at approximately 260^{o}C, which is slightly lower than that obtained for the AN/MA copolymer. However, $|\eta^*|$ is a minimum for the higher MW ABP terpolymer (batch2) at approximately 252^{o}C. These results suggest that the addition of ABP may increase the thermally induced kinetics of the crosslinking reaction for a given molar composition and molecular weight, indicated by the upturn in $|\eta^*|$ for both terpolymers at lower temperatures than that

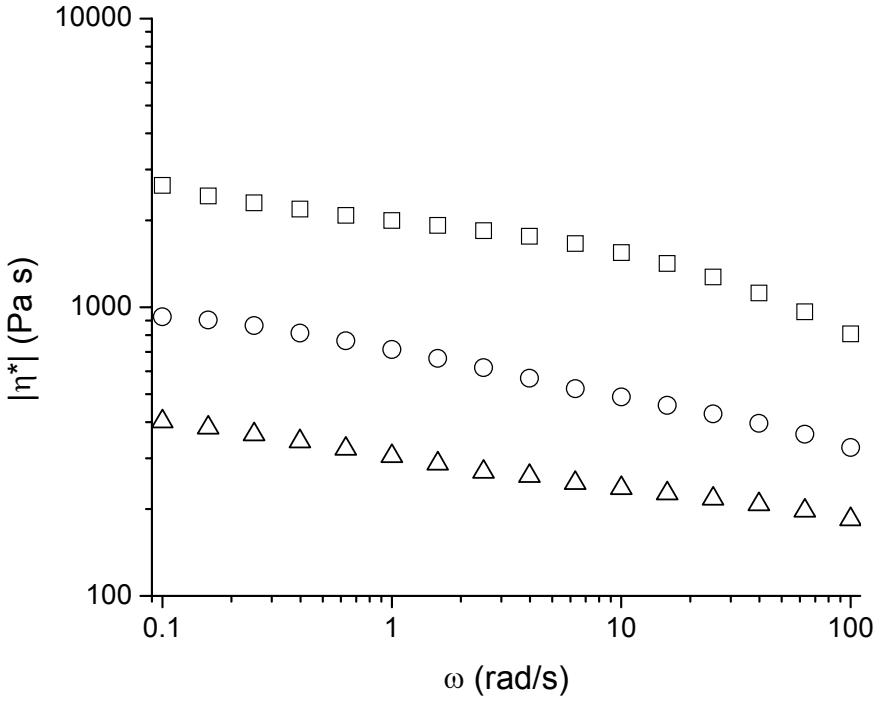

Fig. 4.6: Frequency dependence of complex viscosity (magnitude) at 200°C for the (□) AN/MA copolymer; (o) batch 2 terpolymer; (Δ) batch 1 terpolymer.

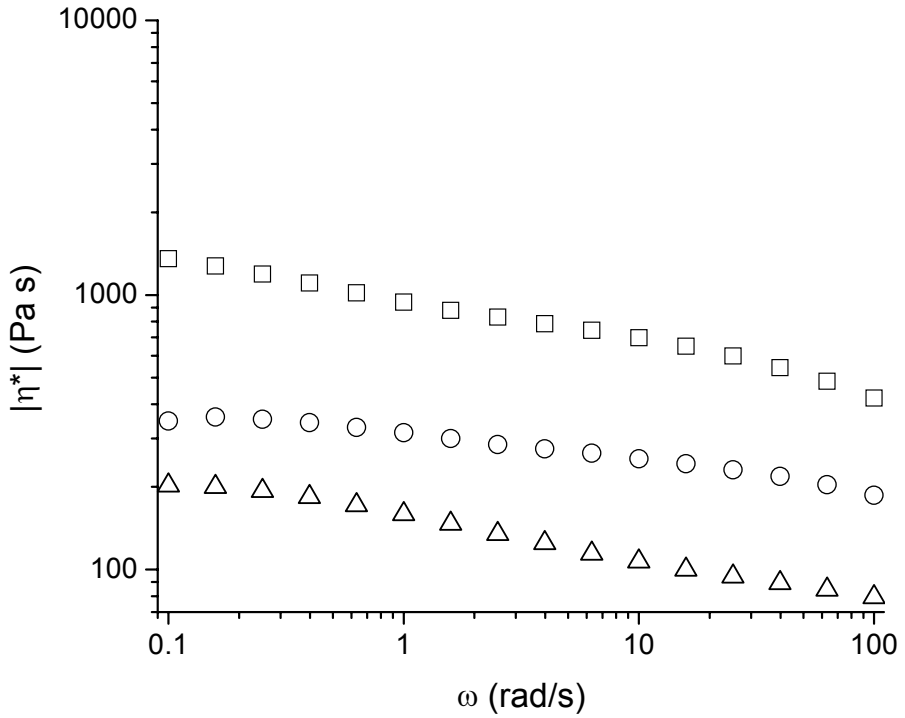

Fig. 4.7: Frequency dependence of complex viscosity (magnitude) at 220°C for the (□) AN/MA copolymer; (o) batch 2 terpolymer; (Δ) batch 1 terpolymer.

observed for the AN/MA copolymer (268^{o}C). Between the two terpolymers, the data also suggest that an increase in molecular weight increases the kinetics of crosslinking. The following discussion rationalizes this observation. A polymer with a specific molecular weight will increase its size when it first branches, and will continue to increase MW as more branches are formed between the growing polymer chains and one approaches network formation. If the starting molecular weight is increased, then the initially larger polymer chains require less chemistry to obtain enhanced viscosity. As a result, viscosity growth will be faster if the starting molecular weight of a crosslinking polymer is increased. Because zero shear melt viscosity is generally proportional to the 3.4 power of the weight average molecular weight (M_w), it is also expected to build at a significantly faster rate as the initial MW is increased.

4.3.3.3 Steady Shear Viscosity

The effect of the ABP termonomer on the melt stability was quantified by tracking η as a function of time over the temperature range of 200-240^{o}C. The data in Figs. 4.9, 4.10, and 4.11 illustrate the levels of η as a function of time at $\dot{\gamma} = 0.1s^{-1}$ and 200, 220, and 240^{o}C, respectively. Values of η at 200^{o}C indicate almost identical melt stability (η) trends for the three materials, suggesting that the kinetics of crosslinking was occurring at similar (slow) rates for each polymer. Levels of η only increased by 3 and 8 % for the AN/MA copolymer and batch 1 terpolymer, respectively, and by 21% for the batch 2 terpolymer. Levels of η versus time at 220^{o}C indicate a 45% increase for the batch 2 terpolymer, followed by 21 and 11% for the AN/MA copolymer and batch 1 terpolymer, respectively. It is apparent from the data in Fig. 4.11 that the kinetics of crosslinking becomes much more significant for all three polymers at 240^{o}C, indicated by the 16, 7, and 6 fold increase in the levels of η for the batch 2, AN/MA, and

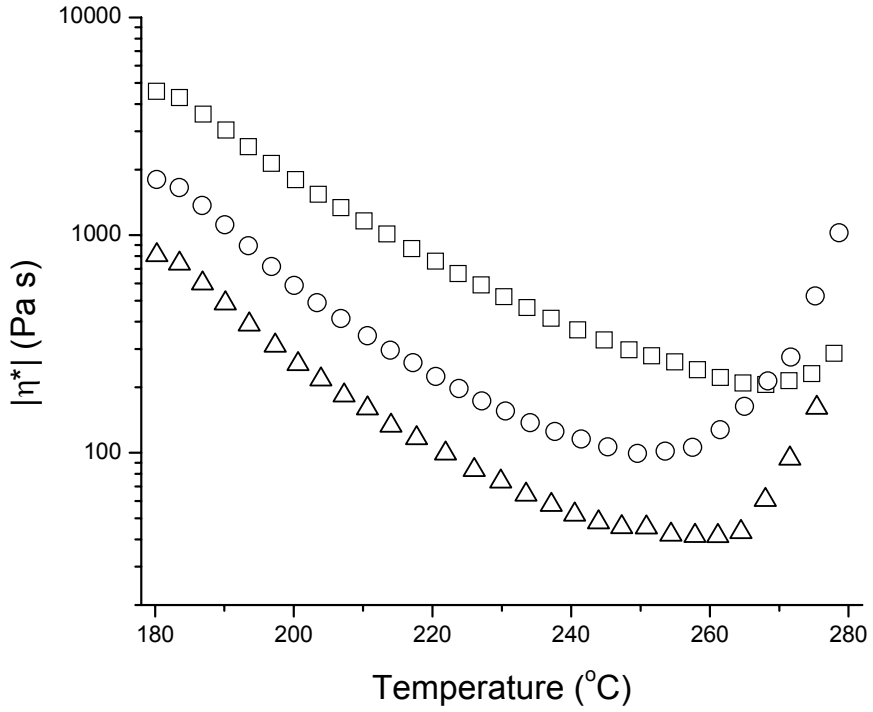

Fig. 4.8: Temperature dependence of the complex viscosity (magnitude) of the (□) AN/MA copolymer; (o) batch 2 terpolymer; (Δ) batch 1 terpolymer. Heating rate 0.033°C/s, ω = 10 rad/s, strain = 2%.

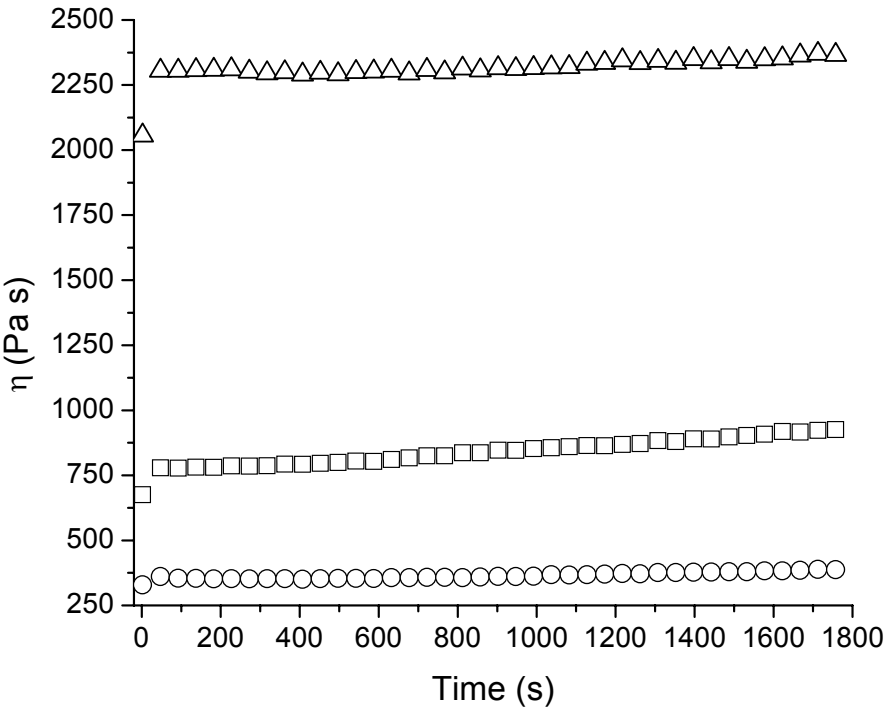

Fig. 4.9: Time dependence of the steady shear viscosity at 200°C, $\dot{\gamma} = 0.1\ s^{-1}$ for (Δ) AN/MA copolymer; (□) batch 2 terpolymer; (o) batch 1 terpolymer.

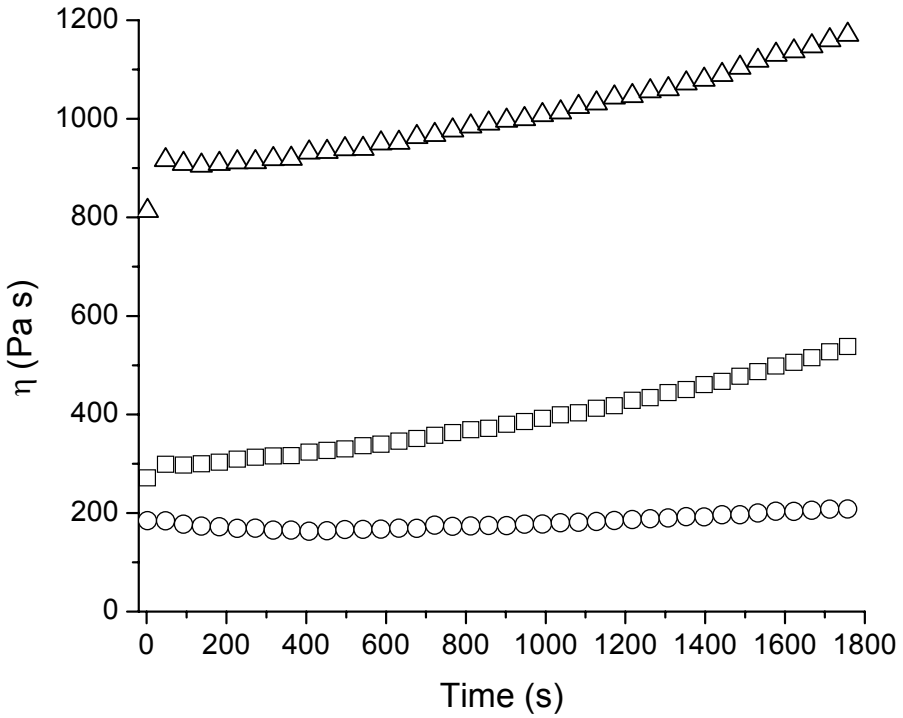

Fig. 4.10: Time dependence of the steady shear viscosity at 220°C, $\dot{\gamma} = 0.1\ s^{-1}$ for (Δ) AN/MA copolymer; (□) batch 2 terpolymer; (o) batch 1 terpolymer.

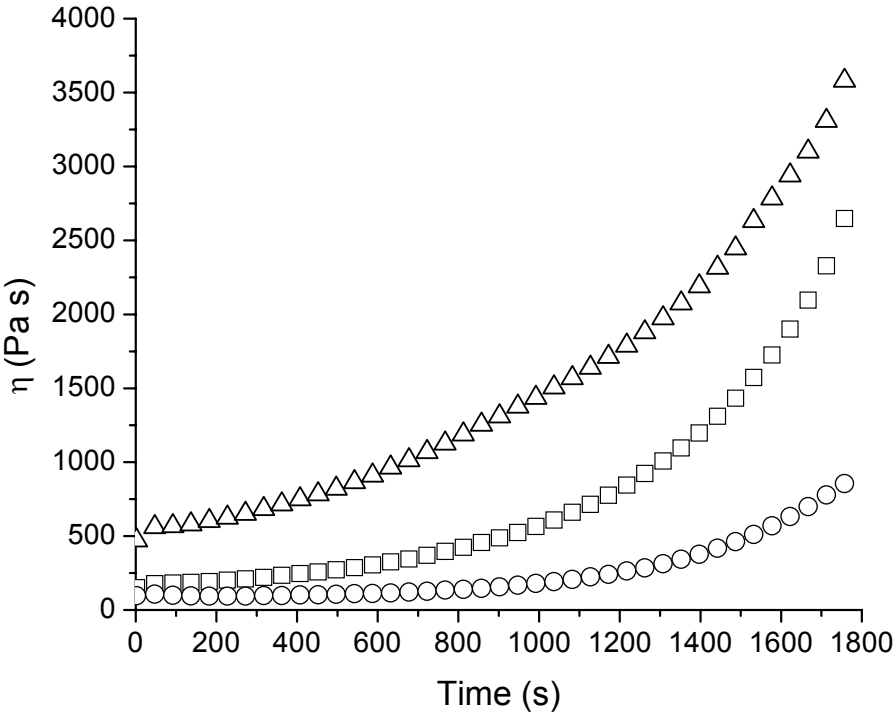

Fig. 4.11: Time dependence of the steady shear viscosity at 240°C, $\dot{\gamma} = 0.1\ s^{-1}$ for (Δ) AN/MA copolymer; (□) batch 2 terpolymer; (o) batch 1 terpolymer.

batch 1 polymers, respectively. As expected, the levels (number values) of η in Figs. 4.9-11 correlate directly with molecular weight, with the highest molecular weight (85/15 AN/MA) copolymer having the highest levels of η over the measurement time, followed by the batch 2 and batch 1 terpolymers, respectively. Also, the data suggest that the rate of increase of η as a function of time, which directly correlates to an increase in the kinetics of degradation, becomes higher with increasing temperature for all three polymers. However, the data in Figs. 4.9-11 indicate that the highest IV copolymer (batch 2 terpolymer) was observed to have the highest magnitude of increase in (levels of) η, followed by the AN/MA copolymer and batch 1 terpolymer. Hence, the data suggest that the magnitude of increase of η as a function of time correlates better to IV than MW, especially when comparing polymers of the same AN content (in this case, 85 mole %) but different comonomer (and/or termonomer) contents.

4.3.4 Chemorheology of AN/MA and AN/MA/ABP polymers

During melt extrusion of co- or terpolymers of AN, MA, and ABP, the viscosity will increase as a result of crosslinking and cyclization, which will be dependent on both processing temperature and residence time in the extruder. The ability to quantitatively describe the changes in viscosity as a function of temperature and time, as well as to identify the effects of molecular weight and ABP, was next evaluated by the use of a chemorheological model. The model, which is similar to that used to describe curing in epoxy resins[17], is represented by the functions in Eqs. 4.1-3, which were applied to the steady shear (time dependent) viscosity data to describe the crosslinking kinetics of the AN/MA and AN/MA/ABP polymers:

$$\ln \eta(t) = \ln \eta_r + kt \qquad (4.1)$$

where

$$\eta_r = \eta_\infty \exp\left(\frac{\Delta E_\eta}{RT}\right) \qquad (4.2)$$

and

$$k = k_\infty \exp\left(\frac{\Delta E_k}{RT}\right) \qquad (4.3)$$

In Eq. 4.1, k and η_o are temperature dependent rate and viscosity constants, respectively, and t is time. For Eqs. 2 and 3, ΔE_η and ΔE_k are the activation energies associated with the temperature dependence of k and η_r, respectively, and T is temperature. Steady shear viscosity versus time data, obtained at 200, 210, 220, and 240°C for each polymer (at $\dot{\gamma}$=0.1 s^{-1}), were used to plot ln η versus time at each temperature. The slopes and intercepts of these plots were used to obtain k and η_r, respectively, at each temperature and composition. The data at 240°C was only used to obtain a slope for the value of k, because (as previously discussed) significant degradation had occurred by time t = 0 at 240°C, which would provide a value for the intercept (and subsequently η_r) of a system that had crosslinked to a significant extent. The natural logarithm of both k and η_r were then plotted as a function of 1/T, from which the slope and intercept of a linear fit of the data for each polymer provided the required constants in Eqs. 4.2 and 4.3. Linear fits of the natural logarithm of η versus time are shown in Fig. 4.12, which were used to obtain k and η_r for the AN/MA copolymer. Although not shown here, similar plots were used to obtain k and η_r for the AN/MA/ABP terpolymers. Linear fits of the plots of the natural logarithms of η_r and k versus 1/T (obtained from the data shown in Fig. 4.12) were used to obtain values for η_∞ and k_∞ from the intercepts and $\Delta E_\eta/R$ and $\Delta E_k/R$ from the slopes, respectively, and are shown in Figs. 4.13 and 4.14 for the 85/15 copolymer. Although not shown here, similar plots to those in Figs. 4.13 and 4.14 were used for both terpolymers. Correlation coefficients greater than 0.98 were

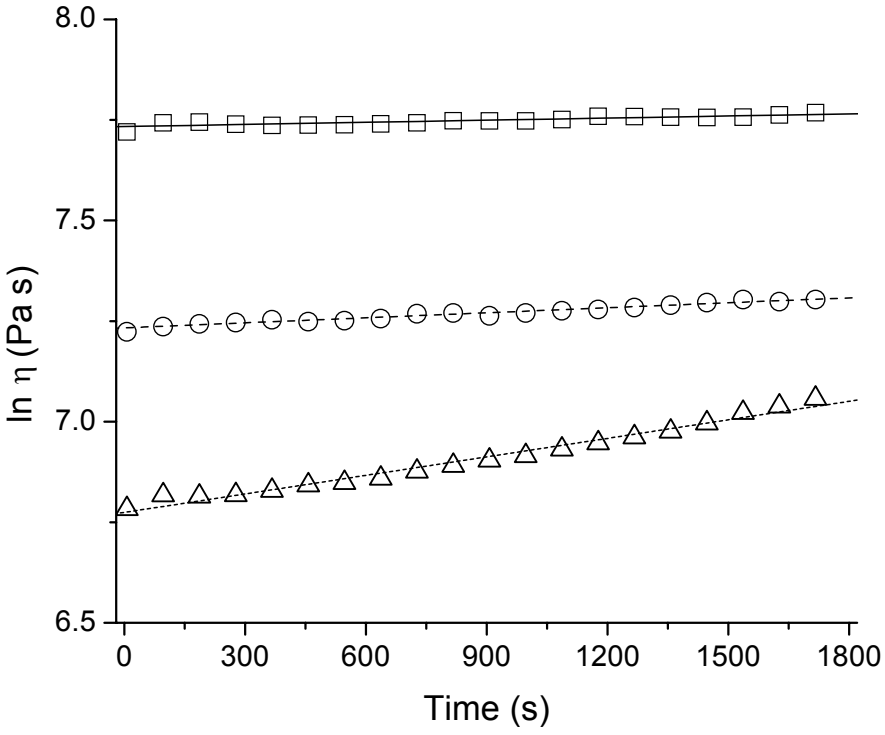

Fig. 4.12: Plots used to obtain k and η_r parameters in Eq. 4.1 for the AN/MA copolymer. Open symbols are steady shear viscosity data at $\dot{\gamma} = 0.1s^{-1}$ and (□) 200°C; (o) 210°C; (Δ) 220°C. Lines are linear fits of the data at (—) 200°C; (— —) 210°C; (---) 220°C.

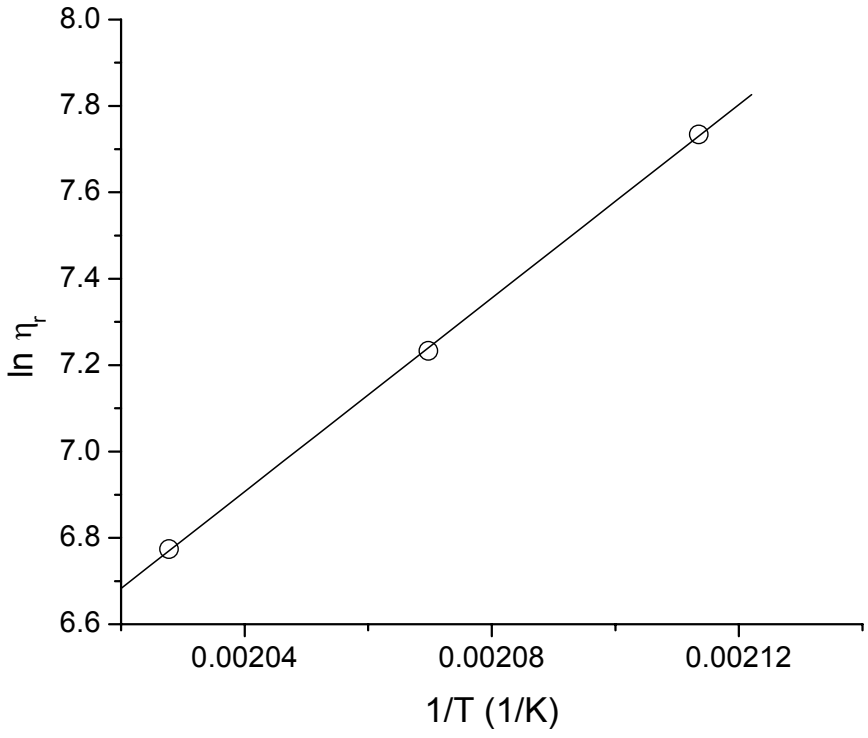

Fig. 4.13: Plot to determine constants in Eq. 4.2 for the AN/MA copolymer. Open symbols are experimental data obtained from the intercepts of the plots in Fig. 4.12. Solid line is a linear fit of the data. Error bars are contained within data points.

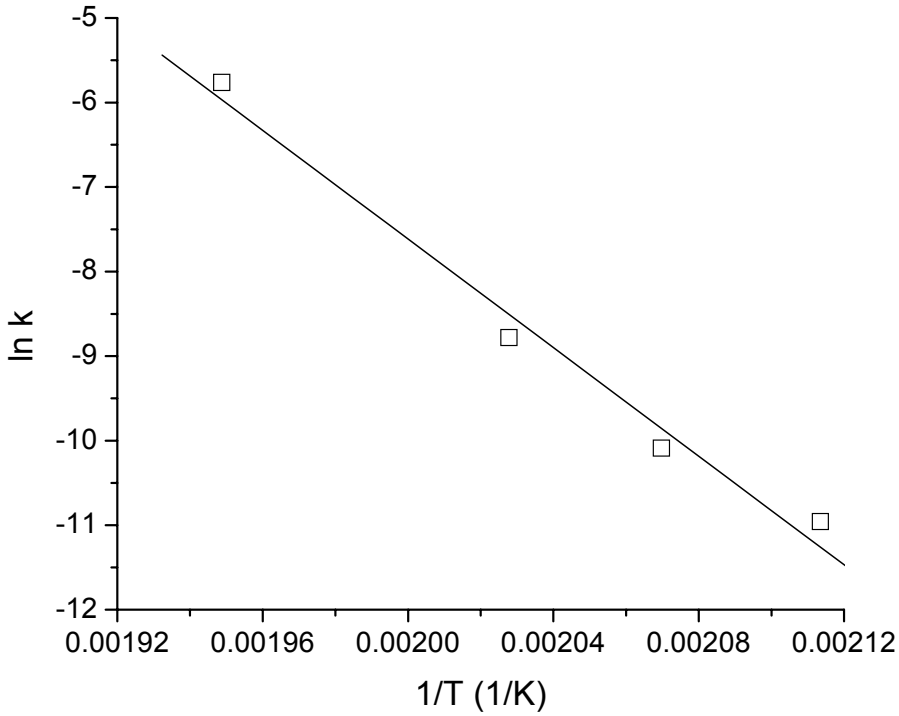

Fig 4.14: Plot to determine constants in Eq. 4.3 for the AN/MA copolymer. Open symbols are experimental data obtained from the slopes of the plots in Fig. 4.12. Solid line is a linear fit of the data. Error bars are contained within data points.

obtained for all linear fits of the data. The data in Table 4.2 illustrate the values of the constants in Eqs. 4.1-3 obtained for the three AN copolymers.

For comparison to the $|\eta^*|$ data in Fig. 4.8, Eq. 4.1 was differentiated with respect to temperature ($d\eta/dT$) to obtain an estimate of the temperature at which viscosity (of the model) is a minimum. As the temperature increases, the viscosity drops because of the activation energy of flow, but increases as the kinetics of the cyclization and crosslinking reaction increases. The temperature at which $d\eta/dT = 0$ represents a balance between the activation energy of flow and the kinetics of crosslinking, and indicates the maximum value at which processing of the AN copolymers should be performed. The temperature, T, listed in Table 4.2 is the value at which the minimum in viscosity was calculated for each polymer. A temperature of approximately 258^{o}C was calculated for the minimum viscosity of the 85/15 copolymer, which is significantly lower than that of 268^{o}C observed in the data in Fig. 4.8. For the batch 1 terpolymer, a temperature of approximately 262^{o}C was calculated, which is only 2^{o}C different than the measured value. The calculated value for the batch 2 terpolymer was approximately 268^{o}C, which is significantly higher than the measured value of 252^{o}C. The calculated temperatures in Table 4.2 suggest that copolymerization of ABP increases the temperature at which the viscosity (of the model) is a minimum. These results suggest increased melt stability, implying a reduction in the thermally induced kinetics of crosslinking. However, it is interesting that between the two terpolymers, the kinetic model predicts a higher temperature for the higher MW (batch 2) terpolymer. Based on the time dependent viscosity data in Figs. 4.9-11, we expected that the model would predict a lower temperature for the batch 2 terpolymer because η for the batch 1 terpolymer is observed to increase at a slower rate as temperature is increased. It is possible that premature crosslinking (prior to t=0) introduced error in the values of η_r, which

molar composition (mole %)	ln k_∞ (s^{-1})	$\Delta E_\eta/R$ (^oK)	$\Delta E_k/R$ (^oK)	ln η_∞ (Pa s)	T (^oC)
85/15	56.64 +/- 6.1	11202 +/- 149	−32125 +/- 2984	−15.94 +/- 0.31	258.4
85/14/1 batch 1	31.24 +/- 8.6	9404 +/- 1066	−19489 +/- 4205	−14.07 +/- 2.2	261.7
85/14/1 batch 2	25.85 +/- 3.2	11641 +/- 220	−16622 +/- 1575	−17.96 +/- 0.45	267.9

Table 4.2: Parameters obtained from chemorheological analysis in Eqs. 1-3.

would have propagated in the determination of the constants in Eq. 4.2. The error also would have been magnified from use of logarithmic plots of the data to determine these constants, and may be the source for the discrepancy between the measured (from Fig. 4.8) and calculated temperatures (Table 4.2) at which viscosity is a minimum.

4.4 Conclusions

This study has identified the temperature and time dependence of η, as well as the temperature and angular frequency dependence of |η*|, of a melt processable 85/15 mole % AN/MA copolymer and two 85/14/1 mole % AN/MA/ABP terpolymers. Based on previous studies, the melt stability and the levels of η and |η*| of both terpolymers appear to be suitable for melt processing at temperatures between 200-220^{o}C[15]. Changes in η versus time and in |η*| versus temperature suggest that copolymerization of ABP increases the kinetics of thermal degradation, resulting in decreased melt stability. Comparison of the η and |η*| data for the two terpolymers suggests that the kinetics of crosslinking also has a significant dependence on molecular weight. For a specific molar composition (in this case, 85 mole %), changes in η versus time suggest that levels of η correlate well to molecular weight, but that the magnitude of the increase in η as a function of time correlates better to intrinsic viscosity. A chemorheological model suggests that copolymerization with ABP slows the kinetics of the crosslinking reaction. However, the model may be somewhat in error due to the difficulty in isolating and measuring the activation energy of flow without the additional effects of crosslinking (thermal degradation).

4.5 Acknowledgments

The authors wish to thank the Department of Energy/Oak Ridge National Laboratory (DOE/ORNL) Freedom Car Project, program grant #4500011036, for financial support.

4.6 References

(1.) Edie, D. D. *Carbon* **1998**, *36*, 345-362.

(2.) Gupta, A. K.; Paliwal, D. K.; Bajaj, P. *Journal of Macromolecular Science-Reviews in Macromolecular Chemistry and Physics* **1991**, *C31*, 1-89.

(3.) Bajaj, P.; Roopanwal, A. K. *Journal of Macromolecular Science-Reviews in Macromolecular Chemistry and Physics* **1997**, *C37*, 97-147.

(4.) Tullo, A. H. *Chemical and Engineering News* **2000**, *78*, 11-12.

(5.) Rangarajan, P.; Yang, J.; Bhanu, V.; Godshall, D.; McGrath, J.; Wilkes, G.; Baird, D. *Journal of Applied Polymer Science* **2002**, *85*, 69-83.

(6.) Bortner, M. J.; Bhanu, V. A.; McGrath, J. E.; Baird, D. G. *Proceedings of the Society of Plastics Engineers ANTEC* **2003**.

(7.) Bhanu, V. A.; Wiles, K. B.; Rangarajan, P.; Glass, T. E.; Godshall, D.; Sankarpandian, M.; Baird, D. G.; Wilkes, G. L.; Banthia, A. K.; McGrath, J. E. *Abstracts of Papers of the American Chemical Society* **2001**, *222*, U332.

(8.) Bhanu, V. A.; Rangarajan, P.; Wiles, K.; Bortner, M.; Sankarpandian, M.; Godshall, D.; Glass, T. E.; Banthia, A. K.; Yang, J.; Wilkes, G.; Baird, D.; McGrath, J. E. *Polymer* **2002**, *43*, 4841-4850.

(9.) Rangarajan, P.; Bhanu, V. A.; Godshall, D.; Wilkes, G. L.; McGrath, J. E.; Baird, D. G. *Polymer* **2002**, *43*, 2699-2709.

(10.) Wiles, K. Masters Thesis. Virginia Polytechnic Institute and State University, 2002.

(11.) Godshall, D.; Rangarajan, P.; Baird, D. G.; Wilkes, G. L.; Bhanu, V. A.; McGrath, J. E. *Polymer* **2003**, *44*, 4221-4228.

(12.) Ehrburger, P.; Donnet, J. B. *Handbook of fiber science and technology: Volume III, high technology fibers*; M. Dekker: New York, **1983**; Chapter 5, pp 169-220.

(13.) Bortner, M. J. PhD Dissertation. Virginia Polytechnic Institute and State University, **2003**.

(14.) Cox, W. P.; Merz, E. H. *Journal of Polymer Science* **1958**, *28*, 619.

(15.) Edie, D. D.; Ogale, A. A. Personal Communication, **2003**.

(16.) Macosko, C. W. *Rheology: principles, measurements, and applications*; VCH: New York, NY, **1994**.

(17.) Gupta, R. K. *Polymer and composite rheology*; Marcel Dekker: New York, **2000**.

5.0 Plasticizing Effects of CO_2

Preface

This chapter addresses research objective 2, and is organized as a manuscript for publication. In particular, the ability of a commercially available rubber toughened AN copolymer (Barex) to absorb CO_2 and the subsequent viscosity effects are evaluated. This chapter establishes the method for plasticization, the measurements of amounts of absorbed CO_2 and reduction in glass transition temperature (T_g), and the viscosity measurements and corrections of the copolymer containing absorbed CO_2.

Absorption of CO_2 and Subsequent Viscosity Reduction of an Acrylonitrile Copolymer

Michael J. Bortner and Donald G. Baird*

Department of Chemical Engineering and Center for Composite Materials and Structures
Virginia Polytechnic Institute and State University
Blacksburg, VA 24061-0211

Abstract

Acrylonitrile (AN) copolymers (AN content greater than about 85 mole percent) are traditionally solution processed to avoid a cyclization and crosslinking reaction that takes place at temperatures where melt processing would be feasible. It is well known that carbon dioxide (CO_2) reduces the glass transition temperature (T_g) and consequently the viscosity of many glassy and some semi-crystalline thermoplastics. However, the ability of CO_2 to act as a processing aid and permit processing of thermally unstable polymers at temperatures below the onset of thermal degradation has not been explored. This study concentrates on the ability to plasticize an AN copolymer with CO_2, which may ultimately permit melt processing at reduced temperatures. To facilitate viscosity measurements and maximize the CO_2 absorption, a relatively thermally stable, commercially produced AN copolymer containing 65 mole percent AN was investigated here. DSC and TGA thermal analyses indicated that CO_2 significantly absorbs into and reduces the T_g of the AN copolymer. Pressurized capillary rheometry indicated that the magnitude of the viscosity reduction is dependent on the amount of absorbed CO_2, which correlates directly to the T_g reduction of the plasticized material. Up to a 60 percent viscosity reduction was obtained over the range of shear rates tested for the plasticized copolymer containing up to 6.7 weight percent CO_2 (31°C T_g reduction), corresponding to as much as a

* dbaird@vt.edu, phone: (540) 231-5998, fax: (540) 231-5022

30°C equivalent reduction in processing temperature. A Williams-Landel-Ferry (WLF) analysis was used to estimate the viscosity reduction based on the T_g reduction (and corresponding amount of absorbed CO_2) in the plasticized AN copolymer, and the predicted viscosity reduction based on using the universal constants was 34 to 85 percent higher than measured, depending on the amount of absorbed CO_2. Van Krevelen's empirical solubility relationships were used to calculate the expected absorbance levels of CO_2, and found to be highly dependent on the choice of constants within the statistical ranges of error of the Van Krevelen relationships.

5.1 Introduction

Because of the thermally unstable nature of acrylonitrile (AN) copolymers, generally containing about 85 mole percent or greater AN when no stabilizer is present[1], they are processed in the presence of toxic, organic solvents, commonly including dimethlyl formamide (DMF) and dimethylacetamide (DMAC). Viscosities for these materials generally become suitable for melt processing when temperatures of approximately 220°C are approached[1]. However, at 220°C a rapid reaction that produces intramolecular cyclic structures with intermolecular crosslinks takes place, rendering these high AN content copolymers intractable prior to extrusion into fiber form[2]. The crosslinking reaction can be slowed by the presence of a stabilizer, such as boric acid, particularly for relatively low molecular weight AN copolymers containing between 85-90 mole percent AN[3]. Acrylic fibers from high molecular weight AN precursors, especially containing greater than 90 mole percent AN, are typically solution processed at low solids content (7-30 weight percent polymer) using toxic organic solvents[4].

The need exists for a less expensive and environmentally benign process (compared to solution spinning in toxic organic solvents) for producing AN copolymer fibers suitable for use as carbon fiber precursors and textiles[5]. The melt processing of AN copolymers could

potentially provide a solution to both of these issues by increasing solids throughput on a per pound basis and eliminating the need for solvent use and recovery[1]. In order to melt process AN copolymers, the kinetics of the crosslinking reaction described above need to be kept to a minimum. Bhanu and coworkers[6] have shown that the crosslinking kinetics for copolymers with AN molar ratios of 85 to 90 percent become significant when a temperature on the order of 220°C was reached. However, the viscosity level was suitable for melt processing these materials at this temperature. The same AN copolymers were shown by Rangarajan and coworkers[1;7] to possess a stable steady shear viscosity over a 30-minute test period when the test temperature was reduced by 20°C to 200°C, indicative of a significant reduction in the kinetics of the crosslinking reaction, but the viscosity was too high for extrusion operations. These results suggest that reducing the processing temperature of AN copolymers by 20°C could sufficiently reduce the kinetics of the crosslinking reaction in high AN content copolymers, permitting melt processing without significant degradation, assuming a viscosity suitable for melt extrusion can be obtained.

Numerous patents and journal articles have been published regarding melt processing of polyacrylonitrile copolymers using a plasticizer[5;8-16]. The majority of studies focused on the use of water to plasticize an AN homopolymer (or copolymer) for melt extrusion. C.D. Coxe[8] showed that water plasticizes AN copolymers and permits melt processing at reduced temperatures, but Porosoff[13] showed that the extrudate needed to be passed through a pressurized solidification zone to prevent foaming of the fiber. Studies have shown that the removal of water from the precursor fiber is quite difficult, and as a result the stabilized and carbonized fibers could not be produced without formation of a microporous structure at the fiber core[5;16]. To permit removal of the water from the fibers, a process was developed combining acetonitrile,

methanol, and water to plasticize AN copolymers and melt process them into carbon fibers [10;11]. The addition of acetonitrile and methanol lowered the boiling point of the water and facilitated its removal from the fibers. However, approximately 25-45 weight percent plasticizer was necessary for processing, and it still required recovery because of the hazardous nature of acetonitrile, which degrades into cyanide at relatively low temperatures. As a result, the process provided no economic benefit over the solution process once commercial production outputs (greater than $2x10^6$ lb per year) were reached.

Potentially melt processable AN copolymers have also been investigated by Bhanu et al.[3;6] and Rangarajan et al.[1;7]. The studies focused on the use of suitable comonomers (primarily MA) in the range of 10 to 15 mole percent to disrupt the long range order and reduce the T_g of AN copolymers, rendering them melt stable. Kinetics of crosslinking were found to be very slow in the melt stable AN copolymers, which presented a problem when attempting thermo-oxidative stabilization (part of the carbonization process) of the resultant fibers[3]. As a result, a third comonomer (acryloyl benzophenone) was copolymerized to initiate the crosslinking reaction via UV irradiation following fiber formation[3]. The terpolymers could be melt processed into fibers with minimal degradation, but it was found that the kinetics of crosslinking became too rapid for melt processing if acrylonitrile contents greater than about 85 mole % were used.

Concern over volatile organic solvent emissions and contamination has also initiated searches to find cleaner solvents for both polymer synthesis and polymer processing[17]. Liquid and supercritical carbon dioxide (Sc-CO_2) have been a recent focal point for organic solvent replacement[18]. The benefits of using CO_2 over typical organic solvents are numerous. Carbon dioxide is non-toxic, non-flammable, environmentally friendly, recoverable, and supercritical conditions (T_c=31.1°C, P_c=7.39 MPa) are easily reached. In the supercritical state, CO_2 is known

to have similar solubilization characteristics to organic solvents (such as hexane) and CFC's. Sc-CO_2 also possesses a diffusivity similar to that of a gas, but a density like that of a liquid, which promotes rapid plasticization in amorphous materials[19]. For these and many more reasons, Sc-CO_2 has proven to be a very versatile alternative in some solvent based applications and consequently has been the focus for a surge of interest in many commercial applications[17], including ceramics processing, paper deacidification, metal cleaning, and plastics and textiles processing[18].

There have only been a few studies reported which have focused on the ability to plasticize thermoplastics with CO_2 and the subsequent effect on the viscosity. The interactions of various amorphous and semi-crystalline polymers with CO_2 have been studied and documented[20;21]. Semi-crystalline polymers, in general, have been shown to absorb CO_2 and be plasticized to a lesser extent than amorphous polymers[21]. Also, polarity has been shown to play a crucial role in CO_2 absorption, with higher polarity increasing the solubility in amorphous polymers[20]. CO_2 has been shown to plasticize a significant number of thermoplastics, including polydimethylsiloxane (PDMS)[22;23], polystyrene (PS)[24;25], polypropylene (PP), low-density polyethylene (LDPE), poly(methyl methacrylate) (PMMA), and poly(vinylidene fluoride) (PVDF)[26]. Absorption of up to 21 weight % CO_2 has been reported for high molecular weight PDMS[23]. However, most thermoplastics (e.g. PS and PMMA) have only been reported to show absorption levels up to about 6 weight percent[25].

Several techniques have been developed to measure the subsequent viscosity reductions associated with polymer/CO_2 solutions, covering all levels of CO_2 absorption[22-25;27-31]. Falling ball viscometers have been used primarily to measure polymer solutions containing low polymer concentrations (less than 5 weight percent) in high levels of absorbed CO_2 (and other

supercritical fluids), but are generally limited to low viscosity and low molecular weight solutions[22;28]. High-pressure couette and parallel plate devices, in which a couette or parallel plate geometry was kept in a sealed, high pressure environment, have been used to measure more viscous melts[29]. Inherent problems with transferring torque measurements under pressure, primarily because of the use of a dynamic seal that reduces instrument sensitivity, has significantly limited the usefulness of these rheometer designs[31]. Back pressure regulated capillary rheometers and extrusion slit dies, with which a hydrostatic pressure was applied at the capillary or slit exit to maintain a single phase thermoplastic/CO_2 melt, have been utilized to measure viscosities of viscous melts containing low concentrations of absorbed CO_2[23;25;30;32]. An extrusion slit die, with an applied hydrostatic pressure at the die exit, has been used to measure viscosity reductions of polystyrene/nanoclay melts containing absorbed CO_2[33]. Viscosity reductions for high molecular weight PDMS, PMMA, PVDF, isotactic PP, LDPE and PS melts have been measured using a back pressure regulated capillary rheometer[23;25;26], with up to 80 percent viscosity reductions reported for polystyrene containing 5 weight percent absorbed CO_2[24].

Despite the existing efforts to absorb CO_2 into thermoplastics and measure the viscosity reduction, none have documented the use of CO_2 to aid in melt processing acrylic copolymers or any other thermally unstable system. More specifically, none of the existing efforts have looked at the equivalent reduction in processing temperature produced by plasticization of acrylic copolymers (or any other thermally unstable polymers) with CO_2. AN copolymers need to be melt processed below temperatures at which the kinetics of the crosslinking reaction become significant, which could be facilitated by the viscosity reduction resulting from CO_2 absorption and plasticization.

The goal of this paper is to establish a framework for the ability of CO_2 to plasticize AN copolymers and facilitate reductions in viscosity and processing temperature. A relatively thermally stable AN copolymer (65 mole % AN) was used as a model system to facilitate absorption and viscosity measurements without significant degradation (crosslinking). The data obtained from this model AN system can then be extended to determine the ability for CO_2 to reduce viscosities and processing temperatures in higher AN content (85 mole % and greater) copolymers where the kinetics of crosslinking become a problem. The ability of this relatively low AN content (65 mole percent) acrylic copolymer to absorb CO_2 was determined from differential scanning calorimetry (DSC) and thermogravimetric analyses (TGA). Viscosity effects generated by means of CO_2 absorption were measured using a capillary rheometer modified to allow the application of static pressures at the capillary exit. Equivalent processing temperature differences between the plasticized and pure copolymer were measured. The viscosity data were analyzed using a Williams-Landel-Ferry (WLF) analysis[34], and the absorbance levels were compared to values calculated from Van Krevelen's solubility relationships. An experimentally determined framework was established to estimate the required CO_2 absorption level necessary for a specified reduction in processing temperature (and corresponding viscosity reduction).

5.2 Experimental

5.2.1 Materials

An extrudable grade AN/MA copolymer made by BP/Amoco, Barex, was used for this study. Barex is a grafted glassy copolymer containing 65 mole percent acrylonitrile (AN), 25 mole percent methyl acrylate (MA) and 10 mole percent toughening elastomer and is designed to be processed in the temperature range of 180-200^{o}C. Barex is available in a 4.8 mm long

cylindrical pellet of approximately 3.2 mm diameter. Air Products medium grade (99.8% pure) carbon dioxide was used for absorption into the Barex copolymer. Air Products 99.998% pure (excluding Argon) nitrogen (N_2) was used to pressurize the exit of the capillary rheometer during viscosity measurements to maintain a single phase melt and prevent the absorbed CO_2 in the polymer melt from flashing off during viscosity measurements. Nitrogen has been shown to be one of the least soluble gases in AN polymers, which possess extremely low gas solubility and diffusivity and were not expected to absorb N_2[35]. These expectations were confirmed experimentally[36].

5.2.2 Sample preparation

Barex pellets were saturated with CO_2 in a sealed, constant volume, pressurized bomb for various amounts of time. A Parr Instruments model 4760 pressure vessel was used to saturate the Barex samples. Approximately 20 grams of polymer were saturated at a time to have sufficient sample for viscosity measurements and thermal analysis. The pressure vessel was initially charged with CO_2 at room temperature in the form of a high pressure gas at 5.86 MPa, and then heated to 120^{o}C, which increased the pressure to 10.3 MPa. It was necessary to use a saturation temperature above the T_g of the copolymer to increase free volume and ensure dispersion of the CO_2 into the polymer. 120^{o}C was chosen as the soak temperature because it was well above the T_g of Barex (85^{o}C) but well below the temperature at which cyclization and crosslinking (thermal degradation) began to occur. Higher temperatures resulted in slight thermal degradation for the longest soak times, and lower temperatures required longer soak times to achieve comparable results. The sample was then held at 120^{o}C for various amounts of time, corresponding to the "soak time" for the CO_2 absorption. Following the soak time, the pressurized bomb was cooled back down to room temperature via forced convection. Once

cooled to room temperature, the pressure vessel was decompressed over the course of 12 minutes, corresponding to a decompression rate of 8.27 x 10^3 Pa/s. The entire heating and cooling process will later be referred to as the "cycle time" of saturation, which does not include the soak time at 120°C.

Further high pressure saturations were performed in a similar manner. Following the batch pressurization and heating to 120°C (corresponding to 10.3 MPa), a Trexel TR-1-5000L high pressure CO_2 pump was used to directly inject liquid CO_2 into the heated pressure vessel and raise the pressure to 17.2 MPa. This pressure was chosen as the upper limit in this study so that reasonable pressures could be maintained in future extrusion studies.

Following saturation of the Barex copolymer with CO_2, the thermal analyses and rheometry were immediately performed to ensure that no CO_2 was lost from the sample. Samples were prepared and tested as quickly as possible following depressurization and removal from the pressure vessel. The maximum time between depressurization and thermal testing was 15 minutes, which we found did not result in any significant loss of CO_2 due to diffusion[36]. The polymer pellets were transferred to the rheometer and placed in a pressurized environment within 5 minutes, again avoiding any significant loss of CO_2 due to diffusion.

5.2.3 Differential Scanning Calorimetry

A Seiko model 220 differential scanning calorimeter (DSC) and a TA Instruments model 2920 modulated DSC were used to make the DSC measurements. Heating and cooling rates of 10°C/min were used. A nitrogen purge was used during measurements in both DSC units. Aluminum pans with pierced lids were used to hold the 5-10 mg samples. The use of pierced lids facilitated the escape of the absorbed CO_2.

Two heats were performed on each sample. The first heat allowed direct visualization of the T_g reduction resulting from absorbed CO_2. The second heat verified that no residual CO_2 was present, which was confirmed if the T_g of the pure material was obtained. Samples containing absorbed CO_2 were cooled to -20°C to further prevent any degassing prior to running the thermal scan, as well as to establish a baseline for easy visualization of the T_g of the plasticized Barex. The test comprised heating from -20°C to 180°C to ensure that all CO_2 had flashed out of the system, cooling back to -20°C, and then performing the second heat.

5.2.4 Thermogravimetric Analysis

A TA Instruments Hi Res TGA 2950 thermogravimetric analyzer (TGA) was used to measure the weight percent of CO_2 that was absorbed into the AN copolymer. A nitrogen purge of 24 ml/min was used. Platinum pans were used to hold 5-10 mg Barex samples containing absorbed CO_2. Measurements were started at room temperature (25°C) and ramped to 250°C at a heating rate of 10°C per minute. Evolution of CO_2 was easily visualized by the weight fraction of the polymer/CO_2 mixture lost following heating through the Tg of the copolymer.

5.2.5 Pressurized Capillary Rheometer

An Instron model 3211 capillary rheometer was used to obtain the viscosity of the pure Barex in the temperature range of 180 to 210°C and of the plasticized Barex at 180°C. The rheometer was modified with the addition of a sealed chamber at the capillary exit for the purpose of creating a static pressure to prevent flashing off of the CO_2 from the copolymer, maintaining a single phase melt. The approach of Luxenburg and coworkers[37], used to measure the viscosity of water plasticized soy protein, was extended for this study. A schematic of the experimental apparatus is shown in Fig. 5.1. A specially constructed pressure assembly was used to apply a constant static pressure to the capillary exit and collect the extrudate during the

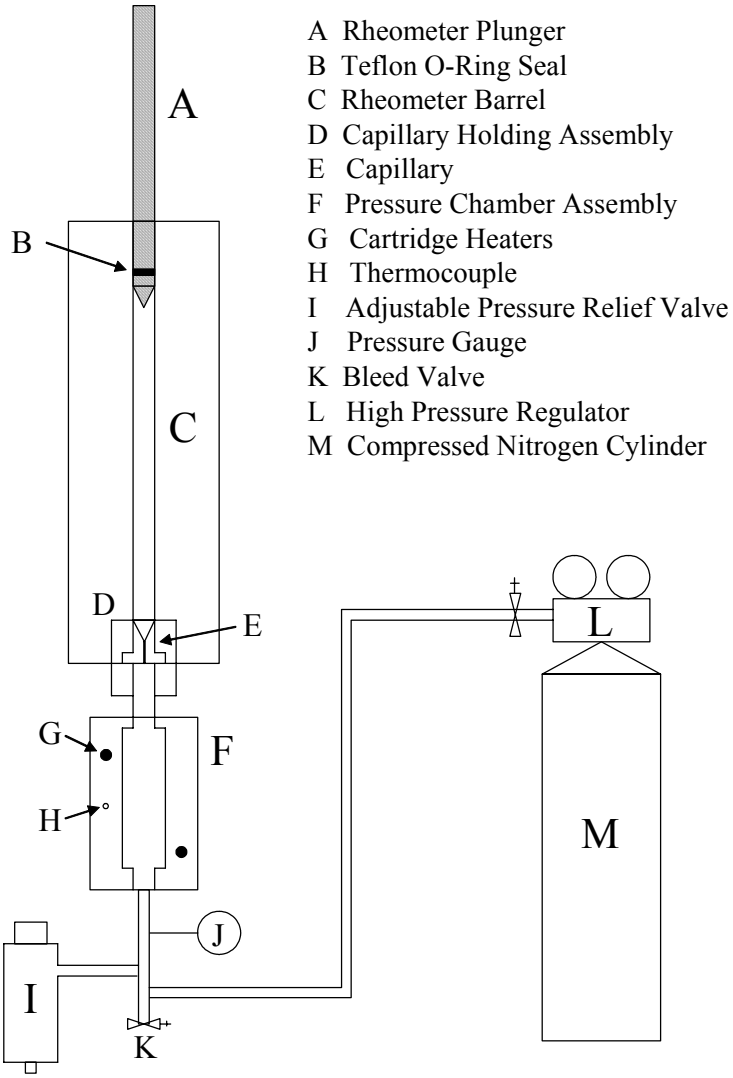

Fig. 5.1: Schematic of the pressurized capillary rheometer for viscosity measurement of polymers containing absorbed CO_2.

viscosity measurements. The use of an adjustable pressure relief valve ensured that the applied static pressure remained constant. This was visually verified with a pressure gauge fitted to the pressurized assembly. Nitrogen was used in the range of 3.4-13.8 MPa to apply a static pressure to the capillary exit. The rheometer piston was sealed using Teflon O-rings, and the pressure chamber assembly was sealed to the capillary using Teflon spacers. An Omega CN9000 temperature controller was used to control the temperature of the pressurized chamber. Two 150-Watt Fire Rod cartridge heaters were used to heat and maintain the chamber temperature.

In order to minimize the loss of CO_2 on loading the barrel of the capillary rheometer with pellets containing absorbed CO_2, the following procedure was utilized. The saturated polymer pellets were transferred from the pressure vessel into the cold rheometer and then sealed from the top with the piston. Static pressure was then applied to the capillary exit with the pressure chamber. With the system pressurized, the polymer could be heated to test temperatures without losing the absorbed CO_2 to the atmosphere, and the effects of plasticization on viscosity could be measured.

5.2.6 Viscosity Measurements

Viscosity measurements were performed on Barex-CO_2 materials containing between 2.7 and 6.7 weight percent absorbed CO_2. For each Barex-CO_2 sample, measurements were conducted at 180^{o}C and compared to the pure copolymer viscosity measured at 180^{o}C. Pure copolymer viscosities were also measured at 190, 200, and 210^{o}C to provide a set of reference viscosity curves for comparison to the Barex-CO_2 viscosity curves. Measurements at each CO_2 absorption level were conducted with capillaries of 1.0 mm diameter and L/D values of 10, 20, and 30, all having a 90^o entry angle. Plunger speeds corresponding to shear rates in the range of 5 to 4000 s^{-1} were used for the measurements.

Viscosity values were obtained by well-known methods from plunger speed and force measurements[38]. In particular, the force required to displace the polymer through the capillary at a constant plunger speed was measured. The actual pressure drop across the capillary (ΔP) was measured as the difference between the upstream force measured by the Instron load cell to push the polymer through the capillary (ΔP_{total}) and the applied static pressure (ΔP_{static}). A correction for the effect of the viscoelastic entry pressure (ΔP_{entry}) was accounted for and determined by the construction of Bagley plots, in which the pressure ($P = \Delta P_{total} - \Delta P_{static} - \Delta P_{friction}$) versus L/D measurements at each shear rate were extrapolated to P=0 and the intercepts were used to determine a set of corrections[38]. The entry pressures determined from the Bagley plots were subtracted from ΔP_{total} to determine the actual pressure drop (ΔP) across the capillary, facilitating determination of a true wall shear stress. The pressure drop correction used to calculate ΔP is defined in Eq. 5.1:

$$\Delta P = \Delta P_{total} - \Delta P_{static} - \Delta P_{entry} - \Delta P_{friction} \qquad (5.1)$$

where $\Delta P_{friction}$ is the correction to account for the friction imposed by the plunger seal, and was directly measured using an empty sample reservoir at the various plunger speeds and corrected for accordingly at each pressure drop measurement (plunger speed). The wall shear stress, τ, was then calculated using Eq. 5.2:

$$\tau = \frac{\Delta P}{L}\frac{D}{4} \qquad (5.2)$$

where L and D are the length and diameter of the capillary, respectively. The apparent shear rate, $\dot{\gamma}_a$, was calculated based on the volumetric flow rate of the polymer through the capillary, Q, and the radius of the capillary, R, as defined in Eq. 5.3:

$$\left|\dot{\gamma}_a\right| = \frac{4Q}{\pi R^3} \tag{5.3}$$

A correction to account for the non-Newtonian nature of the velocity profile in the polymer melt was performed using the classical Rabinowitsch correction to convert from apparent to true shear rate and is shown in Eq. 5.4[39]:

$$\dot{\gamma} = \frac{\dot{\gamma}_a}{4}\left(3 + \frac{d\ln\dot{\gamma}_a}{d\ln\tau}\right) \tag{5.4}$$

The viscosity was then calculated using Eq. 5.5:

$$\eta = \frac{\tau}{\dot{\gamma}} \tag{5.5}$$

Effects of the applied static pressure on the viscosity were also considered. To ensure that the applied static pressure did not have an effect on viscosity, the pure copolymer viscosity was measured at 180°C over the aforementioned shear rate range using applied static pressures of up to 13.8 MPa. These measurements were compared to pure copolymer viscosities measured without applied static pressure to ensure that there were no pressure effects on viscosity.

5.3 Results and Discussion

In the following section, the effects of the amount of absorbed CO_2 on the thermal properties and levels of viscosity reduction of Barex are discussed. Calculated viscosity reductions are then compared to the experimentally measured levels of viscosity reduction (as a function of reduction of T_g) to determine the ability to predict the amount of absorbed CO_2 required for a specified processing temperature reduction. The ability to predict the amount of CO_2 absorption for our saturation conditions is also discussed to determine whether the level of CO2 absorption can be determined for any given set of saturation conditions.

5.3.1 Thermal Analysis

DSC and TGA thermal analyses were used to establish a relationship between the reduction of T_g and the amount of absorbed CO_2 for a given soak time and pressure. Figs. 5.2 and 5.3 illustrate the DSC and TGA scans of Barex following CO_2 absorption at 120°C and both saturation pressures, 10.3 and 17.2 MPa. The data collected for both heats are depicted in the figures for easy visualization of the T_g difference between plasticized and pure Barex (meaning pure in the sense that no residual CO_2 remains). The first heat of the polymer containing CO_2 is represented by the upper curve for each sample, and the second heat (following cool down) is represented by the lower curve. Using only the aforementioned cycle time, a T_g reduction of 15°C was obtained, corresponding to a 2.7 weight percent uptake of CO_2. These results are indicated by the 0 hour soak time in the DSC and TGA scans shown in Figs. 5.2 and 5.3. Longer soak times at 10.3 MPa (120°C) resulted in greater reductions of T_g. A 6 hour soak resulted in a reduction of T_g of 21°C, corresponding to a 4.7 weight percent uptake in CO_2. Beyond the 6 hour soak, no additional uptake of CO_2 was observed. The TGA results shown for the 12 hour soak in Fig. 5.3 clearly indicate that no additional CO_2 was absorbed over the 6 hour saturation. Saturation times in excess of 12 hours caused the polymer to degrade to a very slight extent, indicated by a slight change in the polymer color.

Thermal analysis of the sample saturated at 17.2 MPa was only performed using the 6 hour soak time at 120°C because no significant absorption was observed using longer soak times in the 10.3 MPa saturation experiments. As seen from the DSC results in Fig. 5.2, the glass transition temperature was reduced by 31°C (to 54°C), corresponding to a 6.7 weight percent CO_2 uptake, as indicated by the TGA scans in Fig. 5.3.

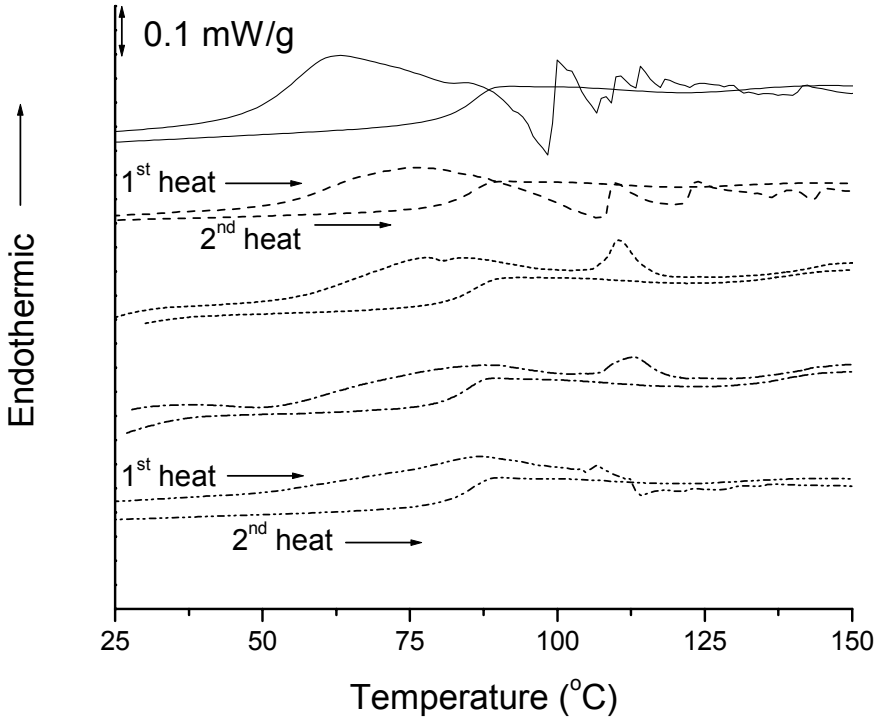

Fig. 5.2: DSC scans of Barex saturated at 120°C for various times at 10.3 and 17.2 MPa CO_2. From top to bottom: (—) 6 hr., 17.2 MPa; (— —) 6 hr., 10.3 MPa; (---) 4 hr., 10.3 MPa; (— - —) 2 hr., 10.3 MPa; (— - - —) 0 hr., 10.3 MPa.

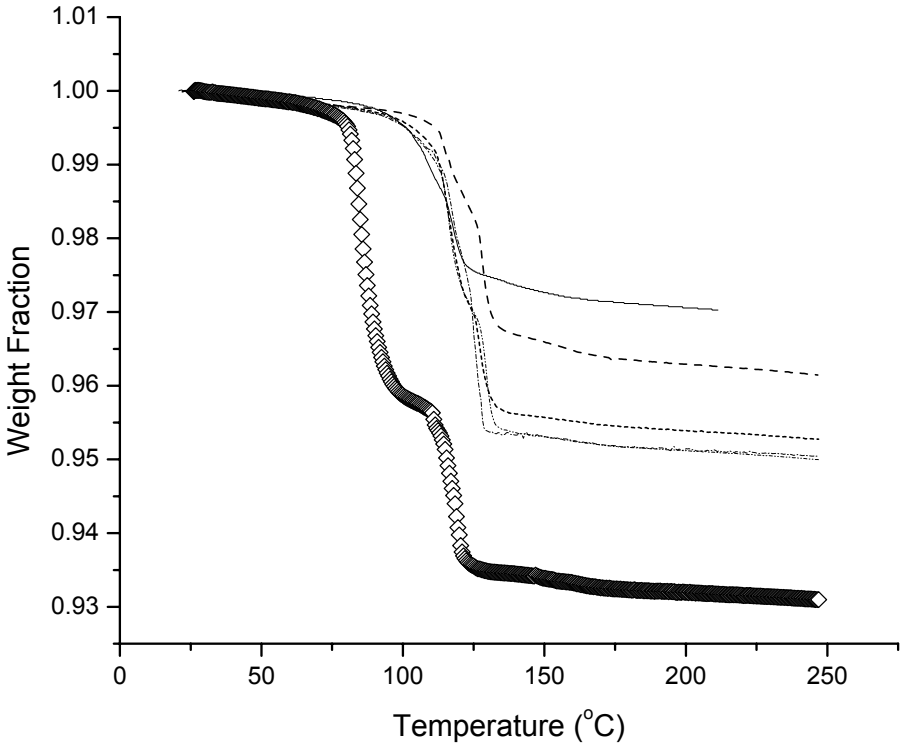

Fig. 5.3: TGA of Barex comparing 10.3 and 17.2 MPa CO_2 soak pressures. Soak temperature was 120°C. 10.3 MPa soak times (from top to bottom): (—) 0, (— —) 2, (---) 4, (— - —) 6, and (— - - —) 12 hours. 6 and 12 hours soak times overlap. (◊) 6 hours, 17.2 MPa soak.

Combining the thermal analysis data from the DSC and TGA results in Figs. 5.2 and 5.3 facilitated an estimate of the amount of CO_2 required to achieve a desired T_g reduction, which is illustrated in Fig. 5.4. The dashed line is an exponential fit of the compiled data, and quite accurately represents the measured range of CO_2 absorption and corresponding T_g reduction levels. The exponential fit of the data is represented in Eq. 5.6:

$$T = 9.1 \exp[0.2W] \tag{5.6}$$

where T is the reduction in glass transition temperature (^oC) resulting from CO_2 absorption and W is the weight percent uptake of CO_2. The fit of the data permits a determination of the amount of CO_2 required to obtain a reduction of T_g within the range of measured data, which will be necessary once a required viscosity reduction is known.

5.3.2 Viscosity Reduction

The ability of CO_2 to reduce the viscosity of Barex was determined by measuring the viscosity versus shear rate for Barex containing absorbed CO_2. Viscosity values were obtained at 180^{o}C for both the pure and plasticized Barex and were compared to determine the magnitude of the viscosity reduction (at 180^{o}C) obtained from CO_2 absorption at each absorption level. The viscosity values of the lowest and highest absorption percentages from the 10.3 MPa saturations (2.7 and 4.7 weight percent CO_2, corresponding to a 15 and 21^{o}C T_g reduction, respectively) and the viscosity values for the highest absorption level at the 17.2 MPa saturation pressure (corresponding to a 6.7 weight percent absorption and 31^{o}C T_g reduction) were measured.

Bagley plots were constructed for both the pure and plasticized (containing 6.7 wt. % CO_2) Barex samples for the highest, lowest, and an intermediate measured shear rate, as shown in Fig. 5.5. The Bagley plots clearly indicate linear pressure dependences over the range of shear rates tested for both pure and plasticized Barex, with correlation coefficients greater than 0.99 for

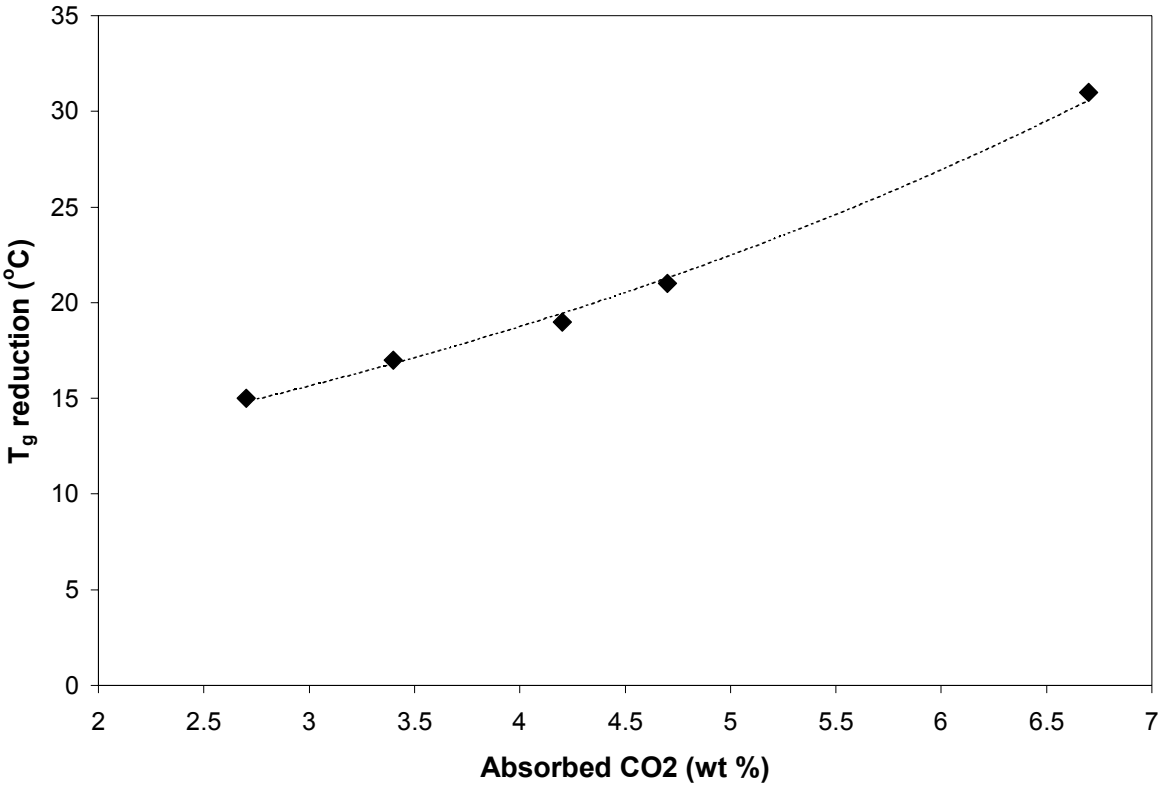

Fig. 5.4: T_g reduction as a function of level of absorbed CO_2. (◆) DSC/TGA data. (--) exponential fit.

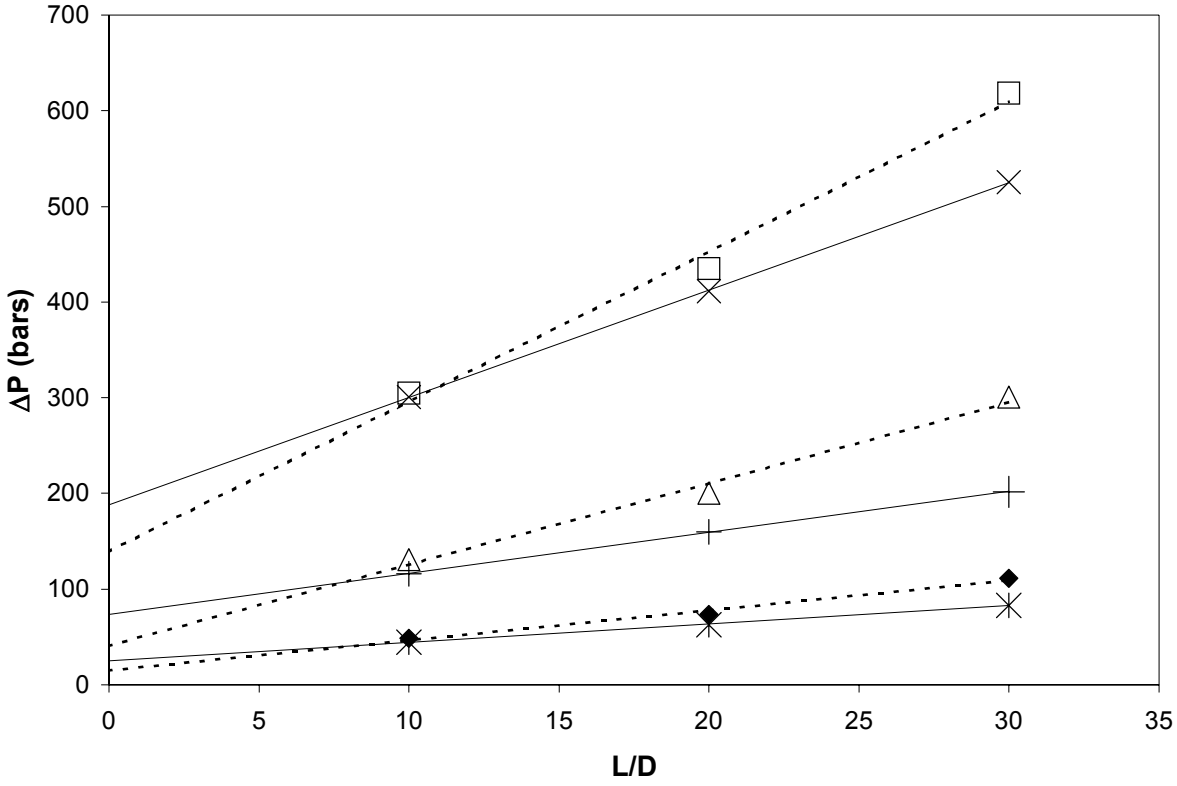

Fig. 5.5: Bagley plots for pure and plasticized (containing 6.7 wt. % CO_2) Barex at 180^{o}C and L/D values of 10, 20, and 30. Capillary diameter 1.0 mm. Pure copolymer apparent shear rates: (◆) 7 s^{-1}, (△) 73 s^{-1}, (□) 1210s^{-1}. Saturated copolymer apparent shear rates: (✳) 7 s^{-1}, (+) 73 s^{-1}, (×) 1210 s^{-1}. Dashed lines represent linear fits of the data for pure Barex at the above shear rates. Solid lines are linear fits of the plasticized Barex data.

the linear fits at each shear rate. These results indicate that viscous heating (which would be indicated by a downward curving slope) was not occurring, and that the viscosity was not pressure dependent (which would be indicated by an upward curving slope).

Differences in the slopes and intercepts of the Bagley plots between pure and plasticized Barex were analyzed. The slope of each linear fit in the Bagley plots, which is directly proportional to the shear stress at each shear rate, was expected to decrease for plasticized Barex, assuming the viscosity decreased upon absorption of CO_2. As expected, the slope at any given shear rate for plasticized Barex in Fig. 5.5 is lower than that for pure Barex, indicating a lower shear stress and, therefore, a lower viscosity. Entry pressures were obtained from the intercepts (at L/D = 0) of the Bagley plots, and the viscosity data for both pure and plasticized Barex at 180^{o}C were corrected for entry pressure at each shear rate accordingly (as described in Eq. 1). It is interesting that the entry pressures for the plasticized Barex were higher than those determined for pure Barex, because we expected that as the viscosity levels were decreased, the entry pressures would decrease in a similar manner. To check for consistency between the linear fit of the pressure drop versus L/D data and the calculated pressure drops (from Eq. 1.), the wall shear stresses were calculated at each shear rate using the slope of the Bagley plots (τ = slope/4). The data are plotted in Fig. 5.6, and over the range of measured shear rates, the shear stresses obtained from the slopes of the Bagley plots were found to be within +/- 0.5% of the shear stresses calculated using Eqs. 5.1 and 5.2. The origin of the higher entry pressures in Barex containing absorbed CO_2 is unknown, but it is possible that absorbed CO_2 may have an effect on the extensional rheology of Barex, and correspondingly affects the entry pressures in an unexpected manner.

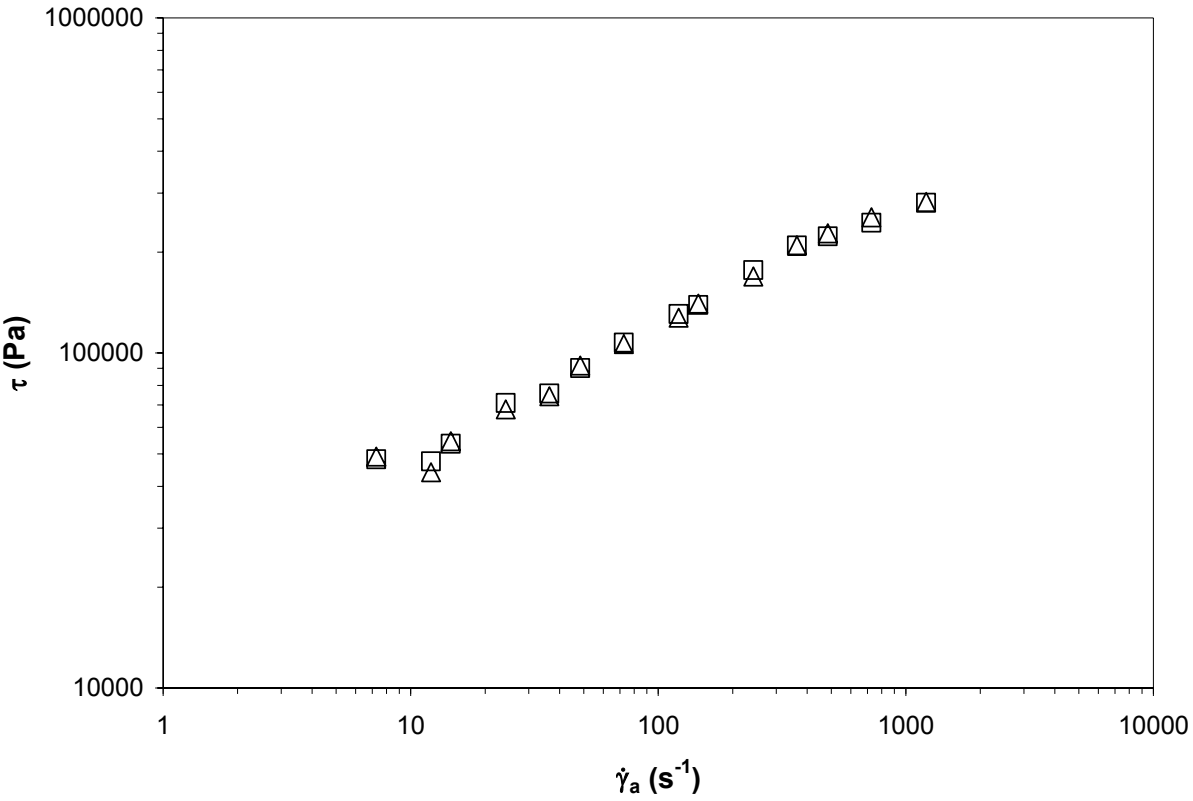

Fig. 5.6: Shear stress for saturated Barex containing 6.7 weight % CO_2 calculated from: (□) slopes of linear fit in Bagley plots of Fig. 5; (△) Eqs. 1 & 2.

Viscosity reductions at each CO_2 absorption level are indicated by the viscosity versus shear rate data in Fig. 5.7, which shows a general trend of greater viscosity reduction for an increase in the amount of adsorbed CO_2. The viscosity versus shear rate data in Fig. 5.7 is for a L/D of 30, but almost identical results were obtained for the other L/D values. An average viscosity reduction of 7 % was obtained for the plasticized Barex containing 2.7 weight percent absorbed CO_2 over the range of shear rates tested. Increasing the amount of absorbed CO_2 to 4.7 weight percent had a significant effect on the viscosity reduction, resulting in an average reduction in viscosity of 32%. Finally, the sample containing 6.7 weight % absorbed CO_2 exhibited a viscosity reduction of about 60 %, which is approximately equivalent to a three fold viscosity reduction.

To ensure that the applied static pressure was ample to prevent foaming, the extrudate of the plasticized Barex was examined using a scanning electron microscope (SEM). As seen in Fig. 5.8, the extrudate showed signs of bubble nucleation, but there was no indication of significant bubble growth. This suggests that the applied static pressure was sufficient to prevent foaming and loss of the CO_2 from the plasticized melt in the rheometer barrel, ensuring a relatively homogeneous melt. Visual inspection of the extrudate processed at lower applied static pressures revealed a milky, cloudy extrudate, which was not observed in the extrudate used to obtain the cross section shown in Fig. 5.8.

5.3.3 Equivalent Processing Temperature Reductions

In order to determine the ability for small amounts of absorbed CO_2 to reduce the processing temperature, the viscosity of Barex containing absorbed CO_2 at 180^{o}C was compared to the pure copolymer viscosity measured at higher temperatures. For each absorption level, the temperature was found where the pure copolymer viscosity overlapped the plasticized copolymer

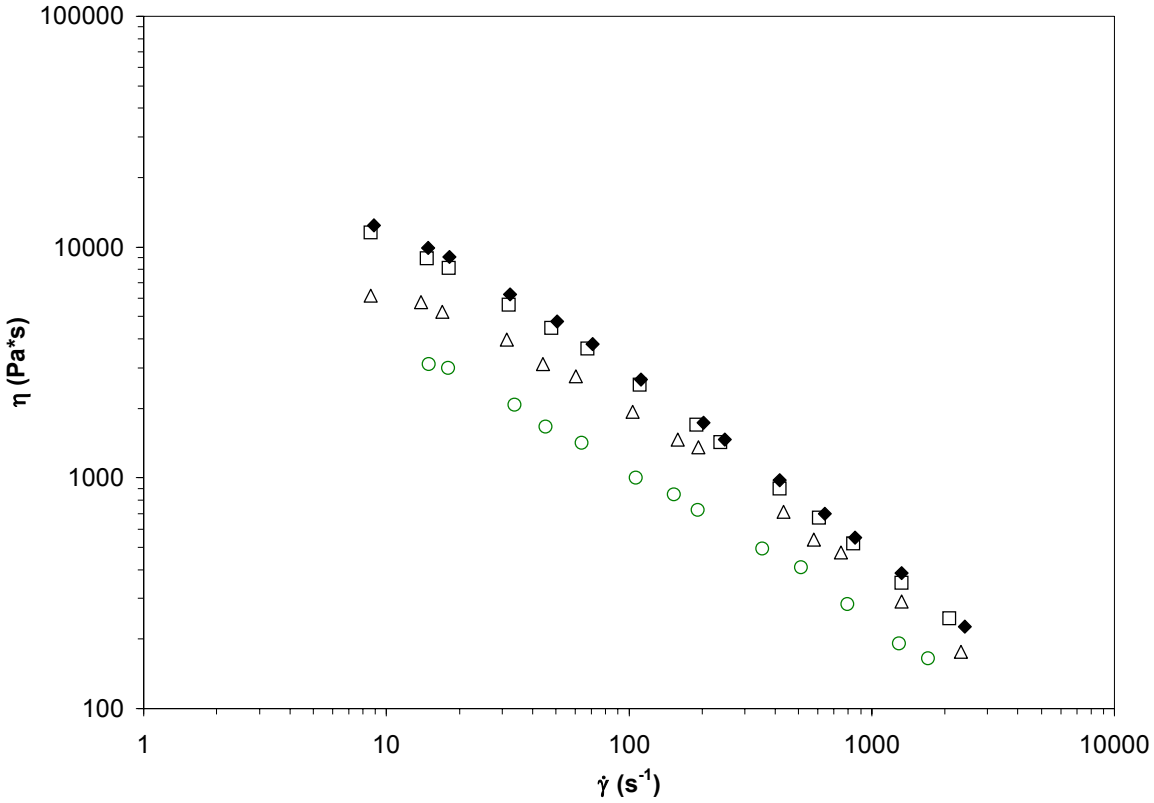

Fig. 5.7: Viscosity versus shear rate data of Barex containing (□) 2.7, (Δ) 4.7, and (○) 6.7 weight percent CO_2. (♦) pure Barex. L/D = 30, 1.0 mm diameter. T = 180°C.

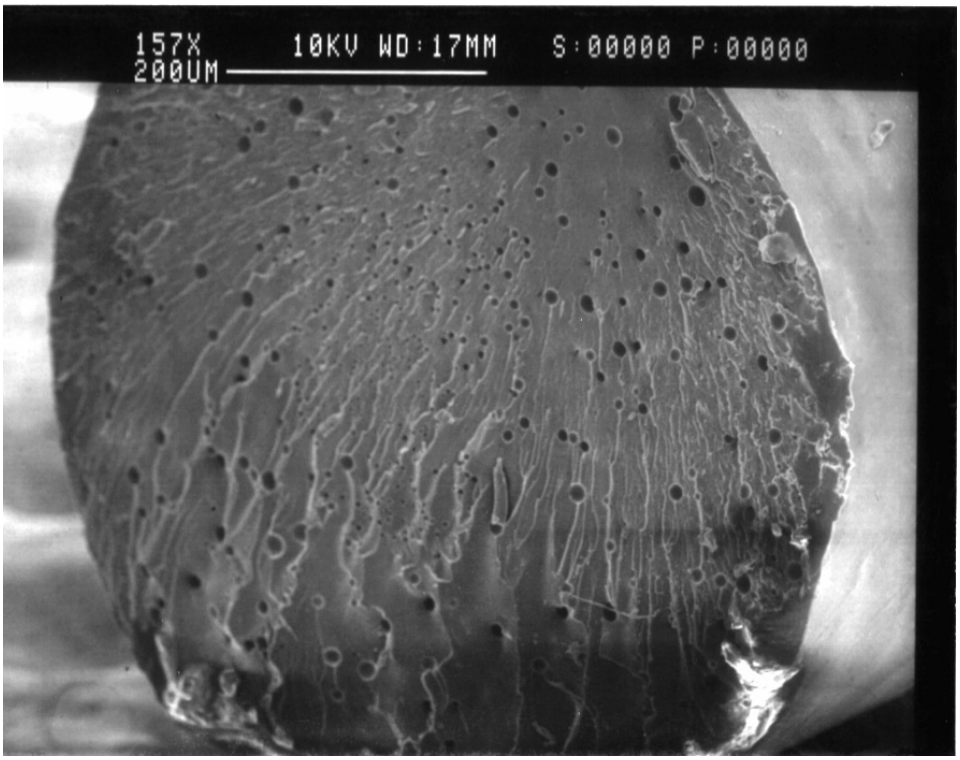

Fig. 5.8: SEM of Barex containing 4.7 weight percent absorbed CO_2 extruded into the pressurized chamber at 180^{o}C. Extrudate is approximately 500 μm in diameter.

viscosity measured at 180°C. The difference between these two temperatures corresponded to a potential equivalent processing temperature difference. Pure copolymer viscosities were measured at temperatures in the range 190-210°C for comparison to the plasticized copolymer. Although not shown, all pure copolymer viscosity data at the elevated temperatures were obtained at three L/D values to obtain a correction for the entry pressure. Bagley plots were constructed for the pure copolymer at the elevated testing temperatures and indicated linear pressure dependences, similar to that observed for the pure copolymer at 180°C in Fig. 5.5.

Equivalent processing temperature reductions were determined for the three CO_2 absorption levels studied. The resulting overall viscosity reduction for the 2.7 weight percent CO_2 uptake was relatively small. Consequently, the temperature difference in viscosity was only a few degrees, and it was difficult to establish a statistical difference. Viscosity reductions from the 4.7 and 6.7 weight percent CO_2 absorptions were much more significant. The viscosity versus shear rate behavior of the pure copolymer at 180 and 190°C is compared to the plasticized polymer containing 4.7 weight percent CO_2 at 180°C in Fig. 5.9. Viscosity levels of Barex containing 4.7 weight % absorbed CO_2 at 180°C overlap the viscosity obtained for the pure copolymer at 190°C, which correlates to an equivalent 10°C difference in processing temperature between the pure and plasticized copolymer. Only the data collected for the L/D of 20 is illustrated in Fig. 5.9 to facilitate clear visualization of the viscosity overlap, but similar results were obtained for all three tested L/D values. The viscosity levels of the pure copolymer at 180 and 210°C are compared to that of the saturated copolymer containing 6.7 weight percent CO_2 at 180°C in Fig. 5.10. The saturated copolymer viscosity levels at 180°C overlap the viscosity versus shear rate data of the pure copolymer at 210°C, suggesting an equivalent 30°C difference in processing temperature between the pure and plasticized copolymer. The amount of absorbed

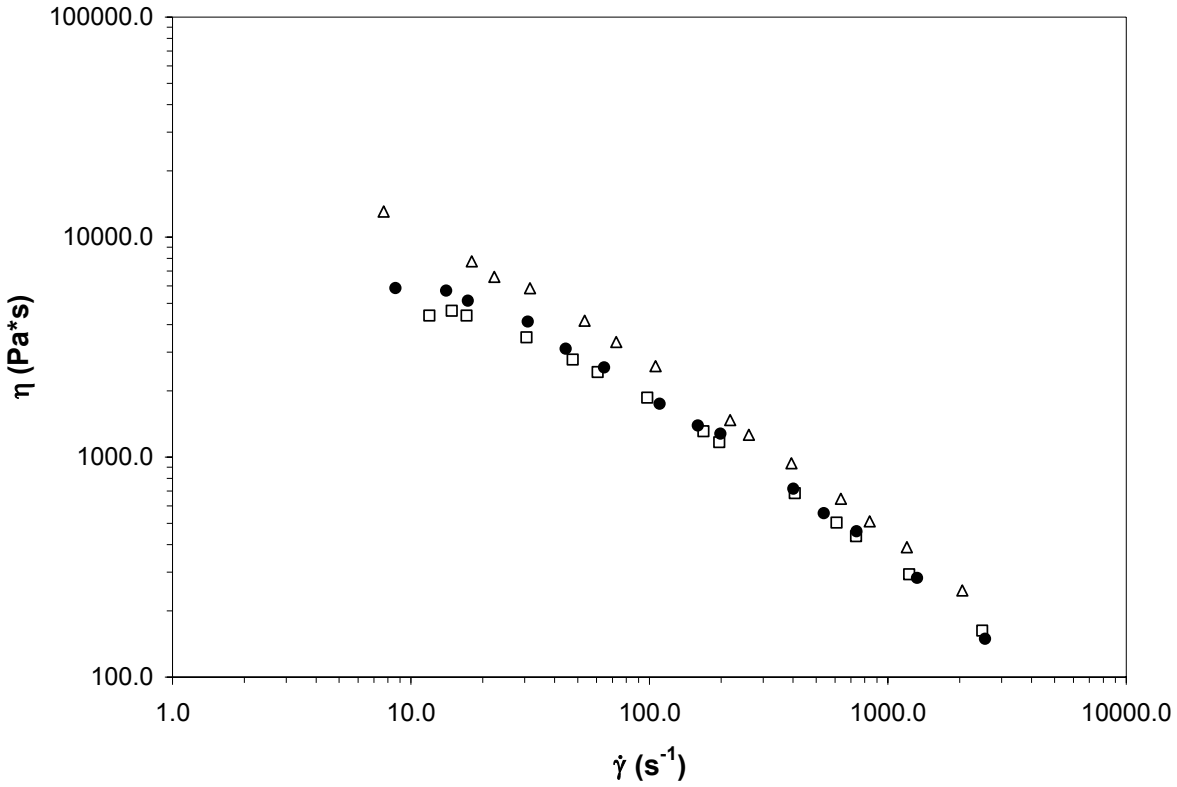

Fig. 5.9: Comparison of viscosity of Barex containing 4.7 weight percent CO_2 at 180°C (●) to that of pure Barex at 190°C (□). (△) pure Barex viscosity at 180°C. L/D = 20. 1.0 mm capillary diameter.

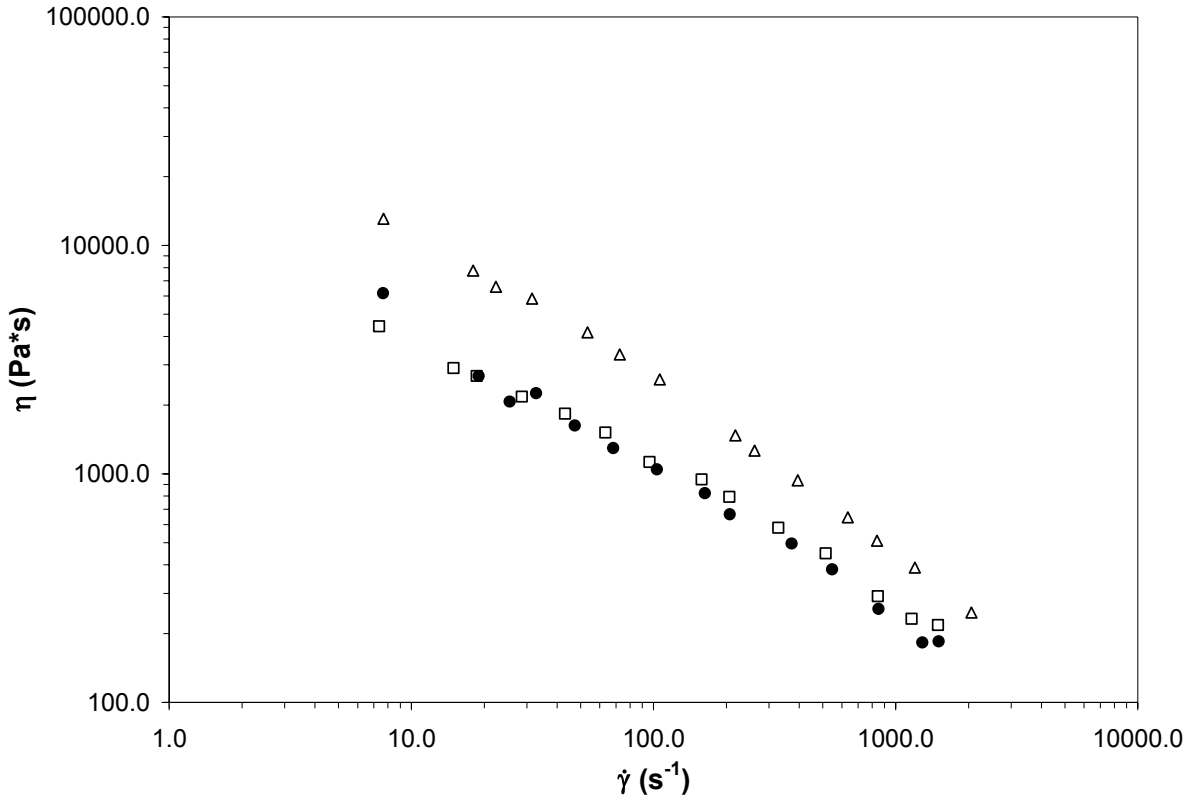

Fig. 5.10: Comparison of viscosity of Barex containing 6.7 weight percent CO_2 at 180°C (●) to that of Barex at 210°C (□). (△) pure Barex viscosity at 180°C. L/D = 20. 1.0 mm capillary diameter.

CO_2 is only increased by approximately 40% over the 4.7 weight % absorption, yet the viscosity reduction is doubled and the equivalent difference in processing temperature is tripled. These trends suggest that the relationship between CO_2 absorption level (T_g reduction) and viscosity reduction is nonlinear.

5.3.4 WLF Analysis

To obtain a specified reduction in processing temperature, a reduction of T_g is necessary to sufficiently reduce the viscosity. We evaluated the ability of the Williams-Landel-Ferry (WLF) equation to predict viscosity reductions based on the measured reductions of T_g for Barex. If the values were in agreement with the measured viscosity reductions, then the WLF analysis could be similarly utilized to predict a required reduction of T_g (based on a specified viscosity reduction or required processing temperature reduction). The WLF equation, which relates the viscosity at a temperature T, η_T, to the viscosity at T_g, η_{Tg}, is shown in Eq. 5.7[40].

$$\log \frac{\eta_T}{\eta_{T_g}} = \frac{C_1\left(T - T_g\right)}{C_2 + \left(T - T_g\right)} \tag{5.7}$$

Writing the WLF equation for the pure and plasticized copolymers and taking the ratio of the two equations resulted in a single equation that relates the glass transition temperature of the pure and plasticized copolymers to the viscosity reduction, as shown in Eq. 8:

$$\frac{\eta\left(T_1\right)^{(1)}}{\eta\left(T_1\right)^{(2)}} = \frac{10^{\left(\frac{-C_1\left(T_1 - T_g^{(1)}\right)}{\left(C_2 + T_1 - T_g^{(1)}\right)}\right)}}{10^{\left(\frac{-C_1\left(T_1 - T_g^{(2)}\right)}{\left(C_2 + T_1 - T_g^{(2)}\right)}\right)}} \tag{5.8}$$

where $\eta(T_1)^{(1)}$ and $\eta(T_1)^{(2)}$ are the viscosities of the pure and plasticized copolymer, respectively, at a given test temperature T_1, and $T_g^{(1)}$ and $T_g^{(2)}$ are the glass transition temperatures of the pure and plasticized copolymers, respectively, obtained from DSC measurements. Eq. 5.8 was used with the universal constants $C_1 = 17.44$ and $C_2 = 51.6$ ^oK to estimate a viscosity reduction

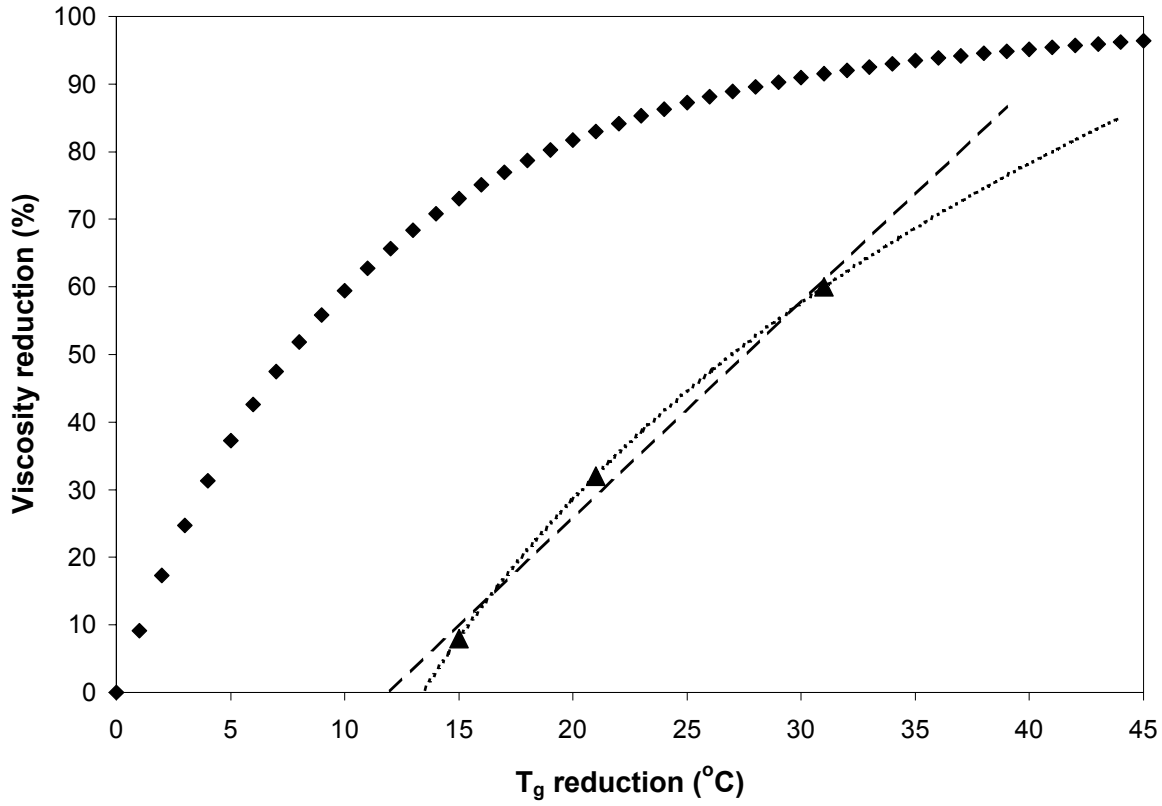

Fig. 5.11: Viscosity reduction for plasticized Barex T_g reduction: (◆) calculated values using Eq. 8 and universal constants; (▲) measured values; (——) linear fit of experimental data, (------) logarithmic fit of experimental data.

based on the DSC measured T_g values for plasticized Barex (from Fig. 5.2) and pure Barex (T_g=85^{o}C). As seen in Fig. 5.11, the predicted viscosity reduction from Eq. 5.8 has a nonlinear relationship to the reduction in T_g. Linear and logarithmic fits of the measured data in Fig. 5.11 resulted in correlation coefficients of 0.99 and 1.0, respectively, suggesting a nonlinear logarithmic relationship between the experimentally measured viscosity reduction and the reduction of T_g. However, the values of the measured viscosity reduction are lower than the predicted values for a given reduction of T_g.

Two possible sources of error, namely pressure effects on viscosity and the assumption of universal constants, were addressed to explain the discrepancy between the measured and calculated viscosity reductions. To ensure that pressure effects on viscosity were not creating a discrepancy, the pure copolymer viscosity was measured with applied static pressures (at the capillary exit) of 6.9 and 13.8 MPa. The reason for concern was that polymers such as polystyrene have been shown to have a viscosity that is pressure sensitive, which leads to a discrepancy between the measured and predicted viscosity reductions[24]. As seen from the data in Fig. 5.12, the copolymer viscosity was unaffected by the application of static pressure at the capillary exit. These results suggest that the applied static pressure had no significant effect on the measured pressure drops and did not contribute any significant source of error over the range of pressures used. As a result, we concluded that the primary source of error between the WLF analysis and the experimentally measured values was attributable to the use of universal constants for C_1 and C_2 in Eq. 5.8.

Another possible contribution to the error was the temperature range utilized with the WLF analysis. The useful range of the WLF analysis is T_g + 100^{o}C[40]. Viscosity measurements were obtained at temperatures of up to T_g + 126^{o}C. Hence, the analysis may have been used just

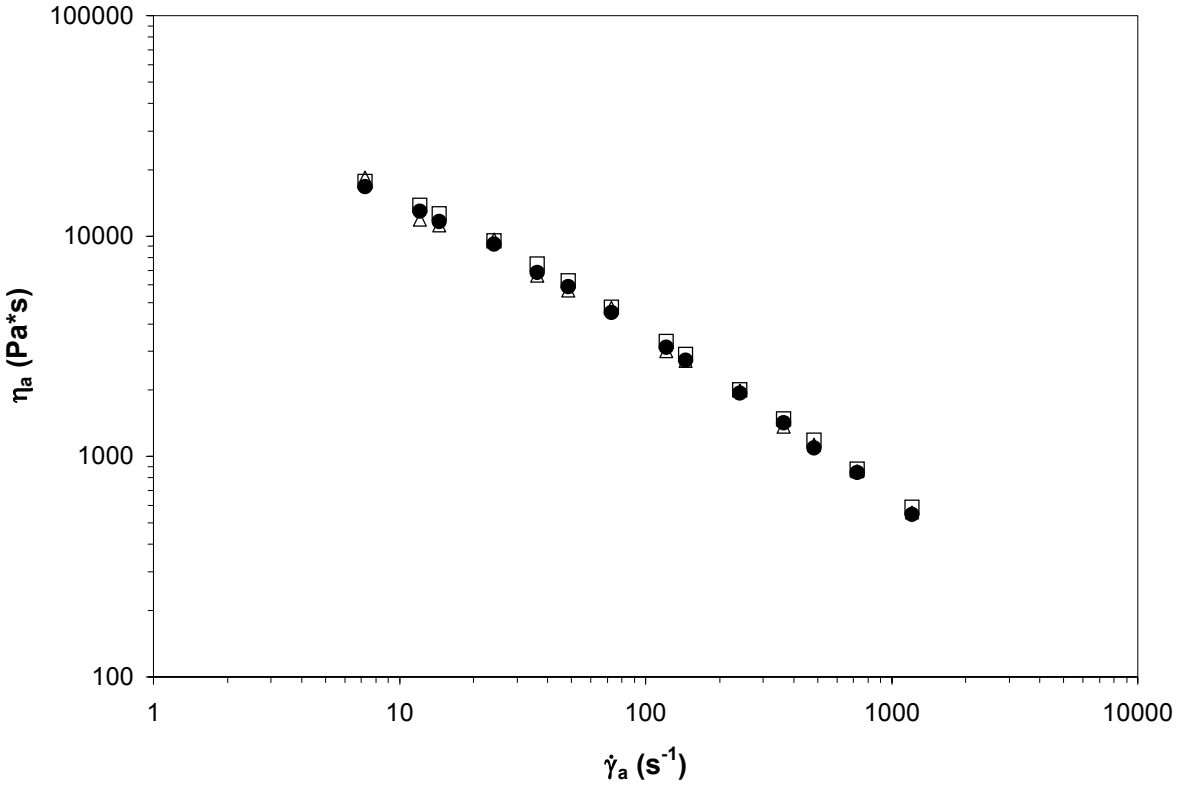

Fig. 5.12: Apparent viscosity of pure AN copolymer at 180°C. (△) 13.8 MPa applied static pressure; (●) 6.9 MPa applied static pressure; (□) no applied static pressure.

outside the range of the WLF equation, which may have also contributed to the discrepancy between calculated and measured viscosity reductions.

The WLF analysis was not able to accurately predict the viscosity reduction based on the measured viscosity values and glass transition temperatures for pure and plasticized Barex, and as a result can not be used with the universal constants to accurately predict a reduction of T_g for a specified viscosity reduction. We believe that determining a reference temperature, T_o, for use in place of T_g in the WLF analysis, would facilitate a relationship between reductions of T_g to viscosity reductions. T_o would be obtained by a best fit of the experimental viscosity data to a master curve, using the constants $C_1 = 8.86$ and $C_2 = 101.6\ ^oK$ in Eq. 5.8[39]. This analysis still requires experimental data, and only facilitates prediction of intermediate values of reductions of T_g as a function of viscosity reduction over the measured range of data.

5.3.5 Absorption Predictions

We next examined the ability to predict the saturation conditions necessary to obtain a specific amount of absorbed CO_2 in Barex. If the saturation conditions required to absorb a specific amount of CO_2 in Barex can be predicted, then the resulting reduction of T_g, viscosity reduction, and ultimately reduction in processing temperature can be determined based only on the temperature and pressure of saturation (assuming that the WLF analysis can be made to work). We calculated the solubility of CO_2 in Barex to determine a relative volume fraction of plasticizer (or diluent) per volume of solution, which was converted to weight percent by the use of an equation of state. These solubility calculations were performed to determine whether the measured amount of absorbed CO_2 agreed with the predicted absorption levels. If the values were in agreement, then we expect that absorption levels for other saturation temperatures and pressures could be predicted. We used Van Krevelen's empirical relationships to determine the

solubility of CO_2 in Barex[41]. Van Krevelen determined empirical relationships for solubility of gases in both glassy amorphous polymers and polymers in the rubbery state[41]. Each set of relationships was evaluated to predict solubility for our polymer/CO_2 system, and the volume of absorbed CO_2 per volume of solution was accordingly calculated. The Sanchez-Lacombe equation of state, which is known to accurately predict the physical properties of near critical and supercritical gases, was then used to calculate the density of the CO_2 at the saturation conditions, facilitating conversion of the calculated volume fraction of absorbed gas into a weight percent[42].

As a first approximation, the amount of absorbed CO_2 can be related to the absorption pressure and polymer solubility by the relationship in Eq. 5.9:

$$\frac{V_A}{V_P} = SP \tag{5.9}$$

where V_A is the volume of CO_2 dissolved into Barex per unit volume of solution, V_P is the volume of Barex per unit volume of solution, P is the pressure of saturation, and S is the solubility of Barex, which can be estimated with an Arrhenius type expression as follows in Eq. 5.10[43]:

$$S = S_0 \exp\left(\frac{-\Delta H_S}{RT}\right) \tag{5.10}$$

where ΔH_S is the molar heat of sorption in J/mol, and S_o is a pre-exponential factor in cm^3/cm^3*Pa. The molar heat of sorption and pre-exponential terms are not readily found, but can be estimated by Van Krevelen's relationships to Lennard Jones temperature (ε/k) of the gas [41]. For elastomers and polymers in the rubbery state, Van Krevelen determined the empirical relationships shown in Eqs. 5.11 and 5.12:

$$10^{-3}\frac{\Delta H_S}{R} = 1.0 - 0.010\frac{\varepsilon}{k} \pm 0.5 \tag{5.11}$$

$$\log S_0 = -5.5 - 0.005\frac{\varepsilon}{k} \pm 0.8 \qquad (5.12)$$

For CO_2, the Lennard Jones temperature is 195.2 K[41]. The mean solubility was calculated to be 3.4E-6 cm^3/cm^3*Pa, which is similar to reported solubilities for other thermoplastics in the rubbery state[44]. For glassy amorphous polymers, Van Krevelen arrived at the empirical relationships in Eqs. 5.13 and 5.14:

$$10^{-3}\frac{\Delta H_S}{R} = 0.5 - 0.010\frac{\varepsilon}{k} \pm 1.2 \qquad (5.13)$$

$$\log S_0 = -6.65 - 0.005\frac{\varepsilon}{k} \pm 1.8 \qquad (5.14)$$

which resulted in a mean calculated solubility of 9.5E-7 cm^3/cm^3*Pa. To convert the volume of CO_2 into a weight fraction, the density was required at the saturation temperature and pressure. The Sanchez-Lacombe equation of state (S-L EOS) is well known to accurately represent the physical properties of CO_2 in both near critical and supercritical states[45]. The EOS is based on a statistical mechanics derivation and relates pressure, density, and temperature as follows in Eq. 5.15:

$$\frac{P}{T} = -\ln\left(1-\rho\right) - \left(1-\frac{1}{r}\right)\rho - \frac{\rho^2}{T} \qquad (15)$$

where P, T, and ρ are reduced pressure, temperature, and density, respectively, with respect to characteristic parameters, and r is the number of lattice sites occupied by a molecule of molecular weight M. The characteristic P, T, and ρ parameters are provided for CO_2 by Garg et al.[19]. Densities of 32.6 and 55.4 kg/m^3 were calculated for CO_2 at 10.3 and 17.2 MPa, respectively, and 120°C.

By assuming that the volume of polymer is approximately the same as the volume of solution, Eq. 5.9 was solved for the mass fraction of CO_2. Using Eqs. 5.11 and 5.12 for a polymer in the rubbery state, it was estimated that approximately 50 and 74 weight percent CO_2 were expected to absorb at 10.3 and 17.2 MPa, respectively, for the 120°C saturation. Using Eqs. 5.13 and 5.14 for a glassy amorphous polymer estimated that approximately 22 and 45 weight percent CO_2 would absorb at 10.3 and 17.2 MPa, respectively, for the 120°C saturation. For comparison, 4.7 and 6.7 weight percent CO_2 were experimentally measured for the Barex copolymer. DMTA results indicated that Barex was indeed in the rubbery state during the saturation, and the calculation using mean solubility for a rubbery polymer overpredicted the experimentally determined values of absorption[36].

When using the Van Krevelen relationships, the sensitivity of S_o and $\Delta H_S/R$ in Eqs. 11-14 must be considered. Recalculating the solubility by using the equations for a polymer in the rubbery state, at the upper limit of the range of statistical error of Eq. 5.11 and the lower limit of Eq. 5.12, and again solving for the volume of CO_2, indicated that 4.8 and 12.6 weight percent CO_2 were expected to absorb into the polymer at 10.3 and 17.2 MPa, respectively, for the saturation carried out at 120°C. These values more closely matched the experimentally measured absorption levels and, in fact, the 10.3 MPa saturation was almost exactly predicted. For comparison, recalculating the absorption values at the upper limit of the range of statistical error of Eq. 5.13 and the lower limit of Eq. 5.14 (for a glassy amorphous polymer), resulted in expected absorptions of less than 1 weight percent for both pressures at 120°C. These results suggest that the Van Krevelen relationships for a polymer in the rubbery state can be used in conjunction with the Sanchez Lacombe EOS to accurately predict absorption levels for other saturation conditions with Barex. However, the statistical error in Eqs. 5.11-14 provides a large

range of values possible when calculating S_o and $\Delta H_s/R$ for the polymer. As a result, the upper limit of the range of statistical error of Eq. 5.11 and the lower limit of Eq. 5.12 must be used when predicting absorption levels for Barex (in the rubbery state).

5.4 Conclusions

This study has shown that an AN copolymer, Barex, has the ability to absorb CO_2 and exhibit a reduction in its T_g of up to 31^oC. The corresponding amount of absorbed CO_2 was up to 6.7 weight percent CO_2 using the 6 hr. saturation at 17.2 MPa. The accompanying viscosity reduction was measured to be up to 60 percent at the highest CO_2 absorption level, corresponding to an equivalent processing temperature reduction of 30^oC. The WLF analysis, when used with universal constants, was not suitable for predicting the reduction of T_g required for a specific viscosity reduction. Within the statistical limits of error, Van Krevelen's solubility relationships for a polymer in the rubbery state can be used to predict the amount of absorbed CO_2 expected for a given set of saturation conditions. The upper limit of the range of statistical error for calculation of $\Delta H_s/R$, and the lower limit for calculating S_o, must be used to accurately predict solubility values for Barex. As a result of the discrepancy in the WLF analysis, we could not theoretically predict the T_g reduction as a function of viscosity reduction. Therefore, experimentally measured T_g and viscosity data are required to determine saturation conditions necessary to obtain a specific processing temperature reduction. Future work will extend to higher AN content copolymers, where the kinetics of crosslinking will become a problem, to determine the dependence of AN content on CO_2 absorption and plasticization.

5.5 Acknowledgments

The authors wish to thank the U.S. Environmental Protection Agency (EPA) Science to Achieve Results (STAR), program grant #R-82955501-0, for financial support.

5.6 References

(1.) Rangarajan, P.; Yang, J.; Bhanu, V.; Godshall, D.; McGrath, J.; Wilkes, G.; Baird, D. *Journal of Applied Polymer Science* **2002**, *85*, 69-83.

(2.) Riggs, D. M.; Shuford, R. J.; Lewis, R. W. *Handbook of composites*; Van Nostrand Reinhold: New York, **1982**; Chapter 11, pp 196-271.

(3.) Bhanu, V. A.; Wiles, K. B.; Rangarajan, P.; Glass, T. E.; Godshall, D.; Sankarpandian, M.; Baird, D. G.; Wilkes, G. L.; Banthia, A. K.; McGrath, J. E. *Abstracts of Papers of the American Chemical Society* **2001**, *222*, U332.

(4.) Gupta, A. K.; Paliwal, D. K.; Bajaj, P. *Journal of Macromolecular Science-Reviews in Macromolecular Chemistry and Physics* **1991**, *C31*, 1-89.

(5.) Min, B. G.; Son, T. W.; Kim, B. C.; Jo, W. H. *Polymer Journal* **1992**, *24*, 841-848.

(6.) Bhanu, V. A.; Rangarajan, P.; Wiles, K.; Bortner, M.; Sankarpandian, M.; Godshall, D.; Glass, T. E.; Banthia, A. K.; Yang, J.; Wilkes, G.; Baird, D.; McGrath, J. E. *Polymer* **2002**, *43*, 4841-4850.

(7.) Rangarajan, P.; Bhanu, V. A.; Godshall, D.; Wilkes, G. L.; McGrath, J. E.; Baird, D. G. *Polymer* **2002**, *43*, 2699-2709.

(8.) Coxe, C. D. Wilmington, DE Patent 2,585,444 **1952**.

(9.) Frushour, B. G. *Polymer Bulletin* **1982**, *7*, 1-8.

(10.) Daumit, G. P., Ko, Y. S., Slater, C. R., Venner, J. G., and Young, C. C. Charlotte, NC Patent 4,921,656 **1990**.

(11.) Daumit, G. P., Ko, Y. S., Slater, C. R., Venner, J. G., Young, C. C., and Zwick, M. M. Charlotte, NC Patent 4,981,752 **1991**.

(12.) Atureliya, S. K.; Bashir, Z. *Polymer* **1993**, *34*, 5116-5122.

(13.) Porosoff, H. Stamford, CT Patent 4,163,770 **1979**.

(14.) DeMaria, F and Young, C. C. Stamford, CT Patent 4,303,607 **1981**.

(15.) Pfeiffer, R. E. and Peacher, S. E. Stamford, CT Patent 4,318,680 **1982**.

(16.) Grove, D.; Desai, P.; Abhiraman, A. S. *Carbon* **1988**, *26*, 403-411.

(17.) Cooper, A.; Howdle, S. *Materials World* **2000**, *8*, 10-12.

(18.) Moore, S.; Samdani, S.; Ondrey, G.; Parkinson, G. *Chemical Engineering* **1994**, *101*, 32.

(19.) Garg, A.; Gulari, E.; Manke, C. W. *Macromolecules* **1994**, *27*, 5643-5653.

(20.) Shieh, Y. T.; Su, J. H.; Manivannan, G.; Lee, P. H. C.; Sawan, S. P.; Spall, W. D. *Journal of Applied Polymer Science* **1996**, *59*, 707-717.

(21.) Shieh, Y. T.; Su, J. H.; Manivannan, G.; Lee, P. H. C.; Sawan, S. P.; Spall, W. D. *Journal of Applied Polymer Science* **1996**, *59*, 695-705.

(22.) Bae, Y. C.; Gulari, E. *Journal of Applied Polymer Science* **1997**, *63*, 459-466.

(23.) Gerhardt, L. J.; Manke, C. W.; Gulari, E. *Journal of Polymer Science Part B-Polymer Physics* **1997**, *35*, 523-534.

(24.) Royer, J. R.; Gay, Y. J.; DeSimone, J. M.; Khan, S. A. *Journal of Polymer Science Part B-Polymer Physics* **2000**, *38*, 3168-3180.

(25.) Kwag, C.; Manke, C. W.; Gulari, E. *Journal of Polymer Science Part B-Polymer Physics* **1999**, *37*, 2771-2781.

(26.) Royer, J. R.; DeSimone, J. M.; Khan, S. A. *Journal of Polymer Science Part B-Polymer Physics* **2001**, *39*, 3055-3066.

(27.) Lee, M.; Park, C. B.; Tzoganakis, C. *Polymer Engineering and Science* **1999**, *39*, 99-109.

(28.) Kiran, E.; Gokmenoglu, Z. *Journal of Applied Polymer Science* **1995**, *58*, 2307-2324.

(29.) Koran, F.; Dealy, J. M. *Journal of Rheology* **1999**, *43*, 1279-1290.

(30.) Mackley, M. R.; Marshall, R. T. J.; Smeulders, J. B. A. F. *Journal of Rheology* **1995**, *39*, 1293-1309.

(31.) Royer, J. R.; Gay, Y. J.; Adam, M.; DeSimone, J. M.; Khan, S. A. *Polymer* **2002**, *43*, 2375-2383.

(32.) Mackley, M. R.; Spitteler, P. H. J. *Rheologica Acta* **1996**, *35*, 202-209.

(33.) Wingert, M. J.; Han, X.; Li, H.; Zeng, C.; Lee, L. J.; Tomasko, D. L.; Koelling, K. W. *Proceedings of the Society of Plastics Engineers ANTEC* **2003**.

(34.) Ferry, J. D. *Viscoelastic properties of polymers*; Wiley: New York, 1980.

(35.) Chiou, J. S.; Paul, D. R. *Journal of Polymer Science Part B-Polymer Physics* **1987**, *25*, 1699-1707.

(36.) Bortner, M. J. PhD Dissertation. Virginia Polytechnic Institute and State University; **2003**.

(37.) Luxenburg, L. A.; Baird, D. G.; Joseph, E. G. *Biotechnology Progress* **1985**, *1*, 33-37.

(38.) Macosko, C. W. *Rheology: principles, measurements, and applications*; VCH: New York, NY, **1994**.

(39.) Bird, R. B.; Armstrong, R. C.; Hassager, O. *Dynamics of polymeric liquids v.1: Fluid mechanics*; Wiley: New York, **1977**.

(40.) Ferry, J. D. *Viscoelastic properties of polymers*; Wiley: New York, **1980**.

(41.) van Krevelen, D. W. *Properties of polymers: their correlation with chemical structure, their numerical estimation and prediction from additive group contributions*; Elsevier: Amsterdam, **1990**.

(42.) Sanchez, I. C.; Lacombe, R. H. *Macromolecules* **1978**, *11*, 1145-1156.

(43.) Baird, D. G.; Collias, D. I. *Polymer processing: principles and design*; Wiley: New York, **1998**.

(44.) Brandrup, J.; Immergut, E. H. *Polymer handbook*; Wiley: New York, **1989**.

(45.) Kiran, E.; Xiong, Y.; Zhuang, W. H. *Journal of Supercritical Fluids* **1993**, *6*, 193-203.

6.0 Effects of AN Content on CO_2 Plasticization

Preface

This chapter addresses research objective 2, and is organized as a manuscript for publication. Specifically, the effects of acrylonitrile (AN) content on the absorption of CO_2 and subsequent viscosity reduction are analyzed.

Absorption of CO_2 in High Acrylonitrile Content Copolymers: Dependence on Acrylonitrile Content

Michael J. Bortner[1], Vinayak A. Bhanu[2], James E. McGrath[2], and Donald G. Baird[1]

[1]*Department of Chemical Engineering and Center for Composite Materials and Structures*
[2]*Department of Chemistry*
Virginia Polytechnic Institute and State University
Blacksburg, VA 24061-0211

Abstract

In continuation of our goal to determine the ability of CO_2 to plasticize acrylonitrile (AN) copolymers and facilitate melt processing at temperatures below the onset of thermal degradation, a systematic study has been performed to determine the influence of AN content on CO_2 absorption and subsequent viscosity reduction. Our previous report focused on the absorption of CO_2 in a relatively thermally stable 65 mole percent AN copolymer. In this study, the ability for CO_2 to absorb in AN copolymers containing 85-98 mole percent acrylonitrile was determined, and subsequent viscosity and equivalent processing temperature reductions were evaluated. 85 and 90 mole percent acrylonitrile/methyl acrylate (AN/MA) copolymers were found to absorb up to 5.6 and 3.0 weight percent CO_2, corresponding to reductions of T_g of 37 and 27^oC, and subsequent viscosity reductions of 61 and 56 %, respectively. CO_2 absorption in these copolymers was found to occur immediately, in contrast to the time dependent absorption observed in the 65 mole % copolymer. An Arrhenius scaling analysis was used to determine the equivalent reductions in processing temperature resulting from the viscosity reductions, and reductions of up to 25 and 9^oC were observed for the 85 and 90 mole % AN copolymers. Based on the specific conditions used for absorption, no significant CO_2 uptake was observed for AN copolymers containing greater than 90 mole percent acrylonitrile. Higher temperatures than

those used here may be required to absorb CO_2 into AN copolymers containing greater than 90 mole % AN.

6.1 Introduction

The need exists for a less expensive and environmentally benign process for producing AN copolymer fibers suitable for use as carbon fiber precursors and textiles[1]. Melt processing AN copolymers could potentially provide a less expensive and more environmentally friendly process as compared to solution spinning by increasing solids throughput on a per pound basis and eliminating the need for solvent use and recovery[2]. But because high AN content (greater than about 85 mole percent AN) copolymers undergo a rapid crosslinking and cyclization reaction at a temperature of 220°C, AN copolymer fiber precursors are conventionally produced using a solution spinning process. Toxic, organic solvents, including dimethyl formamide and dimethyl acetamide, are usually used in the ratio of 70-93 weight percent solvent to process AN/MA copolymers of high AN content (greater than about 85 mole percent AN) into their desired fiber form[3]. Viscosities for these high AN content copolymers can become suitable for melt processing when temperatures of approximately 220°C are approached[2]. However, at 220°C the kinetics of the crosslinking reaction become rapid, rendering these high AN content copolymers intractable prior to extrusion into fiber form[4]. If the temperature is lowered to 200°C, the kinetics of the crosslinking reaction are very slow, resulting in minimal crosslinking and cyclization during extrusion, but the pure AN/MA copolymer viscosities are generally too high for melt processing at these temperatures[2].

Numerous attempts have been made with varying degrees of success to melt process AN copolymers. Water and mixtures of acetonitrile, methanol, and water[5-8] have been investigated to plasticize AN copolymers, facilitating precursor extrusion into fiber form at temperatures

below the onset of thermal degradation. Large plasticizer contents (25-45 weight percent) were required and the acetonitrile had to be recovered because it degrades into cyanide at relatively low temperatures, resulting in a process that had little economic benefit over solution spinning when commercial production rates (~$2x10^6$ lb per year) were reached. Tailored AN/MA copolymers have also been investigated for melt processable PAN copolymer precursors, but 85 mole % AN was the maximum that could be utilized before the kinetics of degradation became significant and prevented melt processing[9]. Advantages and disadvantages of these acrylic melt processing studies were discussed in detail in a recent paper[10].

Carbon dioxide (CO_2) has been studied as a plasticizer to reduce the viscosity of a number of thermoplastic polymers, including polydimethylsiloxane, polystyrene, polypropylene, low-density polyethylene, poly(methyl methacrylate), and poly(vinylidene fluoride). Only a few studies have focused on the ability to absorb CO_2 into a polymer and measure the subsequent viscosity reduction[11-20]. The plasticizing ability of CO_2 in these polymers and the measurement techniques were presented in a recent paper[10]. In general, low levels of absorbed CO_2 (about 6 weight % or less) were observed to reduce the viscosity of the majority of the thermoplastics studied by up to 80 percent. Viscosity reductions and scaling predictions were reported for the thermoplastics containing absorbed CO_2, but the studies did not focus on the use of CO_2 to reduce the processing temperatures of acrylic copolymers or any other thermally unstable polymers.

We recently reported the use of carbon dioxide as a plasticizer to reduce the viscosity of a 65 mole percent acrylic copolymer[10]. Low levels of absorbed CO_2 (6.7 weight percent) were shown to reduce the glass transition temperature (T_g) up to 31^oC and viscosity up to 60% over the range of shear rates tested. The viscosity of the 65 mole % AN copolymer containing

absorbed CO_2 at 180°C was observed to be the same as the pure copolymer viscosity at 210°C, suggesting that the plasticized copolymer could be processed at 30°C below the processing temperature of the pure copolymer[10]. Plasticization of the 65 mole % AN copolymer with CO_2 provided a framework to establish a relationship between the T_g reduction, CO_2 absorption level, viscosity reduction, and equivalent processing temperature reduction obtainable for acrylic copolymers using CO_2 as a plasticizer.

The ability for CO_2 to plasticize high AN content AN/MA copolymers, suitable for use in textile and carbon fiber precursors (containing 85 mole percent or greater AN), has not been investigated. The goal of this paper is to establish a relationship between AN content and the ability of the copolymer to absorb CO_2, and the subsequent effect of CO_2 to plasticize and reduce the viscosity of the acrylonitrile copolymers (suitable for use as textile and carbon fiber precursors). Furthermore, the goal is to determine whether the processing temperature can be lowered enough to prevent the onset of thermal degradation. The role of AN content on the ability to absorb CO_2 was measured via differential scanning calorimetry (DSC), used to measure the T_g reduction, and thermogravimetric analyses (TGA), used to measure the weight percent of absorbed CO_2. Viscosity effects resulting from CO_2 absorption were measured using a capillary rheometer modified to apply static pressures at the capillary exit. Equivalent processing temperature differences between the plasticized and pure copolymers were determined using an Arrhenius scaling analysis and related to the amount of absorbed CO_2 as a function of AN content.

6.2 Experimental

6.2.1 Materials

Acrylonitrile/methyl acrylate (AN/MA) copolymers containing 85, 90, 93, 95, and 98 mole percent AN were utilized in this study. The 85/15 mole percent AN/MA copolymer was produced via a heterogeneous free radical (emulsion) polymerization by Monomer Polymer, Inc. of Feastersville, PA, which was based on research by Bhanu and coworkers[9] and somewhat different than for solution and suspension polymerizations. The 85/15 AN/MA copolymer was produced in a one kg quantity, of which approximately 50 grams were available for our measurements in this study. The kinetics of crosslinking was insignificant (crosslinking was minimal) at 200^{o}C, and the copolymer exhibited a stable steady shear viscosity at this temperature for at least 30 minutes, facilitating viscosity measurements without interfering effects of crosslinking. The 90/10 mole percent AN/MA copolymer was an extrudable grade material produced by BP/Amoco named Amlon. Amlon was developed as a melt processable AN precursor containing less than one mole percent of a stabilizer, but is no longer produced, and as a result only a small quantity (roughly 100 grams) of the copolymer was obtained for our measurements. Possibly because of an unknown stabilizer, Amlon exhibited a stable steady shear viscosity at 220^{o}C for minimally 30 minutes, also facilitating viscosity measurements. The 93, 95, and 98 mole percent AN copolymers were synthesized by a free radical homogeneous (solution) polymerization via the methods discussed in detail by Bhanu et. al.[9]. Kinetics of crosslinking for these AN copolymers was found to be significant, with crosslinking occurring rapidly at 220^{o}C. All of the materials were in powder form except for the Amlon, which was in the form of 3.2 mm diameter pellets with 6.4 mm length.

AN/MA molar ratio	Intrinsic Viscosity (NMP/25°C)	M_n (GPC, g/mol)	M_w (GPC, g/mol)
85/15	0.50	26,500	65,900
90/10	0.5	18,000	55,000
93/7	0.26	N/A	N/A
95/5	0.25	N/A	N/A
98/2	0.25	N/A	N/A

Table 6.1: Intrinsic viscosity and molecular weight data for the AN/MA copolymer samples.

Intrinsic viscosities and molecular weights (if available) for each sample are indicated in Table 6.1. Intrinsic viscosities were measured using a Cannon Ubbelhode viscometer. Absolute molecular weight measurements from gel permeation chromatography (GPC) were obtained at 60°C with a Waters 2690 Separation Module equipped with a differential refractometer detector and an on-line differential viscometric detector (Viscotek T60A) coupled in parallel. NMP containing 0.2 M P_2O_5 was used as a solvent. Sufficient samples were not available to obtain GPC data for the 93, 95, and 98 mole % AN copolymers.

2.2 Sample preparation

The samples that were in powder form were compression molded into pellets of similar size to the 90/10 AN/MA copolymer to ensure that the CO_2 absorption experiments would be performed on samples of equal dimension to the 90/10 copolymer pellets. Diffusion has been shown to be the limiting factor for CO_2 permeability into AN polymers, and as a result the powder samples (possessing a smaller diffusion length) were expected to absorb CO_2 more rapidly than the pellets for a given time scale[21]. It was found that the 85, 93, 95, and 98 mole % AN samples, which were all in powder form, could be molded into pellets at temperatures between 180-200°C in 5 minutes or less. We believe that compression molding at these temperatures permitted preparation of sample pellets for thermal analyses without significant crosslinking (thermal degradation).

Larger quantities of pellets (15-20 grams) were prepared for viscosity measurements of the 85/15 AN/MA copolymer by extrusion into fiber form using a capillary rheometer at 200°C (residence time no greater than 15 minutes). The fibers were then chopped into pellets of similar size to the 90/10 AN/MA copolymer with a pelletizer. The thermal history imparted as a result

of fiber extrusion and pelletization was not a problem because this material was shown to be thermally stable at 200°C for at least 30 minutes[22].

The copolymer pellets were saturated with CO_2 in a sealed, constant volume, pressurized bomb for various amounts of time. A Parr Instruments model 4760 pressure vessel was used to saturate the samples. For the thermal analyses, approximately one gram of polymer was saturated for each test. For the viscosity measurements, approximately 20 grams of polymer were saturated. The pressure vessel was initially charged with CO_2 at room temperature in the form of a high pressure gas at 5.86 MPa, and then heated to 120°C, which increased the pressure to 10.3 MPa. It was necessary to use a saturation temperature above the T_g of the copolymers (ranging from 84-100°C) to increase free volume and ensure dispersion of the CO_2 into the polymer. 120°C was chosen as the soak temperature because it is above the T_g of the copolymers but below the temperature at which significant crosslinking begins to occur. Higher temperatures resulted in thermal degradation of the AN copolymers over the time scale used for the saturations. The sample was then held at 120°C for various amounts of time, corresponding to the "soak time" for the CO_2 absorption. Following the soak time, the pressurized bomb was cooled to room temperature via forced convection. Once cooled to room temperature, the pressure vessel was decompressed over the course of 12 minutes, corresponding to a decompression rate of 8200 Pa/s. The entire heating and cooling process will later be referred to as the "cycle time" of saturation, which does not include the soak time at 120°C.

Further high pressure saturations were performed in a similar manner. Following the batch pressurization and heating to 120°C (corresponding to 10.3 MPa), a Trexel TR-1-5000L high pressure CO_2 pump was used to directly inject liquid CO_2 into the heated pressure vessel and raise the pressure to 17.2 MPa. This pressure was chosen as the upper limit so that

reasonable pressures could be maintained in future extrusion studies. The absorption abilities of both the 85/15 and 90/10 AN/MA copolymer samples were tested at the 10.3 and 17.2 MPa soak pressures. Limited quantities of the three highest AN content samples (93/7, 95/5, and 98/2) were available, and the absorption behavior was only measured at one set of saturation conditions (10.3 MPa saturation pressure).

6.2.3 Differential Scanning Calorimetry

A Seiko model 220 differential scanning calorimeter (DSC) and a TA Instruments model 2920 modulated DSC were used to make the DSC measurements. Heating and cooling rates of 10°C/min were used. A nitrogen purge was used during measurements in both DSC units. Aluminum pans with pierced lids were used to hold the 5-10 mg samples. The use of pierced lids allowed the escape of the absorbed CO_2.

Two heats were performed on each sample. The first heat allowed direct visualization of the T_g reduction resulting from absorbed CO_2. The second heat verified that no residual CO_2 was present, which was confirmed if the T_g of the pure material was obtained. Samples containing absorbed CO_2 were cooled to -20°C to further prevent any degassing prior to running the thermal scan, as well as to establish a baseline for easy visualization of the T_g of the plasticized copolymers. The test comprised heating from -20°C to 180°C to ensure that all CO_2 had flashed out of the system, cooling back to -20°C, and then performing the second heat.

6.2.4 Methods

Thermogravimetric analyses (TGA) and viscosity measurements (obtained with the pressurized capillary rheometer) of the AN copolymers containing absorbed CO_2 were performed in the same manner as described in a recent paper on the 65 mole % AN copolymer[10]. A capillary of diameter 0.027" and an L/D of 111 was used for the viscosity testing so that entry

pressure corrections were not necessary. The actual pressure drop across the capillary (ΔP) was measured as the difference between the upstream force measured by the Instron load cell to push the polymer through the capillary (ΔP_{total}) and the applied static pressure (ΔP_{static}). Pressure drops were calculated as defined in Eq. 6.1:

$$\Delta P = \Delta P_{total} - \Delta P_{friction} - \Delta P_{static} \qquad (6.1)$$

where $\Delta P_{friction}$ is the correction to account for the friction imposed by the plunger seal. The measured entry pressures for the 65 mole % copolymer accounted for approximately 5 percent or less of the total measured pressure drop when tested with this capillary, and accordingly entry pressures corrections were not necessary[22]. This also facilitated viscosity testing of both pure and plasticized copolymers with the small amounts of materials available. Because entry pressure was not accounted for in the viscosity calculations, apparent viscosities are reported with which the shear stress was calculated with the pressure drops obtained from Eq. 6.1. The viscosities were otherwise calculated as in a recent paper[10].

6.2.5 Dynamic Oscillatory Shear Viscosity Measurements

Complex viscosity measurements were performed using a Rheometrics RMS 800 Mechanical Spectrometer. Samples in powder form were compression molded into circular disks of 25.0 mm diameter and 1.0 mm thickness using a press at room temperature. The 90 mole percent AN copolymer, which was the only sample in pellet form, was compression molded into circular disks of the same dimensions at 210°C. Frequency sweeps were made over the range of 0.1-100 rad/s using 25.0 mm parallel plates and 1% strain. Temperatures in the range of 190-230°C were used for the 85/15 AN/MA copolymer, and 225-240°C were used for the 90/10 AN/MA copolymer. Higher temperatures resulted in significant degradation before the measurements could be completed, which take approximately 7 minutes for the frequency range

used. In order to minimize degradation during viscosity measurements, angular frequencies below 0.1 rad/s were not used because of the length of time required to obtain data. Strain sweeps were performed on both the 85 and 90 mole % AN copolymers to determine the linear viscoelastic range of response, and both samples were shown to be linear up to 10% strain[22]. Dynamic oscillatory shear viscosity measurements were only performed on pure copolymers that did not contain absorbed CO_2.

6.3 Results and Discussion

In the following sections, the effect of AN content on the ability to absorb CO_2 using saturation methods described earlier is determined. Viscosity measurements on the 85/15 and 90/10 AN/MA copolymers, both pure and containing absorbed CO_2, are used to determine the ability to reduce the processing temperatures for these materials. The results are compared with the data obtained for the 65 mole % AN copolymer to establish the effects of AN content on the ability of AN copolymers to absorb CO_2 and exhibit a viscosity reduction.

6.3.1 Thermal Analysis

Differential scanning calorimetry (DSC) and thermogravimetric (TGA) analyses were used to determine the reduction of T_g as a function of the amount of absorbed CO_2 for a given soak time and pressure for each sample. Thermal analysis data were then compared between samples to establish a relationship between the AN content and both the amount of absorbed CO_2 and T_g reduction. DSC and TGA data reported in a recent paper on the 65 mole % copolymer were also incorporated to cover the range of 65-98 mole % AN[10].

Thermal analysis data for the 85/15 and 90/10 AN/MA copolymers are shown in Figs. 6.1 and 6.2. The data in Fig. 6.1 represent the DSC scans of the 85/15 and 90/10 AN/MA copolymers saturated at 120^{o}C and both the 10.3 and 17.2 MPa soak pressures, and the TGA

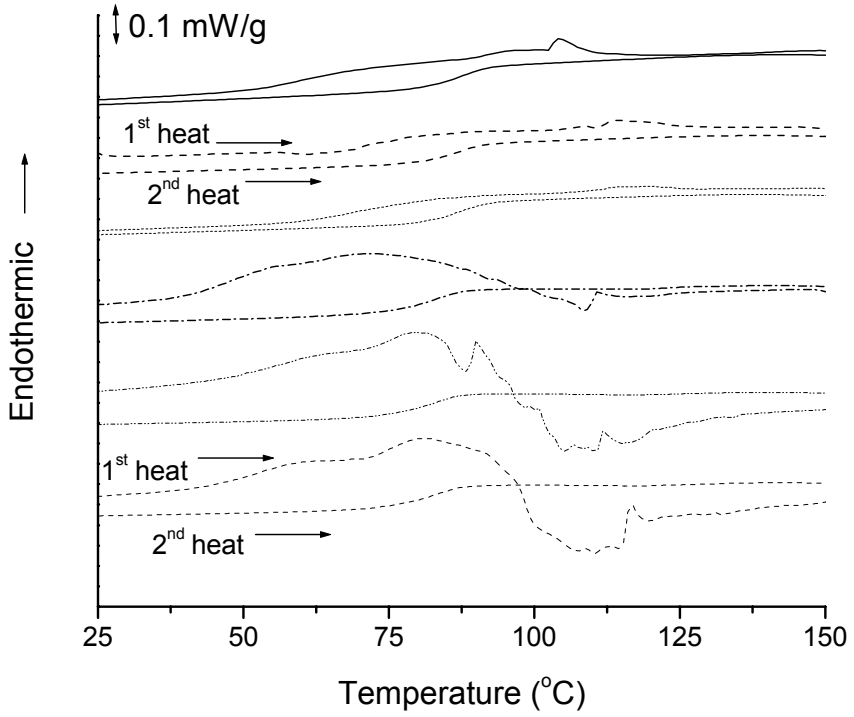

Fig. 6.1: DSC scans of 90/10 and 85/15 AN/MA copolymers containing between 1.8-5.6 wt. % absorbed CO_2. Saturations were performed at 120°C. From top to bottom: 90/10 samples: (—) 6 hr, 17.2 MPa; (— —) 6 hr, 10.3 MPa; (---) 0 hr, 10.3 MPa; 85/15 samples: (— - —) 6 hr, 17.2 MPa; (— - - —) 6 hr, 10.3 MPa; (-----) 0 hr, 10.3 MPa.

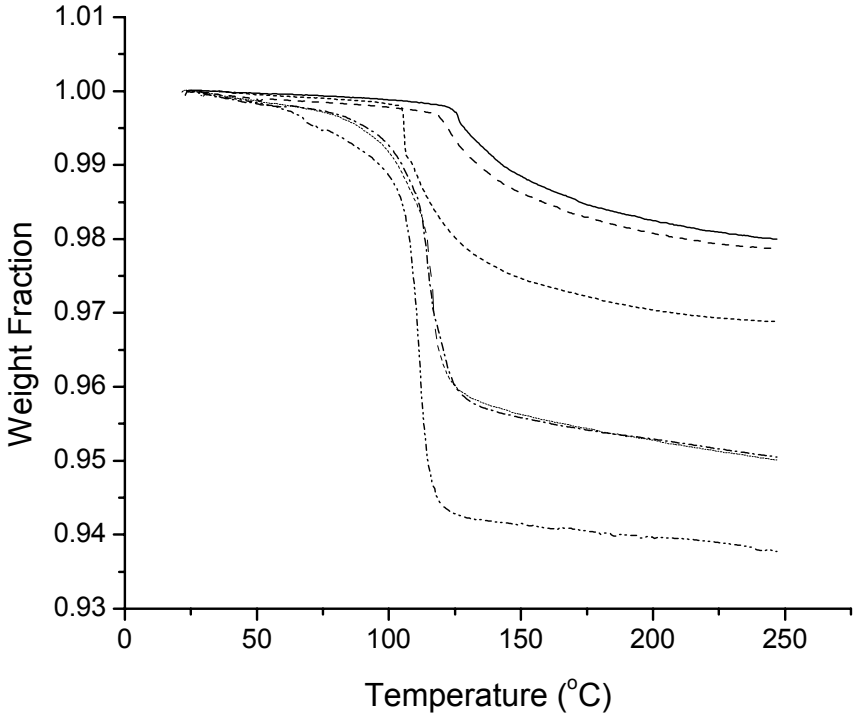

Fig. 6.2: TGA of 90/10 and 85/15 AN/MA copolymers containing 1.8-5.6 wt. % absorbed CO_2. Saturations were performed at 120°C. From top to bottom: 90/10 samples: (—) 0 hr, 10.3 MPa; (— —) 6 hr, 10.3 MPa; (---) 6 hr, 17.2 MPa; 85/15 samples: (- - -) 0 hr, 10.3 MPa; (— - —) 6 hr, 10.3 MPa; (— - - —) 6 hr, 17.2 MPa. 0 and 6 hour saturations overlap for the 85/15 copolymer.

results in Fig. 6.2 provide the corresponding amount of absorbed CO_2 for each saturation. DSC data were collected for both heats and are shown in Fig. 6.1 for easy visualization of the T_g difference between the plasticized and pure copolymers (meaning pure in the sense that no residual CO_2 remains). The first heat of the polymer containing CO_2 is represented by the upper curve for each sample, and the second heat (following cool down) is represented by the lower curve. The DSC and TGA data for the 6 hr., 10.3 MPa saturation at 120°C indicate reductions of T_g up to 30 and 17°C, corresponding to 4.3 and 2.0 weight percent absorption, for the 85 and 90 mole % AN copolymers, respectively. Van Krevelen's relationships were used in a similar manner to that reported in a previous paper[10] to predict the expected wt. % of CO_2 absorption using these saturation conditions. For the 1500 psi saturation at 120°C, 4.8 wt. % CO_2 was expected to absorb in the copolymers, which is close to experimentally measured value for the 85 mole % copolymer, but about twice the value measured for the 90 mole % copolymer.

The thermal analysis data for the 10.3 MPa saturation suggest that the majority of CO_2 absorption occurs very quickly in the high AN content copolymers. DSC data for the 0 hour saturation ("cycle time") is shown for the 90 mole % copolymer in Fig. 6.1, which indicate the same reduction of T_g (17°C in both cases) as for the sample with a 6 hr. soak time under the same saturation conditions. The 0 hour "cycle time" saturation of the 85 mole percent copolymer resulted in a 30°C reduction of T_g, also identical to that obtained for the 6 hour saturation[22]. In a recent paper, absorption of CO_2 in the 65 mole % AN copolymer was found to be dependent on the length of the soak time at the saturation conditions. The results for the 85 and 90 mole percent AN copolymers suggest, unlike the 65 mole % AN copolymer in our previous study, that the majority of the CO_2 absorption occurs almost immediately, with minimal additional absorption occurring over long saturation times. These results are confirmed for both the 85 and

90 mole % copolymer by the TGA data in Fig. 6.2, which show that the 85 mole percent copolymer absorbed 4.3 wt. % CO_2 for both the 0 and 6 hr. soak time, and that only an extra 0.2 wt. % CO_2 is absorbed in the 90 mole percent copolymer after the 6 hr. soak time.

DSC and TGA data are also shown for the 17.2 MPa saturations for both the 85 and 90 mole percent AN copolymers. Raising the saturation pressure to 17.2 MPa increased the reductions of T_g to 37 and 27^{o}C, corresponding to 5.6 and 3.0 weight % absorption for the 85/15 and 90/10 copolymers, respectively, at the 6 hour, 120^{o}C saturation. The absorption level predicted by Van Krevelen's relationships was 12.6 wt. % for these saturation conditions, which is between 2-4 times the experimentally observed absorption values for the 85 and 90 mole % copolymers. Only the 6 hour saturations were performed, primarily because data from a recent paper suggest that no significant absorption would have been observed over longer soak times [22]. We also wanted to minimize any chance of thermal degradation occurring in the polymers, as well as maintain a basis for comparison to the 65 mole % copolymer, with which the 6 hour saturation times were utilized. As previously discussed, shorter soak times could probably have been used to obtain comparable results, but consistency was maintained between our studies by utilizing the 6 hour saturation. The TGA data in Fig. 6.2, in conjunction with the TGA data for the 65 mole % AN copolymer from a recent paper[10], indicate that the amount of absorbed CO_2 decreases as the AN content is increased for the saturation conditions utilized in this study. However, the data suggest that the corresponding reductions of T_g may pass through a maximum at an AN content between 65 and 90 mole percent AN. Up to a 37^{o}C reduction was obtained for the 85/15 copolymer, but only a 31^{o}C reduction was obtained for 65 mole % copolymer and only a 27^{o}C reduction was obtained for the 90 mole % AN copolymer.

Copolymers containing greater than 90 mole % AN were not observed to absorb CO_2 to any significant extent with the saturation methods used in this study. DSC scans following a 6 hour, 10.3 MPa saturation at 120°C are shown in Fig. 6.3 for the 93, 95, and 98 mole percent AN copolymers. The data indicate that no reduction of T_g or absorption of CO_2 is observed using our saturation conditions for these copolymers (containing greater than 90 mole percent AN). We speculate that a critical copolymer ratio exists at approximately 10 mole % copolymer, at which the dipole-dipole interactions of the pendant nitrile groups generate strong intermolecular forces and significantly decrease the free volume of the copolymer. The existence of a critical copolymer ratio was also suggested by Rangarajan et al.[2]. We anticipate that higher saturation temperatures, obtained by direct injection of CO_2 into the copolymer melt, would generate enough free volume to facilitate CO_2 absorption, and will be addressed in future work.

6.3.2 Viscosity Reduction

Viscosity reductions of the 85 and 90 mole percent AN copolymers were measured for comparison to those observed in a previous paper for the 65 mole % AN copolymer to establish a relationship between potential viscosity reductions with our saturation methods and the AN content. Viscosity versus shear rate data for the 85 mole percent AN copolymer containing 5.6 wt. % CO_2 are compared to the pure copolymer viscosity levels at 200°C in Fig. 6.4. An average viscosity reduction of 61% is observed over the range of shear rates tested. The viscosity reduction is approximately equivalent to that obtained for the 65 mole percent AN copolymer, with which a 60% viscosity reduction was obtained with 6.7 weight percent absorbed CO_2. Only 5.6 wt. % CO_2 was absorbed for the 85 mole % AN copolymer, but approximately the same viscosity reduction was observed.

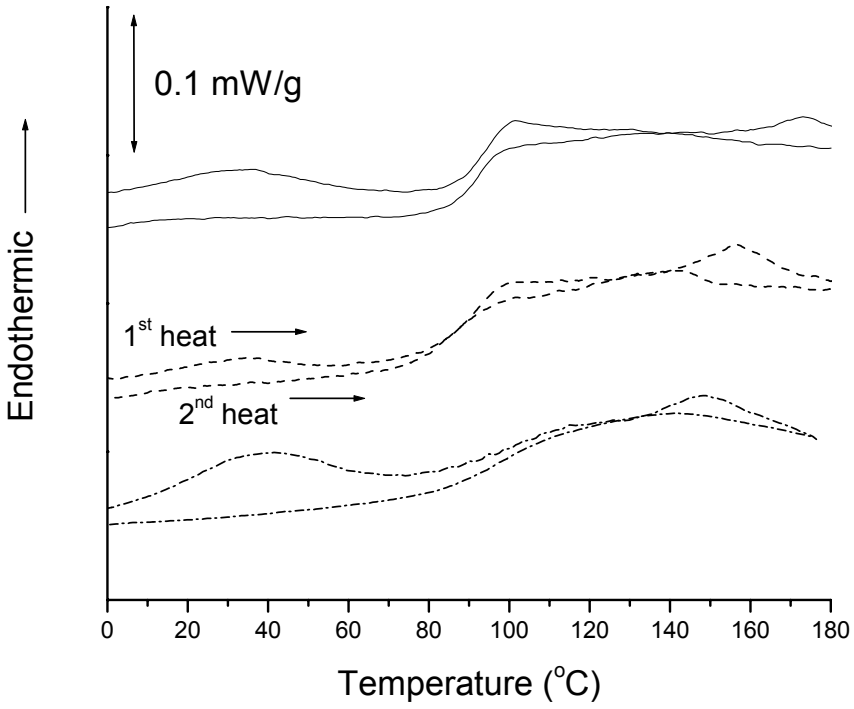

Fig. 6.3: DSC scans of (—) 93/7, (– –) 95/5, and (– - –) 98/2 AN/MA sample saturated at 120°C, 10.3 MPa CO_2 for 6 hours.

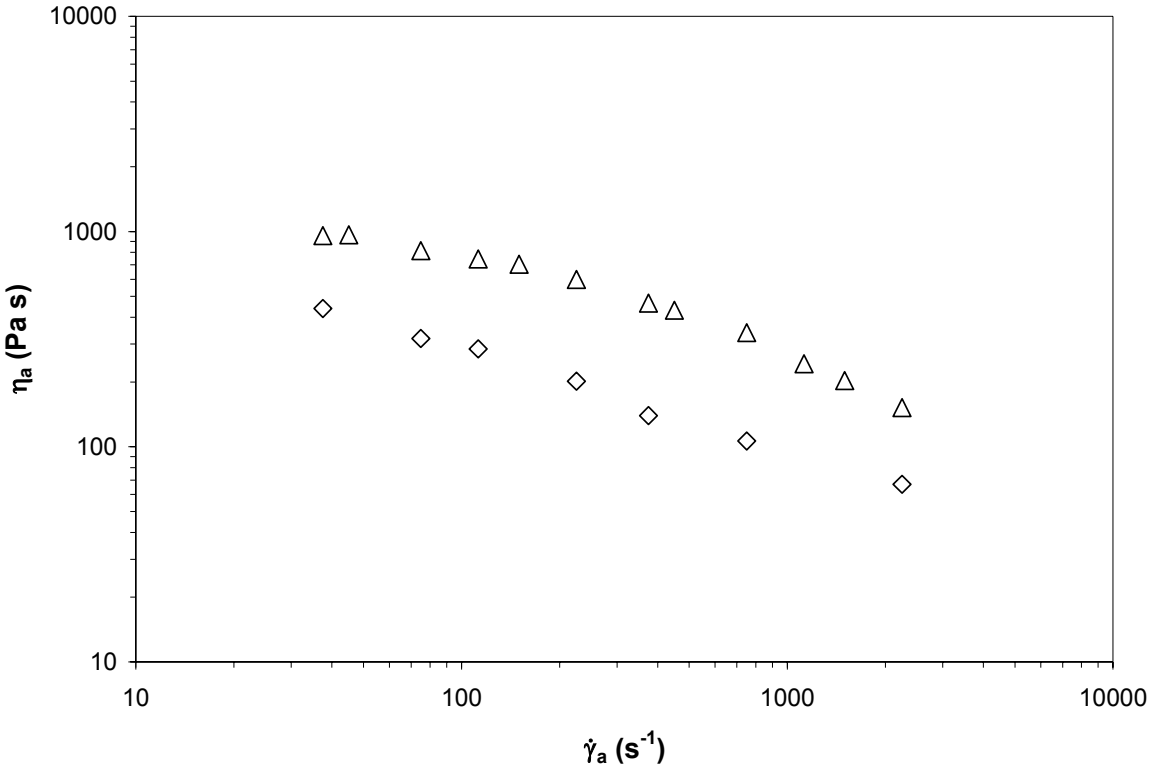

Fig. 6.4: Apparent viscosity versus shear rate for the 85/15 AN/MA copolymer. (△) pure and (◊) plasticized copolymer containing 5.6 weight percent absorbed CO_2. Test temperature 200°C. D = 0.69 mm. L/D = 111.

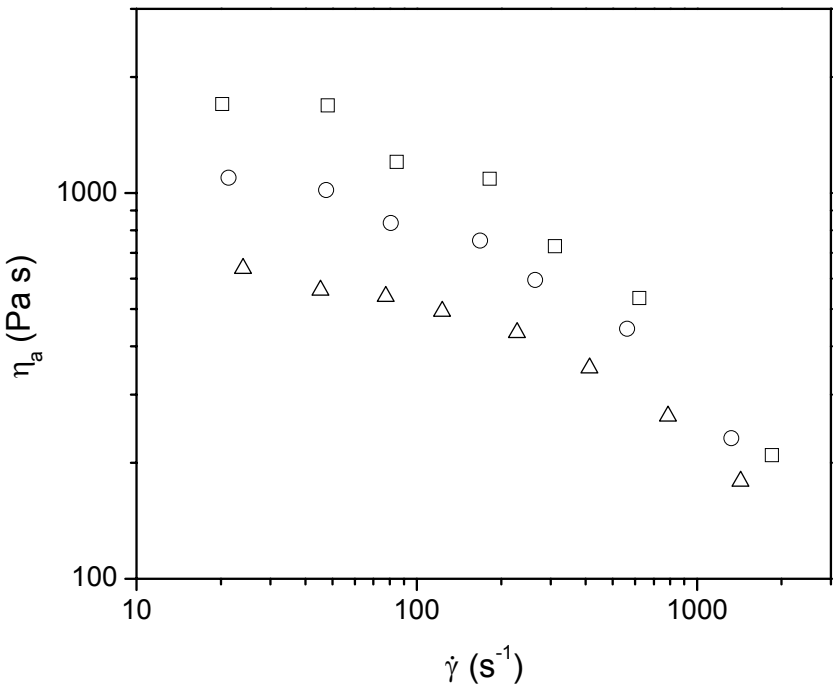

Fig. 6.5: Apparent viscosity versus shear rate for the 90/10 AN/MA copolymer. Data are shown for the (□) pure copolymer and plasticized copolymer containing (○) 2.0 and (△) 3.0 weight percent absorbed CO_2. Test temperature 220°C. D = 0.69 mm. L/D = 111.

Viscosity versus shear rate data for the 90 mole percent AN copolymer containing 2.0 and 3.0 weight percent CO_2 are compared to the pure copolymer viscosity levels at 220^oC in Fig. 6.5. The viscosity versus shear rate curves begin to merge at rates above approximately 400 s^{-1} for both CO_2 absorption levels, corresponding to pressure drops in excess of 70 MPa. Below this pressure, the average viscosity reduction is approximately 31 and 56% for the copolymer containing 2.0 and 3.0 weight % absorbed CO_2, respectively. At pressures in excess of 70 MPa, the range of the viscosity reduction is only 10-15 % and 20-30% for the copolymer containing 2.0 and 3.0 weight percent absorbed CO_2, respectively. As the total pressure drop is increased above 70 MPa, the difference in viscosity between the pure and plasticized copolymer continually decreases within the range evaluated. These trends suggest that pressures above 70 MPa may be causing the viscosity to increase as a result of pressure effects on viscosity for the polymer/CO_2 solution and thereby compensating for the reduction in viscosity due to the plasticizing effect.

It is interesting that a similar viscosity reduction was obtained for the 65, 85, and 90 mole % AN copolymers at the 17.2 MPa saturation pressure, even though different amounts of absorbed CO_2 were present in each sample. The viscosity reduction for all three copolymers was found to be approximately 60%. However, the amount of absorbed CO_2 decreased from 6.7 weight percent for the 65 mole % AN copolymer to 3.0 weight % for the 90 mole % AN copolymer. Similarly, almost identical viscosity reductions of approximately 30% were obtained over the range of shear rates (under 70 MPa) for the 65 and 90 mole % copolymers at the 6 hr, 10.3 MPa soak, which corresponds to 4.7 and 2.0 wt. % absorbed CO_2, respectively. These results suggest that as the AN content is increased, a smaller amount of absorbed CO_2 is required to plasticize the polymer and obtain a comparable reduction in viscosity.

6.3.3 Equivalent Processing Temperature Reductions

In order to determine the ability for small amounts of absorbed CO_2 to reduce the processing temperature, an Arrhenius scaling analysis was used for each absorption level to determine the temperature where the pure copolymer viscosity was equal to that of the plasticized copolymer viscosity. The difference between these two temperatures corresponded to an equivalent processing temperature reduction. This analysis was used because attempts to measure viscosities from the capillary rheometer at elevated temperatures (to obtain an equivalent processing temperature reduction similar to a recent paper[10]) resulted in significant degradation over the rather long (30-45 minute) measurement time. Dynamic oscillatory data collected for the Arrhenius analysis required approximately 7 minutes, in which no significant degradation was observed over the range of temperatures used for these copolymers.

The Arrhenius scaling Eq., which is shown in Eq. 6.2, is often used to describe the dependence of viscosity at temperatures above the upper limit of the WLF Eq. (which is T_g + 100^{o}C):

$$\ln\left(\frac{\eta_T}{\eta_{T_o}}\right)=\left[\frac{E_a}{R}\left(\frac{1}{T}-\frac{1}{T_o}\right)\right] \qquad (6.2)$$

where E_a is the activation energy for the viscous flow, T_o is an arbitrary reference temperature, and R is the ideal gas constant. The viscosity measurements were obtained at 116 and 133^{o}C above the T_g of the 85 and 90 mole percent copolymers, respectively, which are both above the usable temperature range of the WLF Eq.. To determine activation energies of flow, a plot of the viscosities obtained at an angular frequency of 0.1 rad/s was used to generate a plot of η vs. 1/T for each copolymer, and the slope of the plot was used to calculate the activation energy of viscous flow. Dynamic oscillatory shear viscosity measurements obtained for both the 85 and 90

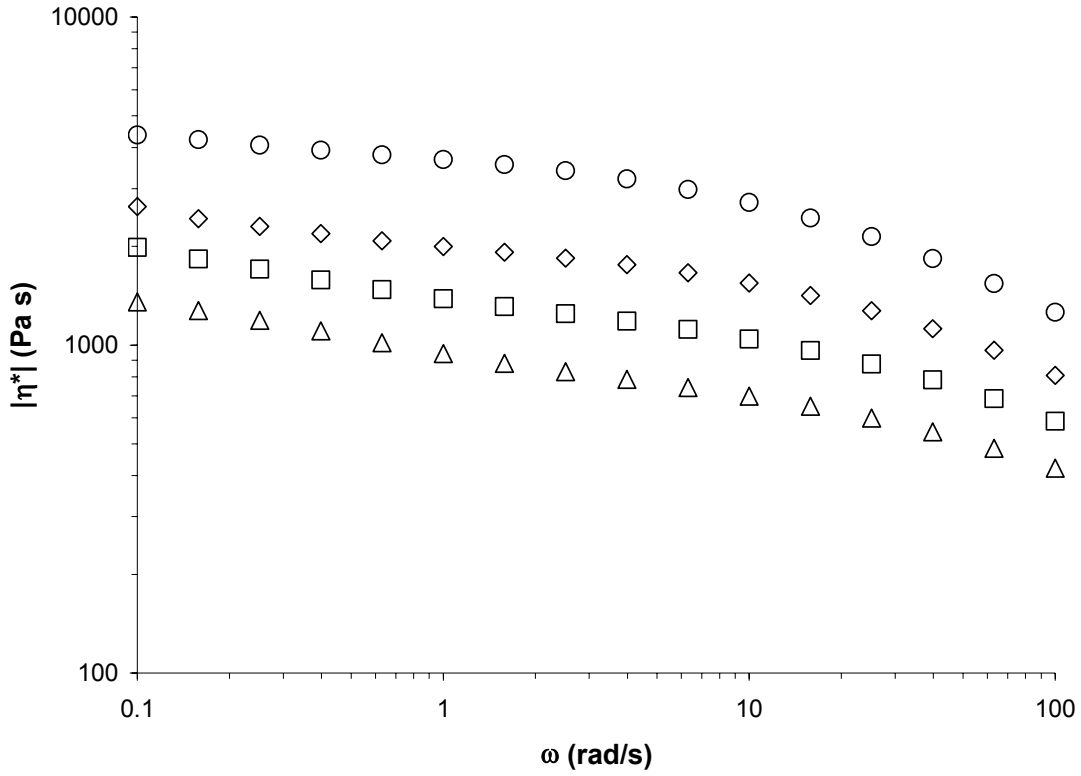

Fig. 6.6: Temperature dependence of the complex viscosity (magnitude) for the 85/15 AN/MA copolymer at (○) 190°C; (◊) 200°C; (□) 210°C; (△) 220°C.

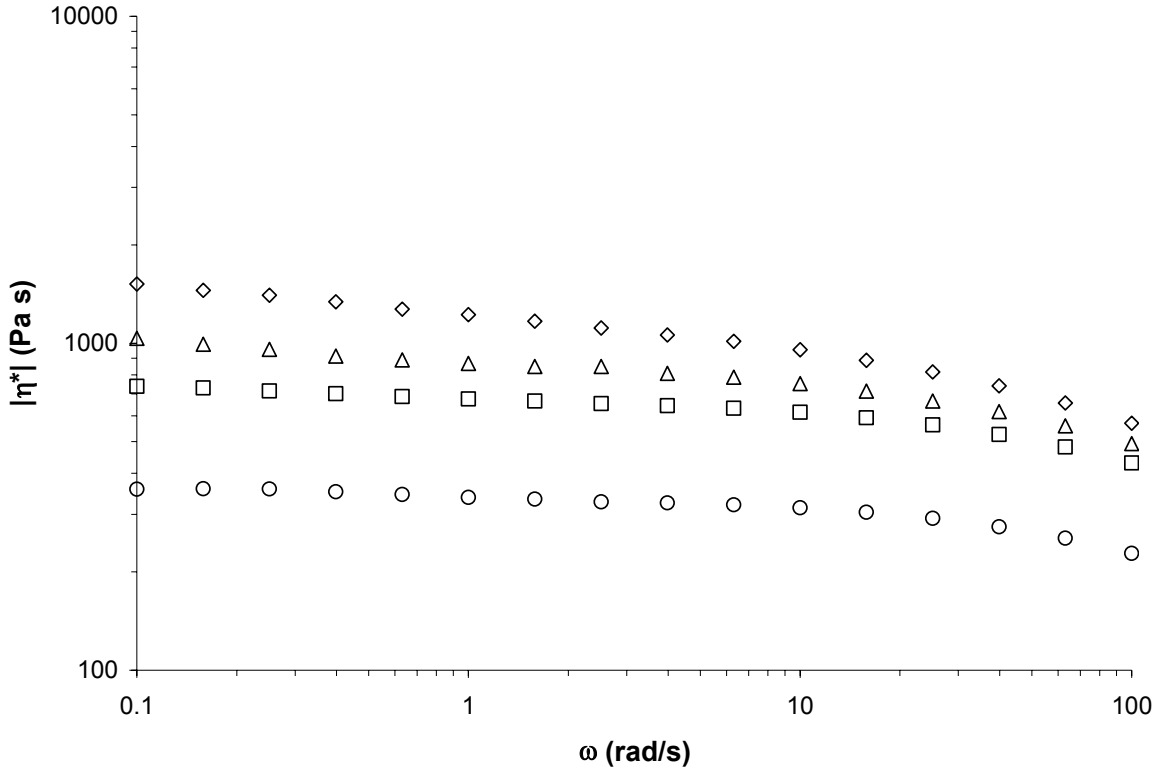

Fig. 6.7: Temperature dependence of the complex viscosity (magnitude) for the 90/10 AN/MA copolymer at (◊) 225°C; (△) 230°C; (□) 235°C; (○) 240°C.

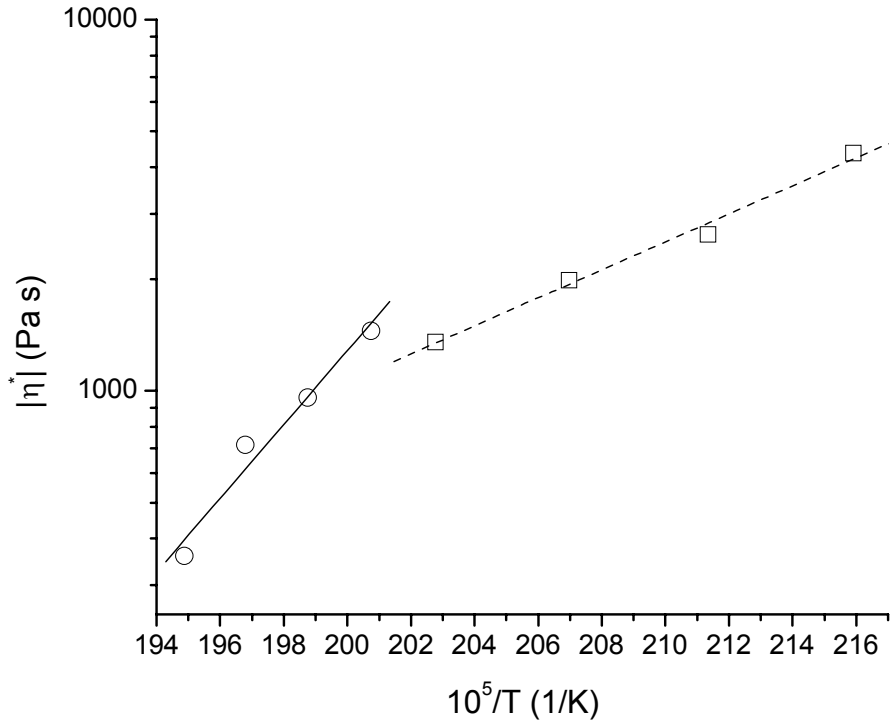

Fig. 6.8: Arrhenius plot to calculate activation energy of flow calculation for the 85/15 and 90/10 AN/MA copolymers. Open symbols are experimental data, lines are linear fits of the data. (□), (—) 85/15 copolymer; (○), (– –) 90/10 copolymer.

mole % AN copolymers at temperatures in the range 190-230°C and 225-240°C, respectively, are illustrated in Figs. 6.6 and 6.7. The data used to calculate the activation energy for the 85 and 90 mole percent copolymers are shown in Fig. 6.8. Activation energies of 8.69 x 10^3 °K and 2.29 x 10^4 °K were determined for the 85 and 90 mole % copolymers, respectively. The activation energy of flow for the 85 mole percent copolymer is comparable to that reported for other thermoplastics, including polypropylene, polyethylene, and polyphenylenesulfide[23]. However, the activation energy for the 90 mole percent copolymer is approximately three times higher than that reported for most thermoplastics[23].

Once the activation energies were calculated, the equivalent processing temperature reductions were determined using Eq. 6.2. Calculations were performed to determine the equivalent processing temperature reductions for three absorption levels: the 85/15 copolymer containing 5.6 wt. % absorbed CO_2, and the 90/10 copolymer containing 2.0 and 3.0 wt. % absorbed CO_2. For each absorption level, the average viscosity reduction obtained over the range of shear rates (from pressurized capillary rheometry) was used to define the ratio (η_T/η_{To}) in Eq. 6.2. T_o was then chosen as the temperature at which the viscosity reductions were measured (with the pressurized capillary rheometer), which was 200 and 220°C for the 85 and 90 mole % copolymers, respectively. The temperature T was then calculated from Eq. 6.2, and the difference between T and T_o corresponded to the equivalent reduction in processing temperature. A temperature difference of 25°C was calculated for the 85 mole percent copolymer containing 5.6 weight percent absorbed CO_2. For the 90 mole percent copolymer, temperature differences of only 4 and 9°C were calculated for the 2.0 and 3.0 weight percent absorptions, respectively. The potential processing temperature reduction obtained for the 85 mole percent copolymer was similar to that obtained for the 65 mole percent copolymer, which we expected because both

materials had similar viscosity reductions. However, the processing temperature reductions for the 90 mole percent copolymer were much lower than expected, primarily because of the exceptionally high value for the activation energy of flow. The complex viscosity data in Fig. 6.7 indicate approximately a six fold drop in viscosity over a 15°C rise in test temperature for the 90 mole % copolymer, which directly correlates to the calculated high value for the activation energy. For comparison, the complex viscosity data for the 85 mole percent AN copolymer in Fig. 6.6 indicate that the viscosity only changes by approximately a factor of 3 over a 40°C temperature range and the range of angular frequencies measured.

6.3.4 Summary of AN content effects

The relationship between the AN content and CO_2 absorption, T_g reduction, viscosity reduction, and equivalent processing temperature reduction are summarized in Table 6.1. The data suggest that the amount of absorbed CO_2 decreases as AN content is increased, at least in copolymers containing greater than 65 mole percent AN. We speculate that less free volume exists, resulting in a reduced ability to absorb CO_2. However, the actual reductions in T_g measured by DSC are not proportional to the levels of absorbed CO_2 measured by TGA, considering that the greatest reduction of T_g was observed for the 85 mole % AN copolymer. This suggests that the T_g reduction may pass through a maximum as a function of AN content between 65 and 90 mole % AN. Even more interesting is that regardless of CO_2 content and reduction of T_g, the 65, 85, and 90 mole percent AN copolymers all exhibit approximately 60 percent viscosity reductions following the 6 hour, 17.2 MPa saturation, which corresponds to 6.7, 5.6, and 3.0 weight percent absorbed CO_2, respectively. Equivalent processing temperature reductions resulting from CO_2 absorption generally decrease as AN content increases, especially between the 85 and 90 mole % copolymers where the equivalent temperature reduction drops

AN content	CO_2 absorption	T_g reduction	Viscosity Reduction	Potential Process T Reduction
(mole %)	(wt. %)	(^oC)	(%)	(^oC)
65	6.7	31	60	30
85	5.6	37	61	26
90	3.0	27	56	9

Table 6.2: Summary of CO_2 absorption experiments on copolymers with AN contents in the range 65-90 mole percent.

from 25 to 9°C, which is a result of the high activation energy of flow for the 90 mole % AN copolymer.

6.4 Conclusions

This study has shown that AN copolymers containing up to 90 mole percent acrylonitrile are plasticized by low levels (2.0-5.6 wt. %) of absorbed CO_2, resulting in a reduction of T_g, viscosity, and (potentially) processing temperature. As AN content is increased, the data suggest that the amount of absorbed CO_2 and equivalent processing temperature reduction decreases. Viscosity reductions over the measured range of shear rates (and below a total pressure drop of 70 MPa) do not appear to depend on AN content up to 90 mole % AN, but rather on the conditions of saturation. The data suggest that reductions of T_g appear to pass through a maximum, possibly around 85 mole percent AN, but sufficient data is not available to confirm this hypothesis. Also, the data suggest that the absorption of CO_2 in high AN content copolymers (85 mole % and greater) occurs immediately, and as a result no soak time is required to absorb CO_2 into the copolymers. These findings will be significant for further studies regarding melt processing of these copolymers.

AN copolymers containing greater than 90 mole percent AN do not absorb CO_2 to any significant extent with our methods of saturation. However, we anticipate that these copolymers (containing greater than 90 mole % AN) can absorb CO_2 and exhibit reductions of T_g and of viscosity if the saturation temperature is increased to temperatures where the free volume of these polymers is significantly increased. This saturation method would have to be performed on a short time scale, and could possibly be performed by direct injection of CO_2 into the copolymer melt in an extruder. Future studies will address the feasibility of direct melt plasticization of AN copolymers containing greater than 90 mole percent acrylonitrile.

6.5 Acknowledgements

The authors wish to thank the U.S. EPA Science to Achieve Results (STAR), program grant #R-82955501-0, and DOE/ORNL Freedom Car Project, program grant # 4500011036 for financial support. Appreciation is also extended to Prof. Dan Edie at Clemson University for supplying the 90/10 AN/MA (Amlon) resin.

6.6 References

(1.) Min, B. G.; Son, T. W.; Kim, B. C.; Jo, W. H. *Polymer Journal* **1992**, *24*, 841-848.

(2.) Rangarajan, P.; Yang, J.; Bhanu, V.; Godshall, D.; McGrath, J.; Wilkes, G.; Baird, D. *Journal of Applied Polymer Science* **2002**, *85*, 69-83.

(3.) Gupta, A. K.; Paliwal, D. K.; Bajaj, P. *Journal of Macromolecular Science-Reviews in Macromolecular Chemistry and Physics* **1991**, *C31*, 1-89.

(4.) Riggs, D. M.; Shuford, R. J.; Lewis, R. W. *Handbook of composites*; Van Nostrand Reinhold: New York, **1982**; Chapter 11, pp 196-271.

(5.) Coxe, C. D. Wilmington, DE Patent 2,585,444 **1952**.

(6.) Porosoff, H. Stamford, CT Patent 4,163,770 **1979**.

(7.) Daumit, G. P., Ko, Y. S., Slater, C. R., Venner, J. G., and Young, C. C. Charlotte, NC Patent 4,921,656 **1990**.

(8.) Daumit, G. P., Ko, Y. S., Slater, C. R., Venner, J. G., Young, C. C., and Zwick, M. M. Charlotte, NC Patent 4,981,752 **1991**.

(9.) Bhanu, V. A.; Rangarajan, P.; Wiles, K.; Bortner, M.; Sankarpandian, M.; Godshall, D.; Glass, T. E.; Banthia, A. K.; Yang, J.; Wilkes, G.; Baird, D.; McGrath, J. E. *Polymer* **2002**, *43*, 4841-4850.

(10.) Bortner, M. J.; Baird, D. G. Absorption of CO_2 and Subsequent Viscosity Reduction of an Acrylonitrile Copolymer. Submitted to *Polymer*, **2003**.

(11.) Gerhardt, L. J.; Manke, C. W.; Gulari, E. *Journal of Polymer Science Part B-Polymer Physics* **1997**, *35*, 523-534.

(12.) Kwag, C.; Manke, C. W.; Gulari, E. *Journal of Polymer Science Part B-Polymer Physics* **1999**, *37*, 2771-2781.

(13.) Royer, J. R.; Gay, Y. J.; DeSimone, J. M.; Khan, S. A. *Journal of Polymer Science Part B-Polymer Physics* **2000**, *38*, 3168-3180.

(14.) Lee, M.; Park, C. B.; Tzoganakis, C. *Polymer Engineering and Science* **1999**, *39*, 99-109.

(15.) Bae, Y. C.; Gulari, E. *Journal of Applied Polymer Science* **1997**, *63*, 459-466.

(16.) Kiran, E.; Gokmenoglu, Z. *Journal of Applied Polymer Science* **1995**, *58*, 2307-2324.

(17.) Koran, F.; Dealy, J. M. *Journal of Rheology* **1999**, *43*, 1279-1290.

(18.) Mackley, M. R.; Marshall, R. T. J.; Smeulders, J. B. A. F. *Journal of Rheology* **1995**, *39*, 1293-1309.

(19.) Royer, J. R.; Gay, Y. J.; Adam, M.; DeSimone, J. M.; Khan, S. A. *Polymer* **2002**, *43*, 2375-2383.

(20.) Royer, J. R.; DeSimone, J. M.; Khan, S. A. *Journal of Polymer Science Part B-Polymer Physics* **2001**, *39*, 3055-3066.

(21.) Chiou, J. S.; Paul, D. R. *Journal of Polymer Science Part B-Polymer Physics* **1987**, *25*, 1699-1707.

(22.) Bortner, M. J. PhD Dissertation. Virginia Polytechnic Institute and State University; **2003**.

(23.) Baird, D. G.; Collias, D. I. *Polymer processing: principles and design*; Wiley: New York, **1998**.

Chapter 7.0: Feasibility of Processing with CO_2

Preface

This chapter addresses research objective 3. The feasibility of processing AN copolymers containing absorbed CO_2 is evaluated by establishing the design equations necessary for a pressure chamber that is used to control bubble nucleation and foaming. Estimates of the chamber size and cooling fluid flow rates are obtained from the resulting system of coupled partial differential equations by decoupling the equations using simplifying assumptions.

7.0 Feasibility of Processing CO_2 Plasticized AN Copolymers

Melt spinning of CO_2 plasticized copolymers in a manner that minimizes foaming requires the design of a pressurized chamber that will allow the fiber to be quenched below its T_g to prevent flashing of the gas. Modeling the system requires the development of the fiber spinning problem via the momentum and continuity Eqs.. Heat transfer occurs simultaneously during the cool down of the fiber to a specified temperature (at or below the T_g of the fiber) and must be accounted for with the thermal energy Eq.. Selection of a suitable pressurizing gas requires an analysis of any mass transfer that takes place in the chamber, which also requires the determination of the amount of CO_2 to be removed from the fiber (if any). The resulting design parameters of the pressure chamber will be determined via a solution of the coupled heat, mass, and momentum transfer equations that describe the fiber spinning operation. In order to formulate and solve the system of equations described above, the operating pressure of the system must first be determined.

7.1 Solubility and Equation of State

A prediction of the required pressures to prevent CO_2 from simply nucleating bubbles and foaming the sample at the die exit is necessary. The desired T_g reduction of the copolymer melt (which is drawn into fiber form in the chamber) governs the concentration of CO_2 required in the fiber. For a desired T_g reduction, a certain pressure is also required to prevent the nucleation of bubbles and consequential foaming from the adsorbed CO_2. A solubility relationship provides the correlation between this pressure required to keep CO_2 from foaming the fiber and the volume fraction of CO_2 in the fiber. The volume fraction can then be directly related to either the weight percent or concentration of CO_2 in the fiber. As a first approximation, the solubility equation in Eq. 7.1 provides the relationship between the pressure required for a

given volume fraction of CO_2 in the fiber, in which the volume fraction can be defined in terms of the weight of adsorbed CO_2 (w_{CO2}) and its density (ρ_{CO2}):

$$\frac{V_{CO_2}}{V_{AN}} = \frac{\frac{w_{CO_2}}{\rho_{CO_2}}}{\frac{w_{AN}}{\rho_{AN}}} = S(T)P \tag{7.1}$$

where w_{AN} and ρ_{AN} are the weight and density of the AN copolymer (estimated as pure AN), P is the pressure required to prevent bubble nucleation, and S(T) is the temperature dependent solubility of CO_2 in the acrylic copolymer. An Arrhenius type expression can be utilized to represent solubility, S(T), as a function of temperature:

$$S = S_0 \exp\left(\frac{-\Delta H_S}{RT}\right) \tag{7.2}$$

where ΔH_S is the molar heat of sorption and S_o is a pre-exponential factor[1]. The molar heat of sorption and pre-exponential terms can be estimated by Van Krevelen's[2] relationships to the Lennard Jones temperature (ε/k) of the gas and the degree of crystallinity (ϕ_c) of the polymer. For elastomers and polymers in the rubbery state, Van Krevelen developed empirical relationships for ΔH_S and S_o in terms of ε/k and for semi crystalline polymer solubility as in Eqs. 7.3-5:

$$10^{-3}\frac{\Delta H_S}{R} = 1.0 - 0.010\frac{\varepsilon}{k} \pm 0.5 \tag{7.3}$$

$$\log S_0 = -5.5 - 0.005\frac{\varepsilon}{k} \pm 0.8 \tag{7.4}$$

$$S_{SC} = S_a\left(1 - \phi_C\right) \tag{7.5}$$

where S_{SC} is the solubility of the semi crystalline polymer based on the solubility of the amorphous polymer (S_a) and the degree of crystallinity. For CO_2, the Lennard Jones temperature is 195.2 K. For this calculation, it will be assumed that the AN copolymer is incompressible, and an average melt density can be used over the desired pressure and temperature range.

As discussed in Chapters 5 and 6, the TGA analyses of CO_2 saturated samples resulted in up to 6.7 weight percent uptake of CO_2 in the AN/MA copolymers. It is believed that direct plasticization of the melt under high pressure in the extruder will result in up to 10 weight percent uptake of CO_2 in the copolymer, resulting in higher T_g reductions. By using an estimated range of 5 to 10 weight percent uptake of CO_2, Eq. 7.1 provides a relationship between the pressure of the system required to prevent foaming (or conversely, the amount of pressure required to get a specified weight fraction of CO_2 into the fiber) and the density of CO_2 at extrusion conditions.

For a pressure determination, a thermodynamic relationship between the pressure and density of the adsorbed CO_2 (in the fiber at extrusion conditions) must be known. The Sanchez-Lacombe equation of state (S-L EOS) is well known to accurately represent polymer systems that are adsorbed with CO_2 in both sub and supercritical forms. The EOS is based on a statistical mechanics derivation and relates pressure, density, and temperature as follows:

$$\frac{\tilde{P}}{\tilde{T}} = -\ln\left(1-\tilde{\rho}\right) - \left(1-\frac{1}{r}\right)\tilde{\rho} - \frac{\tilde{\rho}^2}{\tilde{T}} \qquad (7.6)$$

where $\tilde{P}, \tilde{T}, and\ \tilde{\rho}$ are reduced pressure, temperature, and density, respectively, with respect to characteristic parameters, and r is the number of lattice sites occupied by a molecule of molecular weight M[3]. The reduced variables are defined as follows in Eqs. 7.7-9:

$$\tilde{\rho} \equiv \frac{\rho}{\rho^*} \quad where \quad \rho^* \equiv \frac{M}{r\upsilon^*} \tag{7.7}$$

$$\tilde{T} \equiv \frac{T}{T^*} \quad where \quad T^* \equiv \frac{\varepsilon^*}{R} \tag{7.8}$$

$$\tilde{P} \equiv \frac{P}{P^*} \quad where \quad P^* \equiv \frac{\varepsilon^*}{\upsilon^*} \tag{7.9}$$

For the reduced variables, ε^* is the interaction energy per mer, υ^* is the characteristic volume of a lattice site, and R is the gas constant. The characteristic parameters T*, P*, and ρ* have been optimized for CO_2 in the desired temperature range, and are listed in Table 7.1[4]. Knowing these parameters, an accurate correlation between CO_2 pressure and density can be obtained. For a 5 weight percent CO_2 uptake, a pressure of 1144 psi was calculated for the system. A 10 weight percent uptake, which may be obtainable via high pressure and temperature melt plasticization in the extruder, increases the system pressure to 1617 psi. A table of the calculated parameters is illustrated in Table 7.2. Note units of solubility are cm^3 gas/(cm^3 polymer*Pa). All calculations were performed at 200°C (processing temperature estimate).

component	T* (K)	P* (MPa)	ρ* (g/cm^3)	reference
CO_2	328.1	464.2	1.426	Garg *et al.* (1994)

Table 7.1: Characteristic parameters for use in S-L EOS.

Sanchez Lacombe CO2:					
P^* (MPa)	T^* (K)	ρ^* (g/cm^3)	r	T (K)	P (Pa)
464.2	328.1	1.426	5.25	518	7883337
Van Krevelen CO2:					
ε/k (K)	S_o	$\Delta H_s/R_g$ (K)	S	P (Pa)	
195.2	2.366E-08	-1452	3.903E-07	7883337	

Table 7.2: Calculated parameters for pressure determination.

7.2 Water as a Sealing Fluid

A sketch of the proposed design is illustrated in Figure 7.1. It is desired to use water as the sealing fluid for the pressure chamber. The pressure of the chamber will be higher than the vapor pressure of water at 200°C, so the majority of the water will remain in a liquid state and its density can be treated as such. Therefore, liquid water will be expelled from the chamber through the orifice, which will empty into a water collection bath. A baffle will be installed to prevent water from spraying everywhere. It is desired to keep the water temperature at the temperature of the pressurizing gas, which will be determined based on the amount of CO_2 that can be dissolved into the melt and the resulting T_g reduction, as well as the desired amount of CO_2 to remove from the fiber (which directly affects the T_g). The temperature will be slightly below the T_g of the exiting fiber, currently estimated to be between 60 and 80°C. The chamber will seal around the spinneret pack to prevent loss of water and pressurizing gas from the top of the chamber.

7.3 Macroscopic Mechanical Energy Equation

An important factor in the design is the ratio of the chamber area to the exit area. The cross sectional area of the exit will be much smaller than the cross-sectional area of the pressure chamber. This allows the mean velocity of the water at the top of the pressure chamber to be zero, assuming the chamber is constantly being refilled. As a result, the macroscopic mechanical energy balance can be easily simplified into the following form in Eq. 7.10:

$$\Delta \frac{1}{2} \frac{\left\langle \bar{v}^3 \right\rangle}{\left\langle \bar{v} \right\rangle} + \frac{1}{\rho} \Delta P + \hat{E}_V = 0 \qquad (7.10)$$

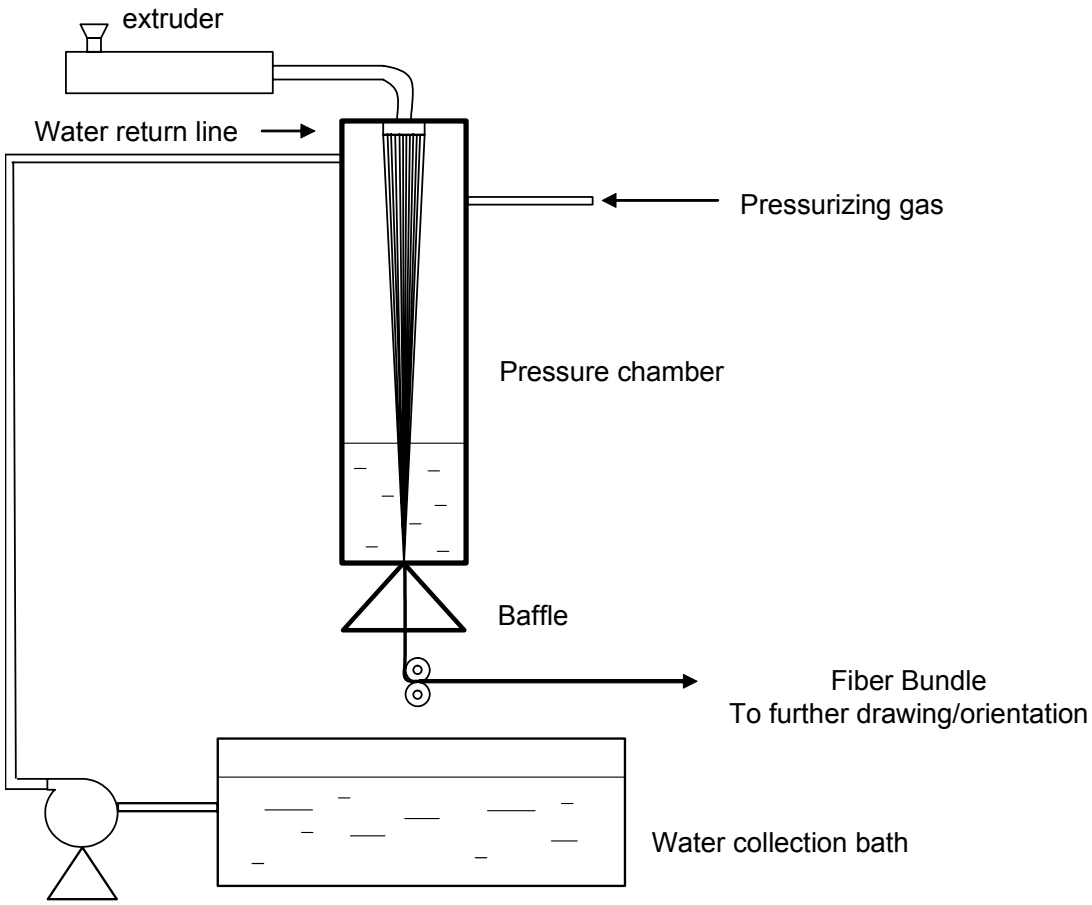

Figure 7.1: Schematic of the pressure chamber design.

where ρ is the density of the sealing fluid and $\hat{E}_V$ is the friction loss factor per unit mass resulting from the contraction at the end of the pressure chamber. The friction loss factor can be represented as follows in Eq. 7.11:

$$\hat{E}_V = \frac{1}{2}\tilde{v}^2 e_v \tag{7.11}$$

where e_v can be represented as seen in Eq. 7.12 for a sudden contraction[5]:

$$e_v = 0.45\left(1 - \left[\frac{R_{orifice}}{R_{chamber}}\right]^2\right) \tag{7.12}$$

The contraction ratio, represented by the ratio of radii between the outlet orifice and the chamber itself, will approach zero and can be reasonably approximated as such. The calculation reveals an estimate for the volumetric flow of water out of the orifice, which for a 5 weight percent uptake of CO_2, is roughly 1948 gal/hr using a 5 mm orifice. This flow rate indicates the rate at which water will also have to be pumped back into the pressure chamber. A flow rate such as this should be easy to maintain with standard pumping equipment and presents itself as a feasible technique. The 5 mm orifice size will easily accommodate a large bundle (easily up to 100 fibers) of 25 μm fibers. It is important to note that the orifice size will need to be carefully implemented because the flow rate is proportional to the square of the radius of the orifice.

In order to determine the length of the chamber, the fiber spinning operation must be modeled. Momentum, heat transfer, and mass transfer must all be accounted for to accurately model the system. Postulating the problem and solving the coupled differential equations will permit the determination of the time necessary to desorb a specified quantity of CO_2 from the

fiber. By knowing the spinning speed of the fiber, a determination of the chamber size can be obtained.

7.4 Equations of Motion

The solution to the fiber spinning problem begins by making postulates about the coordinate dependence of the velocity in both the axial and radial directions (in m/s), temperature (in K), and concentration of CO_2 (c_{CO2}, in g*moles CO_2/cm^3 solution), which are presented in Eqs. 7.13-16:

$$v_z = v_z(r,z) \quad v_r = v_r(r,z) \quad T = T(r,z) \quad c_{CO_2} = c_{CO_2}(r,z) \tag{7.13-16}$$

No tangential (θ) velocity dependence is assumed via a lack of any fiber rotation. The previous assumption requires a symmetric fiber, so a circular fiber will be assumed. It will be assumed that the density is constant, so that fiber's density will be uniform at any given radial or axial fiber distance within a differential element. By the aforementioned assumptions, the continuity equation reduces to Eq. 7.17:

$$\frac{1}{r}\frac{\partial}{\partial r}\left(rv_r\right)+\frac{\partial v_z}{\partial z}=0 \tag{7.17}$$

The mass flow rate, which by conservation of mass must be constant, can also provide the relationship in Eq. 7.18 between fiber density, diameter, and (average) axial velocity:

$$\dot{m} = \rho A(z)\bar{v}_z = \rho\pi R(z)^2\,\bar{v}_z = const. \tag{7.18}$$

where $\bar{v}_z$ is the average axial velocity across the filament cross section. Looking at the equations of motion will provide more information about the velocity profile within the fiber spinning system. It will be assumed that the pressure in the chamber, P, is kept constant and

gravitational forces will be considered negligible (i.e. vertical fiber spinning operation). By assuming that the fiber radius R(z) is changing relatively slowly and uniformly in the axial direction and air drag is neglected, it has been shown that $v_r \approx 0$ [1]. By the aforementioned assumptions, only the z component of the equations of motion remains and takes the form of Eq. 7.19:

$$\rho v_z \frac{\partial v_z}{\partial z} = -\frac{1}{r}\frac{\partial}{\partial r}(r\pi_{rz}) - \frac{\partial \pi_{zz}}{\partial z} \tag{7.19}$$

where π_{zz} and π_{rz} are the relevant components of the total stress tensor defined in Eqs. 7.20 and 7.21:

$$\pi_{zz} = P + \tau_{zz} \tag{7.20}$$

$$\pi_{rz} = \tau_{rz} \tag{7.21}$$

where P is the pressure of the system and τ_{zz} and τ_{rz} are the relevant components of the stress tensor, which will be accounted for via a constitutive viscosity model. It will be assumed that the material behaves as a generalized Newtonian fluid such that the stress tensor, τ, can be generally represented as follows in Eq. 7.22:

$$\tau = -\eta \dot{\gamma} \tag{7.22}$$

where $\dot{\gamma}$ is the shear rate tensor and η is the viscosity of the copolymer/CO_2 melt. The viscosity can be reasonably represented by using the Ostwald-de Waele (power law fluid) model, for which the parameters can be easily determined from experimental data[1]. The general form for the Ostwald-de Waele model is shown in Eq. 7.23:

$$\tau = -\left\{ m \left| \sqrt{\frac{1}{2}\dot{\gamma} : \dot{\gamma}} \right|^{n-1} \right\} \dot{\gamma} \tag{7.23}$$

where *m* and *n* are experimentally (rheologically) determined parameters. Because the problem is only concerned with the zz and rz components of the stress tensor, Eq. 7.23 can be reduced to the form in Eqs. 7.24 and 7.25 for τ_{zz} and τ_{rz}:

$$\tau_{zz} = -m \left| \frac{\partial v_z}{\partial z} \right|^{n-1} \frac{\partial v_z}{\partial z} \tag{7.24}$$

$$\tau_{rz} = -m \left| \frac{\partial v_z}{\partial r} \right|^{n-1} \frac{\partial v_z}{\partial r} \tag{7.25}$$

7.5 Heat Transfer

The next step of the problem requires the analysis of the heat transfer in the system. No phase change during CO_2 desorption (and simultaneous fiber attenuation) will be assumed. It will be assumed that no interactions exist between adjacent fibers. With these assumptions, the thermal energy equation reduces to Eq. 7.26:

$$\rho \hat{C}_P \left(v_z \frac{\partial T}{\partial z} \right) = -\frac{1}{r} \frac{\partial}{\partial r} (r q_r) - \frac{\partial q_z}{\partial z} - \tau_{zz} \frac{\partial v_z}{\partial z} - \tau_{rz} \frac{\partial v_z}{\partial r} \tag{7.26}$$

where q_r is the heat flux in the radial direction, q_z is the flux resulting from the temperature gradient in the axial direction, $\hat{C}_P$ is the heat capacity of the fiber, and T is the temperature of the fiber. It will be assumed that the radial heat flux out of the fiber will be due to convection only (neglecting radiation) and is represented as follows in Eq. 7.27:

$$q_r = h(T - T_a) \tag{7.27}$$

where T_a is the pressurizing gas temperature in the chamber and h is the convective heat transfer coefficient. The axial temperature gradient is related to q_z through Fourier's law of heat conduction, as shown in Eq. 7.28:

$$q_z = -k\frac{\partial T}{\partial z} \tag{7.28}$$

where k is the thermal conductivity of the fiber.

7.6 Mass Transfer

The last item needed to solve the chamber problem is the mass transfer between the fiber and the chamber atmosphere. This represents the actual desorption of CO_2 from the fiber, which is coupled to everything else by temperature dependence in the diffusion coefficient. It will be assumed that CO_2 can only exit the fiber radially, which eliminates any molar flux in the axial direction. This assumption, combined with the lack of any chemical reaction (accumulation), allows the continuity equation (in terms of fluxes) to be reduced to Eq. 7.29:

$$\frac{1}{r}\frac{\partial\left(rN_{r,CO_2}\right)}{\partial r} = 0 \tag{7.29}$$

where $N_{r,CO2}$ is the radial molar flux of CO_2, which if Fickean diffusion is assumed, can be represented by Eq. 7.30:

$$N_{r,CO2} = \frac{-cD}{1-x_{CO2}}\frac{\partial x_{CO2}}{\partial r} \tag{7.30}$$

where c is the molar density of the solution, D is the diffusivity of the system, and x_{CO2} is the mole fraction of CO_2. Fickean diffusion is a valid assumption when the time scale of diffusion is

greater than the relaxation time (or the relaxation time is much greater than the time scale of diffusion), and as a result is generally valid for polymers in the rubbery state.

A relationship is now needed to estimate the diffusivity of the polymer/CO_2 fiber system. The diffusivity can be represented as having an Arrhenius type dependence on temperature as seen in Eq. 7.31:

$$D = D_o \exp\left(\frac{-E_D}{R_g T}\right) \tag{7.31}$$

where R_g is the ideal gas constant, D_o is a characteristic constant for the system represented by Eq. 7.32 (for polymers in the rubbery state) and E_D is the activation energy of diffusion found from Eq. 7.33 (for elastomers)[2]:

$$\log D_o = \frac{E_D * 10^{-3}}{R_g} - 4.0 \tag{7.32}$$

$$10^{-3}\frac{E_D}{R_g} = \left(\frac{\sigma_x}{\sigma_{N_2}}\right)^2 \left[7.5 - 2.5 * 10^{-4}\left(298 - T_g\right)^2\right] \tag{7.33}$$

where T_g is the glass transition temperature of the fiber and σ is a potential length constant (collision diameter) for the gases. In this case, nitrogen is taken as a standard diffusing gas for a reference.

In order to finish the calculations, one must know the relationship between temperature, pressure, and density of the composite fiber (PAN/CO_2) system. At a given temperature and pressure, the density of the fiber (polymer/CO_2 system) needs to be known for Eqs. 7.17,18, 19 and 26. This can be readily obtained from the Sanchez-Lacombe EOS (Eqs. 7.1-4) combined

with mixture properties. Zhu and Paul[6] have calculated T*, P*, and ρ* for PAN of similar molecular weight to that used in these experiments (CO_2 parameters are given in Table 7.1).

7.7 Design Estimates

It is obvious that the system of equations above is rather complex and requires a numerical solution. However, a reasonable (order of magnitude) estimate can be made of the chamber length by decoupling the heat, mass, and momentum transfer. Because the fibers contain relatively small amounts of CO_2, one can make an estimate on the chamber length by knowing the temperature gradient between the spinneret and the chamber exit. Because this gradient is quite large, one can estimate that with a proper selection of atmosphere, the time required to diffuse the gas out of the fiber is small compared to the time required to cool the fiber down to the desired temperature. If one assumes that the heat transfer is the most important issue, Eq. 7.26 can be simplified to a simple ordinary differential equation with an analytical solution by assuming that the temperature gradient in the z direction is the most important factor. This assumption negates the effects of the radial convection and emission into the surrounding heated chamber pressurizing gas. Also, assuming an average velocity $\langle v_z \rangle$ within the chamber that is an average of the take-up and extrusion speeds allows the removal of the τ_{zz} term, which will allow a rough determination of chamber length based solely on heat transfer. It can also be shown that τ_{rz} is small and can be neglected[1].

In order to solve the simplified, decoupled heat transfer problem, the target temperature, thermal diffusivity, and extrusion speed must be specified. The target temperatures were selected based on the T_g of pure and plasticized fiber. The extrusion speed was determined by assuming 0.1 lb/hr of a single fiber extruded through a 200 μm capillary and found to be 0.58

m/s. The value of thermal diffusivity was estimated for the system with parameters that were obtained from other systems in Perry and Chilton[7] and Bird *et al*.[5]. It is difficult to determine a correct value of thermal diffusivity without experimental data for the specific system, but a reasonable selection of thermal diffusivity will at least provide insight into the feasibility of the pressure chamber design. The results for chamber length, based on the aforementioned estimations, are presented in Table 7.3.

Various atmospheres could be used with similar results, and for this calculation will make little difference because mass transfer is not considered. Of course, for a more accurate estimate, mass transfer would also have to be considered to estimate the resulting effects of changing the surrounding atmosphere to contain CO_2. Considering only mass transfer and neglecting heat transfer, similar estimates (to that where only heat transfer was considered) can be made regarding required residence time to remove a given amount of CO_2 and cool the fiber below its T_g (which for AN copolymers will be between 65-100^{o}C). If a comparable time is obtained based on the residence time of the fiber in the chamber listed for the various take up speeds in Table 7.3, where only heat transfer was considered, then a consistent estimate has been obtained. Assuming only mass transfer is occurring, a diffusivity can be estimated at a mean temperature in the chamber, and it can be assumed that the diffusion is not temperature dependent. Also, a mean fiber diameter needs to be selected. This can be done by using the solution for R(z) for isothermal, Newtonian fiber spinning, as shown in Eq. 7.34[1].

$$R(z) = R_o \exp\left[-\frac{1}{2} z \frac{\ln D_R}{L}\right] \tag{7.34}$$

where D_R is the draw ratio, which can be estimated from the ratio of diameters of the pre and post drawn fiber. Averaging 1000 points over any arbitrary length from an initial fiber radius of

200 μm to 25 μm gives an average radius of 84 μm. This value can then be incorporated into Crank and Park's[8] graphical solutions for diffusion of a cylinder. The diffusivity is estimated from Eqs. 7.31-33 at various mean temperatures, depending on the target temperature. The result is the determination of time based on various concentrations of CO_2 in the pressurizing gas, as well as based on the desired amount of CO_2 to be removed. The results are depicted in Tables 7.4 and 7.5. The calculation used to obtain the data in Table 7.4 are based on having 0.25 moles of CO_2 in the pressurizing gas per mole of CO_2 in the fibers. For Table 7.5, the calculations are based on having 0.50 moles of CO_2 in the pressurizing gas per mole of CO_2 in the fiber. As expected, as CO_2 concentration is increased in the pressurizing gas, or if the amount desired to remove is increased, the time to do so also increases, which when compared to Table 7.3 results in a longer chamber length and/or slower take up speed. A couple of discrepancies exist at the small removal amounts (25%), mainly because of the inaccuracy in assuming a diffusivity that is not temperature dependent.

The estimates found by decoupling the partial differential equations provide insight into the design of the pressure chamber. It is too early to assign definite values to any of the variables at this point, but the estimates provide an engineering estimate into the influence of the chamber design based on the various adjustable parameters. In addition, the estimates seem to be reasonable, and for a preliminary indication suggest that implementation of the pressure vessel is feasible.

	to get to 65° C	*to get to 75° C*	*to get to 85° C*
take up speed (m/min)	**z (m)**	**z (m)**	**z (m)**
500	1.80	1.75	1.70
400	0.90	0.88	0.85
300	0.60	0.58	0.57
200	0.45	0.44	0.43
100	0.36	0.35	0.34

Table 7.3: Chamber length (z) required for various take up speeds to reach a fixed temperature from 200°C in N_2.

for target T 85 C			for target T 75 C			for target T 65 C	
CO2 removed from fiber (%)	*time (s)*		*CO2 removed from fiber (%)*	*time (s)*		*CO2 removed from fiber (%)*	*time (s)*
25	1.0		25	0.4		25	0.5
50	1.6		50	1.8		50	1.9
75	3.0		75	4.0		75	4.2

Table 7.4: Effect of varying CO_2 concentration in the chamber atmosphere and the desired amount removed. Calculations are based on having 0.25 moles of CO_2 in the pressurizing gas per mole of CO_2 in the fibers.

for target T 85 C			for target T 75 C			for target T 65 C	
CO2 removed from fiber (%)	*time (s)*		*CO2 removed from fiber (%)*	*time (s)*		*CO2 removed from fiber (%)*	*time (s)*
25	1.3		25	1.6		25	0.8
50	1.9		50	2.6		50	3.0
75	4.0		75	5.2		75	6.9

Table 7.5: Effect of varying CO_2 concentration in the chamber atmosphere and the desired amount removed. Calculations are based on having 0.50 moles of CO_2 in the pressurizing gas per mole of CO_2 in the fiber.

One area for concern with the pressure chamber design may be regarding the selection of the cooling and sealing fluid. CO_2 is known to be relatively soluble in water, with a solubility of approximately 90 cm^3/100 mL water at 20°C[7]. Reaction of CO_2 with water forms carbonic acid, which can become a problem over long periods of time as the acidity builds in the recirculating fluid, causing corrosion the equipment in contact with the fluid (especially the pressure chamber). Two solutions to this problem are rather feasible: one solution is to regularly perform water changes to prevent excessive build in the acidity, and the other solution s to use a different recirculating fluid, such as a low molecular weight polymer fluid or a polymer solution.

7.8 References

(1.) Baird, D. G.; Collias, D. I. *Polymer Processing: Principles and Design*; Wiley: New York, **1998**.

(2.) van Krevelen, D. W. *Properties of polymers: Their correlation with chemical structure, their numerical estimation and prediction from additive group contributions*; Elsevier: Amsterdam, **1990**.

(3.) Sanchez, I. C.; Lacombe, R. H. *Macromolecules* **1978**, *11*, 1145-1156.

(4.) Garg, A.; Gulari, E.; Manke, C. W. *Macromolecules* **1994**, *27*, 5643-5653.

(5.) Bird, R. B.; Bird, R. B. *Transport phenomena*; Wiley: New York, **1960**.

(6.) Zhu, S. X.; Paul, D. R. *Macromolecules* **2002**, *35*, 2078-2083.

(7.) Perry, R. H.; Chilton, C. H.; Perry, J. H. *Chemical engineers' handbook*; McGraw-Hill: New York, **1973**.

(8.) Crank, J.; Park, G. S. *Diffusion in Polymers*; Academic Press: London, **1968**.

8.0 Recommendations

8.0 Recommendations

1) The predictions of the chemorheological curing model suggest conflicting results to the measured shear rheological properties (in particular, melt stability) of the AN co- and ter-polymers. A closer investigation with a series of 85/15 AN/MA copolymers of different molecular weight may facilitate a better understanding of the discrepancy. It is also possible that the kinetics of crosslinking is not first order, as assumed by the curing model. Evaluation of a second order kinetic model would be useful.
2) The precursors that were developed thus far were converted into carbon fibers with a tensile strength of ~1 GPa and a tensile modulus of approximately 70 GPa. A post spin drawing process may be required to maximize orientation in the PAN based carbon fiber precursors to optimize these mechanical properties. However, current carbonization studies with the most recent terpolymer (85/14/1 AN/MA/ABP, batch 3 in Table 3.1) have not been completed. Fibers from this precursor are expected to have better mechanical properties, but some additional orientation may still be required to obtain the project goals of a tensile strength of 2.7 GPa and a tensile modulus of 170 GPa.
3) From the CO_2 absorption studies, it was apparent that a predictive method is still necessary to determine the absorption conditions required for a processing temperature reduction, and in particular to relate the absorption of CO_2 to the viscosity reduction. Determination of the WLF constants for the Barex (65/25/10 AN/MA/elastomer) material could be performed by obtaining additional viscosity versus shear rate data of Barex containing a fixed amount of absorbed CO_2 at multiple temperatures and then shifting the data to a reference temperature. This may also provide a method to predict the viscosity reduction for an amount of absorbed CO_2 in other AN copolymers. To determine if use

of these constants provide a better predictive equation for AN containing systems in general, additional viscosity versus shear rate data for copolymers with varying AN content (containing a fixed amount of absorbed CO_2) can be measured at multiple temperatures.

4) To fully realize the effects of CO_2 plasticization in AN copolymers, direct injection of liquid CO_2 into the polymer melt would potentially facilitate higher absorptions and plasticization levels. It could also provide a method to plasticize AN copolymers containing greater than 90 mole % AN. Extrusion using a two stage screw, that facilitates injection of CO_2 in the polymer melt, can be combined with a specially designed slit die using multiple transducers to measure the viscosity of the polymer melt containing absorbed CO_2.
5) The effect of varying the applied static pressure to the capillary exit has not been fully explored, and will be required when designing a pressurized chamber for processing AN copolymers containing absorbed CO_2. The effects of applied static pressure in the (relatively arbitrary) range of 1000-3000 psi should be evaluated by extruding AN copolymers with a particular absorption level at a selected pressure, cooling the extrudate, and analyzing it with scanning electron microscopy. The pressure can then be varied for a given CO_2 absorption over the pressure range, followed by adjusting the CO_2 absorption level. This will provide important information relating absorption level and pressure required to prevent bubble nucleation and growth in the copolymers containing absorbed CO_2.

Appendix A: Steady and Dynamic Rheological Data

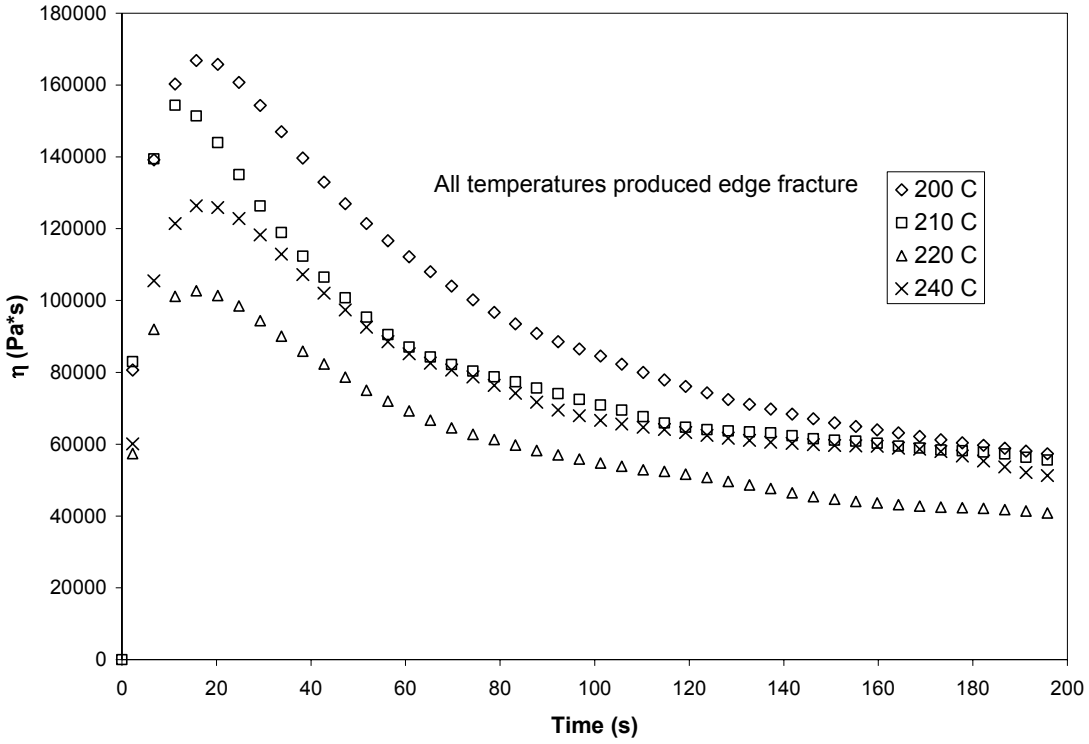

Fig. A1: Steady shear viscosity versus time for the highest molecular weight 85/14/1 AN/MA/ABP terpolymer (batch 1 in Table 3.1). Note that edge fracture occurred (i.e. sample would not flow) at all temperatures used, which covered the range 200-240^{o}C. $\dot{\gamma}$=0.1 s^{-1}. Measurements obtained in air with 25 mm parallel plates.

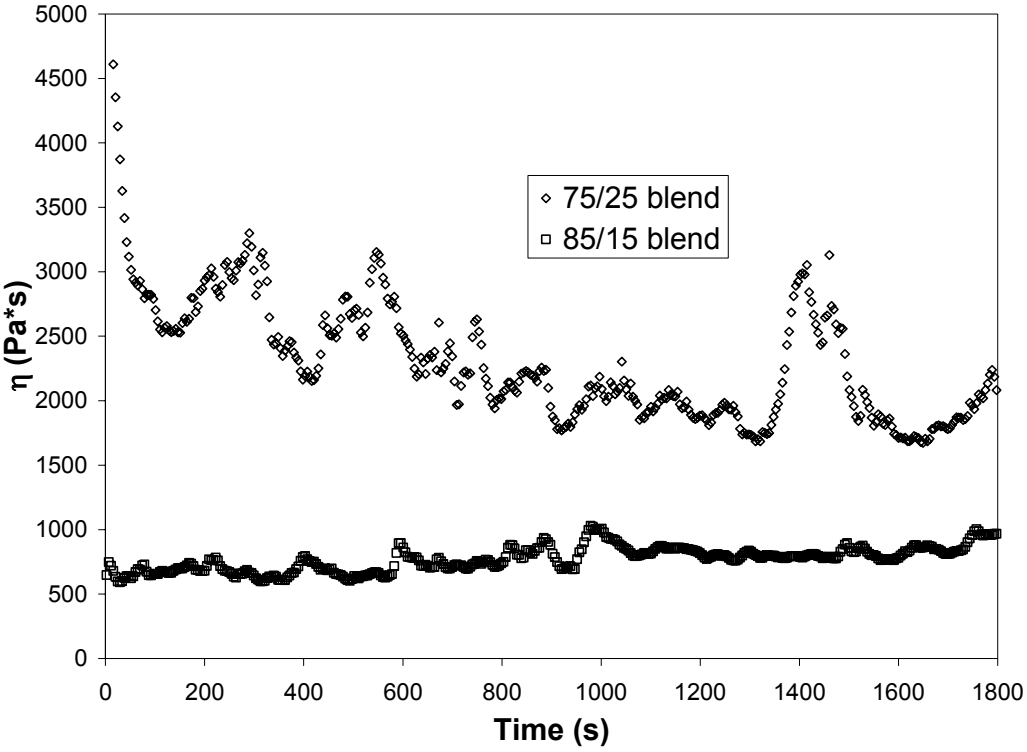

Fig A2: Steady shear viscosity versus time for blends of the 85/15 AN/MA copolymer and 85/14/1 batch 1 terpolymer (see Table 3.1). Data shown for blends of 75 and 85 weight % AN/MA to 25 and 15 weight % of AN/MA/ABP, respectively. $\dot{\gamma}$=0.1 s^{-1}. T=220^{o}C. Measurements obtained in air with 25 mm parallel plates.

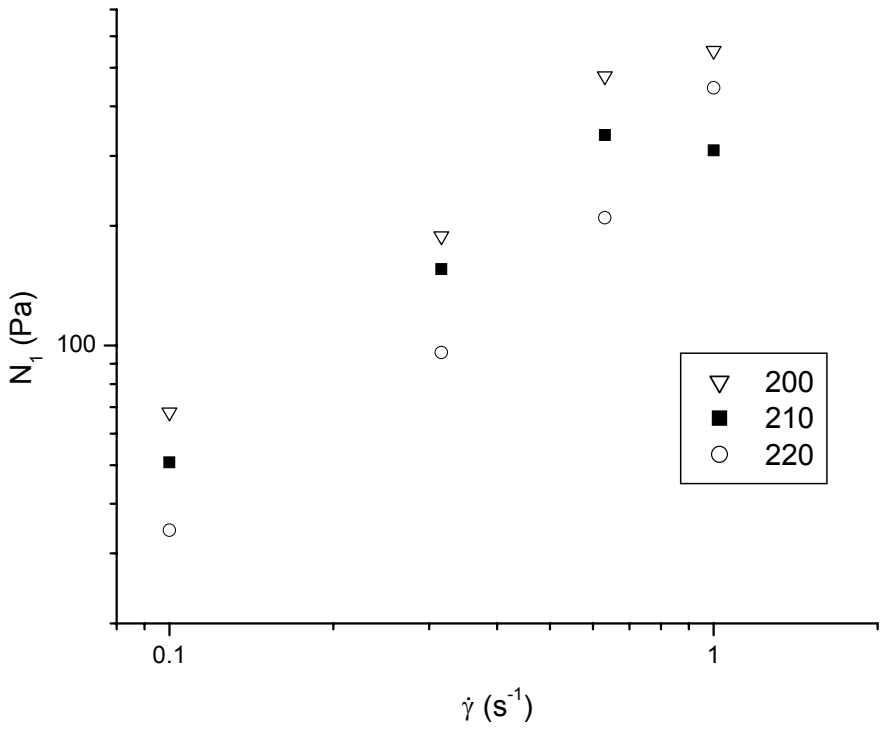

Fig A3: Normal force (N_1) measurements for the 85/15 AN/MA copolymer at 200, 210, and 220^{o}C. Data are an average of 3 runs. Discrepancies may have been observed at the highest rate tested (1.0 s^{-1}). Measurements were obtained with 25 mm diameter cone and plate fixtures in an inert atmosphere.

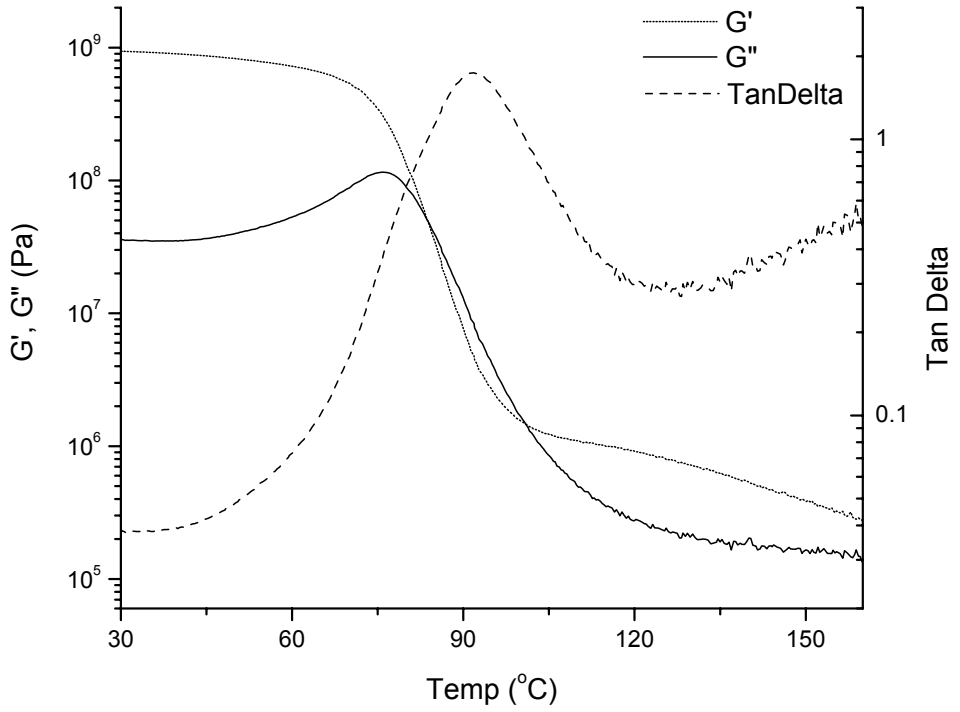

Fig. A4: Dynamic mechanical thermal analysis (DMTA) of Barex. Heating rate 2.5°C/min. ω = 10 rad/s.

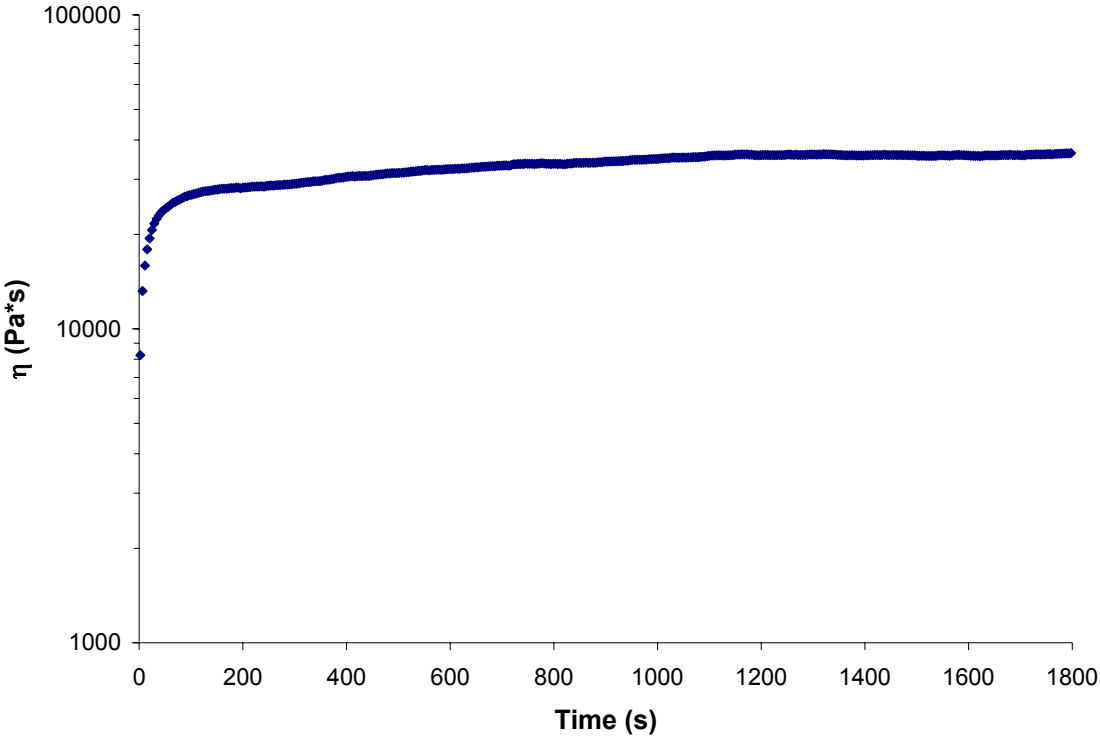

Fig A5: Steady shear viscosity versus time for Barex at 180^{o}C. $\dot{\gamma}$=0.1 s^{-1}.

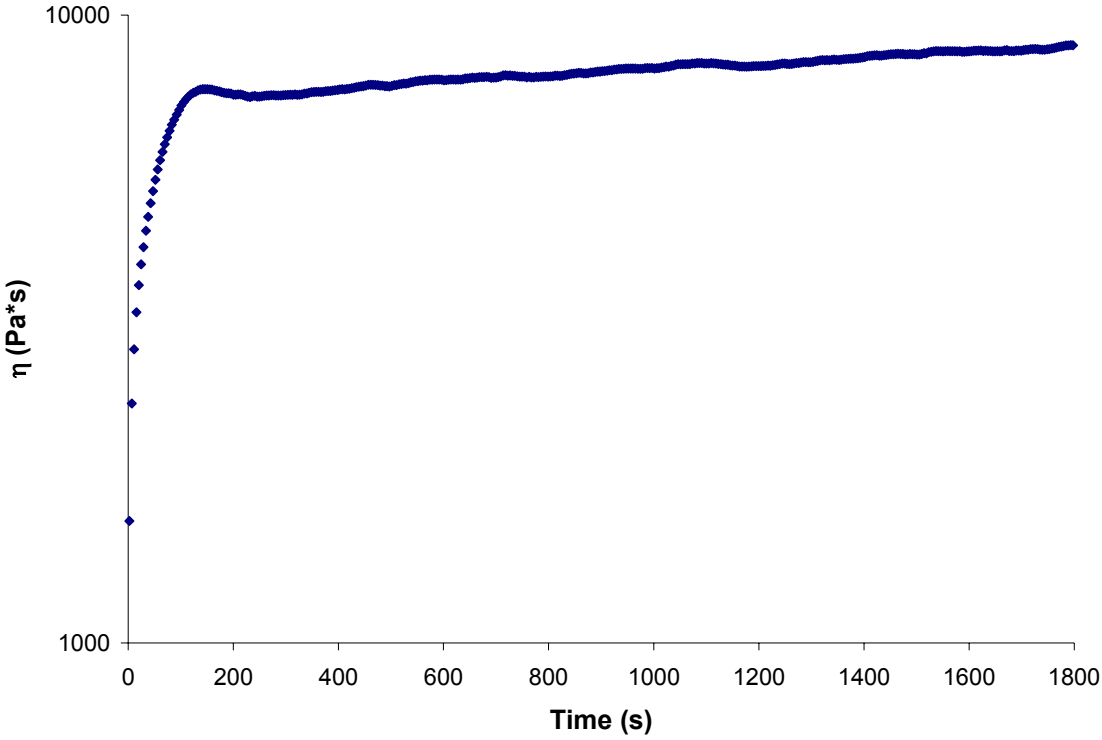

Fig A6: Steady shear viscosity versus time for Amlon at 220^{o}C. $\dot{\gamma}$=0.1 s^{-1}.

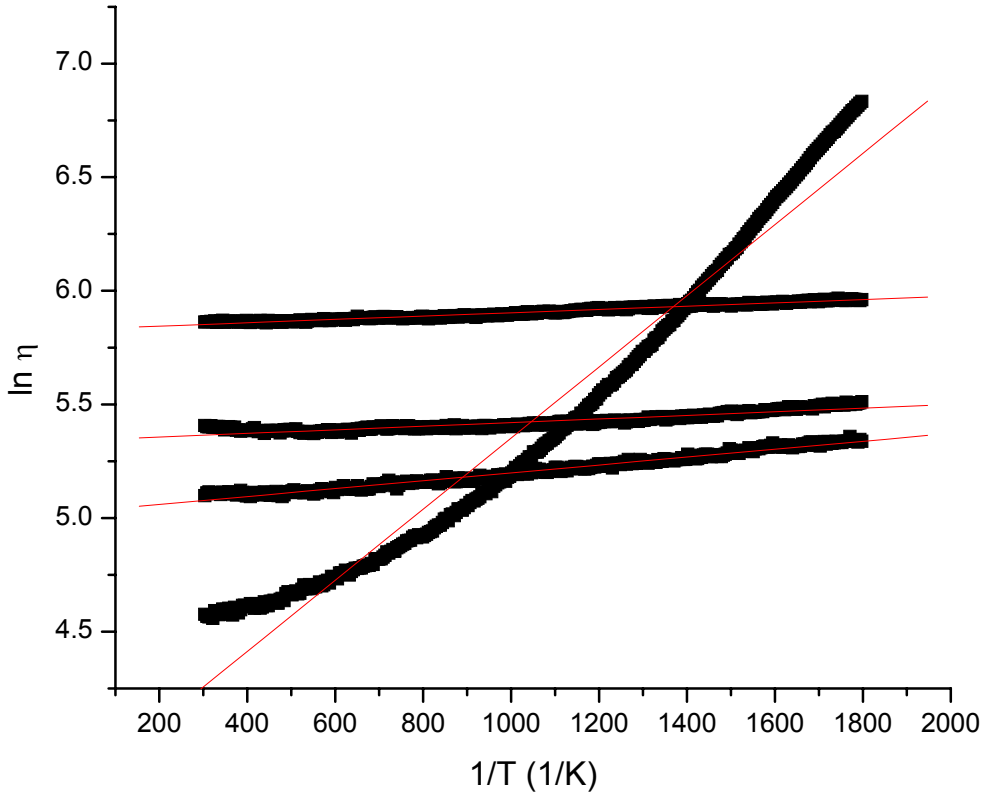

Fig. A7: Steady shear viscosity data and linear fits used for chemorheological relationship of batch 2 terpolymer (labeled as batch 1 in Chapter 4).

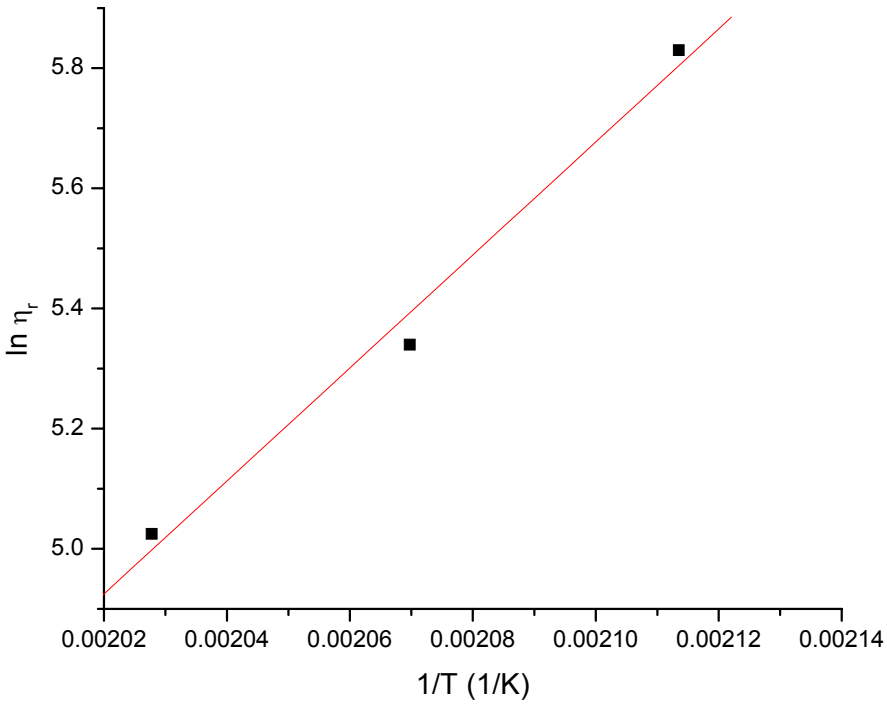

Fig. A8: Plot to determine constants in Eq. 4.2 for the batch 2 terpolymer (labeled as batch 1 in Ch. 4).

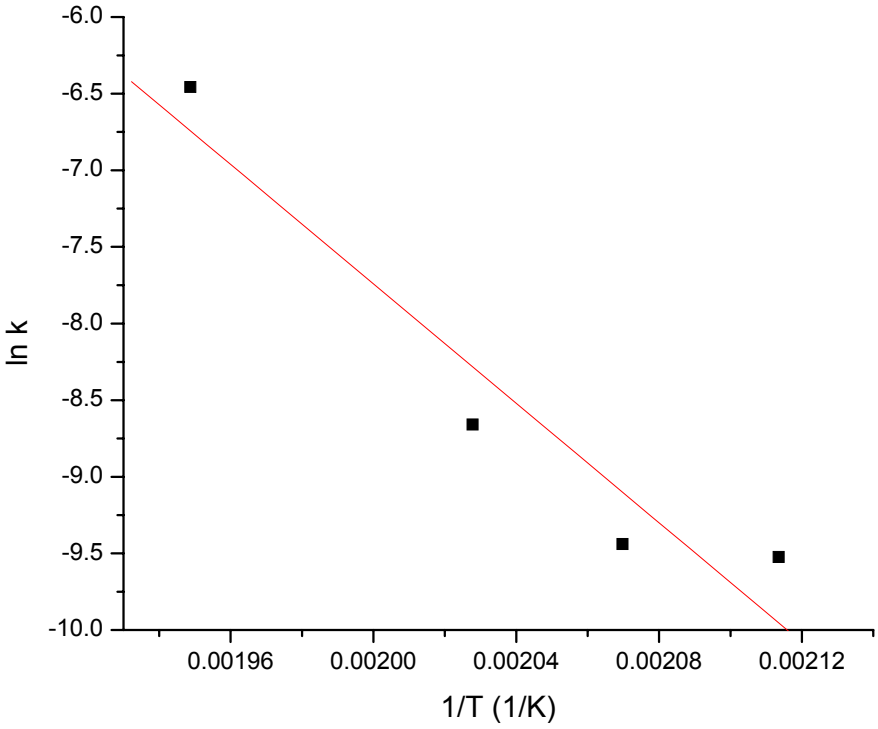

Fig. A9: Plot to determine constants in Eq. 4.3 for the batch 2 terpolymer (labeled as batch 1 in Ch. 4).

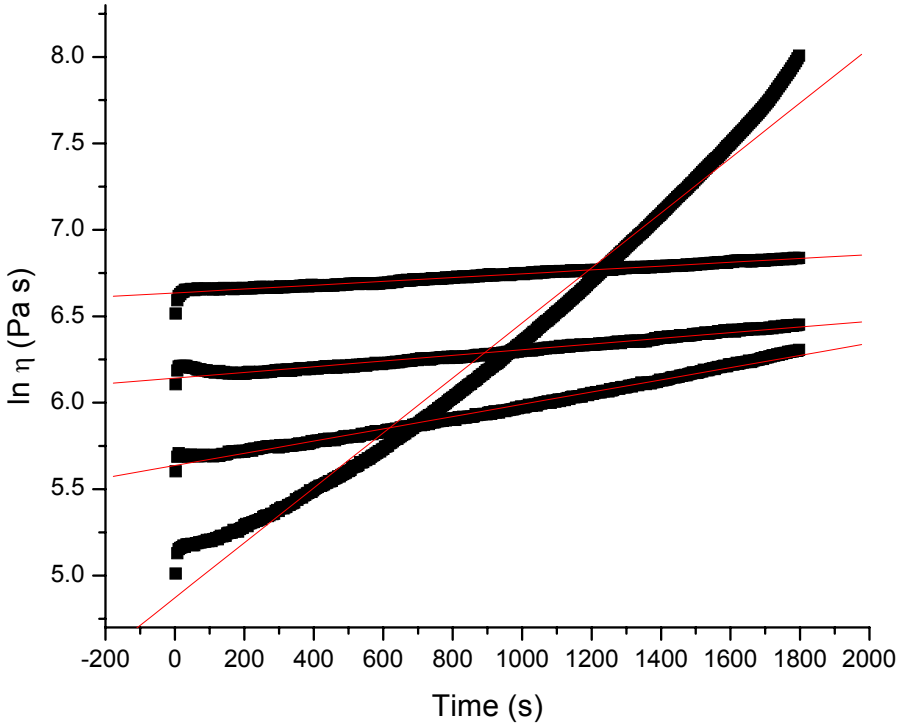

Fig. A10: Steady shear viscosity data and linear fits used for chemorheological relationship of batch 3 terpolymer (labeled as batch 2 in Chapter 4).

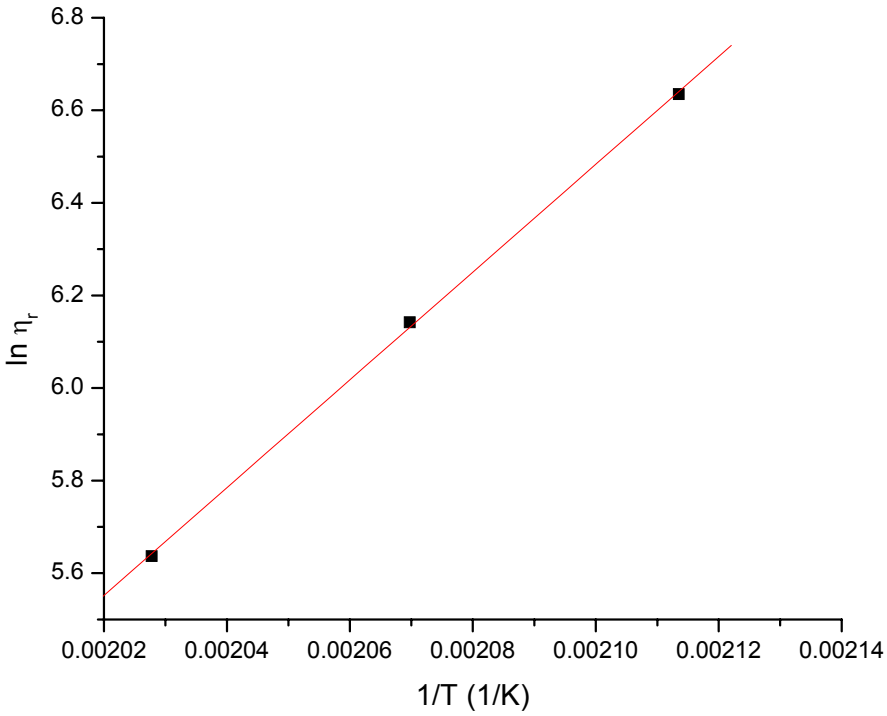

Fig. A11: Plot to determine constants in Eq. 4.2 for the batch 3 terpolymer (labeled as batch 2 in Ch. 4).

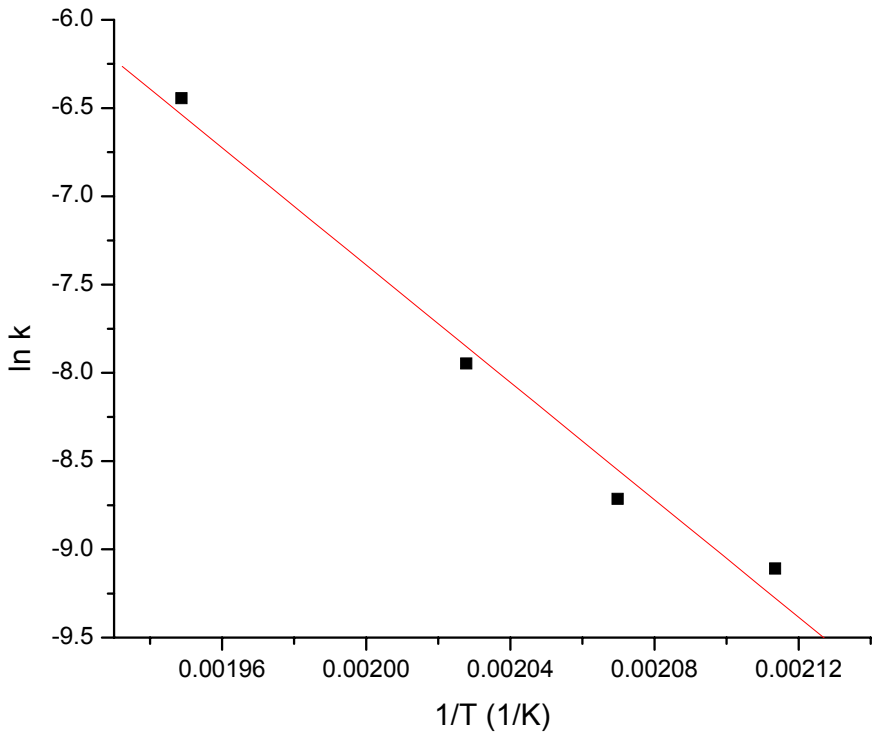

Fig. A12: Plot to determine constants in Eq. 4.3 for the batch 3 terpolymer (labeled as batch 2 in Ch. 4).

180 C dynamic frequency sweep

Freq rad/s	G' Pa	G" Pa	tan_delta	Torque g-cm	Strain %	PhaseAngl °	Eta* Pa-s
0.1	267.49	1187.25	4.43849	0.37927	0.99614	77.303	12170.1
0.15849	397.122	1781.52	4.48609	0.56873	0.99599	77.434	11516.5
0.25119	597.247	2662.85	4.45853	0.84971	0.99527	77.358	10864.3
0.39811	924.586	3977.66	4.3021	1.27128	0.99508	76.914	10257.7
0.63097	1486.96	5913.33	3.97679	1.89952	0.99579	75.885	9663.63
1.00003	2411.83	8699.59	3.60706	2.8107	0.99519	74.505	9027.45
1.58496	3958.82	12645.3	3.19421	4.12156	0.99426	72.616	8360.13
2.51202	6476.95	18122.1	2.79794	5.9826	0.99368	70.333	7661.06
3.98132	10457.3	25447.6	2.43347	8.54365	0.99262	67.66	6910.39
6.31006	16595.9	35063	2.11276	12.0225	0.99065	64.671	6147.68
10.0007	25612.5	47199.8	1.84284	16.5883	0.98739	61.514	5369.73
15.8501	38616.8	61926.7	1.60362	22.4165	0.98182	58.053	4604.43
25.1206	56310.8	79148.8	1.40557	29.5582	0.97267	54.57	3866.79
39.8135	79530.5	98942.6	1.24408	37.8806	0.95384	51.208	3188.46
63.1006	1.09E+05	1.21E+05	1.10819	46.4321	0.91372	47.938	2574.2
100	1.44E+05	1.43E+05	0.99361	52.8517	0.83111	44.816	2032.69

Table A1: Dynamic frequency sweep data for the 85/15 AN/MA copolymer at 180°C.

190 C dynamic frequency sweep

Freq rad/s	G' Pa	G" Pa	tan_delta	Torque g-cm	Strain %	PhaseAngl °	Eta* Pa-s
0.1	46.3106	434.621	9.38491	0.6836	4.99934	83.918	4370.8
0.15849	79.4168	665.859	8.38436	1.04892	4.99994	83.198	4231.07
0.25119	127.009	1014.42	7.98698	1.59901	4.99949	82.863	4069.99
0.39811	195.485	1551.19	7.93508	2.44528	4.99934	82.817	3927.22
0.63097	309.961	2377.31	7.66969	3.75052	5.00053	82.571	3799.61
1.00003	519.925	3644.11	7.00891	5.75871	5.00068	81.88	3680.9
1.58496	924.109	5554.22	6.01036	8.80842	5.00053	80.554	3552.5
2.51202	1698.15	8369.03	4.92833	13.3644	5.00247	78.53	3399.48
3.98132	3059.56	12407.1	4.0552	19.9994	5.00262	76.147	3209.69
6.31006	5443.85	18019.5	3.31006	29.4601	5.00262	73.19	2983.15
10.0007	9385.12	25580.6	2.72566	42.6353	5.00157	69.853	2724.59
15.8501	15584.9	35420.6	2.27276	60.4968	4.9971	66.251	2441.48
25.1206	24869.7	47680.8	1.91723	83.8499	4.98399	62.454	2140.75
39.8135	38133.2	62397.9	1.63631	113.125	4.9448	58.57	1836.75
63.1006	56091.9	79369.1	1.41498	146.952	4.83312	54.75	1540.23
100	79272.4	97862.5	1.23451	179.702	4.56095	50.991	1259.41

Table A2: Dynamic frequency sweep data for the 85/15 AN/MA copolymer at 190°C.

200 C dynamic frequency sweep

ω (rad/s)	G' (Pa)	G" (Pa)	tan δ	torque (g*cm)	η* (Pa*s)
0.1	38.917	261.37	6.7161	0.82729	2642.5
0.15849	50.785	381.56	7.5133	1.2051	2428.7
0.25119	79.826	572.15	7.1675	1.8085	2299.8
0.39811	120.51	861.91	7.1525	2.7247	2186.1
0.63097	173.9	1301.2	7.4826	4.1101	2080.6
1	262.08	1979.2	7.5521	6.2509	1996.4
1.585	423.84	3011.7	7.1057	9.5217	1918.9
2.512	730.12	4569	6.2578	14.493	1841.9
3.9813	1312.4	6881	5.2429	21.944	1759.5
6.3101	2367.4	10208	4.3119	32.836	1660.7
10.001	4212.4	14879	3.5322	48.46	1546.3
15.85	7319.6	21225	2.8998	70.339	1416.5
25.121	12253	29531	2.4101	100.02	1272.7
39.813	19734	40031	2.0286	138.9	1121
63.101	30535	52665	1.7247	186.51	964.75
100	45187	67080	1.4845	237.97	808.8

Table A3: Dynamic frequency sweep data for the 85/15 AN/MA copolymer at 190°C.

210 C dynamic frequency sweep

ω (rad/s)	G' (Pa)	G" (Pa)	tan δ	torque (g*cm)	η* (Pa*s)
0.1	31.666	196.01	6.1899	0.62156	1985.5
0.15849	46.919	286.35	6.103	0.90843	1830.8
0.25119	72.184	421.99	5.846	1.3402	1704.4
0.39811	106.01	620.14	5.8499	1.9695	1580.3
0.63097	152.74	918.36	6.0126	2.9147	1475.5
1	217.19	1367.3	6.2955	4.3349	1384.4
1.585	320.1	2053.7	6.416	6.5076	1311.4
2.512	496.28	3089.1	6.2244	9.8006	1245.5
3.9813	829.27	4639.5	5.5946	14.769	1183.8
6.3101	1423.2	6904.1	4.8512	22.1	1117.1
10.001	2466.3	10133	4.1084	32.711	1042.8
15.85	4280.5	14656	3.4238	47.906	963.27
25.121	7269.8	20779	2.8582	69.037	876.33
39.813	12009	28795	2.3977	97.448	783.62
63.101	19165	38878	2.0286	133.53	686.91
100	29268	50764	1.7344	174.1	585.97

Table A4: Dynamic frequency sweep data for the 85/15 AN/MA copolymer at 210°C.

220 C dynamic frequency sweep

ω (rad/s)	G' (Pa)	G" (Pa)	tan δ	torque (g*cm)	η* (Pa*s)
0.1	20	134.04	6.7021	0.4243	1355.3
0.15849	31.665	199.58	6.303	0.63262	1275
0.25119	51.632	294.54	5.7045	0.93616	1190.4
0.39811	79.796	432.4	5.4188	1.3766	1104.5
0.63097	115.84	631.43	5.4508	2.01	1017.4
1	164.1	927.2	5.6504	2.9483	941.58
1.585	232.08	1373.9	5.9199	4.3628	879.12
2.512	343.1	2056	5.9923	6.5304	829.77
3.9813	537.27	3080.7	5.734	9.8006	785.46
6.3101	886.82	4603.3	5.1907	14.701	742.92
10.001	1508	6820.4	4.5228	21.92	698.46
15.85	2602.4	9983.5	3.8363	32.397	650.92
25.121	4463.9	14382	3.2219	47.286	599.46
39.813	7501.1	20312	2.7079	67.761	543.85
63.101	12234	28017	2.29	94.474	484.49
100	19236	37501	1.9495	125.91	421.46

Table A5: Dynamic frequency sweep data for the 85/15 AN/MA copolymer at 220°C.

220 C dynamic

Freq	G'	G"	tan_delta	Torque	Strain	PhaseAngl	Eta*
rad/s	Pa	Pa		g-cm	%	°	Pa-s
0.1	1184.43	1209.12	1.02084	0.52725	0.99571	45.591	16925.8
0.15849	1489.66	1555.02	1.04387	0.67036	0.99506	46.23	13587.1
0.25119	1793.99	2034.79	1.13422	0.84447	0.99506	48.599	10799.4
0.39811	2170.13	2722.54	1.25455	1.08342	0.99469	51.442	8745.4
0.63097	2645.13	3722.47	1.4073	1.42069	0.99445	54.603	7237.41
1.00003	3274.53	5175.25	1.58045	1.90564	0.99463	57.677	6124.01
1.58496	4133.43	7262.56	1.75703	2.59927	0.99426	60.354	5272.33
2.51202	5342.27	10311.3	1.93013	3.61351	0.99462	62.611	4622.97
3.98132	7176.45	14533.1	2.02512	5.04314	0.99456	63.72	4071.12
6.31006	9988.26	20503.1	2.05272	7.09945	0.99503	64.027	3614.33
10.0007	14136.9	28826.8	2.03911	9.98544	0.99413	63.876	3210.42
15.8501	20439.6	40016.8	1.95781	13.9554	0.99273	62.943	2834.97
25.1206	29855.6	54726.2	1.83303	19.287	0.98893	61.386	2481.64
39.8135	43471	73498.6	1.69075	26.1028	0.97711	59.398	2144.8
63.1006	62853.7	96794.9	1.54	34.128	0.94522	57.002	1829.01
100	89180.8	1.24E+05	1.39251	41.7377	0.87261	54.317	1528.9

Table A6: Dynamic frequency sweep data for Amlon at 220°C.

225 C dynamic

Freq	G'	G"	tan_delta	Torque	Strain	PhaseAngl	Eta*
rad/s	Pa	Pa		g-cm	%	°	Pa-s
0.1	47.2612	154.754	3.27443	0.05041	0.99573	73.018	1518.09
0.15849	63.3828	227.853	3.59487	0.0737	0.99607	74.455	1452.68
0.25119	83.8829	342.254	4.08014	0.10978	0.99584	76.229	1402.85
0.39811	117.422	519.964	4.42815	0.1662	0.99661	77.274	1338.97
0.63097	156.955	787.325	5.01624	0.25024	0.99635	78.726	1272.36
1.00003	228.387	1201.67	5.26154	0.38145	0.99681	79.239	1223.14
1.58496	342.152	1819.18	5.31688	0.57724	0.99679	79.348	1167.9
2.51202	439.094	2762.15	6.29057	0.87274	0.99745	80.967	1113.38
3.98132	877.172	4132.4	4.71105	1.32025	0.99897	78.016	1061.07
6.31006	1407.54	6245.24	4.43699	2.00257	0.99989	77.299	1014.55
10.0007	2382.84	9252.05	3.88279	2.99286	1.00132	75.558	955.327
15.8501	3999.07	13485.8	3.37223	4.41365	1.00298	73.483	887.453
25.1206	6748	19403.3	2.87542	6.44083	1.00218	70.824	817.783
39.8135	11175.9	27301.6	2.44291	9.18007	0.99469	67.738	740.967
63.1006	17983	37362.2	2.07764	12.5934	0.97081	64.298	657.121
100	28022.6	49568.4	1.76887	16.2476	0.91208	60.519	569.411

Table A7: Dynamic frequency sweep data for Amlon at 225^{o}C.

230 C dynamic

Freq	G'	G"	tan_delta	Torque	Strain	PhaseAngl	Eta*
rad/s	Pa	Pa		g-cm	%	°	Pa-s
0.1	21.0573	101.322	4.81174	0.03223	0.99549	78.26	1034.87
0.15849	29.0713	154.839	5.32619	0.0491	0.99618	79.366	994.04
0.25119	39.9857	237.33	5.93537	0.075	0.99607	80.437	958.138
0.39811	51.6012	359.939	6.97541	0.11331	0.99609	81.842	913.366
0.63097	65.7961	557.444	8.4723	0.17496	0.99633	83.268	889.61
1.00003	96.834	862.057	8.90242	0.27044	0.9965	83.591	867.452
1.58496	144.763	1339.8	9.25512	0.42024	0.99679	83.833	850.238
2.51202	194.775	2125.49	10.9125	0.66633	0.99789	84.764	849.67
3.98132	433.86	3190.05	7.35271	1.00596	0.99879	82.255	808.629
6.31006	775.178	4905.3	6.32797	1.55416	1.00033	81.02	787.025
10.0007	1331.13	7410.68	5.56722	2.36076	1.00223	79.817	752.873
15.8501	2471.2	11046.6	4.47011	3.55334	1.00341	77.39	714.165
25.1206	4434.83	16123.1	3.63557	5.25066	1.00369	74.621	665.667
39.8135	7796.36	23350.2	2.99501	7.68203	0.99748	71.536	618.317
63.1006	13236.9	32700	2.47037	10.7585	0.97482	67.962	559.069
100	21599.2	44377.3	2.05458	14.18	0.91838	64.047	493.545

Table A8: Dynamic frequency sweep data for Amlon at 230^{o}C.

235 C dynamic

Freq rad/s	G' Pa	G" Pa	tan_delta	Torque g-cm	Strain %	PhaseAngl ?	Eta* Pa-s
0.1	9.27294	73.2646	7.90091	0.23124	10.0088	82.787	738.489
0.15849	13.8836	114.796	8.26847	0.36202	10.0073	83.104	729.594
0.25119	20.1931	178.49	8.83918	0.56245	10.0088	83.545	715.11
0.39811	28.0993	277.578	9.87847	0.87355	10.0082	84.22	700.805
0.63097	39.5031	431.658	10.9272	1.35734	10.0094	84.771	686.981
1.00003	56.3691	673.579	11.9494	2.11668	10.0097	85.216	675.913
1.58496	84.6644	1051.22	12.4163	3.30283	10.0106	85.395	665.394
2.51202	139.863	1637.26	11.7062	5.14911	10.0163	85.117	654.144
3.98132	238.537	2555.49	10.7132	8.04685	10.0216	84.667	644.66
6.31006	455.937	3964.71	8.69574	12.5211	10.0288	83.44	632.457
10.0007	874.155	6089.77	6.96646	19.32	10.038	81.831	615.174
15.8501	1674.2	9233.26	5.51504	29.4947	10.047	79.723	592.035
25.1206	3150.21	13781.7	4.37483	44.4481	10.0499	77.125	562.77
39.8135	5775.29	20150.4	3.48907	65.7135	10.0207	74.007	526.497
63.1006	10162.3	28689.3	2.82312	94.2881	9.90242	70.495	482.34
100	17113.4	39500.8	2.30818	129.049	9.58219	66.576	430.486

Table A9: Dynamic frequency sweep data for Amlon at 235^{o}C.

Freq rad/s	G' Pa	G" Pa	tan_delta	Torque g-cm	Strain %	PhaseAngl ?	Eta* Pa-s
0.1	5.94689	39.765	6.68668	0.12589	10.0079	81.494	402.071
0.15849	9.14227	59.9466	6.55708	0.18985	10.0073	81.329	382.611
0.25119	13.3571	90.0435	6.74127	0.28499	10.0073	81.562	362.39
0.39811	20.7799	134.855	6.48968	0.42724	10.0088	81.24	342.737
0.63097	30.9859	201.678	6.5087	0.63891	10.0088	81.265	323.384
1.00003	46.4866	301.317	6.48181	0.9547	10.0094	81.23	304.872
1.58496	66.6465	450.533	6.76004	1.42632	10.0106	81.585	287.348
2.51202	92.7161	668.811	7.21354	2.11572	10.016	82.107	268.79
3.98132	132.384	1027.74	7.7633	3.24889	10.0219	82.66	260.272
6.31006	189.096	1540.48	8.14654	4.87018	10.0303	83.002	245.963
10.0007	284.355	2344.36	8.2445	7.41827	10.041	83.084	236.137
15.8501	444.983	3559.33	7.9988	11.2836	10.055	82.874	226.31
25.1206	752.463	5400.05	7.17649	17.164	10.0628	82.067	217.042
39.8135	1331.61	8156.54	6.12533	25.9642	10.0422	80.728	207.581
63.1006	2399.53	12210.9	5.08889	38.6761	9.93431	78.883	197.216
100	4305.49	17914.1	4.16076	55.5678	9.6406	76.486	184.242

Table A10: Dynamic frequency sweep data for the low MW 85/14/1 terpolymer (batch 2 in Table 3.1) at 200^{o}C.

Freq rad/s	G' Pa	G" Pa	tan_delta	Torque g-cm	Strain %	PhaseAngl ?	Eta* Pa-s
0.1	4.18731	26.2188	6.26149	0.08312	10.0073	80.926	265.51
0.15849	6.62334	38.379	5.79451	0.12193	10.0073	80.209	245.735
0.25119	10.044	57.9223	5.76684	0.18406	10.0082	80.162	234.033
0.39811	15.4671	86.2592	5.57694	0.2744	10.0088	79.834	220.128
0.63097	23.3994	127.898	5.46589	0.40715	10.0094	79.632	206.067
1.00003	34.7902	188.585	5.42065	0.60054	10.01	79.548	191.762
1.58496	50.8237	279.339	5.49624	0.88924	10.0112	79.688	179.137
2.51202	72.8214	419.334	5.75839	1.33378	10.0172	80.148	169.429
3.98132	97.6705	618.312	6.33059	1.9627	10.0222	81.024	157.229
6.31006	138.694	920.912	6.6399	2.9226	10.0312	81.435	147.589
10.0007	187.427	1387.75	7.40422	4.39979	10.0431	82.308	140.024
15.8501	286.198	2101.54	7.34298	6.67196	10.0553	82.245	133.813
25.1206	437.553	3176.57	7.25986	10.0957	10.0639	82.157	127.647
39.8135	714.206	4814.19	6.74062	15.2909	10.0428	81.561	122.242
63.1006	1234.58	7246.63	5.8697	22.8456	9.93401	80.332	116.497
100	2166.51	10759.7	4.9664	33.1075	9.64194	78.616	109.757

Table A11: Dynamic frequency sweep data for the low MW 85/14/1 terpolymer (batch 2 in Table 3.1) at 210^{o}C.

Freq rad/s	G' Pa	G" Pa	tan_delta	Torque g-cm	Strain %	PhaseAngl ?	Eta* Pa-s
0.1	4.65285	25.6619	5.5153	0.08166	10.0079	79.723	260.802
0.15849	7.38105	38.598	5.22934	0.12303	10.007	79.174	247.95
0.25119	11.0635	56.6689	5.12215	0.18078	10.0079	78.953	229.861
0.39811	16.9077	83.752	4.95347	0.26754	10.0088	78.587	214.618
0.63097	24.7114	121.028	4.89765	0.38678	10.0088	78.46	195.771
1.00003	35.9681	175.27	4.87294	0.56029	10.0097	78.403	178.917
1.58496	52.897	249.802	4.72242	0.79969	10.0109	78.044	161.103
2.51202	72.5404	351.906	4.85118	1.12596	10.0169	78.352	143.034
3.98132	109.135	493.074	4.51801	1.58359	10.0234	77.52	126.844
6.31006	143.496	699.34	4.87358	2.24033	10.0309	78.405	113.138
10.0007	182.492	993.051	5.4416	3.17215	10.0425	79.587	100.961
15.8501	238.568	1445.3	6.05823	4.60822	10.0556	80.627	92.4195
25.1206	336.056	2119.83	6.30796	6.75714	10.0634	80.992	85.4399
39.8135	497.697	3148.58	6.3263	10.014	10.0416	81.018	80.0652
63.1006	784.007	4690.19	5.98234	14.7767	9.93282	80.51	75.3601
100	1293.13	6931.58	5.36031	21.2638	9.63941	79.433	70.5117

Table A12: Dynamic frequency sweep data for the low MW 85/14/1 terpolymer (batch 2 in Table 3.1) at 220^{o}C.

Freq rad/s	G' Pa	G" Pa	tan_delta	Torque g-cm	Strain %	PhaseAngl ?	Eta* Pa-s
0.1	12.3214	91.8967	7.45832	0.14501	4.99934	82.363	927.187
0.15849	20.2968	141.64	6.97844	0.2238	4.99949	81.845	902.82
0.25119	33.4636	214.231	6.40192	0.33917	4.99994	81.122	863.207
0.39811	50.8282	320.242	6.30048	0.50728	5.00083	80.981	814.476
0.63097	78.0519	476.664	6.10702	0.7556	5.00038	80.701	765.512
1.00003	116.484	704.439	6.0475	1.11725	5.00172	80.611	713.983
1.58496	179.913	1039.18	5.77602	1.65056	5.00262	80.178	665.406
2.51202	270.032	1527.95	5.65842	2.43047	5.00694	79.978	617.681
3.98132	413.503	2221.85	5.37323	3.5429	5.01096	79.457	567.65
6.31006	607.414	3237.19	5.32947	5.1695	5.01692	79.373	521.974
10.0007	934.39	4797.39	5.13425	7.68384	5.02527	78.978	488.718
15.8501	1519.56	7089.64	4.66558	11.4186	5.03391	77.903	457.452
25.1206	2496.1	10438	4.18174	16.9202	5.03942	76.551	427.233
39.8135	4228.89	15208	3.5962	24.83	5.0281	74.46	396.473
63.1006	7126.69	21791.9	3.05779	35.576	4.95985	71.891	363.351
100	11765	30487.2	2.59135	48.8034	4.77374	68.898	326.785

Table A13: Dynamic frequency sweep data for the intermediate MW 85/14/1 terpolymer (batch 3 in Table 3.1) at 200^{o}C.

Freq rad/s	G' Pa	G" Pa	tan_delta	Torque g-cm	Strain %	PhaseAngl ?	Eta* Pa-s
0.1	7.67439	55.4013	7.21899	0.08748	4.99964	82.113	559.301
0.15849	12.8949	86.2058	6.68529	0.13635	5.00008	81.493	549.974
0.25119	21.2116	133.249	6.2819	0.21107	5.00038	80.955	537.151
0.39811	32.8969	202.865	6.16669	0.32151	5.00053	80.789	516.227
0.63097	50.7947	300.311	5.91225	0.47656	5.00143	80.4	482.714
1.00003	76.7535	450.158	5.86498	0.71458	5.00187	80.324	456.641
1.58496	113.438	668.565	5.89366	1.06148	5.00351	80.37	427.847
2.51202	175.616	993.078	5.65482	1.57955	5.00649	79.971	401.464
3.98132	255.78	1465.06	5.72779	2.33158	5.01126	80.097	373.548
6.31006	387.407	2181.26	5.63042	3.477	5.01677	79.929	351.09
10.0007	557.465	3239.43	5.81099	5.16689	5.02452	80.236	328.68
15.8501	913.935	4833.85	5.28905	7.74692	5.03361	79.293	310.376
25.1206	1513.74	7195.99	4.75379	11.5946	5.04002	78.121	292.727
39.8135	2578.53	10592.3	4.10789	17.15	5.02855	76.318	273.818
63.1006	4398.93	15384.3	3.49727	24.8421	4.96268	74.043	253.576
100	7393.79	21880.6	2.95932	34.5394	4.78022	71.329	230.961

Table A14: Dynamic frequency sweep data for the intermediate MW 85/14/1 terpolymer (batch 3 in Table 3.1) at 210^{o}C.

Freq rad/s	G' Pa	G" Pa	tan_delta	Torque g-cm	Strain %	PhaseAngl ?	Eta* Pa-s
0.1	4.89852	34.4266	7.02795	0.05439	4.99979	81.902	347.732
0.15849	8.20953	56.3394	6.86269	0.08906	4.99994	81.709	359.232
0.25119	12.8214	87.5642	6.82953	0.13843	4.99994	81.67	352.314
0.39811	19.2894	135.138	7.00586	0.21356	5.00068	81.877	342.891
0.63097	32.0083	205.326	6.41477	0.32511	5.00083	81.139	329.345
1.00003	47.4153	311.499	6.56959	0.49302	5.00157	81.345	315.077
1.58496	71.0582	470.337	6.61904	0.74439	5.00217	81.409	300.118
2.51202	93.4578	710.206	7.59922	1.12192	5.00634	82.503	285.16
3.98132	153.901	1084.37	7.04593	1.71681	5.01052	81.922	275.095
6.31006	237.022	1656.76	6.9899	2.62664	5.01662	81.858	265.232
10.0007	376.875	2503.74	6.64343	3.98043	5.02512	81.44	253.176
15.8501	650.93	3796.25	5.83205	6.06607	5.03421	80.27	243.005
25.1206	1132.29	5687.61	5.02311	9.14552	5.04091	78.741	230.855
39.8135	1960.21	8474.03	4.32303	13.687	5.03004	76.975	218.464
63.1006	3402.26	12395	3.64317	19.9653	4.96507	74.651	203.698
100	5800.28	17730.7	3.05686	27.9253	4.78484	71.885	186.553

Table A15: Dynamic frequency sweep data for the intermediate MW 85/14/1 terpolymer (batch 3 in Table 3.1) at 220^{o}C.

Appendix B: Capillary Rheometry

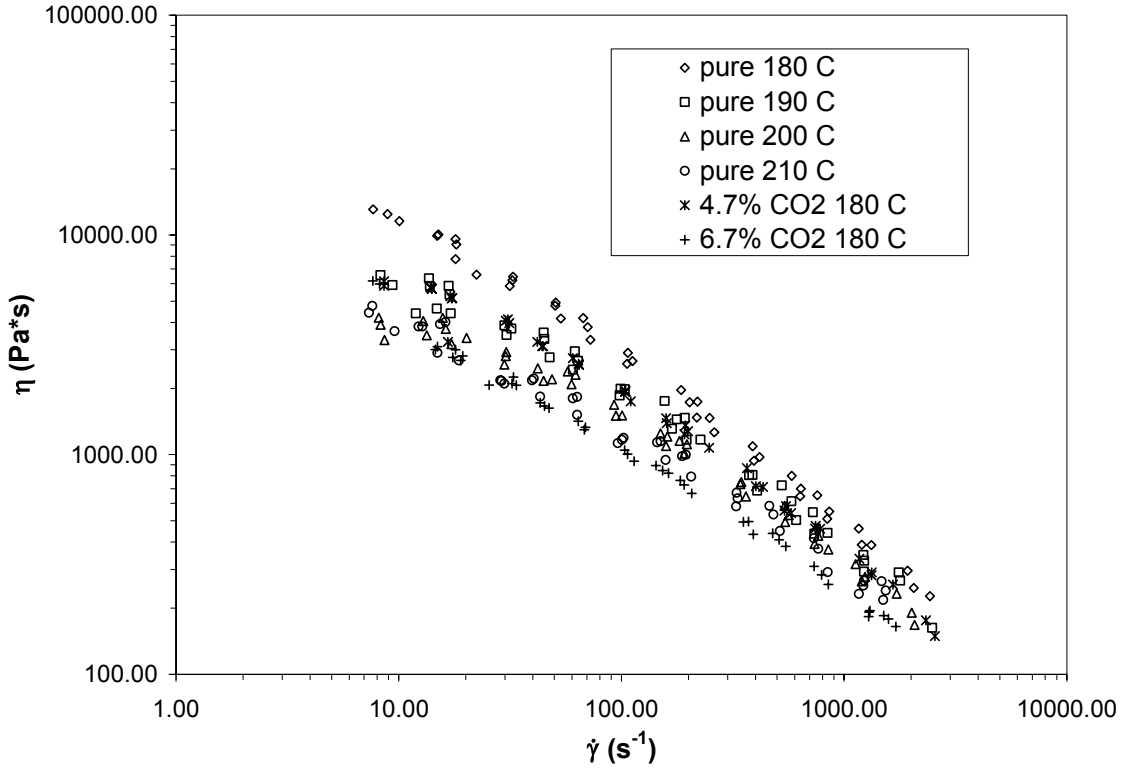

Fig B1: Comparison of viscosity of saturated Barex (at 180^{o}C) to pure Barex at 180, 190, 200, 210^{o}C. Data have been corrected as outlined in Chapter 5.

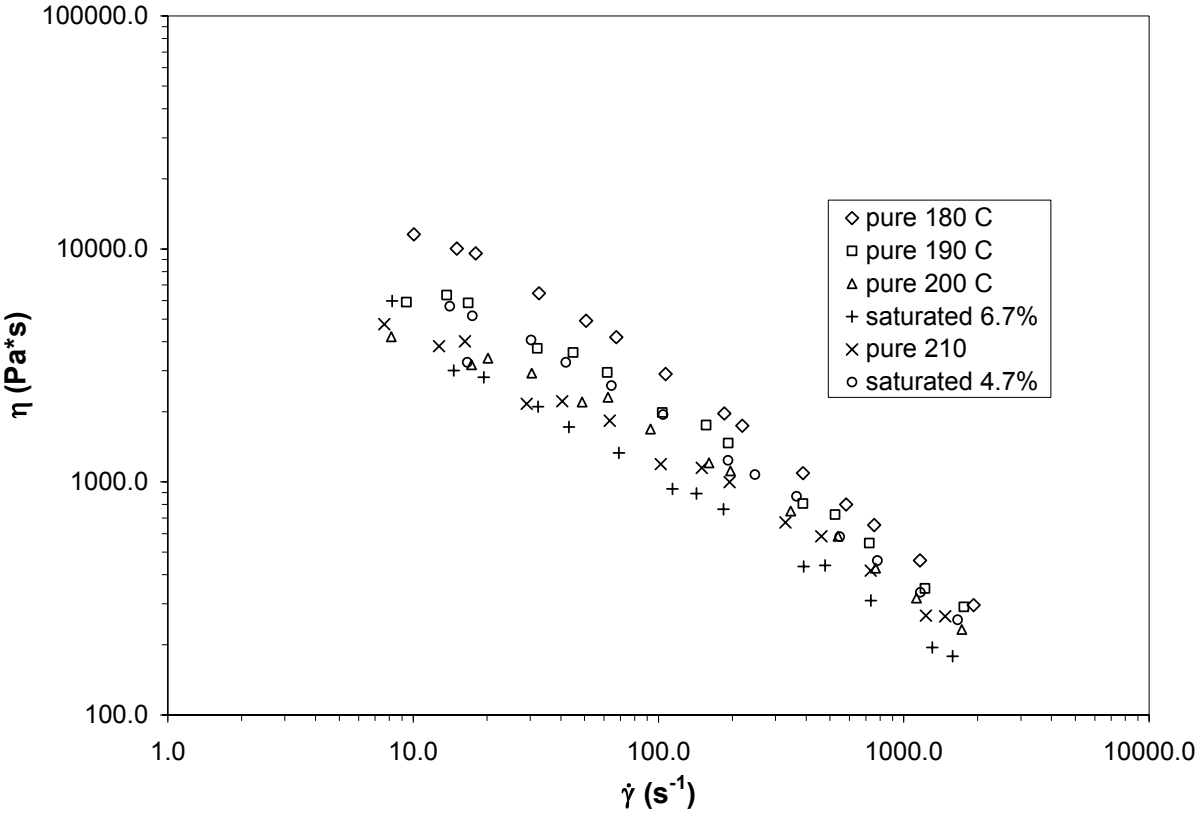

Fig B2: Viscosity versus shear rate data from Fig B1 for a L/D = 10.

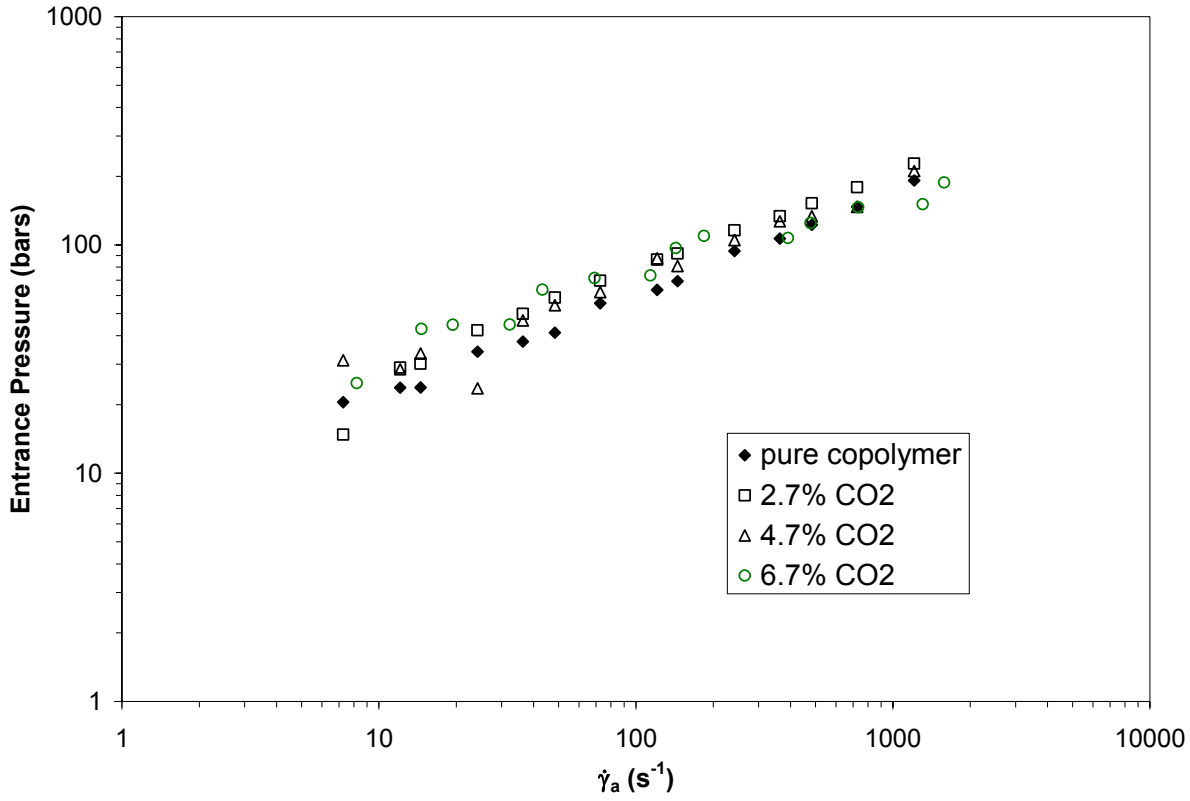

Fig B3: Entrance pressures for pure and plasticized Barex at 180°C.

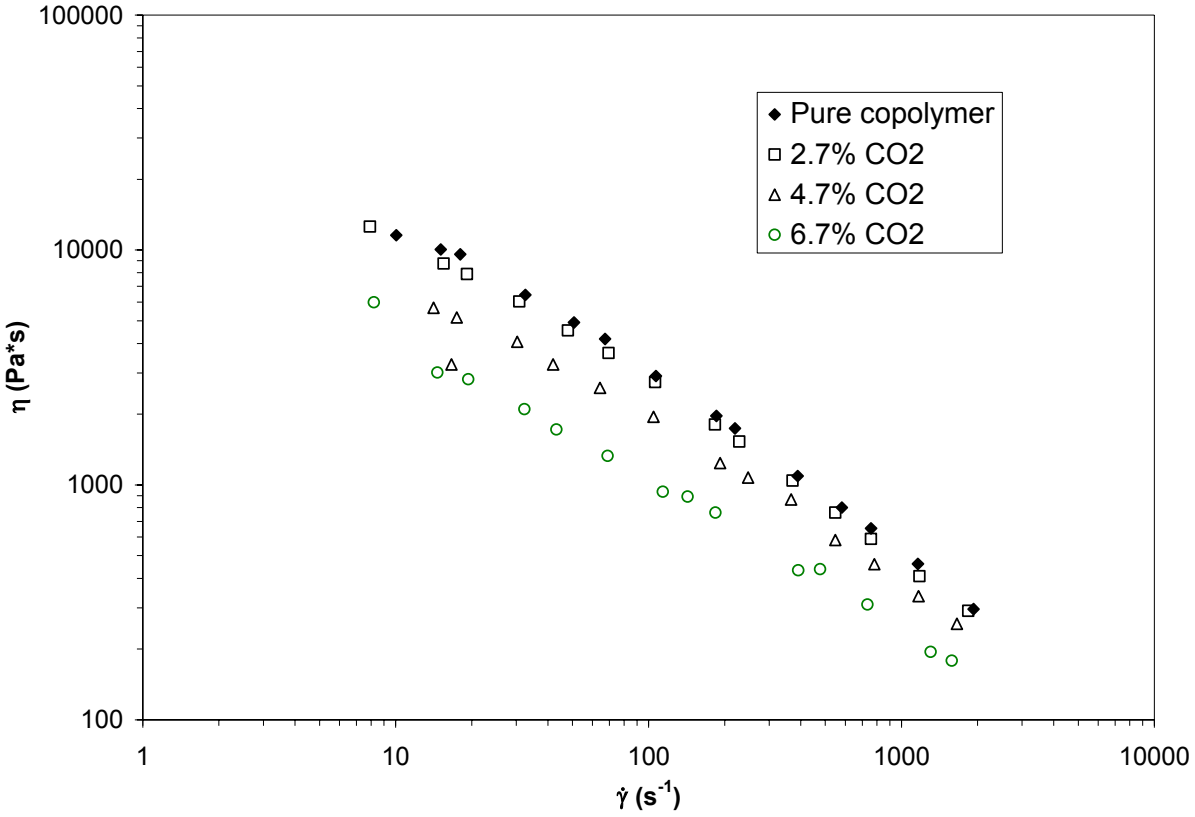

Fig B4: Viscosity reduction of plasticized Barex at 180°C using a L/D = 10. Data has been corrected, as outlined in Chapter 5.

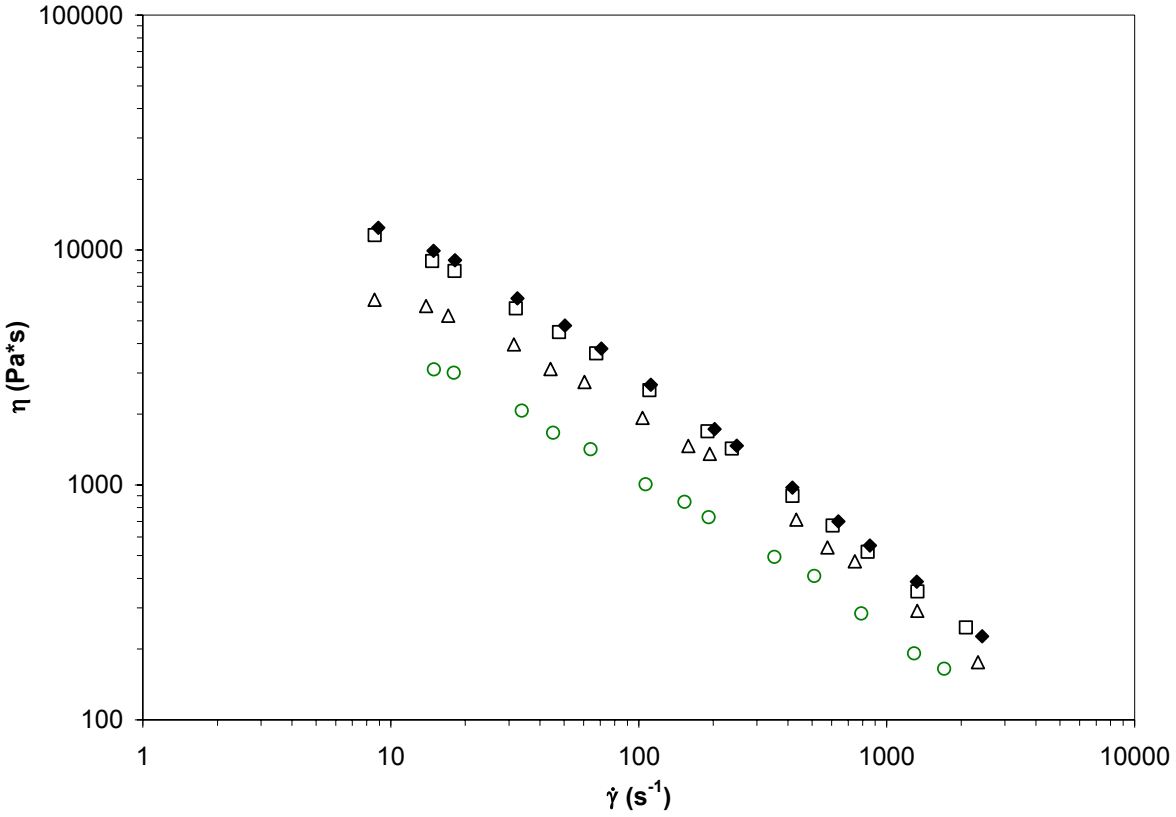

Fig B5: Viscosity reduction of plasticized Barex at 180°C using a L/D = 30. Data has been corrected, as outlined in Chapter 5.

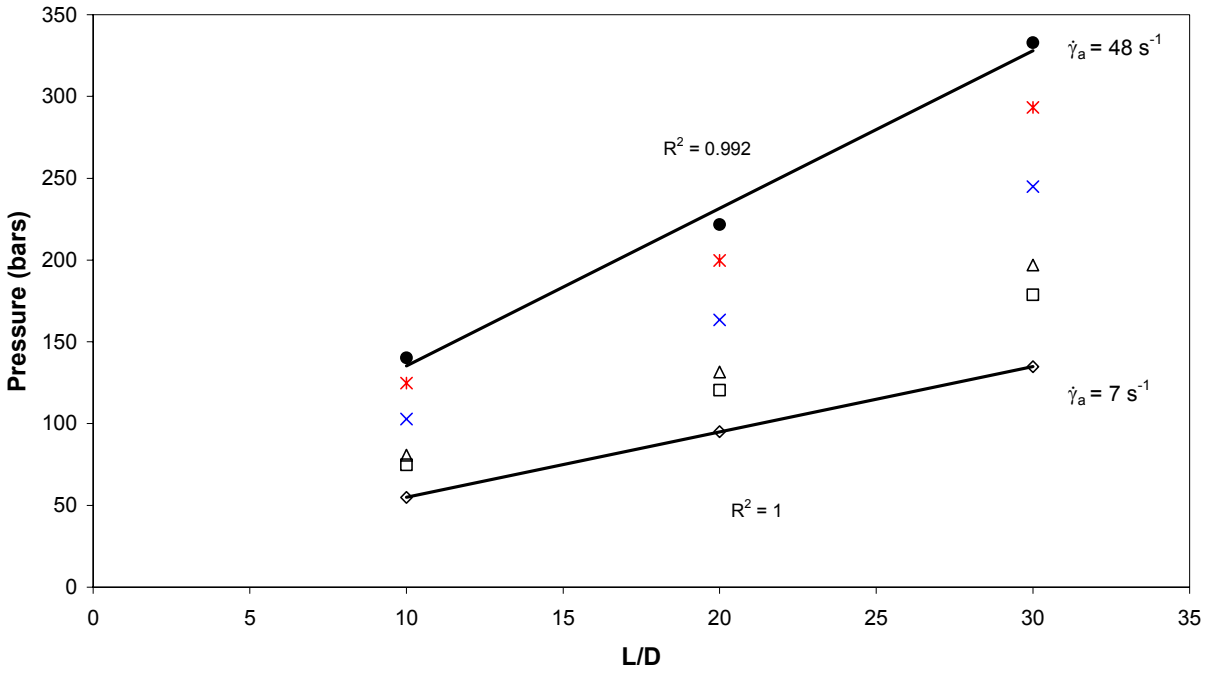

Fig B6: Bagley plots for saturated Barex at 180^{o}C containing 2.7 wt. % absorbed CO_2. Solid lines are linear fits at the highest and lowest rates (in this graph). Similar results were obtained at apparent shear rates up to 1210 s^{-1}.

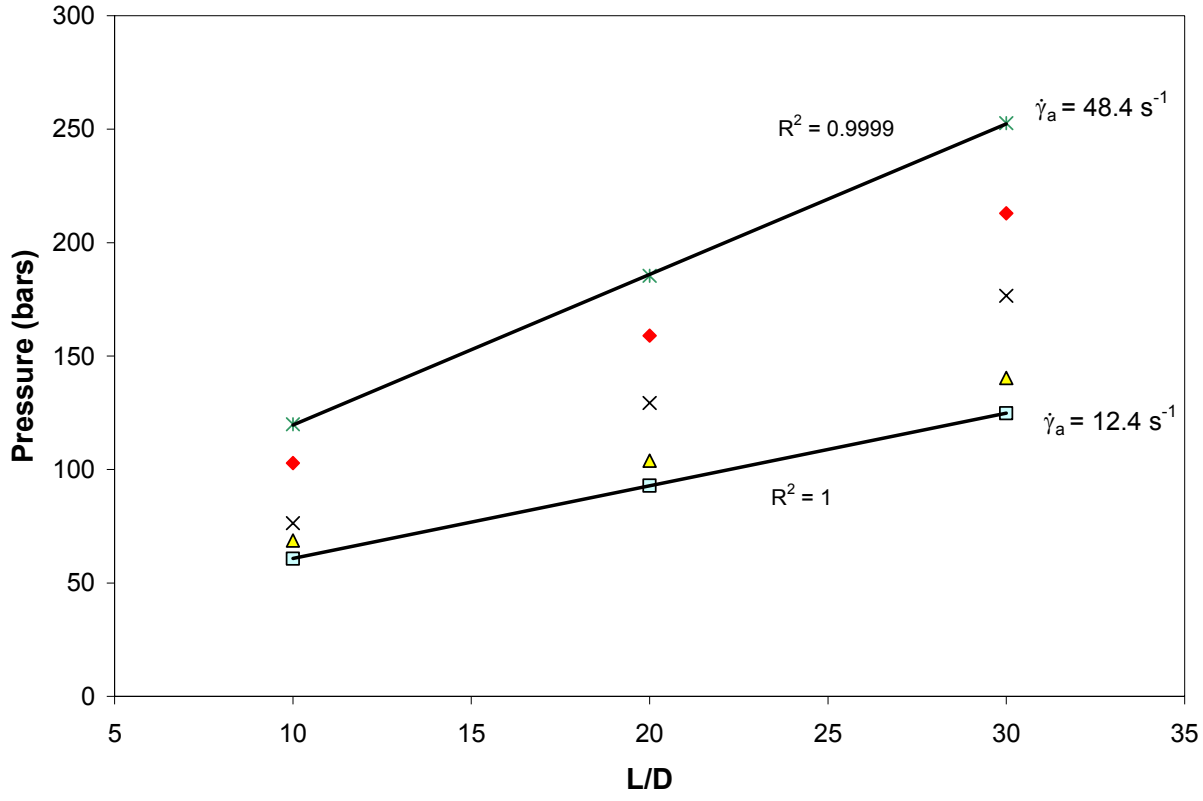

Fig B7: Bagley plots for saturated Barex at 180°C containing 4.7 wt. % absorbed CO_2. Solid lines are linear fits at the highest and lowest rates (in this graph). Similar results were obtained at apparent shear rates up to 1210 s^{-1}.

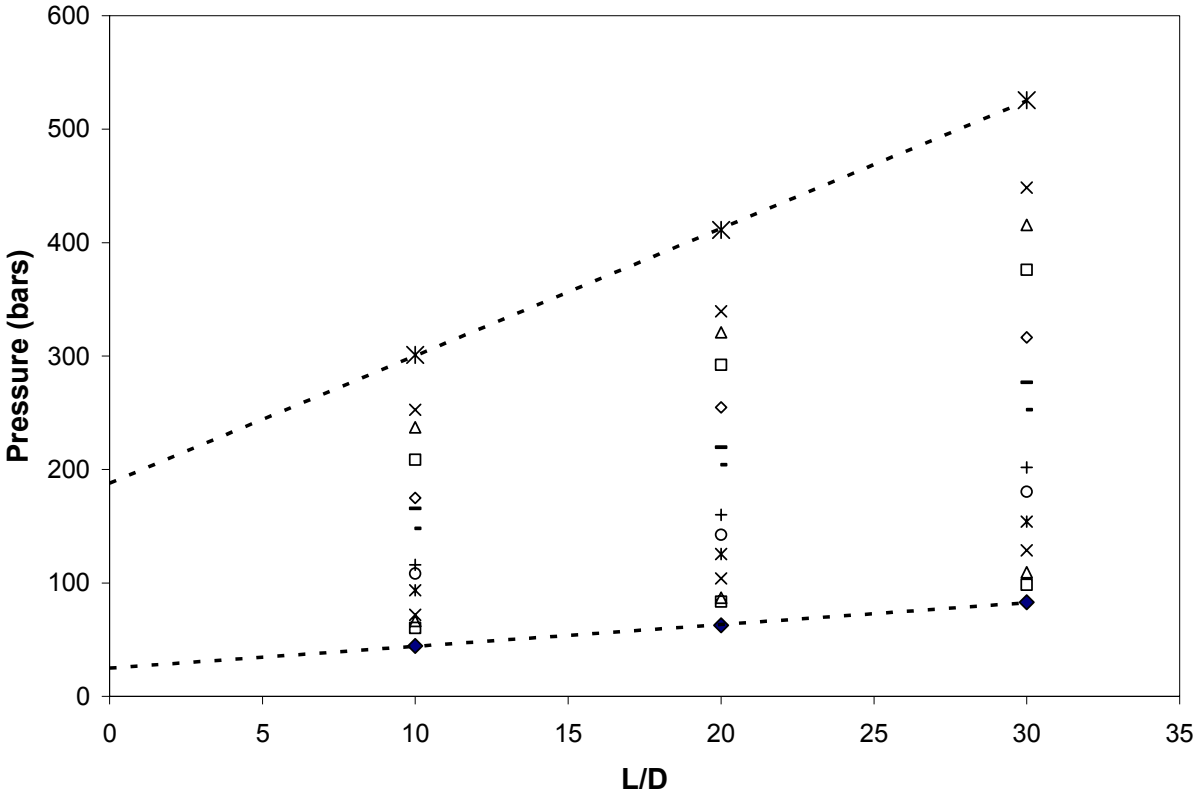

Fig B8: Bagley plots for saturated Barex at 180°C containing 6.7 wt. % absorbed CO_2, covering the shear rate range 7-1210 s^{-1}. Dashed lines are linear fits at the highest and lowest rates.

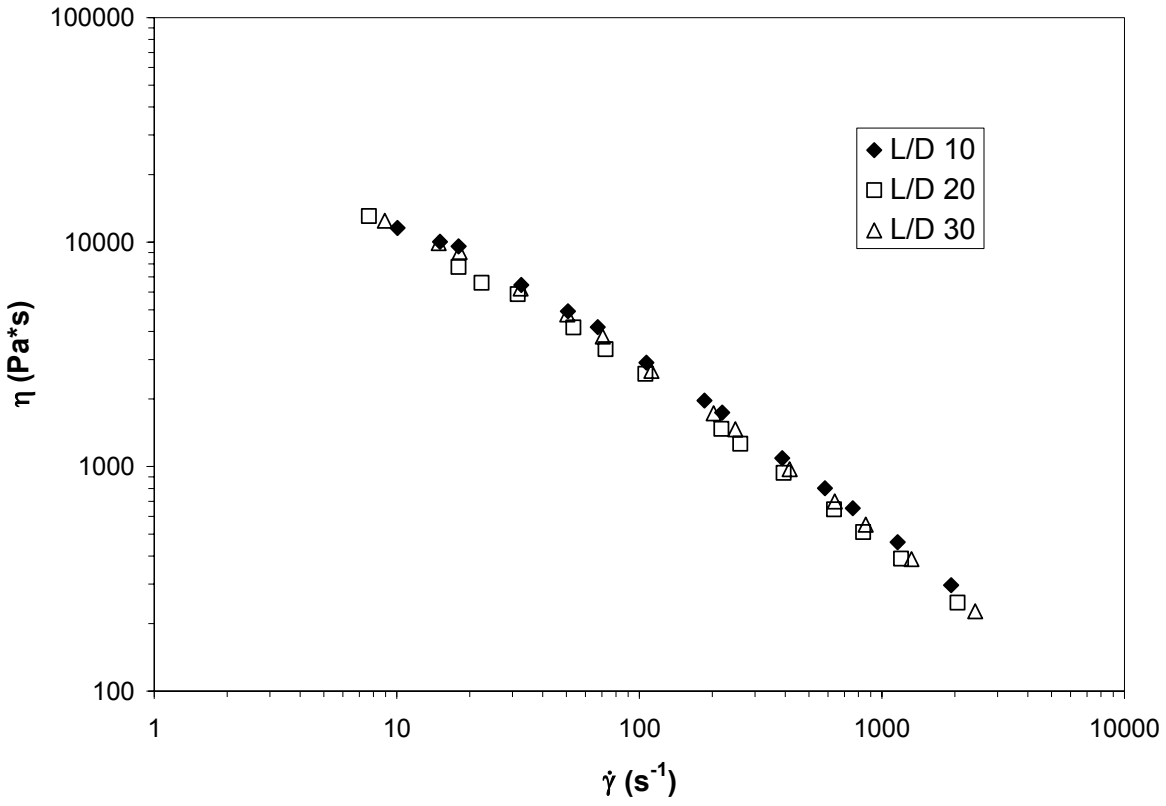

Fig. B9: Corrected viscosity data obtained from the Instron capillary rheometer (ICR, 90 degree entry angle) for pure Barex at three L/Ds. This served as a check for consistency in the data corrections, visualized by the data overlap. Data obtained at 180°C.

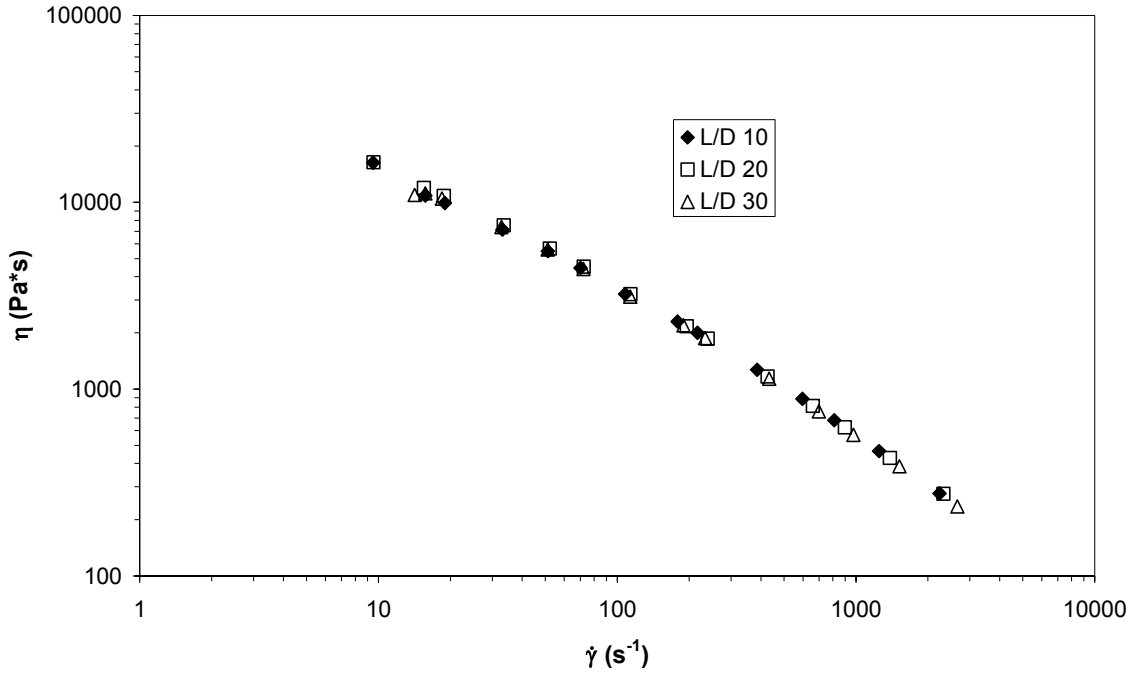

Fig. B10: Corrected viscosity data obtained from the Goettfert capillary rheometer (GCR, 180 degree entry angle) for pure Barex at three L/Ds. Data obtained at 180^{o}C.

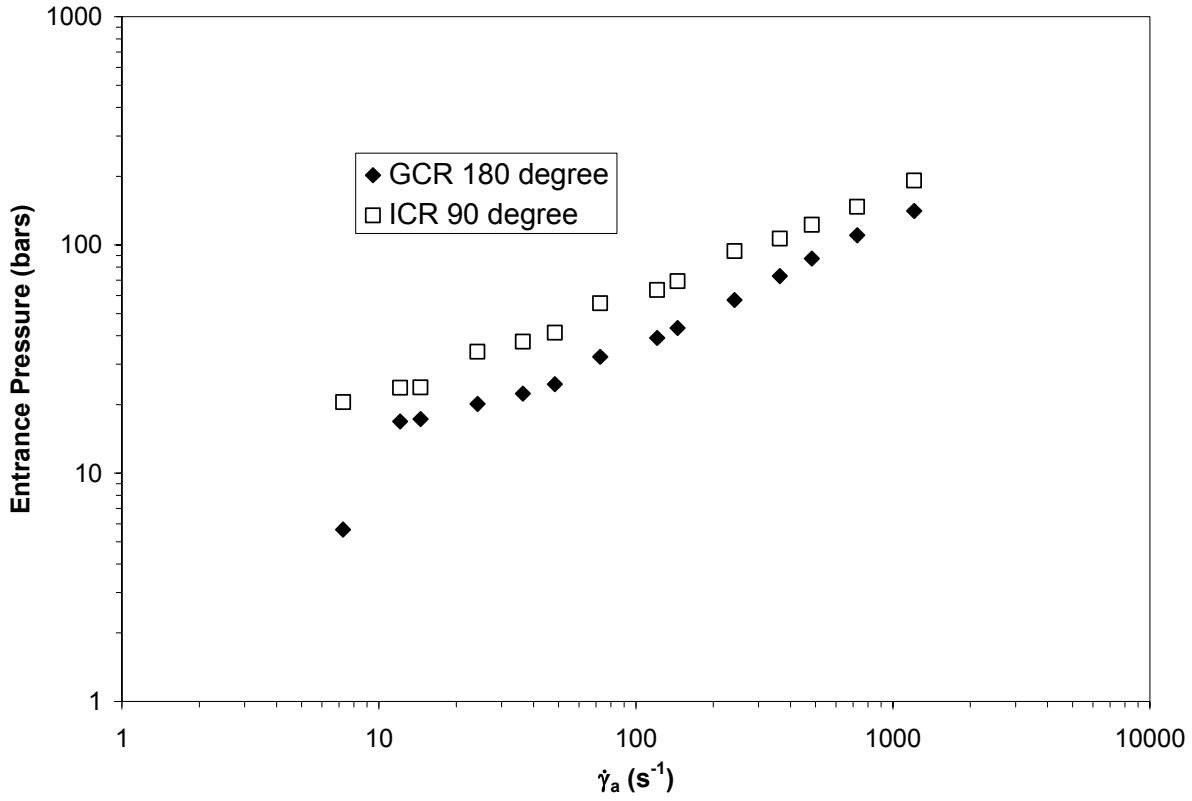

Fig B11: Comparison of the entry pressures obtained from the GCR and ICR to determine effects of entry angle on entrance pressure. Data obtained at 180°C.

Sample: PureBarex
Temp: 180 °C

Piston: 0.953 cm

Capillary: 0.039 in (diameter)
10.00 (L/D)

piston velocity (cm/min)	weight (kg)	pressure (bar)	Q (cm3/s)	apparent s. rate (s^{-1})	apparent s. stress (Pa)	apparent viscosity (Pa*s)	actual s. rate (s^{-1})	actual s. stress (Pa)	actual viscosity (Pa*s)	entrance Δp (bar)
0.06	48.7	67.0	0.001	7.26E+00	1.67E+05	2.31E+04	1.01E+01	1.16E+05	1.16E+04	2.05E+01
0.10	61.2	84.2	0.001	1.21E+01	2.11E+05	1.74E+04	1.51E+01	1.51E+05	1.00E+04	2.37E+01
0.12	67.3	92.7	0.001	1.45E+01	2.32E+05	1.60E+04	1.80E+01	1.72E+05	9.58E+03	2.37E+01
0.20	85.8	118.1	0.002	2.42E+01	2.95E+05	1.22E+04	3.26E+01	2.10E+05	6.44E+03	3.41E+01
0.30	99.9	137.4	0.004	3.63E+01	3.44E+05	9.47E+03	5.07E+01	2.49E+05	4.92E+03	3.77E+01
0.40	111.9	154.0	0.005	4.84E+01	3.85E+05	7.95E+03	6.73E+01	2.82E+05	4.18E+03	4.13E+01
0.60	130.7	180	0.007	7.26E+01	4.50E+05	6.19E+03	1.07E+02	3.11E+05	2.91E+03	5.55E+01
1.0	152.3	210	0.012	1.21E+02	5.24E+05	4.33E+03	1.85E+02	3.65E+05	1.97E+03	6.36E+01
1.2	161.6	222	0.014	1.45E+02	5.56E+05	3.83E+03	2.20E+02	3.82E+05	1.74E+03	6.95E+01
2.0	191.5	264	0.024	2.42E+02	6.59E+05	2.72E+03	3.88E+02	4.24E+05	1.09E+03	9.40E+01
3.0	212.8	293	0.036	3.63E+02	7.32E+05	2.02E+03	5.82E+02	4.66E+05	8.01E+02	1.07E+02
4.0	233.1	321	0.048	4.84E+02	8.02E+05	1.66E+03	7.58E+02	4.95E+05	6.53E+02	1.23E+02
6.0	262.4	361	0.071	7.26E+02	9.03E+05	1.24E+03	1.16E+03	5.36E+05	4.61E+02	1.47E+02
10.0	305.1	420	0.119	1.21E+03	1.05E+06	8.68E+02	1.93E+03	5.71E+05	2.96E+02	1.92E+02

Capillary: 0.039 in (diameter)
20.0 (L/D)

piston velocity (mm/s)	weight (kg)	pressure (bar)	Q (mm3/s)	apparent s. rate (s^{-1})	apparent s. stress (Pa)	apparent viscosity (Pa*s)	actual s. rate (s^{-1})	actual s. stress (Pa)	actual viscosity (Pa*s)
0.06	73.2	100.7	0.001	7.26E+00	1.26E+05	1.74E+04	7.67E+00	1.00E+05	1.31E+04
0.10	98.3	135.2	0.001	1.21E+01	1.69E+05	1.40E+04	1.80E+01	1.39E+05	7.75E+03
0.12	102.9	141.7	0.001	1.45E+01	1.77E+05	1.22E+04	2.24E+01	1.47E+05	6.59E+03
0.20	132.1	181.8	0.002	2.42E+01	2.27E+05	9.40E+03	3.15E+01	1.85E+05	5.86E+03
0.30	156.8	216	0.004	3.63E+01	2.70E+05	7.43E+03	5.34E+01	2.23E+05	4.17E+03
0.40	170.5	235	0.005	4.84E+01	2.93E+05	6.06E+03	7.25E+01	2.42E+05	3.33E+03
0.60	200.0	275	0.007	7.26E+01	3.44E+05	4.74E+03	1.06E+02	2.75E+05	2.59E+03
1.0	233.1	321	0.012	1.21E+02	4.01E+05	3.31E+03	2.18E+02	3.21E+05	1.47E+03
1.2	242.4	334	0.014	1.45E+02	4.17E+05	2.87E+03	2.61E+02	3.30E+05	1.26E+03
2.0	282.9	389	0.024	2.42E+02	4.87E+05	2.01E+03	3.94E+02	3.69E+05	9.38E+02
3.0	315.7	435	0.036	3.63E+02	5.43E+05	1.50E+03	6.35E+02	4.10E+05	6.46E+02
4.0	337.9	465	0.048	4.84E+02	5.81E+05	1.20E+03	8.38E+02	4.28E+05	5.10E+02
6.0	378.7	521	0.071	7.26E+02	6.51E+05	8.98E+02	1.20E+03	4.68E+05	3.89E+02
10.0	434.7	598	0.119	1.21E+03	7.48E+05	6.18E+02	2.05E+03	5.08E+05	2.47E+02

Capillary: 0.039 in (diameter)
30.0 (L/D)

piston velocity (mm/s)	weight (kg)	pressure (bar)	Q (mm3/s)	apparent s. rate (s^{-1})	apparent s. stress (Pa)	apparent viscosity (Pa*s)	actual s. rate (s^{-1})	actual s. stress (Pa)	actual viscosity (Pa*s)
0.06	111.6	153.6	0.001	7.26E+00	1.28E+05	1.76E+04	8.91E+00	1.11E+05	1.24E+04
0.10	145.7	200.6	0.001	1.21E+01	1.67E+05	1.38E+04	1.49E+01	1.47E+05	9.91E+03
0.12	160.3	221	0.001	1.45E+01	1.84E+05	1.27E+04	1.82E+01	1.64E+05	9.04E+03
0.20	200.5	276	0.002	2.42E+01	2.30E+05	9.51E+03	3.24E+01	2.02E+05	6.22E+03
0.30	237.1	326	0.004	3.63E+01	2.72E+05	7.49E+03	5.05E+01	2.40E+05	4.76E+03
0.40	264.0	363	0.005	4.84E+01	3.03E+05	6.26E+03	7.06E+01	2.68E+05	3.80E+03
0.60	300.8	414	0.007	7.26E+01	3.45E+05	4.75E+03	1.12E+02	2.99E+05	2.67E+03
1.0	351.7	484	0.012	1.21E+02	4.03E+05	3.33E+03	2.02E+02	3.50E+05	1.73E+03
1.2	368.7	507	0.014	1.45E+02	4.23E+05	2.91E+03	2.49E+02	3.65E+05	1.47E+03
2.0	422.0	581	0.024	2.42E+02	4.84E+05	2.00E+03	4.16E+02	4.06E+05	9.74E+02
3.0	467.3	643	0.036	3.63E+02	5.36E+05	1.48E+03	6.39E+02	4.47E+05	7.00E+02
4.0	501.3	690	0.048	4.84E+02	5.75E+05	1.19E+03	8.57E+02	4.73E+05	5.52E+02
6.0	554.0	762	0.071	7.26E+02	6.35E+05	8.75E+02	1.32E+03	5.13E+05	3.88E+02
10.0	618.7	851	0.119	1.21E+03	7.10E+05	5.87E+02	2.42E+03	5.50E+05	2.27E+02

Table B1: ICR capillary data for pure Barex at 180°C.

Sample: saturated Barex
Temp: 180 °C

Piston: 0.953 cm

Capillary: 0.039 in (diameter)
10.00 (L/D)

piston velocity (cm/min)	weight (kg)	pressure (bars)	Q (cm^3/s)	corrected ΔP (bars)	apparent s. rate (s^{-1})	apparent s. stress (Pa)	apparent viscosity (Pa*s)	actual s. stress (Pa)	actual viscosity (Pa*s)	entrance Δp (bar)
0.06	90.0	124	0.001	54.935	7.26E+00	1.37E+05	1.89E+04	9.95E+04	1.26E+04	1.51E+01
0.10	104.4	144	0.001	74.753	1.21E+01	1.87E+05	1.54E+04	1.35E+05	8.75E+03	2.06E+01
0.12	108.8	150	0.001	80.809	1.45E+01	2.02E+05	1.39E+04	1.51E+05	7.90E+03	2.03E+01
0.20	124.8	172	0.002	102.829	2.42E+01	2.57E+05	1.06E+04	1.86E+05	6.03E+03	2.83E+01
0.30	140.8	194	0.004	124.849	3.63E+01	3.12E+05	8.60E+03	2.18E+05	4.54E+03	3.75E+01
0.40	152.0	209	0.005	140.263	4.84E+01	3.51E+05	7.25E+03	2.53E+05	3.65E+03	3.90E+01
0.60	165.6	228	0.007	158.980	7.26E+01	3.97E+05	5.48E+03	2.91E+05	2.74E+03	4.26E+01
1.0	192	264	0.012	195.314	1.21E+02	4.88E+05	4.04E+03	3.31E+05	1.81E+03	6.28E+01
1.2	200	275	0.014	206.324	1.45E+02	5.16E+05	3.55E+03	3.50E+05	1.53E+03	6.65E+01
2.0	226	310	0.024	241.556	2.42E+02	6.04E+05	2.50E+03	3.87E+05	1.04E+03	8.67E+01
3.0	250	345	0.036	275.687	3.63E+02	6.89E+05	1.90E+03	4.17E+05	7.62E+02	1.09E+02
4.0	270.4	372	0.048	303.212	4.84E+02	7.58E+05	1.57E+03	4.47E+05	5.89E+02	1.24E+02
6.0	296	407	0.071	338.445	7.26E+02	8.46E+05	1.17E+03	4.82E+05	4.09E+02	1.46E+02
10.0	338	465	0.119	395.697	1.21E+03	9.89E+05	8.18E+02	5.35E+05	2.91E+02	1.82E+02

Capillary: 0.039 in (diameter)
20.00 (L/D)

piston velocity (cm/min)	weight (kg)	pressure (bars)	Q (cm^3/s)	corrected ΔP (bars)	apparent s. rate (s^{-1})	apparent s. stress (Pa)	apparent viscosity (Pa*s)	actual s. stress (Pa)	real actual viscosity (Pa*s)
0.06	119.2	164	0.001	95.122	7.26E+00	1.19E+05	1.64E+04	1.00E+05	1.05E+04
0.10	137.6	189	0.001	120.445	1.21E+01	1.51E+05	1.24E+04	1.25E+05	8.08E+03
0.12	145.6	200	0.001	131.455	1.45E+01	1.64E+05	1.13E+04	1.39E+05	7.44E+03
0.20	168.8	232	0.002	163.384	2.42E+01	2.04E+05	8.44E+03	1.69E+05	5.42E+03
0.30	195.2	269	0.004	199.718	3.63E+01	2.50E+05	6.88E+03	2.03E+05	4.15E+03
0.40	211.2	291	0.005	221.738	4.84E+01	2.77E+05	5.73E+03	2.28E+05	3.12E+03
0.60	230.4	317	0.007	248.162	7.26E+01	3.10E+05	4.27E+03	2.57E+05	2.35E+03
1.0	271	373	0.012	304.313	1.21E+02	3.80E+05	3.14E+03	3.02E+05	1.63E+03
1.2	283	390	0.014	320.829	1.45E+02	4.01E+05	2.76E+03	3.18E+05	1.34E+03
2.0	317	436	0.024	367.071	2.42E+02	4.59E+05	1.90E+03	3.50E+05	9.06E+02
3.0	354	487	0.036	417.717	3.63E+02	5.22E+05	1.44E+03	3.86E+05	6.74E+02
4.0	380	523	0.048	454.051	4.84E+02	5.68E+05	1.17E+03	4.12E+05	5.02E+02
6.0	412	567	0.071	498.091	7.26E+02	6.23E+05	8.58E+02	4.40E+05	3.35E+02
10.0	460	633	0.119	564.152	1.21E+03	7.05E+05	5.83E+02	4.78E+05	2.27E+02

Capillary: 0.039 in (diameter)
30.00 (L/D)

piston velocity (cm/min)	weight (kg)	pressure (bars)	Q (cm^3/s)	corrected ΔP (bars)	apparent s. rate (s^{-1})	apparent s. stress (Pa)	apparent viscosity (Pa*s)	actual s. stress (Pa)	real actual viscosity (Pa*s)
0.06	148.0	204	0.001	134.758	7.26E+00	1.12E+05	1.55E+04	9.97E+04	1.16E+04
0.10	180.0	248	0.001	178.798	1.21E+01	1.49E+05	1.23E+04	1.32E+05	8.96E+03
0.12	193.2	266	0.001	196.965	1.45E+01	1.64E+05	1.13E+04	1.47E+05	8.14E+03
0.20	228.0	314	0.002	244.859	2.42E+01	2.04E+05	8.43E+03	1.80E+05	5.64E+03
0.30	263.2	362	0.004	293.303	3.63E+01	2.44E+05	6.74E+03	2.13E+05	4.47E+03
0.40	292.0	402	0.005	332.940	4.84E+01	2.77E+05	5.73E+03	2.45E+05	3.63E+03
0.60	324.8	447	0.007	378.081	7.26E+01	3.15E+05	4.34E+03	2.80E+05	2.53E+03
1.0	376	517	0.012	448.546	1.21E+02	3.74E+05	3.09E+03	3.21E+05	1.69E+03
1.2	394	542	0.014	473.318	1.45E+02	3.94E+05	2.72E+03	3.39E+05	1.43E+03
2.0	440	606	0.024	536.626	2.42E+02	4.47E+05	1.85E+03	3.75E+05	8.97E+02
3.0	484	666	0.036	597.182	3.63E+02	4.98E+05	1.37E+03	4.07E+05	6.71E+02
4.0	520	716	0.048	646.727	4.84E+02	5.39E+05	1.11E+03	4.35E+05	5.18E+02
6.0	564	776	0.071	707.283	7.26E+02	5.89E+05	8.12E+02	4.68E+05	3.52E+02
10.0	632	870	0.119	800.868	1.21E+03	6.67E+05	5.52E+02	5.16E+05	2.47E+02

Table B2: ICR capillary data for Barex at 180°C containing 2.7% absorbed CO_2.

Sample: saturated Barex
Temp: 180 °C

Piston: 0.953 cm

Capillary: 0.039 in (diameter)
10.00 (L/D)

piston velocity (cm/min)	weight (kg)	pressure (bars)	Q (cm^3/s)	corrected ΔP (bars)	apparent s. rate (s^{-1})	apparent s. stress (Pa)	apparent viscosity (Pa*s)	actual s. rate (s^{-1})	actual s. stress (Pa)	actual viscosity (Pa*s)	entrance Δp (bar)
0.06	86.4	119	0.001	49.980	7.26E+00	1.25E+05	1.72E+04	1.66E+01	5.41E+04	3.26E+03	2.83E+01
0.10	94.2	130	0.001	60.715	1.21E+01	1.52E+05	1.25E+04	1.41E+01	8.01E+04	5.67E+03	2.87E+01
0.12	100.0	138	0.001	68.698	1.45E+01	1.72E+05	1.18E+04	1.74E+01	8.99E+04	5.16E+03	3.27E+01
0.20	105.6	145	0.002	76.405	2.42E+01	1.91E+05	7.90E+03	3.02E+01	1.23E+05	4.07E+03	2.72E+01
0.30	124.8	172	0.004	102.829	3.63E+01	2.57E+05	7.08E+03	4.19E+01	1.37E+05	3.26E+03	4.81E+01
0.40	137.2	189	0.005	119.894	4.84E+01	3.00E+05	6.19E+03	6.43E+01	1.67E+05	2.59E+03	5.33E+01
0.60	148.0	204	0.007	134.758	7.26E+01	3.37E+05	4.64E+03	1.05E+02	2.04E+05	1.95E+03	5.33E+01
1.0	174	239	0.012	169.990	1.21E+02	4.25E+05	3.51E+03	1.92E+02	2.38E+05	1.24E+03	7.49E+01
1.2	179	247	0.014	177.697	1.45E+02	4.44E+05	3.06E+03	2.48E+02	2.66E+05	1.07E+03	7.13E+01
2.0	202	277	0.024	208.526	2.42E+02	5.21E+05	2.15E+03	3.66E+02	3.17E+05	8.68E+02	8.15E+01
3.0	224	308	0.036	239.354	3.63E+02	5.98E+05	1.65E+03	5.48E+02	3.19E+05	5.82E+02	1.12E+02
4.0	240.8	331	0.048	262.475	4.84E+02	6.56E+05	1.36E+03	7.81E+02	3.59E+05	4.60E+02	1.19E+02
6.0	260.8	359	0.071	290.000	7.26E+02	7.25E+05	9.99E+02	1.17E+03	3.93E+05	3.36E+02	1.33E+02
10.0	302	415	0.119	346.152	1.21E+03	8.65E+05	7.15E+02	1.66E+03	4.25E+05	2.56E+02	1.76E+02

Capillary: 0.039 in (diameter)
20.00 (L/D)

piston velocity (cm/min)	weight (kg)	pressure (bars)	Q (cm^3/s)	corrected ΔP (bars)	apparent s. rate (s^{-1})	apparent s. stress (Pa)	apparent viscosity (Pa*s)	actual s. rate (s^{-1})	actual s. stress (Pa)	real actual viscosity (Pa*s)
0.06	100.0	138	0.001	68.698	7.26E+00	8.59E+04	1.18E+04	8.60E+00	5.05E+04	5.87E+03
0.10	117.6	162	0.001	92.920	1.21E+01	1.16E+05	9.60E+03	1.40E+01	8.03E+04	5.72E+03
0.12	125.6	173	0.001	103.930	1.45E+01	1.30E+05	8.95E+03	1.73E+01	8.90E+04	5.14E+03
0.20	144.0	198	0.002	129.253	2.42E+01	1.62E+05	6.68E+03	3.09E+01	1.28E+05	4.12E+03
0.30	165.6	228	0.004	158.980	3.63E+01	1.99E+05	5.48E+03	4.45E+01	1.39E+05	3.11E+03
0.40	184.8	254	0.005	185.404	4.84E+01	2.32E+05	4.79E+03	6.46E+01	1.65E+05	2.56E+03
0.60	200.8	276	0.007	207.425	7.26E+01	2.59E+05	3.57E+03	1.10E+02	1.93E+05	1.75E+03
1.0	234	321	0.012	252.566	1.21E+02	3.16E+05	2.61E+03	1.60E+02	2.22E+05	1.39E+03
1.2	250	344	0.014	274.586	1.45E+02	3.43E+05	2.36E+03	1.99E+02	2.54E+05	1.28E+03
2.0	277	381	0.024	312.020	2.42E+02	3.90E+05	1.61E+03	4.01E+02	2.88E+05	7.18E+02
3.0	306	421	0.036	351.657	3.63E+02	4.40E+05	1.21E+03	5.39E+02	3.00E+05	5.56E+02
4.0	334.4	460	0.048	391.293	4.84E+02	4.89E+05	1.01E+03	7.40E+02	3.40E+05	4.60E+02
6.0	364.8	502	0.071	433.131	7.26E+02	5.41E+05	7.46E+02	1.33E+03	3.75E+05	2.83E+02
10.0	400	551	0.119	481.576	1.21E+03	6.02E+05	4.98E+02	2.55E+03	3.82E+05	1.49E+02

Capillary: 0.039 in (diameter)
30.00 (L/D)

piston velocity (cm/min)	weight (kg)	pressure (bars)	Q (cm^3/s)	corrected ΔP (bars)	apparent s. rate (s^{-1})	apparent s. stress (Pa)	apparent viscosity (Pa*s)	actual s. rate (s^{-1})	actual s. stress (Pa)	real actual viscosity (Pa*s)
0.06	116.8	161	0.001	91.819	7.26E+00	7.65E+04	1.05E+04	8.60E+00	5.29E+04	6.15E+03
0.10	140.8	194	0.001	124.849	1.21E+01	1.04E+05	8.60E+03	1.39E+01	8.01E+04	5.77E+03
0.12	152.0	209	0.001	140.263	1.45E+01	1.17E+05	8.05E+03	1.70E+01	8.96E+04	5.26E+03
0.20	178.4	246	0.002	176.596	2.42E+01	1.47E+05	6.08E+03	3.14E+01	1.24E+05	3.97E+03
0.30	204.8	282	0.004	212.930	3.63E+01	1.77E+05	4.89E+03	4.41E+01	1.37E+05	3.12E+03
0.40	233.6	321	0.005	252.566	4.84E+01	2.10E+05	4.35E+03	6.05E+01	1.66E+05	2.75E+03
0.60	263.2	362	0.007	293.303	7.26E+01	2.44E+05	3.37E+03	1.04E+02	2.00E+05	1.93E+03
1.0	307	423	0.012	353.859	1.21E+02	2.95E+05	2.44E+03	1.59E+02	2.32E+05	1.47E+03
1.2	330	455	0.014	385.788	1.45E+02	3.21E+05	2.21E+03	1.93E+02	2.62E+05	1.36E+03
2.0	378	520	0.024	450.748	2.42E+02	3.76E+05	1.55E+03	4.32E+02	3.08E+05	7.12E+02
3.0	404	556	0.036	487.081	3.63E+02	4.06E+05	1.12E+03	5.78E+02	3.13E+05	5.42E+02
4.0	444	611	0.048	542.131	4.84E+02	4.52E+05	9.34E+02	7.45E+02	3.53E+05	4.73E+02
6.0	484	666	0.071	597.182	7.26E+02	4.98E+05	6.86E+02	1.33E+03	3.87E+05	2.91E+02
10.0	536	738	0.119	668.747	1.21E+03	5.57E+05	4.61E+02	2.33E+03	4.10E+05	1.76E+02

Table B3: ICR capillary data for Barex at 180°C containing 4.7% absorbed CO_2.

Sample: saturated Barex
Temp: 180 °C

Piston: 0.953 cm

Capillary: 0.039 in (diameter)
10.00 (L/D)

piston velocity (cm/min)	weight (kg)	pressure (bars)	Q (cm^3/s)	corrected ΔP (bars)	apparent s. rate (s^{-1})	apparent s. stress (Pa)	apparent viscosity (Pa*s)	actual s. rate (s^{-1})	actual s. stress (Pa)	actual viscosity (Pa*s)	entrance Δp (bar)
0.06	82.4	113	0.001	44.475	7.26E+00	1.11E+05	1.53E+04	8.21E+00	4.91E+04	5.98E+03	2.48E+01
0.10	94.0	129	0.001	60.440	1.21E+01	1.51E+05	1.25E+04	1.46E+01	4.40E+04	3.01E+03	4.28E+01
0.12	98.4	135	0.001	66.496	1.45E+01	1.66E+05	1.15E+04	1.94E+01	5.46E+04	2.82E+03	4.47E+01
0.20	102.4	141	0.002	72.001	2.42E+01	1.80E+05	7.44E+03	3.23E+01	6.79E+04	2.10E+03	4.48E+01
0.30	118.0	162	0.004	93.470	3.63E+01	2.34E+05	6.44E+03	4.32E+01	7.43E+04	1.72E+03	6.37E+01
0.40	128.8	177	0.005	108.334	4.84E+01	2.71E+05	5.60E+03	6.89E+01	9.18E+04	1.33E+03	7.16E+01
0.60	134.4	185	0.007	116.041	7.26E+01	2.90E+05	4.00E+03	1.14E+02	1.06E+05	9.34E+02	7.35E+01
1.0	158	217	0.012	147.970	1.21E+02	3.70E+05	3.06E+03	1.43E+02	1.28E+05	8.93E+02	9.70E+01
1.2	170	235	0.014	165.586	1.45E+02	4.14E+05	2.85E+03	1.84E+02	1.40E+05	7.63E+02	1.09E+02
2.0	177	244	0.024	174.945	2.42E+02	4.37E+05	1.81E+03	3.91E+02	1.69E+05	4.33E+02	1.07E+02
3.0	202	277	0.036	208.526	3.63E+02	5.21E+05	1.44E+03	4.78E+02	2.09E+05	4.38E+02	1.25E+02
4.0	222.4	306	0.048	237.152	4.84E+02	5.93E+05	1.23E+03	7.34E+02	2.28E+05	3.10E+02	1.46E+02
6.0	233.6	321	0.071	252.566	7.26E+02	6.31E+05	8.70E+02	1.30E+03	2.54E+05	1.95E+02	1.51E+02
10.0	269	370	0.119	301.010	1.21E+03	7.53E+05	6.22E+02	1.58E+03	2.83E+05	1.79E+02	1.88E+02

Capillary: 0.039 in (diameter)
20.00 (L/D)

piston velocity (cm/min)	weight (kg)	pressure (bars)	Q (cm^3/s)	corrected ΔP (bars)	apparent s. rate (s^{-1})	apparent s. stress (Pa)	apparent viscosity (Pa*s)	actual s. rate (s^{-1})	actual s. stress (Pa)	real actual viscosity (Pa*s)
0.06	95.6	132	0.001	62.642	7.26E+00	7.83E+04	1.08E+04	7.65E+00	4.73E+04	6.18E+03
0.10	110.8	152	0.001	83.561	1.21E+01	1.04E+05	8.63E+03	1.90E+01	5.09E+04	2.68E+03
0.12	113.2	156	0.001	86.864	1.45E+01	1.09E+05	7.48E+03	2.55E+01	5.28E+04	2.07E+03
0.20	125.6	173	0.002	103.930	2.42E+01	1.30E+05	5.37E+03	3.28E+01	7.39E+04	2.25E+03
0.30	141.2	194	0.004	125.399	3.63E+01	1.57E+05	4.32E+03	4.73E+01	7.71E+04	1.63E+03
0.40	153.6	211	0.005	142.465	4.84E+01	1.78E+05	3.68E+03	6.82E+01	8.85E+04	1.30E+03
0.60	166.4	229	0.007	160.081	7.26E+01	2.00E+05	2.76E+03	1.03E+02	1.08E+05	1.05E+03
1.0	198	273	0.012	204.122	1.21E+02	2.55E+05	2.11E+03	1.63E+02	1.34E+05	8.23E+02
1.2	210	288	0.014	219.536	1.45E+02	2.74E+05	1.89E+03	2.07E+02	1.38E+05	6.66E+02
2.0	235	324	0.024	254.768	2.42E+02	3.18E+05	1.32E+03	3.72E+02	1.84E+05	4.96E+02
3.0	262	361	0.036	292.202	3.63E+02	3.65E+05	1.01E+03	5.47E+02	2.09E+05	3.83E+02
4.0	283.2	390	0.048	320.829	4.84E+02	4.01E+05	8.29E+02	8.51E+02	2.18E+05	2.57E+02
6.0	296.8	408	0.071	339.546	7.26E+02	4.24E+05	5.85E+02	1.29E+03	2.36E+05	1.83E+02
10.0	349	480	0.119	411.111	1.21E+03	5.14E+05	4.25E+02	1.51E+03	2.79E+05	1.85E+02

Capillary: 0.039 in (diameter)
30.00 (L/D)

piston velocity (cm/min)	weight (kg)	pressure (bars)	Q (cm^3/s)	corrected ΔP (bars)	apparent s. rate (s^{-1})	apparent s. stress (Pa)	apparent viscosity (Pa*s)	actual s. rate (s^{-1})	actual s. stress (Pa)	real actual viscosity (Pa*s)
0.06	110.4	152	0.001	83.011	7.26E+00	6.92E+04	9.53E+03	1.75E+01	4.85E+04	2.77E+03
0.10	121.6	167	0.001	98.425	1.21E+01	8.20E+04	6.78E+03	1.49E+01	4.63E+04	3.10E+03
0.12	129.6	178	0.001	109.435	1.45E+01	9.12E+04	6.28E+03	1.80E+01	5.40E+04	3.00E+03
0.20	143.6	198	0.002	128.703	2.42E+01	1.07E+05	4.43E+03	3.38E+01	6.99E+04	2.07E+03
0.30	162.0	223	0.004	154.026	3.63E+01	1.28E+05	3.54E+03	4.52E+01	7.52E+04	1.67E+03
0.40	181.2	249	0.005	180.450	4.84E+01	1.50E+05	3.11E+03	6.40E+01	9.07E+04	1.42E+03
0.60	196.8	271	0.007	201.920	7.26E+01	1.68E+05	2.32E+03	1.07E+02	1.07E+05	1.00E+03
1.0	234	321	0.012	252.566	1.21E+02	2.10E+05	1.74E+03	1.53E+02	1.30E+05	8.47E+02
1.2	251	346	0.014	276.788	1.45E+02	2.31E+05	1.59E+03	1.92E+02	1.39E+05	7.28E+02
2.0	280	385	0.024	316.425	2.42E+02	2.64E+05	1.09E+03	3.53E+02	1.74E+05	4.94E+02
3.0	323	445	0.036	375.879	3.63E+02	3.13E+05	8.63E+02	5.11E+02	2.09E+05	4.09E+02
4.0	352	484	0.048	415.515	4.84E+02	3.46E+05	7.16E+02	7.92E+02	2.24E+05	2.84E+02
6.0	376	517	0.071	448.546	7.26E+02	3.74E+05	5.15E+02	1.29E+03	2.48E+05	1.92E+02
10.0	432	595	0.119	525.616	1.21E+03	4.38E+05	3.62E+02	1.71E+03	2.81E+05	1.65E+02

Table B4: ICR capillary data for Barex at 180°C containing 6.7% absorbed CO_2.

Sample: Dajac 85/15
Temp: 200 °C

Piston: 0.953 cm

pure polymer
Capillary: 0.027 in (diameter)
111.11 (L/D)

piston velocity (cm/min)	weight (kg)	pressure (bar)	Q (cm3/s)	apparent s. rate (s^{-1})	apparent s. stress (Pa)	apparent viscosity (Pa*s)
0.03	40.4	55.6	0.0004	1.13E+01	1.25E+04	1.11E+03
0.06	72.8	100.2	0.0007	2.25E+01	2.25E+04	1.00E+03
0.10	116.0	159.6	0.0012	3.75E+01	3.59E+04	9.58E+02
0.12	140.4	193.2	0.0014	4.50E+01	4.35E+04	9.66E+02
0.20	197.6	271.9	0.0024	7.50E+01	6.12E+04	8.16E+02
0.30	271.2	373.2	0.0036	1.13E+02	8.40E+04	7.46E+02
0.40	341.6	470	0.0048	1.50E+02	1.06E+05	7.05E+02
0.60	436.0	600	0.0071	2.25E+02	1.35E+05	6.00E+02
1.0	564.0	776	0.0119	3.75E+02	1.75E+05	4.66E+02
1.2	626.0	862	0.0143	4.50E+02	1.94E+05	4.31E+02
2.0	822.0	1131	0.0238	7.50E+02	2.55E+05	3.39E+02
3.0	884.0	1217	0.0356	1.13E+03	2.74E+05	2.43E+02
4.0	984.0	1354	0.0475	1.50E+03	3.05E+05	2.03E+02
6.0	1104.0	1519	0.0713	2.25E+03	3.42E+05	1.52E+02

polymer containing 5.6 wt. % CO2
Capillary: 0.027 in (diameter)
111.11 (L/D)

piston velocity (mm/s)	weight (kg)	pressure (bars)	Q (cm^3/s)	corrected ΔP (bars)	apparent s. rate (s^{-1})	apparent s. stress (Pa)	apparent viscosity (Pa*s)
0.03	78.4	108	0.000	38.970	1.13E+01	8.77E+03	7.79E+02
0.06	92.8	128	0.001	58.788	2.25E+01	1.32E+04	5.88E+02
0.10	103.2	142	0.001	73.102	3.75E+01	1.64E+04	4.39E+02
0.20	127.2	175	0.002	106.132	7.50E+01	2.39E+04	3.18E+02
0.30	153.6	211	0.004	142.465	1.13E+02	3.21E+04	2.85E+02
0.60	196.8	271	0.007	201.920	2.25E+02	4.54E+04	2.02E+02
1.0	219.2	302	0.012	232.748	3.75E+02	5.24E+04	1.40E+02
2.0	308.0	424	0.024	354.960	7.50E+02	7.99E+04	1.06E+02
6.0	536.0	738	0.071	668.747	2.25E+03	1.50E+05	6.69E+01

Table B5: ICR capillary data for the 85/15 AN/MA copolymer (in Table 3.1), both pure and containing 5.6 wt % absorbed CO_2. T = 200°C.

pure Amlon		*Amlon containing 2.0 wt % CO2*		*Amlon containing 3.0 wt % CO2*	
rate	**apparent viscosity**	**rate**	**apparent viscosity**	**rate**	**apparent viscosity**
(s^{-1})	*(Pa s)*	*(s^{-1})*	*(Pa s)*	*(s^{-1})*	*(Pa s)*
20.2	1700.7	21.3	1095.3	24	638
48.1	1686.3	47.4	1016.8	45.3	560
84.7	1204.4	80.8	834.7	77.4	539
181.8	1089.1	167.9	752.6	123	493
311	728	264.5	595.6	228	435
621.8	533.5	562.8	444.1	413	352
1848.9	209.1	1322.8	231.4	787	264
				1430	179

Table B6: ICR capillary data for Amlon, both pure and containing 2.0 and 3.0 wt % absorbed CO_2. T = 220^{o}C.

Appendix C: Thermal Analysis Data

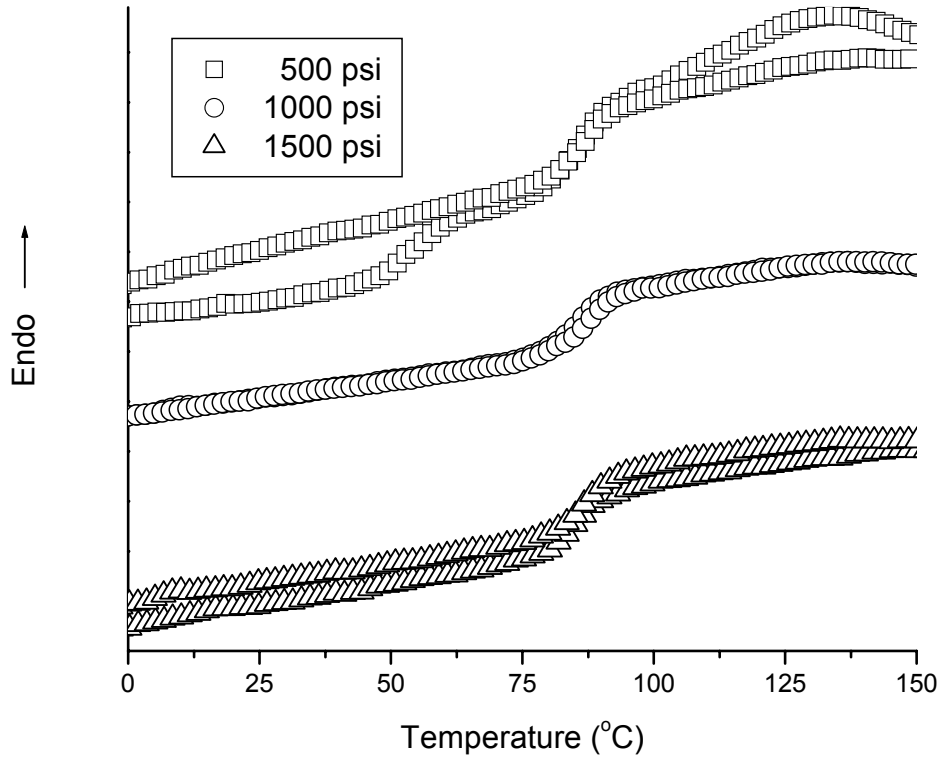

Fig C1: DSC of Barex saturated with nitrogen at the above listed pressures and 120°C, and analyzed by the methods outlined in Chapter 5.

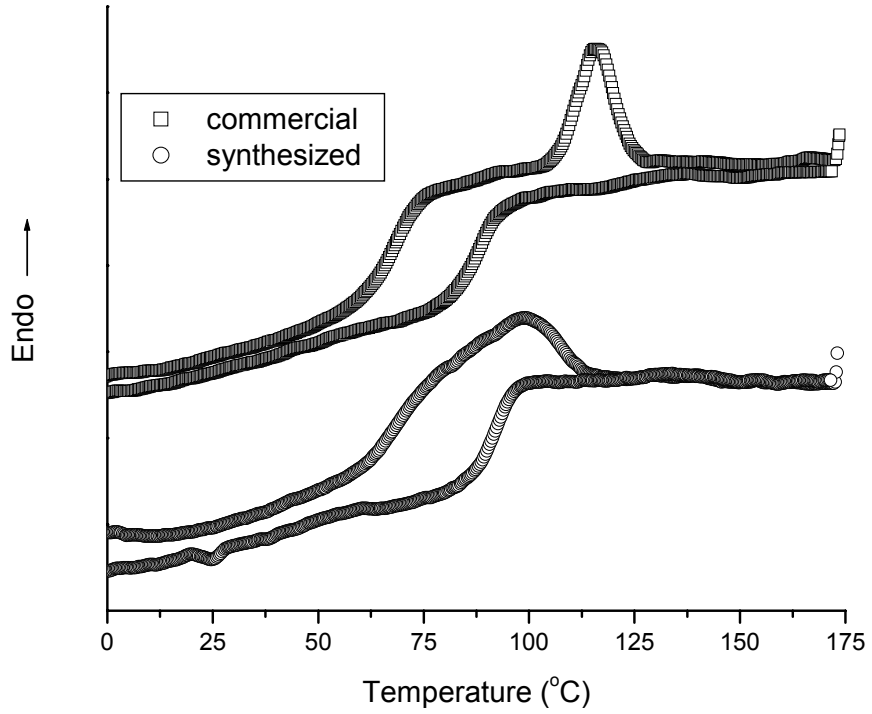

Fig C2: DSC scans of Amlon and an Amlon-like polymer synthesized at VT Chemistry. Both samples were saturated for 24 hrs. at 120°C, 1500 psi CO_2.

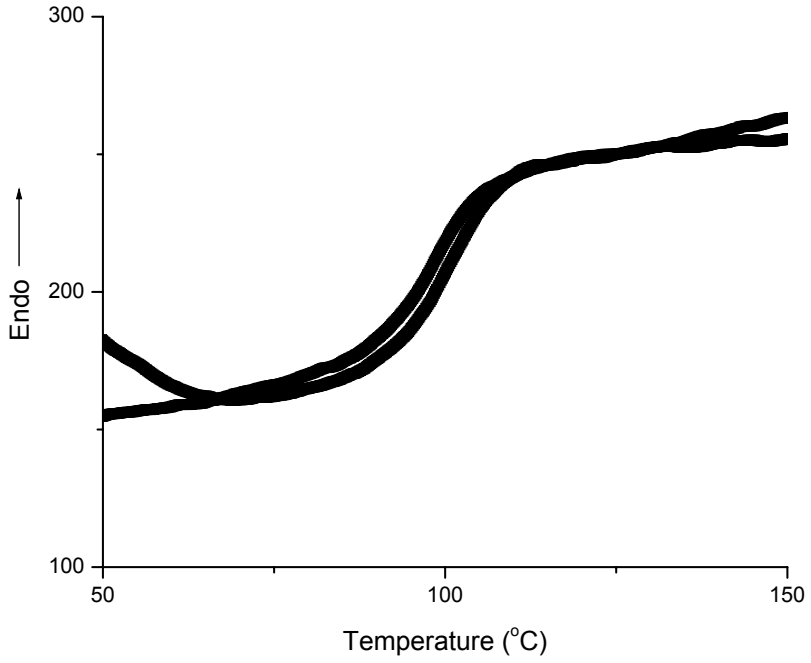

Fig. C3: DSC scans of a 94/6 AN/MA copolymer produced by VT Chemistry. Sample was saturated for 6 hours at 120°C, 1500 psi CO_2.

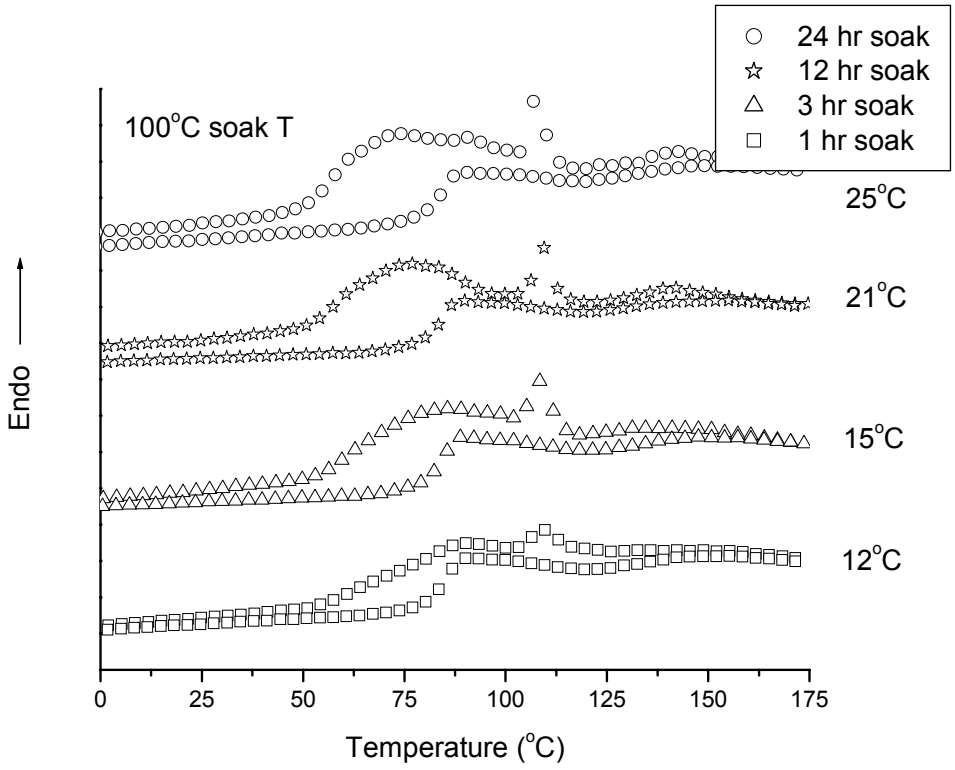

Fig C4: DSC scans of plasticized Barex saturated at 100°C, 1500 psi CO_2.

Appendix D: Effects of Sparse LCB on Draw Resonance

Preface

This appendix is organized as a manuscript for future publication. The work contained within this appendix was performed to become familiar with laboratory equipment, and resulted in some significant findings. In particular, the effect of sparse long chain branching (LCB) on the extensional strain hardening of metallocene polymerized linear low-density polyethylenes (LLDPEs) is evaluated, and correlated to an isothermal melt spinning instability known as draw resonance. Usually, the onset of draw resonance is attributed to the shear rheology of materials. This study attempts to isolate extensional rheological effects on draw resonance.

Effects of Sparse LCB on the Onset and Propagation of Draw Resonance in LLDPEs

Michael J. Bortner, Phillip J. Doerpinghaus and Donald G. Baird*

Department of Chemical Engineering and Center for Composite Materials and Structures
Virginia Polytechnic Institute and State University
Blacksburg, VA 24061-0211

Abstract

The influence of sparse long chain branching on the onset and propagation of isothermal draw resonance in fiber spinning of polyethylene melts was investigated. Six polyethylene melts were used in this study: three sparsely branched metallocene polyethylenes, a linear low-density metallocene polyethylene, a conventional linear low-density polyethylene, and a conventional low-density polyethylene (LDPE). The sparsely branched metallocene polyethylenes have almost identical shear rheology and molecular weight distributions, but strain harden to different extents under extensional deformation because of slight differences in the amount of sparse long chain branching. Critical draw ratios and the ratios of minimum to maximum diameter were found to be different for each of these polyethylenes. The two linear low-density polyethylenes, which have no long chain branching, had critical draw ratios similar to those of the sparsely branched polyethylenes, but failed (necked to the point of filament breakage) during monofilament extrusion at draw ratios significantly lower than those measured for the sparsely branched polyethylenes. In contrast, the LDPE, which has the highest degree of branching and largest molecular weight distribution, had a much higher critical draw ratio than that obtained for the other five polyethylenes. These results suggest that the degree of extensional strain hardening, arising from differences in long chain branching, has a significant effect on the onset

* dbaird@vt.edu, phone: (540) 231-5998, fax: (540) 231-5022

and propagation of draw resonance in isothermal fiber spinning. In the case of LLDPE, broadening the MWD seemed to affect the drawability of LLDPE, but had no effect on the critical draw ratio.

Introduction

Draw resonance is an instability that arises when reaching a critical draw ratio on stretching a fluid filament. It is manifested as a periodic fluctuation in the diameter of the filament in which the amplitude and period change with draw ratio. It is distinguished from the effects of surface tension (which promotes filament breakup), as a filament is uniform in diameter until a critical draw ratio is reached. In the case of polymer melts being processed in the form of blown film, it is manifested as periodic fluctuations in the film thickness, which leads to periodic fluctuations in the bubble diameter[1]. In the case of film casting, the film thickness is observed to vary periodically when a critical draw ratio is reached[1]. Draw resonance has also been extensively reported to occur in fiber spinning, in which it is manifested as a periodic fluctuation in the diameter of the fiber[1,2,3,4,5,6,7,8].

Draw resonance has been observed in both viscoelastic melts, such as polyethylene[1,3,9], polypropylene[3,10], polystyrene[3,9], and polyethylene terepthalate[7,8,9], and in Newtonian fluids such as silicone oil[11]. A critical draw ratio of 20.21 was calculated for a Newtonian fluid by using the solution for isothermal, Newtonian fiber spinning and a linearized stability analysis, which involves the introduction of finite (small) amplitude disturbances[5]. The theory compares well to the measured critical draw ratio of 22 (accounting for die swell) observed for silicone oil (viscosity of 100 Pa*s), which seems to be Newtonian[11,12]. Pearson and Shah[13] extended the analysis to a power law fluid, and found that the critical draw ratio is below 20.21 for a shear thinning fluid and above 20.21 for a shear

thickening fluid. They found that the critical draw ratio depends not only on the power law index of the fluid, but also on a dimensionless number S, which is directly proportional to the Stanton number, St:

$$S = k(T_o - T_a)(St)e^{-St} \qquad (1)$$

where k is the viscosity temperature coefficient of the viscosity function ($\eta_o \propto \exp[-k(T-T_a)]$) and St is the Stanton number, defined in Eq. 2:

$$St = 2\sqrt{\frac{\pi \upsilon_0^{\frac{1}{3}}}{\dot{\rho m}}\frac{\varsigma L}{\bar{C}_p}} \qquad (2)$$

where ζ is the ratio $U/v_z^{2/3}$ (units: $cal/cm^{8/3}{\cdot}s^{1/3}\,^oC$). These findings suggest that draw resonance is dependent on mass flow rate, draw down length, die diameter, and take up speed. Fisher and Denn[5] extended the Newtonian analysis to the viscoelastic case using the White-Metzner model, and found that the critical draw ratio decreases as the degree of shear thinning (as determined by the power law index) increases. It was also found that as the Deborah number (directly related to elasticity) of the fluid increases, a region exists in which draw resonance is unattainable. These findings suggest that increased elasticity improves stability, but that shear thinning in a fluid decreases the critical draw ratio (increases the instability), with critical draw ratios as low as 3 to 5 for power law fluid indices from 0.33 to 0.5, respectively. A PS melt with a power law index of 0.5 exhibited a critical draw ratio of 5, in good agreement with the theoretical prediction[9].

There are several processing factors that affect the onset and propagation of draw resonance in melt spinning of polymeric fluids. In general, draw resonance has been observed under isothermal conditions, occurs even when the extrusion rate and take-up speed are constant, and persists for a long period of time[6]. The onset of draw resonance usually occurs at a

specific draw-down ratio, known as the critical draw ratio. As the draw-down ratio of the fiber is increased above the critical draw ratio in constant extrusion rate experiments, the ratio of the maximum to minimum diameter and period of the fluctuation (distance between maximum and minimum diameters) have also been observed to increase[11]. The amplitude of the diameter fluctuation has been found to be highly dependent on the length of the melt draw down zone[14]. Shorter draw zones (corresponding to higher extension rates) have been found to increase the magnitude of the maximum to minimum diameter ratios for a given draw ratio[14]. Increased flow rates and die diameters have also been shown to lower the critical draw ratio and increase the amplitude and period of oscillation[6]. In general, nonisothermal spinning conditions have been shown to suppress the onset of the instability[6].

The effects of extensional strain hardening on the onset and propagation of draw resonance has been suggested, but not thoroughly investigated. It has been suggested that strain hardening may be a stabilizing factor, as observed by Gregory[15] and Weinberger et al.[9] for low density (highly branched) polyethylene (LDPE), in which draw resonance was either unattainable or only observed at much higher draw ratios than LLDPE. Furthermore, Minoshima and White[1] observed that between LDPE, LLDPE, and high-density polyethylene (HDPE), LDPE is the most stable to draw resonance, followed by HDPE and LLDPE, respectively. Conflicting data for draw resonance in LDPE has prevented any definitive determinations of the effects of extensional strain hardening, especially considering the theory of Pearson and Shah[13] which suggests that LDPE, which in general shear thins to a greater extent than linear low density polyethylene (LLDPE), should have a lower critical draw ratio. However, most of the experimental data suggest that (in general) LLDPE has a lower critical draw ratio than LDPE and, therefore, is more prone to draw resonance. No definitive results regarding the effect of

long chain branching on extensional strain hardening, and the corresponding effects on draw resonance, have been presented to date.

The purpose of this paper is to isolate the effects of slight differences in sparse long chain branching, corresponding to differences in extensional strain hardening, on the onset and propagation of draw resonance in LLDPEs. The effect of sparse long chain branching on the rheology is evaluated by means of shear and extensional rheological measurements. Critical draw ratios for the onset of draw resonance in each resin are then determined, and the propagation of draw resonance in each material is monitored. These results for the four mPEs suggest that a relationship between long chain branching, extensional strain hardening, the drawability, and the nature of draw resonance exists. Furthermore, the effect of extensional rheology on the general stability of filament formation is considered. Results for a conventional LDPE and LLDPE are included in order to investigate the effects of high levels of branching and MWD on draw resonance.

Experimental

Materials

Six commercially produced polyethylene resins were chosen for this study. The resins, molecular weight distributions, degrees of long chain branching (LCB), and melt indices are listed in Table 1. Molecular characterization data was obtained as described by Doerpinghaus and coworkers[16]. The first four resins in the table are metallocene-catalyzed polyethylenes (mPEs), which were specifically chosen to compare the effects of level of sparse long chain branching on the onset and propagation of the draw resonance instability. The Affinity PL1840 and PL1880 resins are solution polymerized ethylene-octene copolymers manufactured by DOW Chemical using INSITE® catalyst technology. The Exact 0201 and 3132 are manufactured by

Sample	MI [dg/min]	Molecular Weight Data [g/mol]			Long Chain Branches [1/10000 C]
		M_w	M_w/M_n	M_z	
Dow Affinity PL1840	1.0	87400	2.43	160200	0.57
Dow Affinity PL1880	1.0	115800	2.12	183700	0.18
Exxon Exact 0201	1.1	88700	2.14	158900	0.79
Exxon Exact 3132	1.2	111000	2.04	180400	--
Mobil NTX 101	0.9	122700	3.44	319700	--
Equistar NA 952	2.0	235500	17.1	2619300	39[a]

Table D1: Melt index, molecular weight distribution, and degree of long chain branching for the six PE resins. [a] obtained from C^{13} NMR measurements[17]

ExxonMobil using EXXPOL® catalyst technology. The Exact 0201 resin is an ethylene-octene copolymer, and Exact 3132 is an ethylene-hexene copolymer. The remaining two resins are a conventional linear low-density polyethylene (LLDPE) and a conventional low density polyethylene (LDPE). The LLDPE, NTX-101, is an ethylene-hexene copolymer manufactured by ExxonMobil using a Ziegler-Natta gas-phase polymerization process. The NA952 LDPE is an ethylene homopolymer manufactured by Equistar using a high temperature and pressure free-radical polymerization process.

The PL 1840, PL1880, and Ex0201 resins are all identified as having sparse degrees of LCB based on dilute solution measurements[17]. The data in Table 1 indicate that the Exact 0201 has the highest degree of sparse LCB, with 0.79 LCB per 10^4 carbon atoms, and the PL1880 has the lowest degree of LCB of the three resins, with 0.18 LCB per 10^4 carbon atoms. Exact 3132 is specified as a strictly linear mPE. The NA952 LDPE has a much higher degree of LCB (39 LCB per 10^4 carbon atoms, which includes all LCB of 6 carbons or greater) than the sparsely branched LLDPEs, comparable to that of other commercially produced LDPEs. Similar to other conventional LLDPEs and to Exact 3132, the NTX-101 resin is also a strictly linear mPE without any (measurable) sparse LCB, but with a somewhat broader molecular weight distribution than that of Exact 3132.

Dynamic oscillatory and steady shear measurements

A Rheometrics Mechanical Spectrometer Model 800 torsional rheometer was used to obtain the shear viscoelastic measurements for the six PEs. Parallel plate fixtures with a diameter of 25 mm were used for the small amplitude dynamic oscillatory measurements. Cone and plate fixtures, with a diameter of 25 mm and a cone angle of 0.1 radians, were used to obtain the steady shear measurements. All measurements were carried out in an inert nitrogen

atmosphere to prevent thermo-oxidative degradation. Samples were prepared by compression molding of 25 mm disks at 170°C, and allowed to cool slowly without applied pressure. Measurements were performed at a temperature of 150°C. Errors for the dynamic oscillatory and steady shear viscosity measurements were calculated to be ± 5% and ± 10%, respectively.

Extensional rheological measurements

Transient uniaxial extensional measurements were obtained using a Rheometrics Extensional Rheometer (RER) Model 9000. The rheometer has a pulling rod and one stationary end, based on the design suggested by Münstedt[18]. Transient extensional data were obtained over the extension rate range 0.1-1.00 s^{-1}. Cylindrical samples were prepared via compression molding at 170°C and allowed to cool slowly without applied pressure to ensure samples had minimal (negligible) residual stresses. The cylindrical samples had a nominal length of 22 mm and diameter of 5.7 mm. The samples were bonded to test clips using a high temperature epoxy. For the measurements, the samples were mounted to the rheometer and immersed in a neutrally buoyant silicone oil bath maintained at 150°C. When thermal equilibrium was reached, an extension rate was applied, and a leaf spring-LVDT assembly was used to measure the force required to deform the sample. Data was only kept from samples that exhibited uniform deformation throughout the experiment. Hencky strains of 3.0 were reached for each sample. The extensional results at each rate are an average of three runs, with a maximum deviation of 10% over the range of strain used for the branched materials. The linear resins exhibited an error less than 10% up to a Hencky strain of 2.0, but above 2.0 strain units generally exhibited nonuniform deformation (necking occurred). As a result, the extensional data was usually truncated above a Hencky strain of 2.0 for the conventional (non branched) LLDPEs.

Fiber spinning

Monofilament fibers for each sample were generated by use of a capillary rheometer modified with a heated chamber to facilitate isothermal fiber spinning. The fibers were extruded through a capillary of 1.8 mm diameter and a L/D of 40. A shear rate, $\dot{\gamma}$, of 0.8 s^{-1} was used, which corresponded to calculated wall shear stresses (τ_w) in the range 2.7-3.7 x 10^4 Pa, which were low enough to prevent other forms of instability (such as melt fracture) from distorting the onset and magnitude of the draw resonance phenomenon. The heated chamber was fitted to the end of the capillary rheometer and heated with two 150-watt Fire Rod heating cartridges controlled by an Omega CN9000 temperature controller. An isothermal fiber spinning temperature of 170^{o}C was used to obtain the monofilament samples. Upon exiting the heated chamber, the fibers were immediately quenched in a water bath. A chamber length of 18 cm was used, and a constant length of 18.2 cm was maintained between the capillary and quench bath. The polymer fibers were drawn down using a Dayton 390:1 high torque take-up motor controlled by a Dayton electronic motor speed controller. Draw down ratios in the range 7-25 were used to obtain the fiber samples. A fiber sample of approximately 5-7 m was obtained at each draw ratio for the six PE resins.

Diameter measurements

Diameter measurements were performed using a constant tension caliper, accurate to ± 0.01 mm. The diameter was measured and recorded every 2 cm over the length of the fiber. For determination of the critical draw ratio, a laser micrometer was used for accurate diameter measurements near the critical draw ratio for each polyethylene. A TSI Inc. diameter acquisition unit linked to a Holix 5000 series laser gauge head was used to obtain diameter measurements accurate to ± 0.005 mm. The fibers were passed through the laser micrometer at a rate of 1.8 cm/s, with diameter measurements recorded once per second.

Results and Discussion

In the following sections, the effects of varying degrees of LCB on the shear and extensional rheology, and on the onset and propagation of draw resonance are analyzed.

Shear rheology

The shear viscosity flow curves for each of the six resins are plotted in Fig. 1. Each flow curve consists of steady shear and dynamic oscillatory data. The steady shear data covers the shear rate range of 0.001 – 0.1 s^{-1} and the dynamic oscillatory covers the frequency range of 0.1 – 100 rad s^{-1}. The low frequency intersection between steady and dynamic oscillatory data is in good agreement for all resins. Analysis of the shear viscosity curves indicates that the zero-shear viscosity, onset of shear-thinning behavior, and degree of shear thinning are influenced by molecular structure. The Affinity PL1840, Affinity PL1880, Exact 0201, and NA952 resins all exhibit a common zero-shear viscosity plateau of approximately 45,000 Pa s. The NTX101 and Exact 3132 resins exhibit lower zero-shear viscosities of 22,000 and 15,000 Pa s, respectively. The NA952 resin transitions to non-Newtonian flow behavior at shear rates as low as 0.01 s^{-1}, while the sparsely branched mPE resins begin shear thinning at 0.05 s^{-1}. The onset of shear-thinning behavior in the linear resins appears to be influenced by molecular weight distribution. The NTX101 exhibits a broad transition to non-Newtonian flow beginning at $\dot{\gamma} = 0.1$ s^{-1}, while the transition for the linear mPE resin is much more acute at $\dot{\gamma} = 2$ s^{-1}. The degree of shear thinning is most pronounced in the densely branched NA952 resin with a 98% reduction in shear viscosity over the five decades in shear rate investigated. The viscosity reduction in the sparsely branched resins is also notable at 95%. The NTX101 and Exact 3132 resins exhibit considerably less shear thinning than the branched resins with only an 8-fold and 4-fold decrease in shear viscosity, respectively.

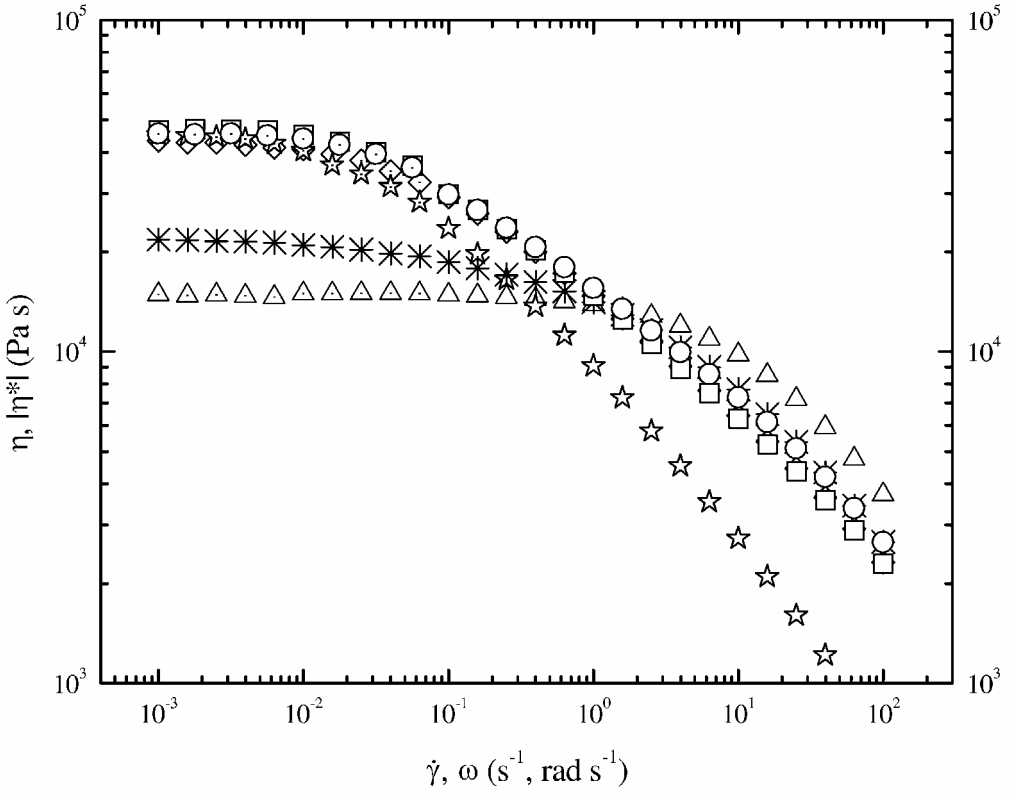

Fig. D1: Steady shear and complex viscosities at 150 °C. (◇) Exact 0201, (△) Exact 3132, (☆) NA952, (∗) NTX101, (□) Affinity PL1840, (○) Affinity PL1880. Dotted symbols represent steady shear measurements; open symbols represent dynamic oscillatory measurements.

Despite similarities in the shear viscosity curves of the sparsely branched mPE resins, the molecular structure of these materials is different. One of the most prominent differences is the weight-average molecular weight according to the GPC-LALLS data tabulated in Table 1. Doerpinghaus and Baird[16] shifted the viscosity data in Fig. 1 as a function of M_w to separate the effects of the LCB in these materials. The sparsely branched resins exhibit a noticeable degree of zero-shear viscosity enhancement, while the densely branched LDPE shows a significant reduction in the zero-shear viscosity. Although enhancement was observed in the sparsely branched metallocene resins, the degree of enhancement did not scale with the measured degree of long-chain branching. More specifically, the Exact 0201 resin (having 0.79 LCB/10^4 carbons) does not show any additional enhancement in the zero-shear viscosity over the Affinity PL1840 resin (having 0.57 LCB/10^4 carbons). The onset of shear thinning was also affected by shifting the viscosity flow curves, which indicated a two-order magnitude decrease in the onset of shear thinning between the linear mPE (Exact 3132) resin and the sparsely branched mPE resins. These results suggest that the shear viscosity behavior is significantly affected by slight differences in LCB in the mPE resins, especially when comparing either the PL1840 or Exact 0201 to the PL1880 or Exact 3132 (linear) resin.

In addition to the shear viscosity, the dynamic moduli indicate that long-chain branching gives rise to increased elasticity. The dynamic storage and loss moduli data for each resin over the frequency range of 0.1 – 100 rad/s are presented in Figs. 2 and 3, respectively. The data in Figs. 2 and 3 indicate that in the low frequency range, G' appears to be a better indicator of molecular structure than G''. The differentiation between the branched PE resins, NTX101, and Exact 3132 possibly indicates a stronger dependence on the effects of long-chain branching content and molecular weight distribution. At high frequencies, the storage moduli appear to

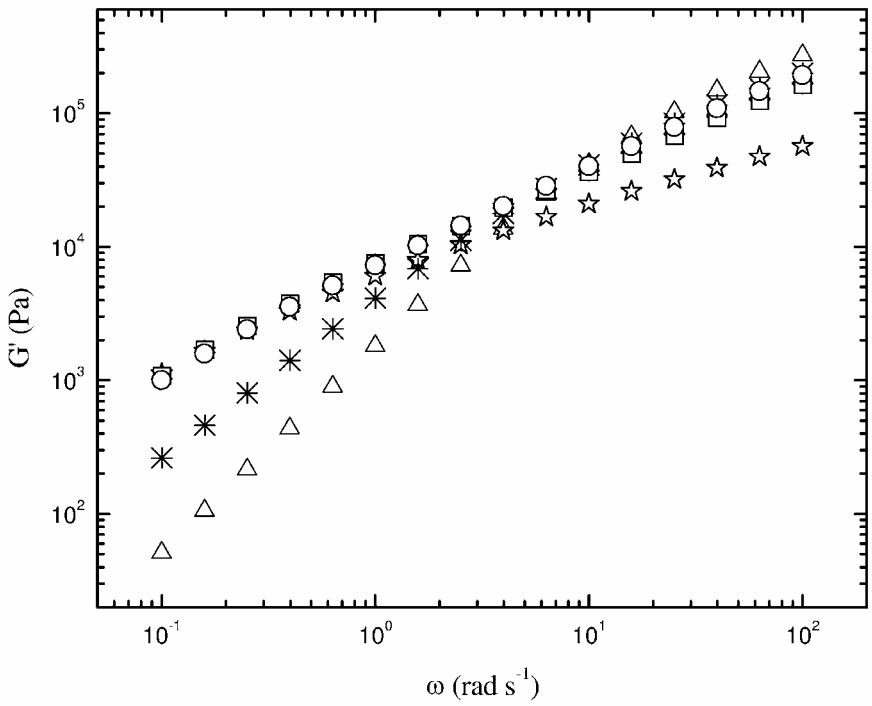

Fig. D2: Dynamic storage moduli at 150 °C. (◇) Exact 0201; (△) Exact 3132; (☆) NA952; (∗) NTX101; (□) Affinity PL1840; (○) Affinity PL1880.

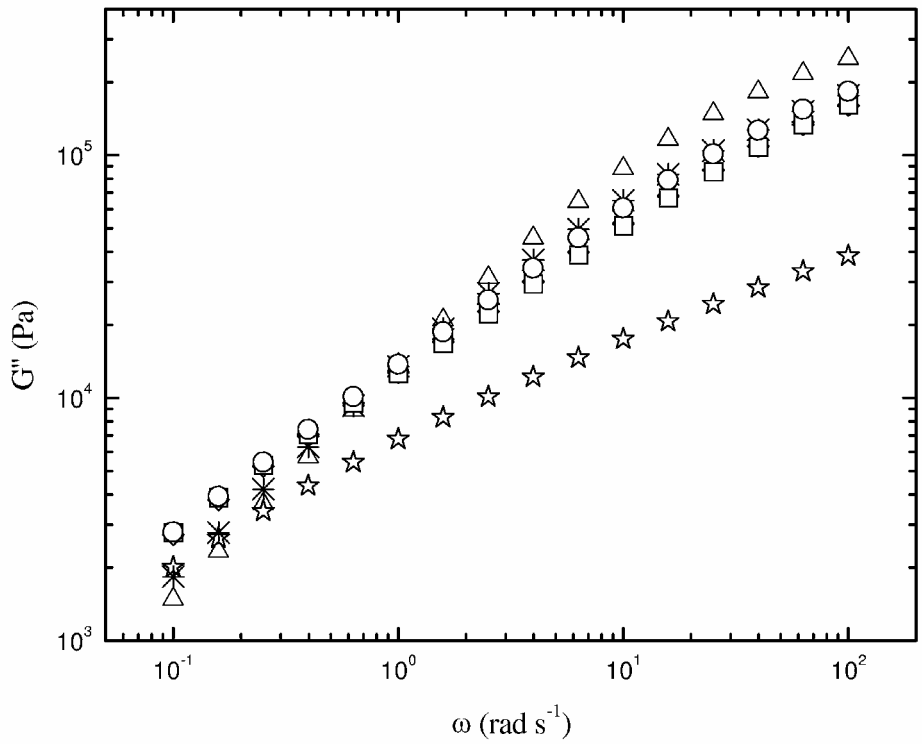

Fig. D3: Dynamic loss moduli at 150 °C. (◇) Exact 0201; (△) Exact 3132; (☆) NA952; (∗) NTX101; (□) Affinity PL1840; (○) Affinity PL1880.

converge with the exception of the highly branched LDPE resin. The loss moduli data, which dominates the magnitude of the material response over the low frequency range, indicate a general trend of a monotonic growth in G'' for five of the six PE resins. The exception is the NA952 resin, which does not increase as rapidly with frequency as the other PE resins at high frequencies.

The shear rheological data of the branched mPEs suggest that the resins behave almost identically in shear, especially the PL1840 and Exact 0201, with which no distinguishable differences in shear rheology could be detected following normalization to molecular weight[16]. The PL1880 resin, which has a slightly lower degree of LCB, also has a very similar shear viscosity, G', and G" curve to that of the PL1840 and Exact 0201, and deviations in the shear rheology can only be discerned upon normalization to molecular weight[16].

Extensional rheology

The transient extensional growth behavior, obtained at $\dot{\varepsilon}=0.1\ s^{-1}$, is shown in Fig. 4 for the PE resins. The NA952 exhibits a substantial degree of extensional strain-hardening behavior as η_E^+ continues to rise with increasing time. Exact 0201, PL1840, and PL1880 also show some extensional strain-hardening behavior, but at a much reduced magnitude. Conversely, the linear polyethylenes show no extensional strain hardening as η_E^+ reaches a steady plateau. In fact, it was very difficult to obtain homogenous deformation of the linear materials because of a necking instability often associated with strain softening materials[19]. For the three sparsely branched resins, the data indicate that Exact 0201 exhibits the highest degree of extensional strain hardening, and PL1880 exhibits the lowest over the measurement time. These results indicate that as the degree of sparse LCB (as measured by GPC-LALLS) increases, a higher degree of extensional strain hardening is observed.

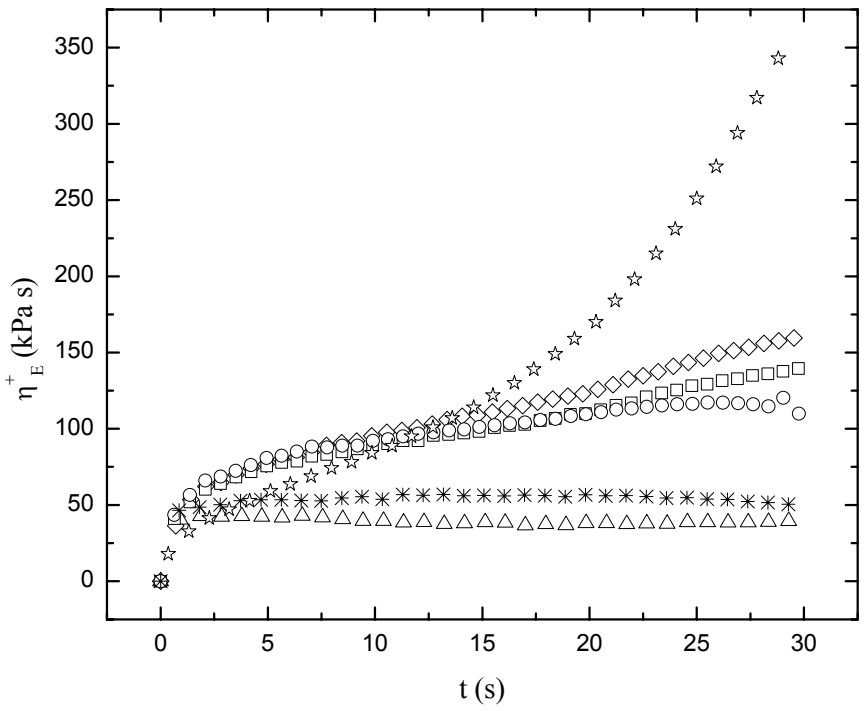

Fig. D4: Transient extensional viscosities for the LDPE, mPE sparsely branched resins, and linear LLDPEs at 150°C and an extension rate of 0.1 s^{-1}. (☆) NA952; (◇) PL1840; (□) Exact 0201; (○) PL1880; (∗) NTX-101; (△) Exact 3132.

Critical draw ratios

The critical draw ratio (CrDr), defined as the draw ratio (DR) at which the draw resonance instability begins to occur, was determined for each resin. The data in Fig. 5 illustrate the periodic diameter fluctuations measured along the length of the fiber (in this case, for Exact 0201) during the instability, and provide an example as to the type of fluctuations being measured during draw resonance. Because draw resonance in fiber spinning is described as a surging and necking phenomenon, we expected that higher degrees of LCB would increase extensional strain hardening, and hence, should increase resistance to necking. Therefore, we expected that of the four mPEs, Exact 3132 would have the lowest critical draw ratio, followed by PL1880, PL1840, and Exact 0201. Critical draw ratios for NTX-101 and Exact 3132 also facilitated a comparison between a metallocene produced LLDPE and a conventional Ziegler-Natta LLDPE. Because it has the highest measured degree of LCB, the NA952 LDPE was expected to have a significantly higher critical draw ratio than the other 5 resins.

Critical draw ratios and the corresponding error in the measurements are shown in Table 2. The LDPE, which has the highest degree of LCB, broadest MWD, and strain hardens to the highest extent (as shown by the transient extensional viscosity measurements in Fig. 4) has the highest critical draw ratio of 12.78, which was approximately 30% higher than the highest measured critical draw ratio for the sparsely branched LLDPEs. However, the data obtained for the sparsely branched and linear LLDPEs suggest some conflicting results. The lowest critical draw ratio of 8.02 was obtained for PL1880 (which contains a low level of sparse LCB), which was significantly lower than 9.25 and 9.70 reported for the NTX101 and Ex3132 linear resins, respectively. The highest measured critical draw ratio for the sparsely branched resins is 9.84 for PL1840, which is not statistically different than that obtained for NTX101 (CrDr of 9.70).

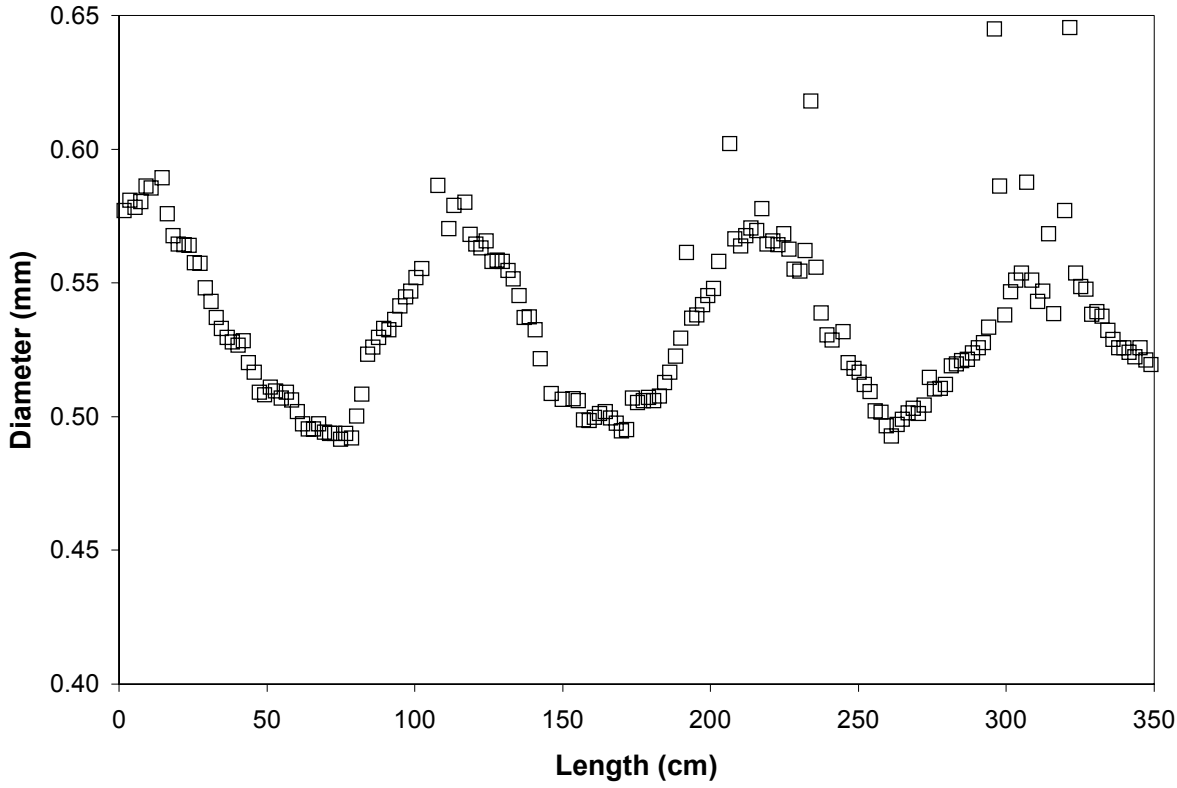

Fig. D5: Example of draw resonance in Exact 0201, showing the fluctuation in diameter over the fiber length. Draw ratio 9.42. T = 170^{o}C.

resin	CrDr	Error
Ex3132	9.70	0.27
NTX101	9.25	0.24
Ex0201	9.24	0.26
PL1840	9.84	0.25
PL1880	8.02	0.22
NA952	12.78	-

Table D2: Critical draw ratios for the six PE resins.

Finally, Exact 0201, which was found to have the highest degree of sparse LCB and extensional strain hardening for the mPE resins, has a significantly lower critical draw ratio than NTX101, which has no sparse LCB and does not exhibit extensional strain hardening.

To facilitate a consistent comparison between the samples, the critical draw ratios were compared with resins from the same manufacturer to ensure that effects from additives and lubricants (that vary between manufacturers) were not distorting the data. For the Dow LLDPEs with sparse LCB, a significantly higher critical draw ratio (of 9.84) was measured for PL1840 than PL1880 (8.02), which was expected based on the higher degree of extensional strain hardening (see Fig. 4). Comparison of the critical draw ratios obtained for the ExxonMobil resins indicates that the strictly linear and sparsely branched mPEs (Exact 3132 and 0201, respectively) did not have statistically different critical draw ratios. Also, NTX101 (conventional LLDPE) was found to have an almost identical critical draw ratio to that of the sparsely branched Exact 0201. The results suggest that a slight increase in LCB of the Dow Chemical resins stabilizes the PE to draw resonance, but the data obtained for the ExxonMobil resins are not consistent with the degree of LCB and extensional strain hardening.

Comparison of the critical draw ratios measured for the sparsely branched mPEs indicates that Exact 0201, which has the highest degree of sparse LCB, has a significantly higher CrDr than PL1880, but a lower CrDr than PL1840, which has a slightly lower degree of LCB. From the extensional data for Exact 0201 and PL1840 (from Fig. 4), it was expected that Exact 0201 might be more stable to the onset of draw resonance, considering that it exhibited a higher degree of extensional strain hardening than PL1840. Also, the critical draw ratios for the sparsely branched mPEs and the LLDPEs (Exact 3132 and NTX101) are not consistent with the degrees of extensional strain hardening. The reason for these discrepancies is unknown at present.

Diameter ratios and period lengths

Propagation of the draw resonance instability can be monitored by the ratios of the maximum to minimum diameters and the length of the period between the maximum (or minimum) diameters. If draw resonance is viewed as a surging and necking phenomenon, then by the arguments provided earlier, it is expected that higher degrees of LCB (and extensional strain hardening) should help to decrease the length of necking as take-up speed is increased, and accordingly minimize the amount of polymer that surges (or necks) at a given instant. These arguments suggest that as LCB (or extensional strain hardening) is increased, then the period length and diameter ratio for a given resin should increase at a slower rate than the same resin with a lower degree of LCB.

Diameter ratios for the three sparsely branched mPEs are shown in Fig. 6. The data clearly indicate that PL1880, which has the least amount of LCB and extensional strain hardening of the three sparsely branched LLDPEs, is subject to rapid changes in diameter ratio immediately after reaching the critical draw ratio. As the draw ratio is increased, the instability propagates more quickly in PL1880 than in PL1840 or Exact 0201 up to a draw ratio of approximately 13.5. However, the data suggest that Exact 0201 is the least stable mPE at draw ratios above 13.5, where the diameter ratio increases at a faster rate than the Affinity resins. The diameter ratios of PL1840 appear to increase at the slowest rate relative to that of the other mPEs. Based on the lower critical draw ratio obtained for Exact 0201 (compared to PL1840), it is not surprising that the PL1840 resin is more stable to the propagation of the instability (as it was to the onset of draw resonance). The period length data for the three sparsely branched mPEs are shown in Fig. 7, and almost identical trends as for the diameter ratios (in Fig. 6) are observed. Below a draw ratio of 13.5, the period length increases at a similar rate (as a draw

ratio increases) for the three sparsely branched mPEs. Above this DR, the Exact 0201 shows the highest rate of period length increase.

We next compared the linear and sparsely branched Exact resins to determine if differences in LCB and extensional strain hardening, within the ExxonMobil resins, had an effect on the propagation of the instability. The data in Figs. 8 and 9 show the diameter ratios and period lengths, respectively, for the two resins. From the data obtained for Exact 3132, it appears that the strictly linear mPE is more unstable than the slightly branched material, with higher rates of increase of both diameter ratios and period lengths. The data only extend to a draw ratio of approximately 12.5, above which Exact 3132 necked to an extent that draw resonance was not observed, and, in fact, fiber breakage occurred. It is clear that draw resonance increases at a very high rate for the slightly branched (Exact 0201) resin, but the fiber was able to be drawn up to draw ratios of approximately 18, which is significantly higher than for the linear resin. These data suggest that the presence of sparse LCB increased drawability of the resin to a significantly higher degree than that of the linear resin. Based on extensional strain hardening observed for Exact 0201 (and not found with the Exact 3132 linear mPE), we also expected Exact 0201 to be more stable to the propagation of draw resonance above the critical draw ratio, and in fact observed these trends over the available data range. However, it is surprising that the measured critical draw ratio is higher for the linear mPE (Exact 3132) than for the one containing low levels of LCB (Exact 0201).

In order to distinguish differences in the propagation of draw resonance between Ziegler-Natta and metallocene polymerized LLDPEs containing no LCB, we next compared the Exact 3132 and NTX101 resins. The diameter ratio and period length data measured for these two resins are shown in Figs. 10 and 11, respectively. Both sets of data suggest that the Ziegler-Natta

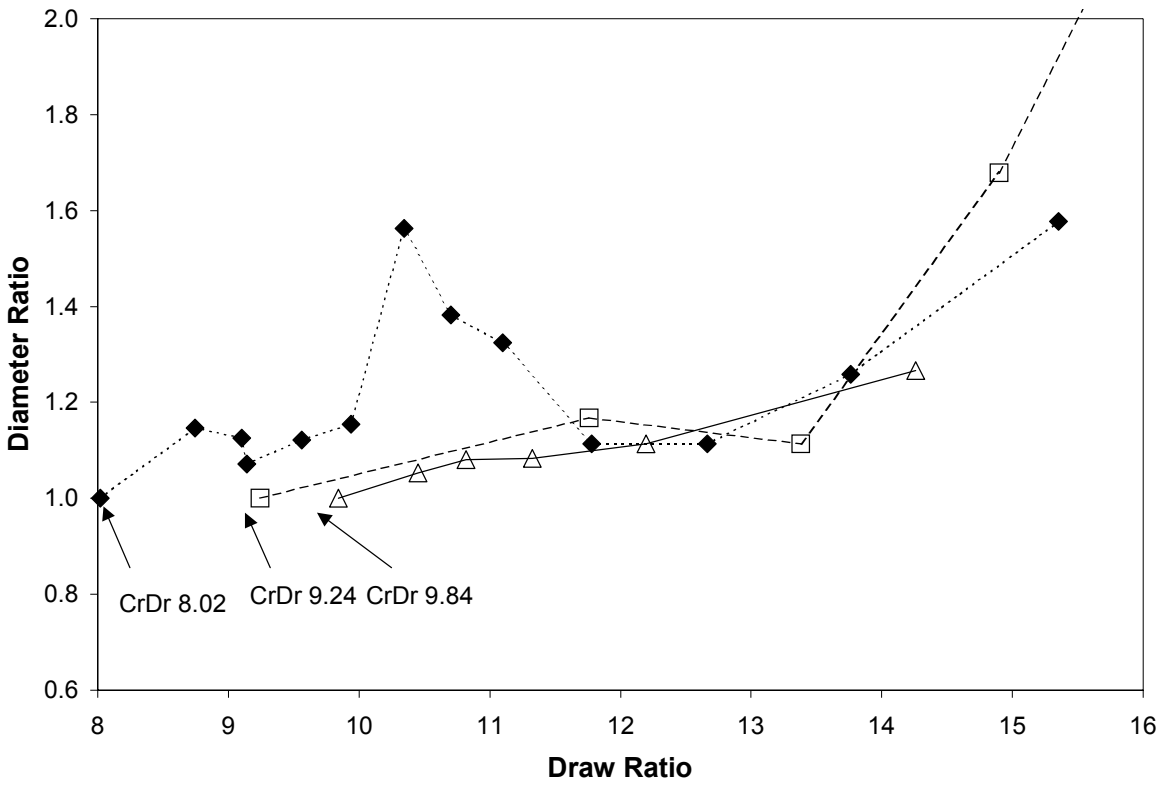

Fig. D6: Diameter ratios for the sparsely branched mPE resins. Lines are data point connectors for reference only. (◆), (---) PL1880; (△), (—) PL1840; (□), (– –) Exact 0201. T = 170°C.

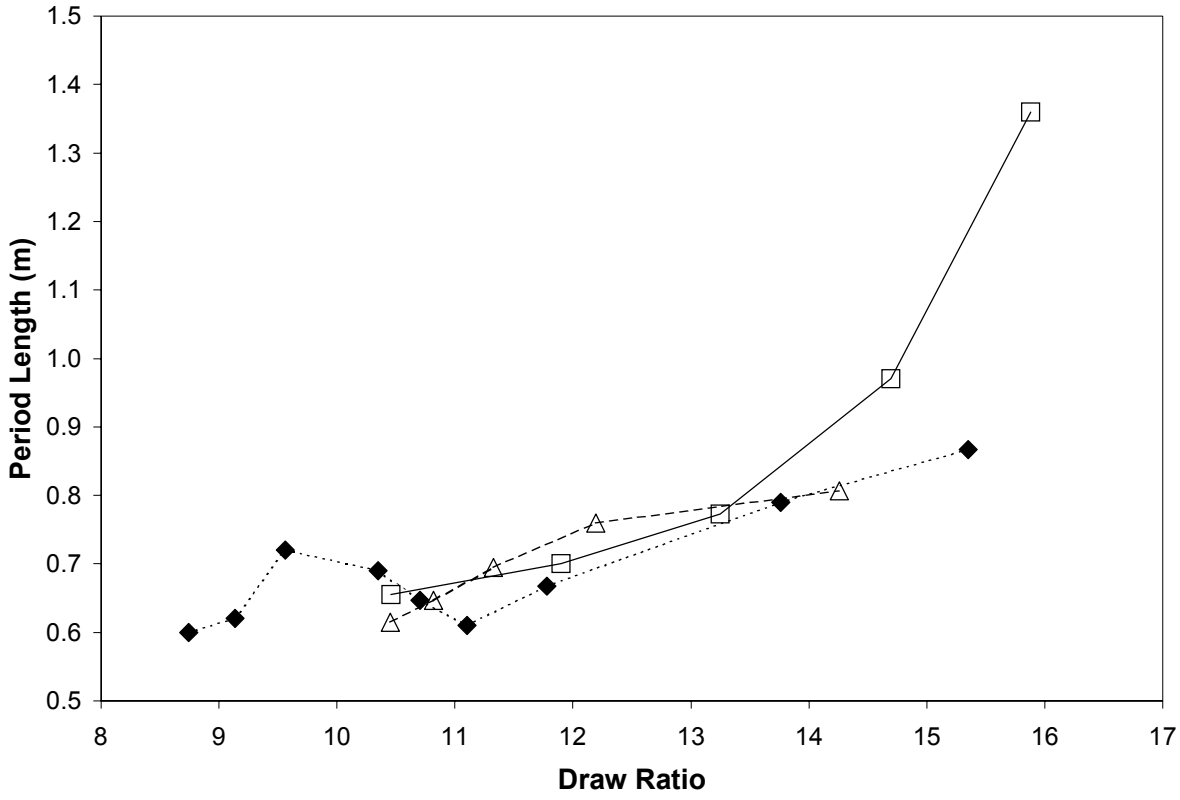

Fig. D7: Period lengths for the sparsely branched mPE resins. Lines are data point connectors for reference only. (◆), (---) PL1880; (△), (—) PL1840; (□), (– –) Exact 0201. T = 170°C.

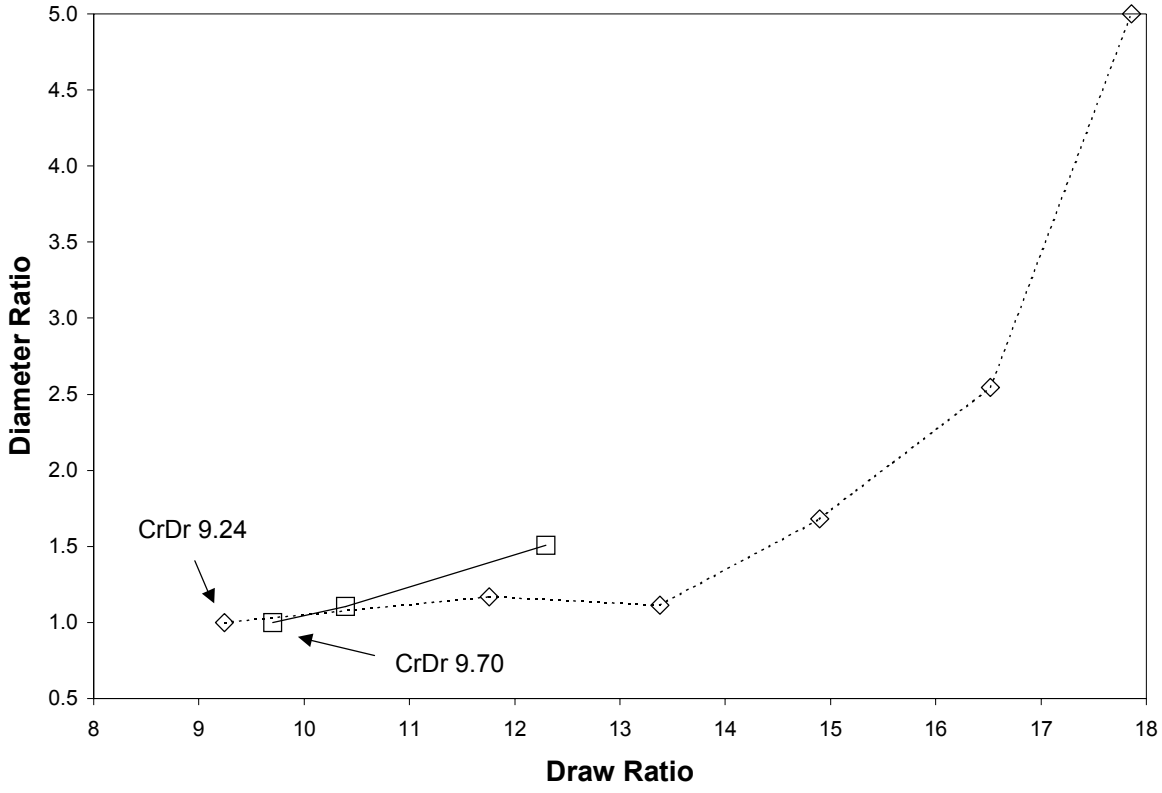

Fig. D8: Diameter ratios for the ExxonMobil mPE resins. Lines are data connectors for reference only. (□), (—) Exact 3132; (◊),(---) Exact 0201. T = 170°C.

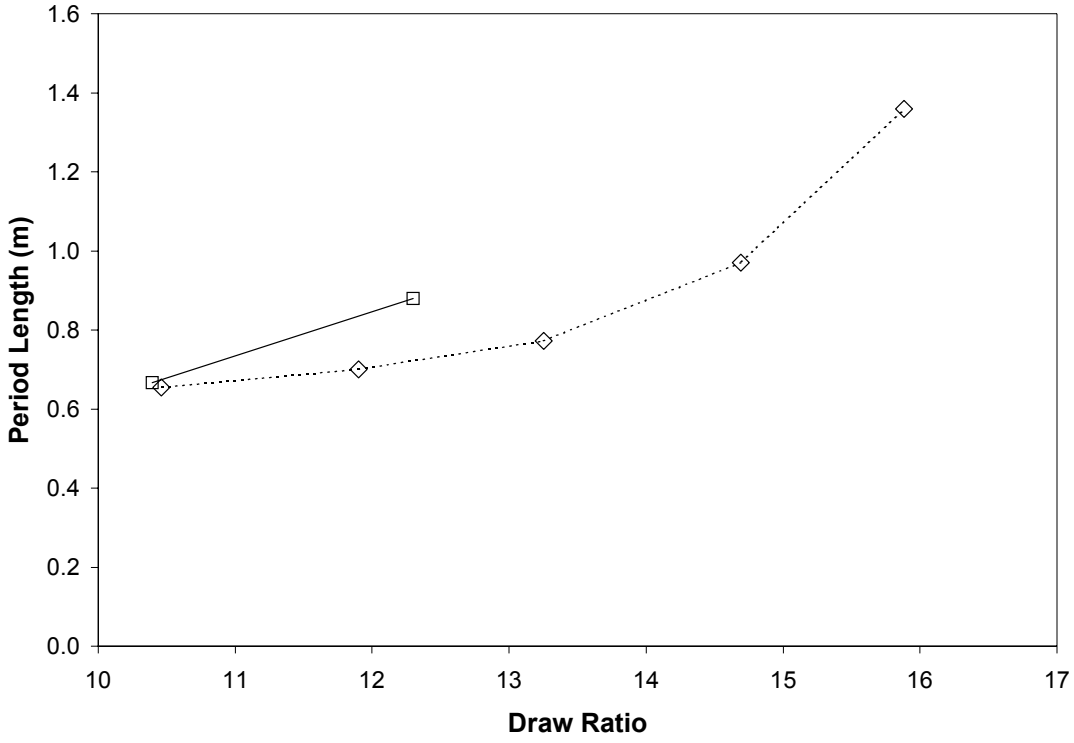

Fig. D9: Period lengths for the ExxonMobil mPE resins. Lines are data connectors for reference only. (□), (—) Exact3132; (◊), (---) Exact 0201. T = 170^{o}C.

produced LLDPE is more stable to the propagation of draw resonance, with a slower rate of increase of diameter ratio and period length as draw ratio is increased. These findings are again surprising, considering that NTX101 exhibited a lower critical draw ratio, suggesting less stability to the onset of draw resonance. It is interesting to note that monofilament fibers could be drawn at higher draw ratios (up to 14) for the NTX-101 resin without filament failure, significantly higher than observed in Exact 3132 (which failed at a draw ratio of 12). This suggests that the broader MWD of NTX-101 facilitates increased drawability of the melt, and also stabilizes it to the propagation of draw resonance (as seen by the data in Figs. 10 and 11). However, these draw ratio values are significantly lower than those obtainable with the sparsely branched resins, again suggesting that sparse LCB and extensional strain hardening increase the melt strength and drawability of the fibers and suppress "necking" of the fibers during spinning.

Conclusions

The goal of this work was to determine the effects of sparse long chain branching on the onset and propagation of draw resonance and general drawability in isothermal fiber spinning. In general, the sparsely branched mPEs were able to be drawn to a significantly higher degree than the LLDPEs, suggesting that the presence of slight degrees of LCB (and hence, extensional strain hardening) plays a significant role in spinning stability. When analyzing the slight differences in degrees of sparse LCB between the mPE resins, the results suggest that comparison of resins from different manufacturers produced inconsistent results, possibly attributable to additives and lubricants in the resins. However, comparison of the Dow Affinity resins suggests that the slightly higher degree of LCB in PL1840 produces significantly higher stability to draw resonance relative to that of PL1880. These trends are observed in both the onset and propagation of the instability. The data for the ExxonMobil resins are inconclusive. In

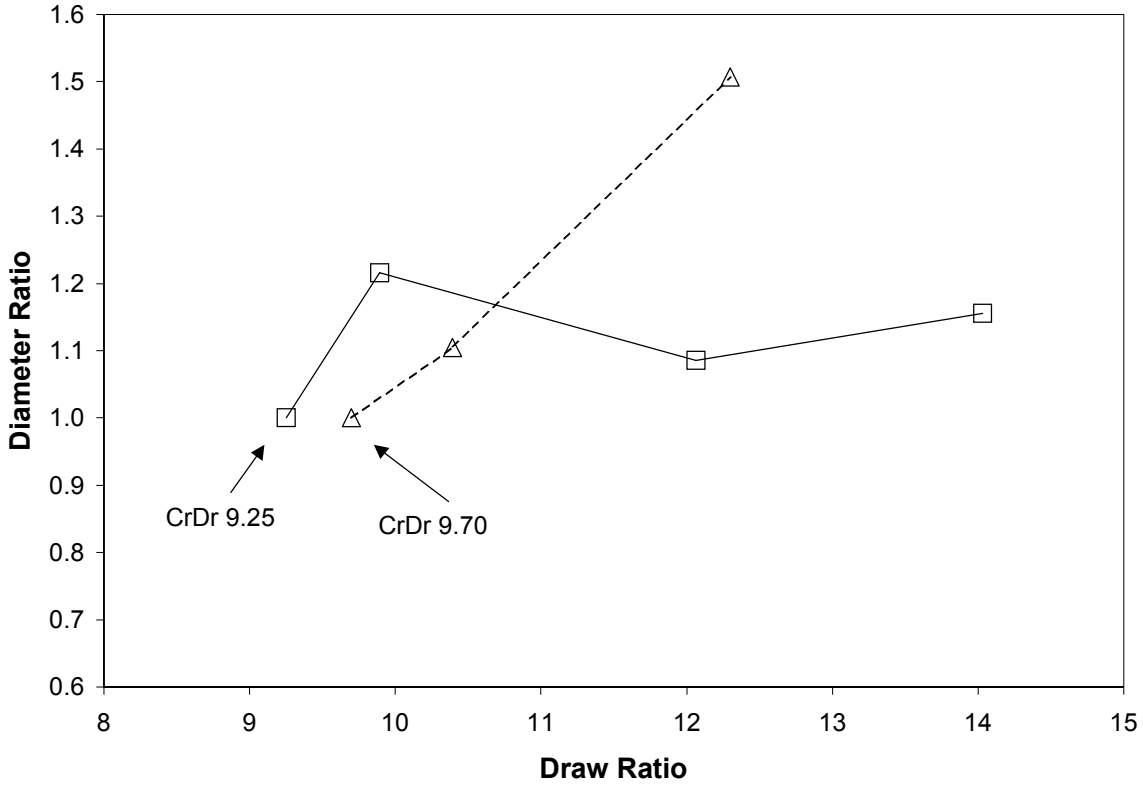

Fig. D10: Diameter ratios for the linear ExxonMobil mPE and Ziegler Natta LLDPE. Lines are data connectors for reference only. (□), (—) NTX101; (△), (---) Exact 3132. T = 170°C.

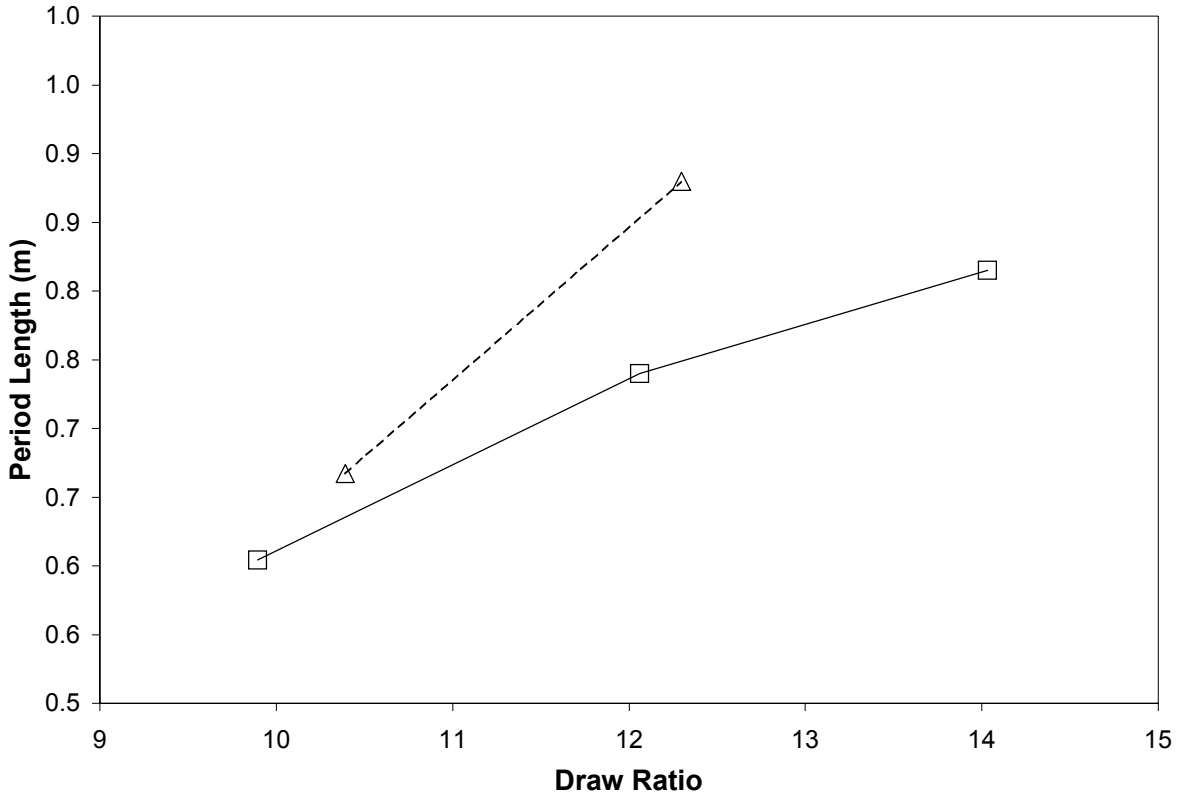

Fig. D11: Period lengths for the linear ExxonMobil mPE and Ziegler Natta LLDPE. Lines are data connectors for reference only. (□), (—) NTX101; (△), (---) Exact 3132. T = 170°C.

general, the results suggest that extensional strain hardening resulting from LCB does have a significant effect on the nature of draw resonance in PE, and appears to stabilize the resins by preventing the "necking" phenomenon in the fiber melt during draw resonance. In the case of conventional LLDPE, which has a broader MWD than the metallocene LLDPE, higher draw ratios could be reached before necking occurred. However, the critical draw ratio for the onset of draw resonance was not significantly affected.

Acknowledgements

The authors wish to thank the ExxonMobil Chemical Company, the Dow Chemical Company, and the Equistar Chemical Company for donating the PE resins used in this study. Appreciation is also extended to A. Willem deGroot and David Gillespie at the Dow Chemical Company for providing the LCB and MWD data. The authors also wish to thank Prof. Dan Edie, and the Center for Advanced Engineering Fibers and Films, for use of their laser micrometer.

References

(1.) Minoshima, W.; White, J. L. *Journal of Non-Newtonian Fluid Mechanics* **1986**, *19*, 275-302.

(2.) Baird, D. G.; Collias, D. I. *Polymer Processing: Principles and Design*; Wiley: New York, **1998**.

(3.) Petrie, C. J. S.; Denn, M. M. *AIChE Journal* **1976**, *22*, 209-236.

(4.) White, J. L.; Khushal, C. D.; Clark, E. S. *Journal of Applied Polymer Science* **1974**, *18*, 2539-2568.

(5.) Han, C. D.; Lamonte, R. R.; Shah, Y. T. *Journal of Applied Polymer Science* **1972**, *16*, 3307-3323.

(6.) Fisher, R. J.; Denn, M. M. *Chemical Engineering Science* **1975**, *30*, 1129-1134.

(7.) Fisher, R. J.; Denn, M. M. *AIChE Journal* **1976**, *22*, 236-245.

(8.) Ishihara, H.; Kase, S. *Journal of Applied Polymer Science* **1975**, *19*, 557-565.

(9.) Kase, S. *Journal of Applied Polymer Science* **1974**, *18*, 3279-3304.

(10.) Weinberger, C. B.; Cruz-Saenz, G. F.; Donnelly, G. J. *AIChE Journal* **1976**, *22*, 441-448.

(11.) Zeichner, G. R. PhD Die\ssertation. University of Delaware, **1973**.

(12.) Donnelly, G. J.; Weinberger, C. B. *Industrial Engineering Chemistry Fundamentals* **1975**, *14*, 334-337.

(13.) Ishihara, H.; Kase, S. *Journal of Applied Polymer Science* **1976**, *20*, 169-191.

(14.) Pearson, J. R. A.; Shah, Y. T. *Industrial Engineering Chemistry Fundamentals* **1974**, *13*, 134-138.

(15.) Gregory, B. H. *Polymer Rheology and Plastics Processing*London, 1975, p 91.

(16.) Doerpinghaus, P. J.; Baird, D. G. *Journal of Rheology* **2003**, *47*, 717-736.

(17.) deGroot, A. W.; Gillespie, D. Personal Communication; **2002**.

(18.) Munstedt, H.; Laun, H. M. *Rheologica Acta* **1979**, *18*, 492.

(19.) Dealy, J. M.; Wissbrun, K. F. *Melt rheology and its role in plastics processing theory and applications*; Van Nostrand Reinhold: New York, **1990**.

Appendix E: Rheological Data Establishing Processing Window for AN Copolymers

This appendix is organized in the form of notes with which rheological data was used to establish a processing window for AN copolymer systems. Further details, especially regarding effects of termonomers and synthesis methods, can be found in the references provided in Chapter 4 (by Wiles, Bhanu, and Rangarajan). This is just to provide an overview of the variables investigated and subsequent narrowing of parameters to produce a window for melt processable AN co- and terpolymers.

Chronology of Experiments:

- 85/15 mole % AN/MA identified as first melt stable copolymer, solution polymerized polymer with intrinsic viscosity 0.45 dL/g, rheological data of initial solution processed polymers shown in Fig. E1 for various intrinsic viscosities (molecular weights):

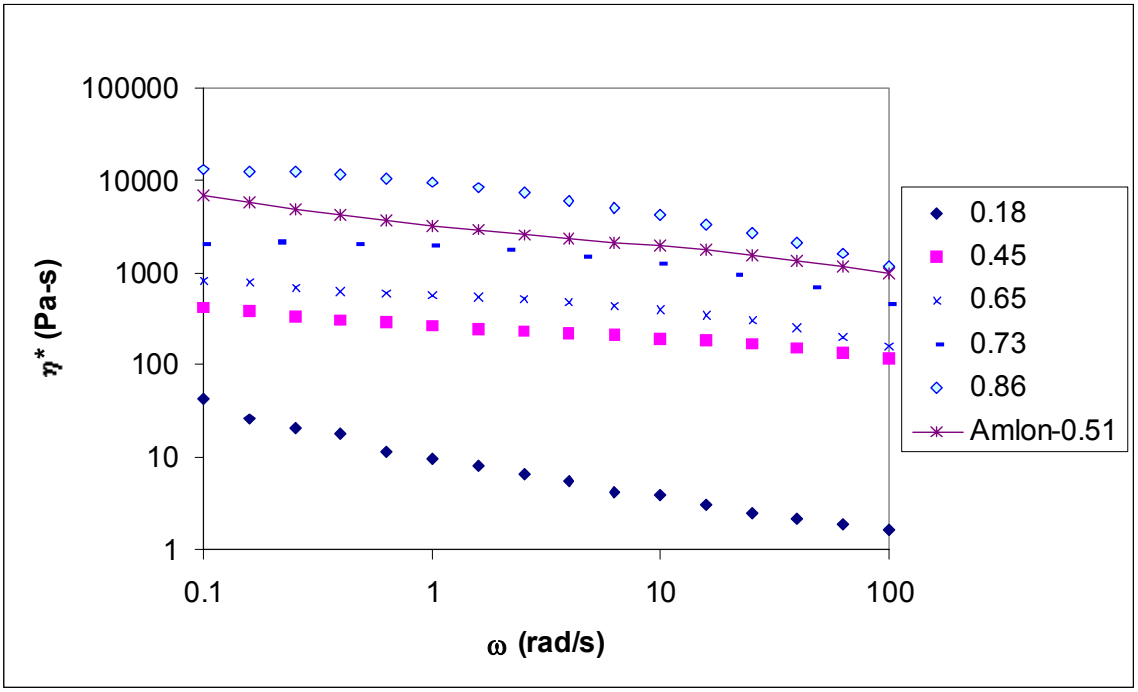

Fig. E1: Magnitude of the complex viscosity at 200°C for solution synthesized AN copolymers.

- Problems:
    - copolymers could not be stabilized by conventional thermo-oxidative means
    - despite having reasonable viscosity levels, time dependence of viscosity not indicated by dynamic data, nor does it shear sample to the same extent as in extrusion … as a result, samples that appeared melt processable would crosslink quickly during batch melt extrusion/spinning operations and fail to produce fiber

- Solution to rheological measurement problem: Use of steady shear rheological measurements to determine time dependence of viscosity (shear rate 0.1 s^{-1}). Shear rate chosen to ensure consistent measurement without edge fracture, also to minimize chance of overloading transducer on rheometer.
- It was believed that terpolymerization of acids would catalyze stabilization, i.e. itaconic, methacrylic, or acrylic acid. Effect of itaconic acid in 1-4 mole % shown in Figs. E2-E4:

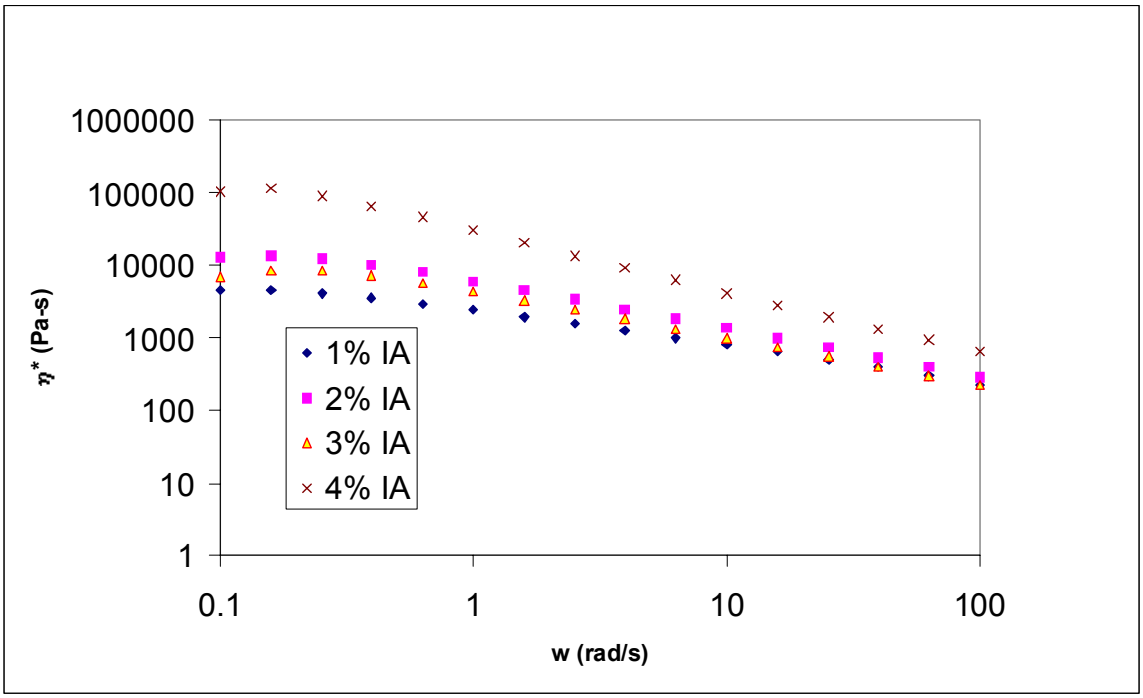

Fig E2: Magnitude of the dynamic viscosity at 200°C for solution synthesized 85 mole % AN terpolymers containing 1-4 mole % itaconic acid and the remainder MA.

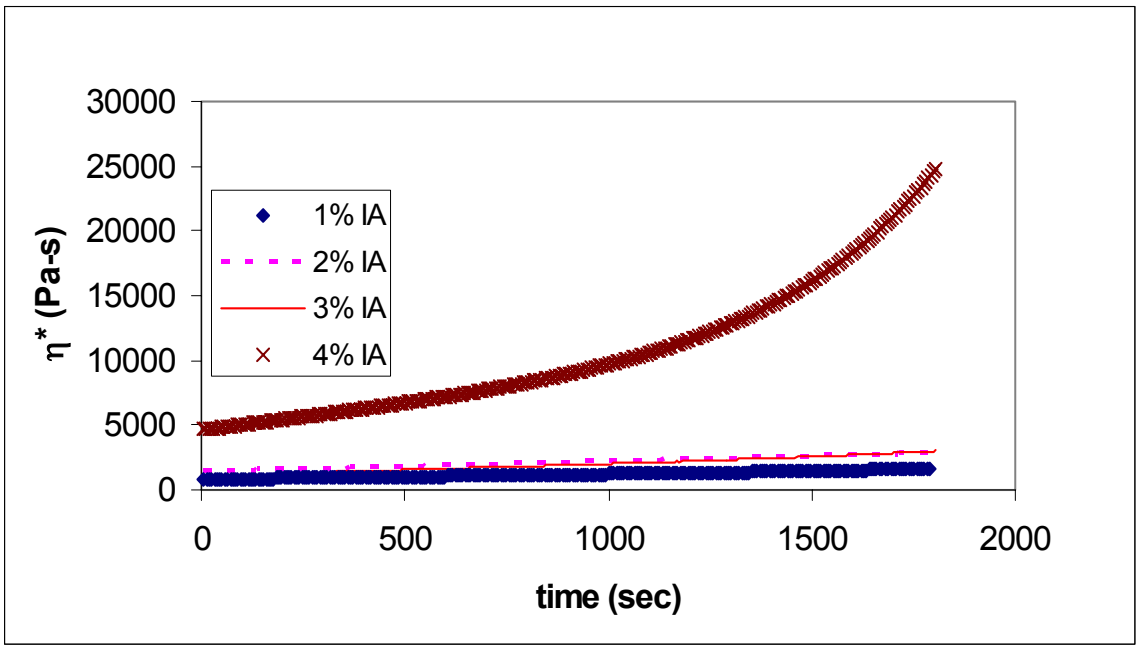

Fig E3: Steady shear viscosity as a function of time at 200°C for 85/15 AN/MA terpolymers containing 1-4 wt. % itaconic acid. Viscosity rises only ~100% in the 1-3 mole % IA samples, but by 400% with 4 mole % acid.

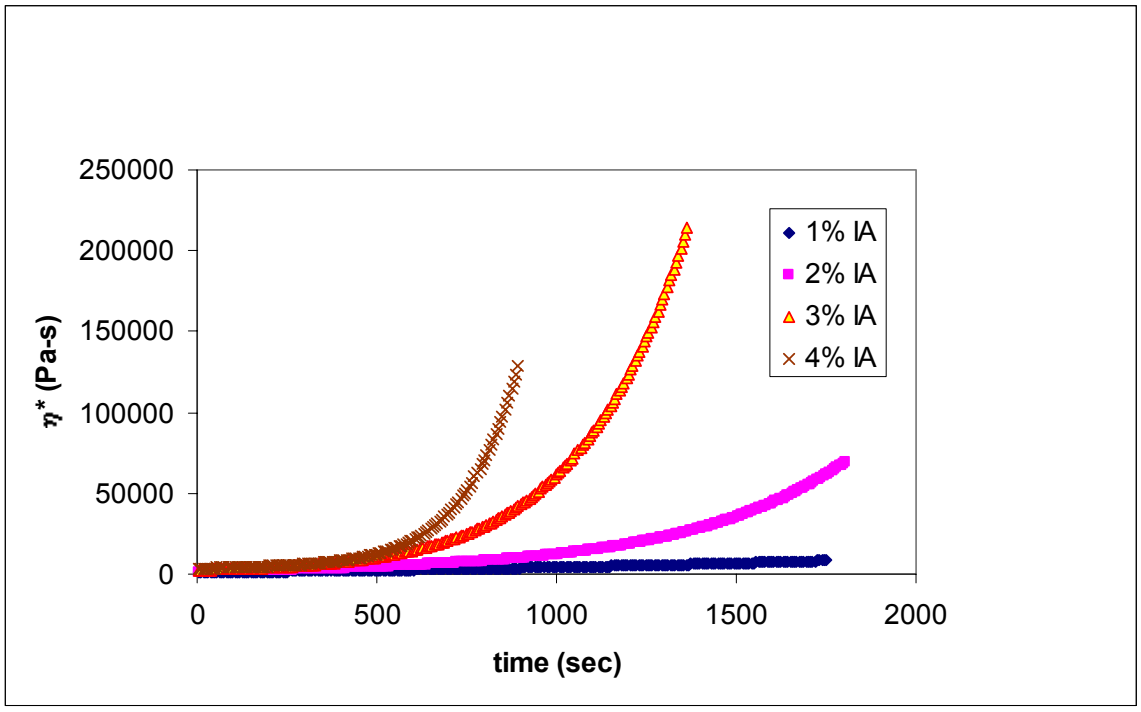

Fig E4: Steady shear viscosity as a function of time at 220°C for 85 mole % AN terpolymers containing 1-4 mole % itaconic acid. Viscosity rises between 700% to 84 fold between the 1-3 mole % IA samples.

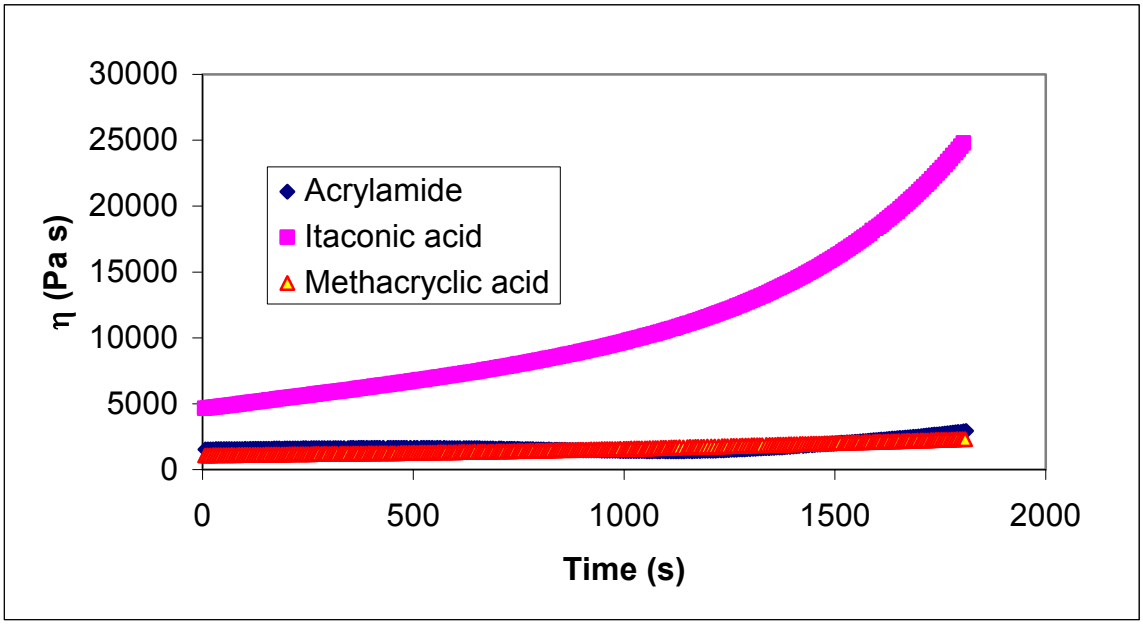

Fig E5: Steady shear viscosity as a function of time at 220°C for 85/11/4 mole % AN/MA terpolymers containing either acrylamide, itaconic acid, or methacrylic acid. Viscosity rises between 7 to 84 fold between the 1-3 mole % IA samples.

- The data in Figs. E4 and E5 suggest that viscosity too high at 200°C, and crosslinks too quickly at 220°C. As a result, acid based terpolymers resulted in systems that were too unstable to pull a consistent filament at temperatures where the viscosity was reasonable for melt processing. Despite having reasonable viscosity levels in Fig. E5, AN terpolymers of methacrylic acid possessing a significant molecular weight for melt strength and mechanical properties could not be processed

- Project focus was now shifted to maximizing AN content to obtain reasonable viscosity levels for melt processing.

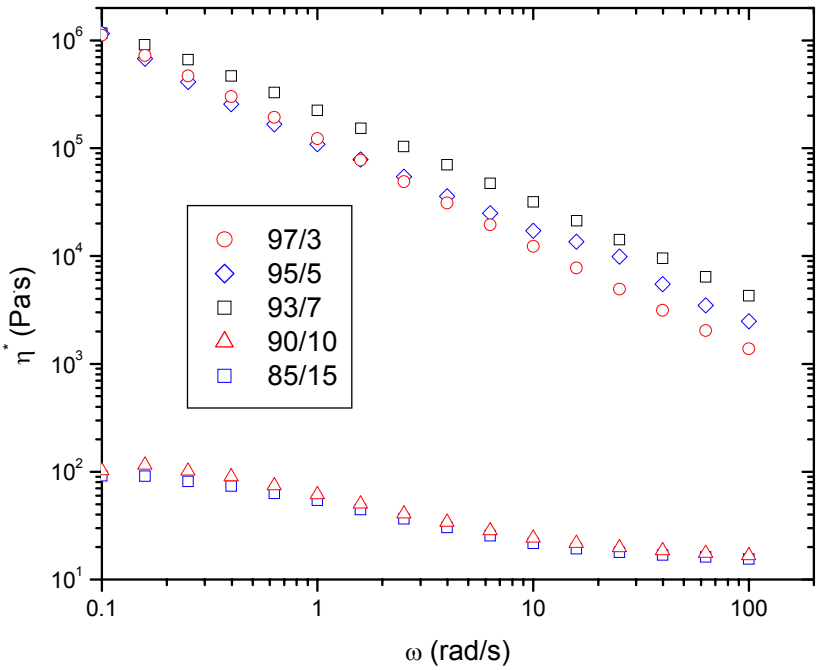

Fig. E6: Magnitude of the complex viscosity at 220°C for AN/MA copolymers produced by homogeneous (solution) polymerization method. Note discontinuity between 90 and 93 mole % AN. IV of all polymers ~0.25 dL/g.

- A series of copolymers was produced to determine effect of AN content on viscosity. It is obvious here that above 90 mole % AN, there is a discontinuous increase in viscosity. As a result, it was generally found that AN copolymers with AN content > 90 mole % could not be successfully characterized (rheologically), nor processed into fibers. In fact, resins would begin to degrade before flowing.

- Also, at this point, external stabilizers were considered to facilitate melt spinning without interfering in stabilization post precursor formation

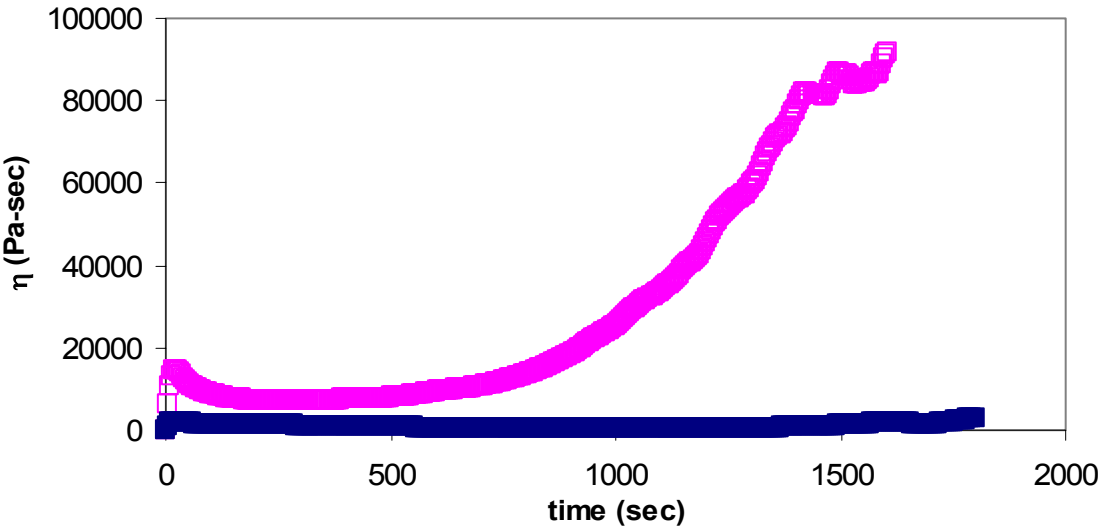

Fig. E7: Steady shear viscosity of a 90/10 AN/MA copolymer at 220^{o}C with and without an external stabilizer (boric acid). Blue curve shows viscosity of polymer containing stabilizer.

- Boric acid shown to significantly reduce crosslinking and increase melt stability. Polymer in Fig E7 was 90/10 AN/MA, I.V. 0.52 dL/g. Viscosity of pure polymer too high for melt processing, also too unstable. Boric acid was identified as a stabilizing additive
- AN content lowered to 88 mole % (88/12 AN/MA), resultant resin could be processed into fiber form and converted into carbon fibers, but results were not reproducible

- To address project goals of more environmentally friendly process, synthesis method shifted away from solution method to suspension and emulsion methods
- Also, alpha methyl styrene was terpolymerized to disrupt long range order/improve melt stability of AN copolymers.

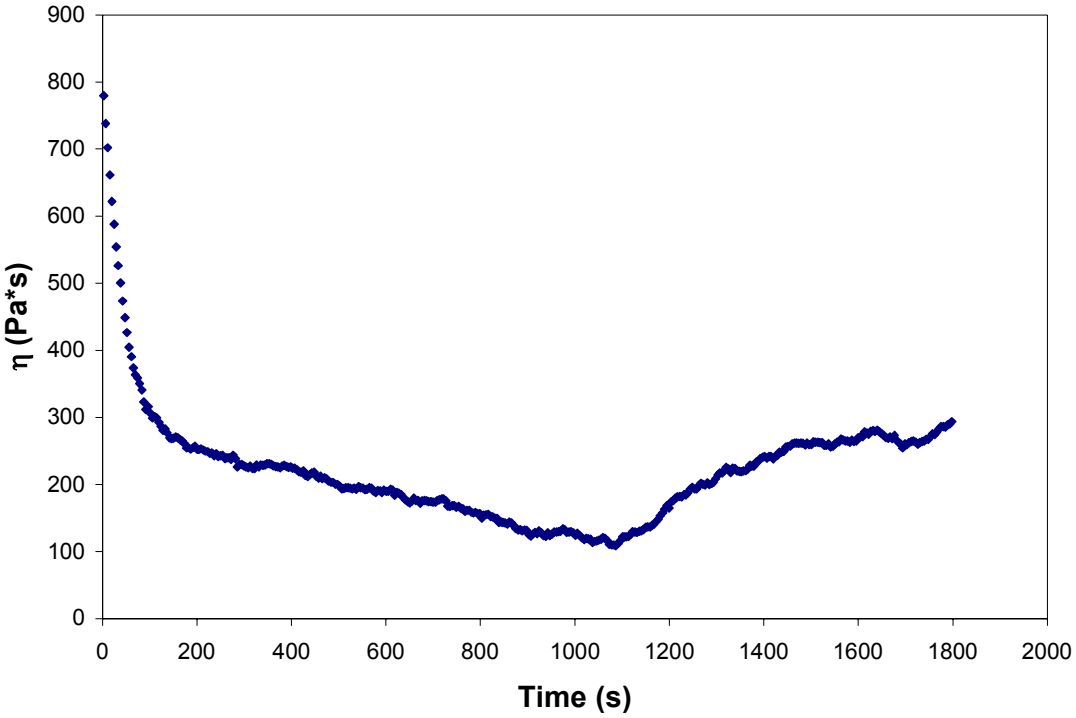

Fig. E8: Steady shear viscosity as a function of time for an emulsion polymerized 88/12 AN/MA copolymer, mechanically blended with 2 wt. % boric acid (BA), at 220^{o}C.

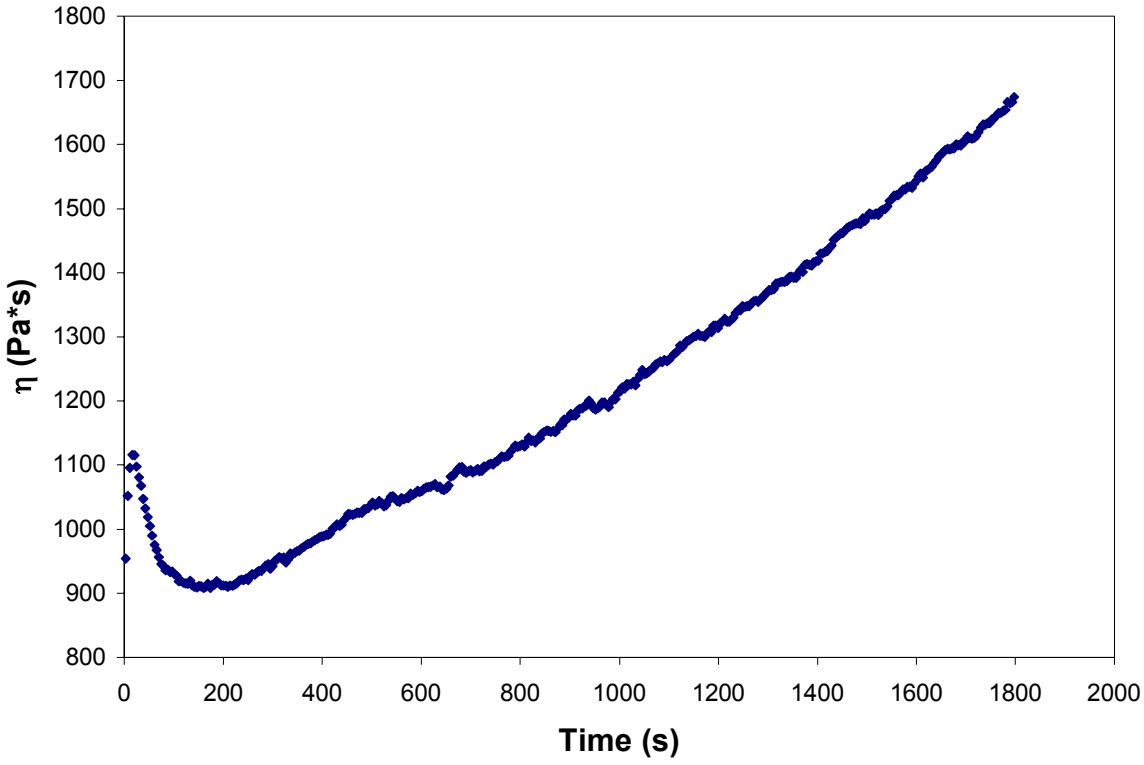

Fig. E9: Steady shear viscosity of 87.5/12.3/0.2 AN/MA/alpha methyl styrene (AMS) emulsion polymerized terpolymer, mechanically blended with 2 wt. % BA, at 220^{o}C.

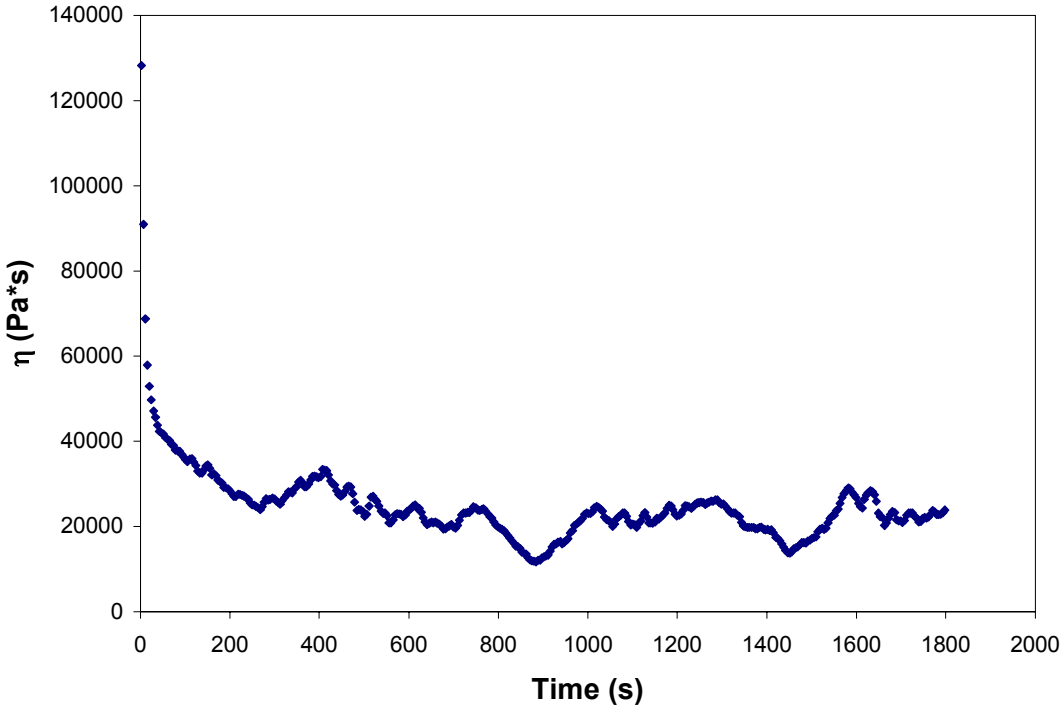

Fig E10: Steady shear viscosity of 92/5.5/2.5 AN/MA/ (AMS) emulsion polymerized terpolymer, mechanically blended with 2 wt. % BA, at 220^{o}C.

- Note between 87.5 to 92.5 mole % AN (Figs. E9 and E10)that the steady viscosity increases ~ 2 orders of magnitude

- Emulsion polymerizations were reproducible, but there was also interest in a suspension polymerization, which is a one step process (the material falls out of solution) and it is a water-based system (environmentally friendly). The emulsion process requires break up of the latex and then separation of product (2 step process). Hence, a suspension synthesis route was very desirable for this project.

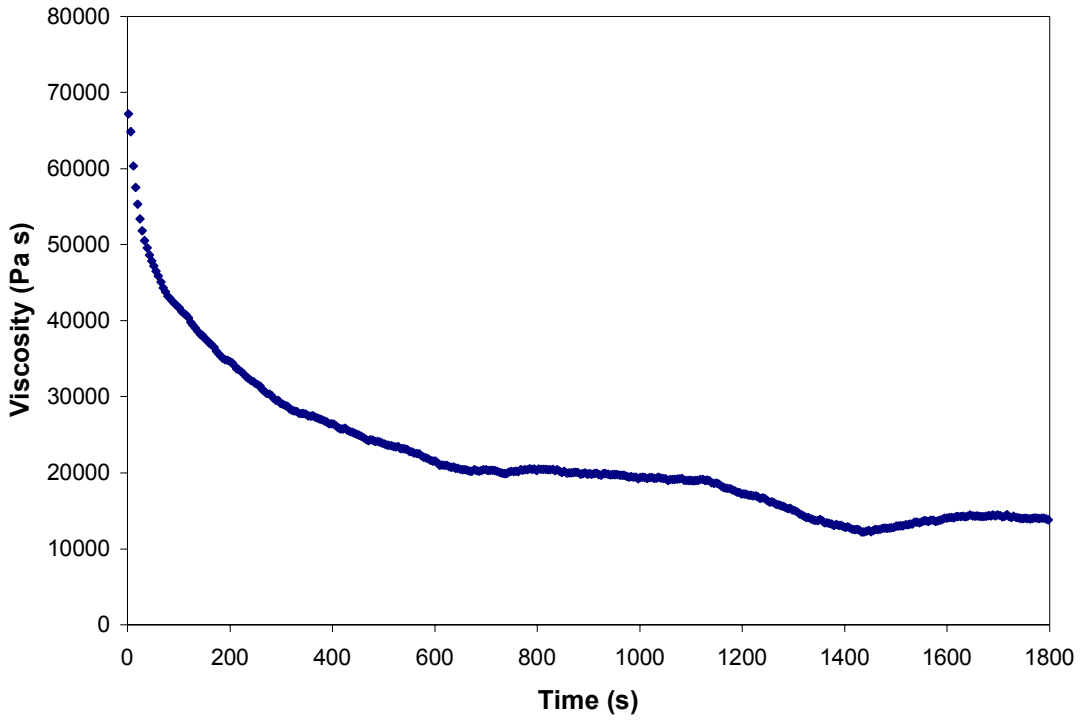

Fig E11: Steady shear viscosity of suspension polymerized 88/12 AN/MA copolymer (containing 2 wt. % BA) at 220^{o}C. Note the viscosity is relatively stable, but too high for melt processing.

- Suspension polymerized materials could not be reproducibly synthesized, and the polymerization method was also difficult. Emulsion materials were very

reproducible, and as a result this polymerization method was identified as the best to synthesize melt processable materials consistently and reliably.

- Thus far, most co- and terpolymers were produced with intrinsic viscosity (IV) between 0.25-0.5 dL/g, but focus was directed on pinpointing a polymerization method and AN content (emulsion synthesis, 85-90 mole % AN, boric acid identified as melt processable). Still problem of poor properties in the carbonized fibers, either because the molecular weight was too low or the materials would flow during stabilization and lose orientation as temperature during stabilization was increased. Hence, focus now shifted to suitable termonomer and molecular weight.

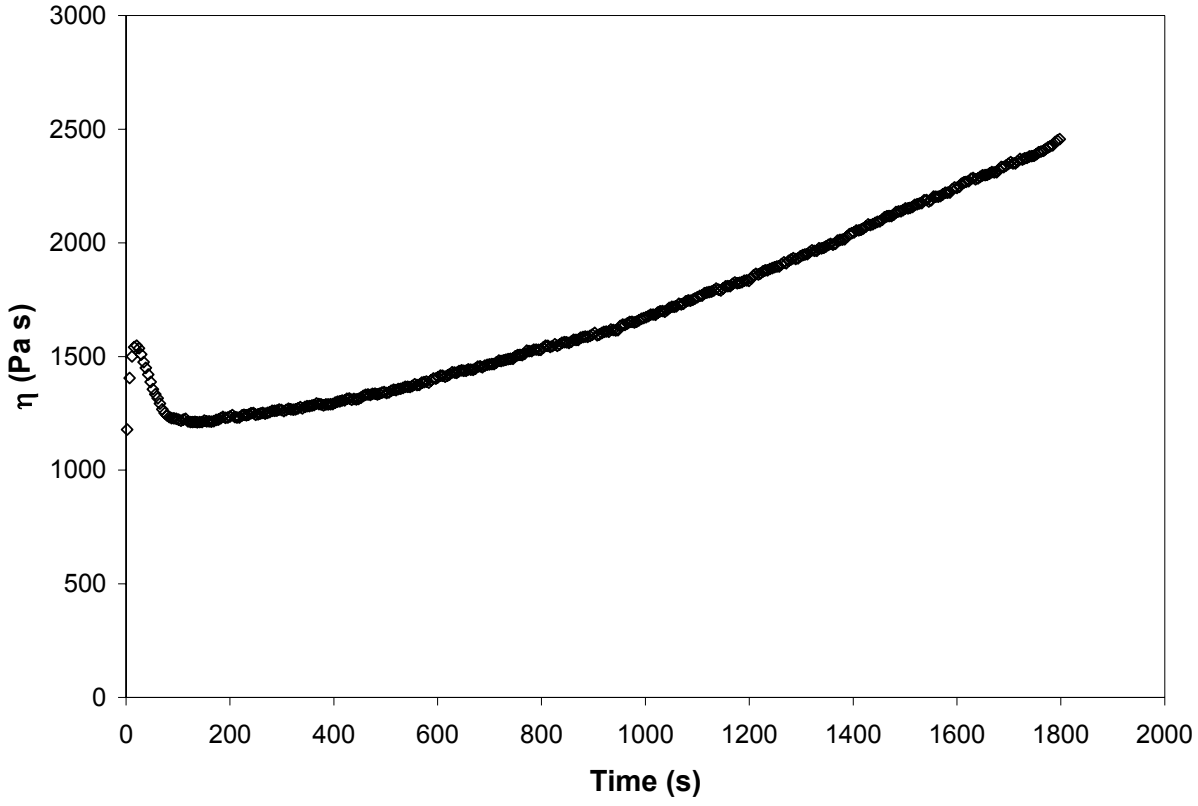

Fig E12: Steady shear viscosity of 87.5/12.3/0.2 AN/MA/AMS (+2 wt. % BA) at 220^{o}C. I.V. 0.5 dL/g.

- Sample in Fig E12 was able to be melt spun and converted into carbon fibers. It was reproduced multiple times in 5-10 gram quantities. However, scaling the materials up to 70-80 gram quantities resulted in inconsistent results, as seen in Fig E13.

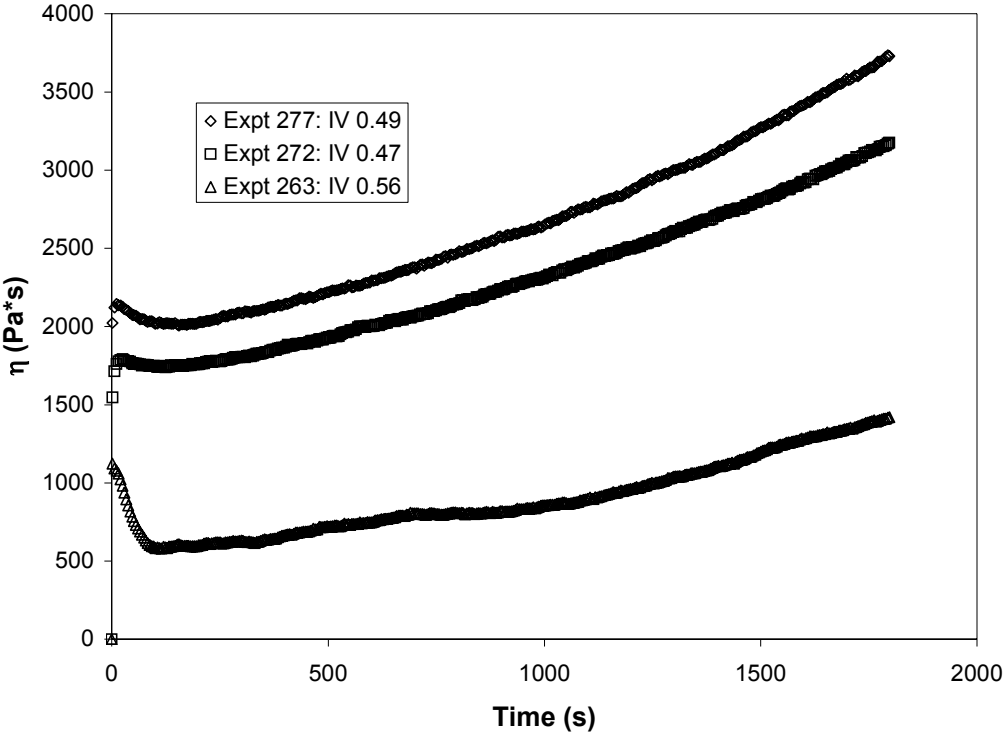

Fig E13: Steady shear viscosity of scaled up AN/MA/AMS terpolymers containing 87.5 mole % AN at 220^{o}C. All samples contained 2 wt. % BA.

- Most of these materials could be melt processed into precursor fiber form, but the precursor fibers could not be carbonized by thermo-oxidative means.
- It was determined that lack of reproducibility was due to pushing upper limit of AN content, which around 89% caused significant changes in the viscosity, as seen in Fig E14:

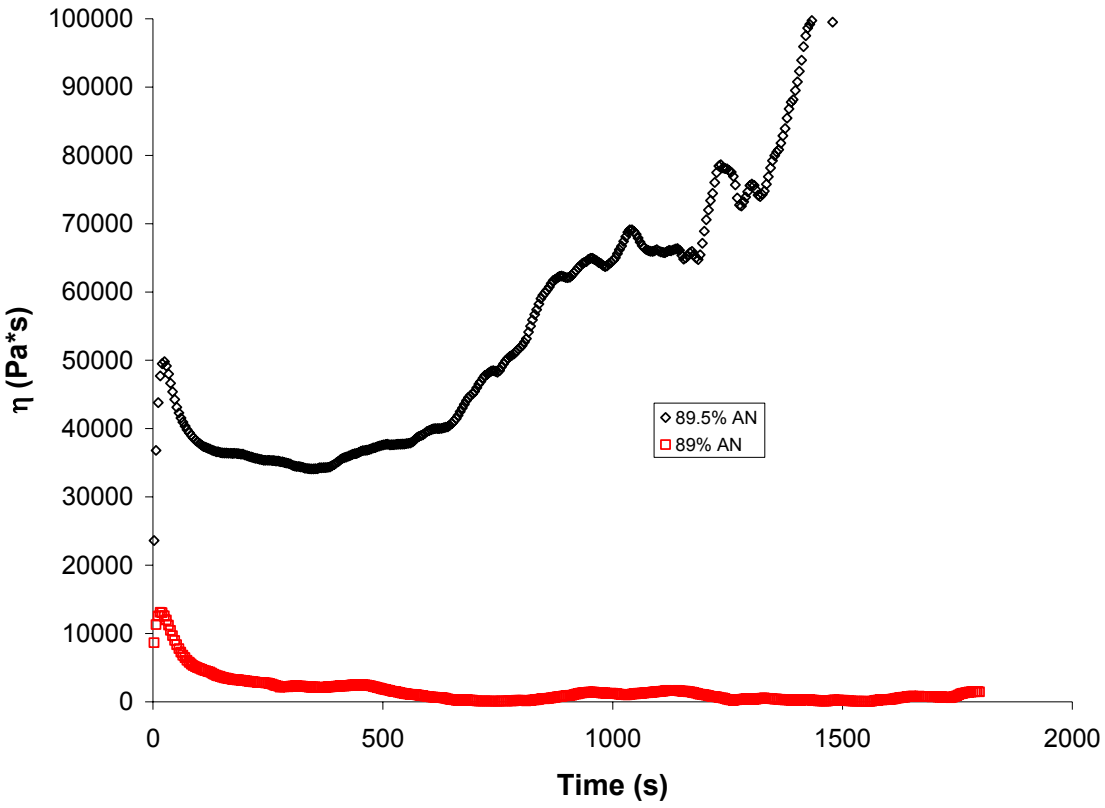

Fig E14: Steady shear viscosity of 89 and 89.5 mole % AN/MA emulsion copolymers containing 2 wt % BA at 220^{o}C.

- To prevent reproducibility problems, especially at AN content levels around 88-89% where 1 mole % difference significantly affects properties, 85 mole % was chosen as a base, which was proven to produce some materials that to this point have been successfully melt spun and converted into carbon fibers.
- About this point, it was decided to pursue acryloyl benzophenone as a termonomer, which is photoactive and could ideally be initiated following formation of precursor fibers. The expectation was to prevent thermal initiation of the UV component at melt temperatures, but following to initiate crosslinking via UV following precursor generation to accelerate crosslinking and prevent flowing of fibers during stabilization. The theory worked: a comparison of the viscosity of 85/15 AN/MA and 85/14/1 AN/MA shown in Fig. E15, and an example of multiple experiments used to narrow the intrinsic viscosity is presented in Fig. E16.

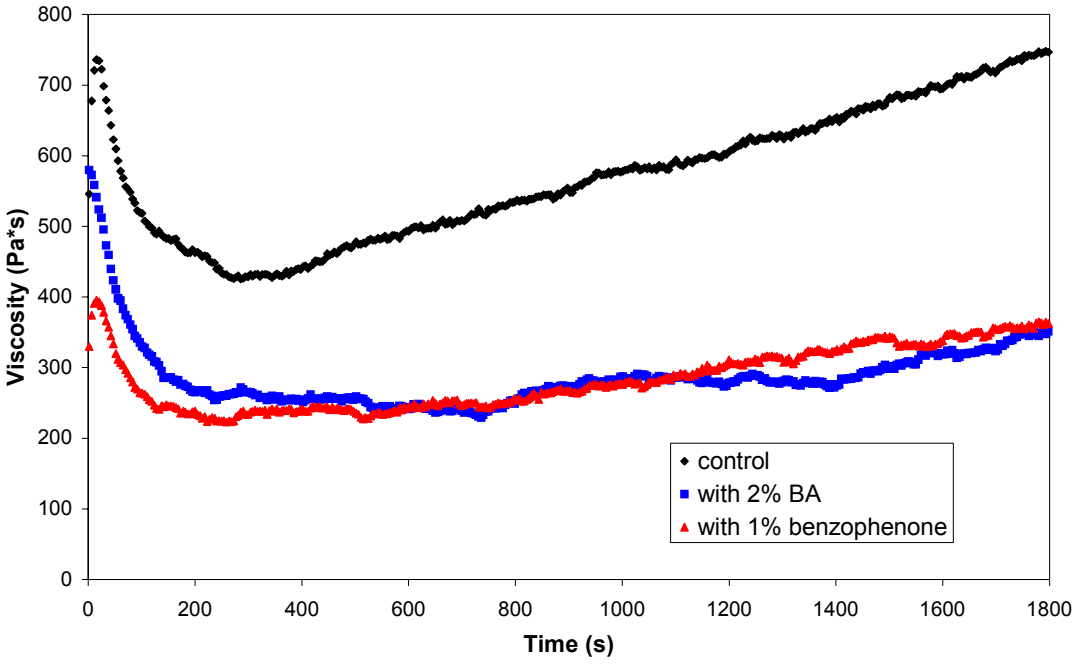

Fig E15: Steady shear viscosity of 85/15 and 85/14/1 polymers at 220°C, IV 0.45 dL/g.

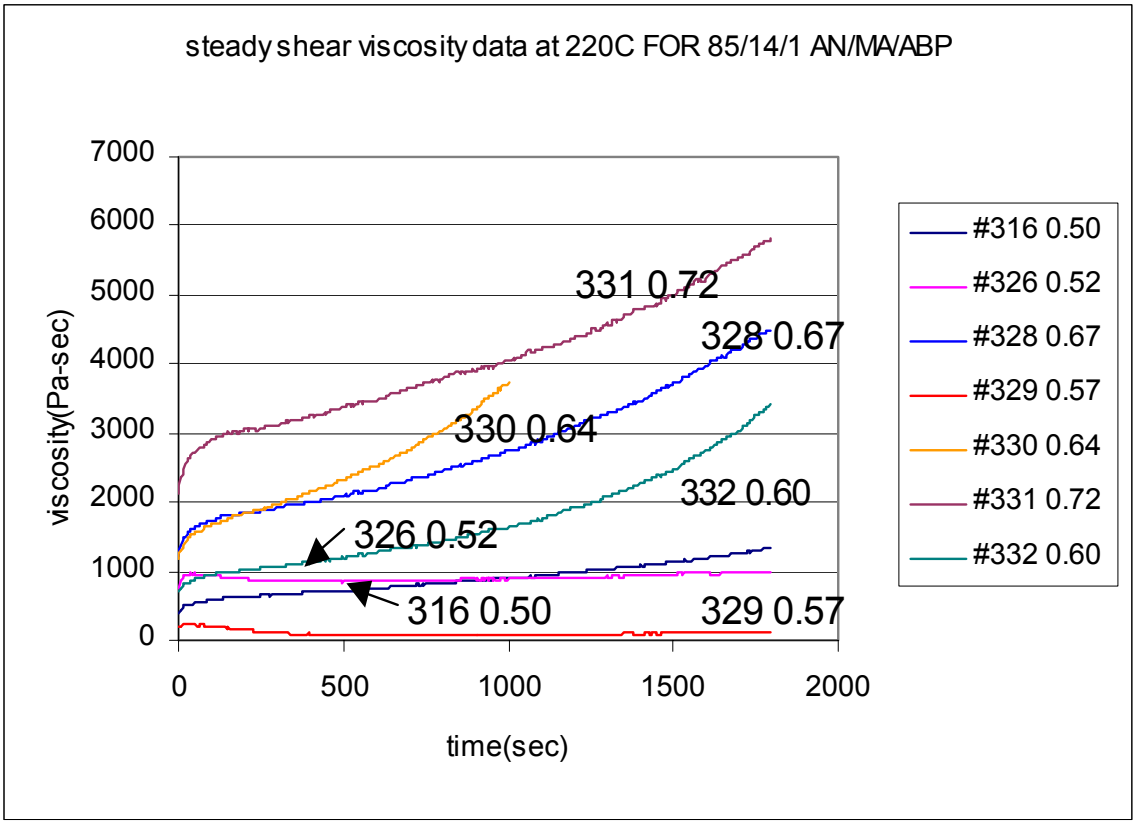

Fig E16: Narrowing of IV (molecular weight) for 85/14/1 AN/MA/ABP terpolymers. Numbers in legend and on graph refer to experiment numbers (#316-332) and IV (0.50-0.72).

- At this point, the materials discussed in Chapter 3 were systematically scaled up to 1 kg quantities by an industrial collaborator (see Ch. 3 and 4). 85/15 and 85/14/1 AN/MA and AN/MA/ABP terpolymers were identified as melt processable and scaled up. IV was narrowed to a maximum of ~0.6 as seen in Fig E16, above which kinetics of crosslinking too high and cause viscosity to rise too quickly over time. Further experimentation with various termonomers and additives have been briefly investigated, but these conditions produced a precursor polymer that could be industrially scaled up, melt spun, and converted into carbon fibers with reasonable properties (see Fig. E17).

Precursor fiber:

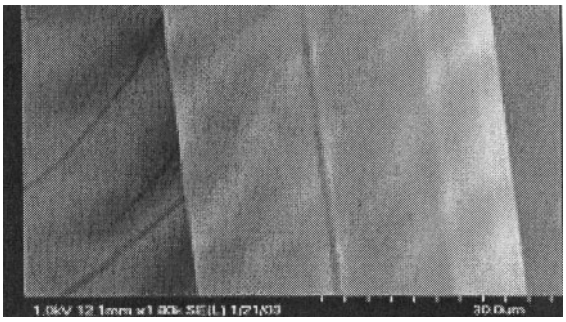

Carbonized fiber:

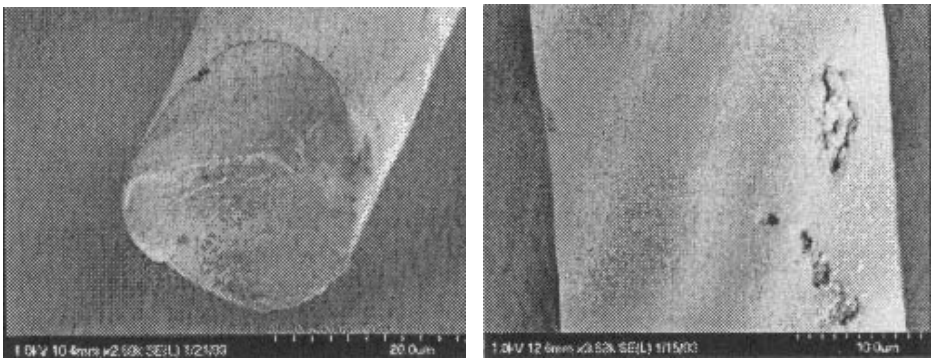

Figure E17: SEM images of carbon fibers and precursor fibers, spun at 210^{o}C, from the 85/15 scaled up resin (as described in Ch. 3). Carbon fibers produced with similar resins having tensile strength of approximately 1.0 GPa and tensile modulus of approximately 120 GPa.

Vita

The author was born in York, PA on January 18, 1977. He spent the majority of his childhood in Glen Rock, PA, where he graduated from Susquehannock High School in 1994. Upon completion of high school, he went on to attend The Pennsylvania State University, where he received his B.S. in Chemical Engineering with a focus in polymer characterization and processing in December 1998. The author performed undergraduate research for the API (American Petroleum Institute) under the direction of Dr. Thomas Daubert, in which he developed prediction methods for physical properties of petroleum fractions. The combination of his interest in polymers and research led the author to Virginia Tech for graduate school in January 1999. Under the direction of Dr. Donald G. Baird, he performed research on the melt processing of acrylic copolymers for carbon fiber precursors, and received his Ph.D. in Chemical Engineering in November of 2003. He was offered and accepted a position as a research scientist at Nanosonic, Inc. in Blacksburg, VA.

Michael Jeremiah Bortner